May 2019

# Electrically-Driven Ion Transmission Through Two-Dimensional Nanomaterials

Saheed Abidemi Bukola
*Clemson University*, bsaolu@gmail.com

# ELECTRICALLY-DRIVEN ION TRANSMISSION THROUGH TWO-DIMENSIONAL NANOMATERIALS

---

A Dissertation
Presented to
the Graduate School of
Clemson University

---

In Partial Fulfillment
of the Requirements for the Degree
Doctor of Philosophy
Chemistry

---

by
Bukola Saheed Abidemi
May 2019

---

Accepted by:
Professor Stephen E. Creager, Committee Chair
Professor Carlos D. Garcia
Professor William Pennington
Professor Joseph Thrasher

ABSTRACT

Two-dimensional nanomaterials such as graphene and hexagonal boron nitride are being intensively studied as selective barriers in separation technology owing to their unique subatomic selectivity. In their pristine forms, they are impermeable to atoms, molecules, and ions except for thermal protons. Graphene, with its angstrom-scale thickness, is regarded as the thinnest membrane so its transport selectivity comes from the selectivity of active sites at which permeant transmission occurs. This dissertation tested the hypothesis that the selectivity ratio of hydrogen isotopes (protium, Deuterium, and tritium) through membrane could be improved by incorporating graphene and related 2D materials in the membrane electrode assembly of a polymer electrolyte membrane electrolysis cell. The mechanism by which protons or deuterons traverse the energy barrier of 2D materials was also investigated with a focus on the temperature dependence of isotopic selectivity in crossing rates. By carefully positioning a 2D material within the ionomer membranes of a membrane electrode assembly, the isotopic ion filtering functionalities of graphene and analogs were enhanced. Proton transmission through graphene was found to occur at a very high rate (1.0 A $cm^{-2}$ achieved at a potential bias of < 200 mV) with a selectivity ratio of at least 10 compared to deuteron transmission. The transmission rates of Protons and deuterons across single-layer graphene were measured as a function of temperature. An electrochemical model based on charge-transfer resistance was invoked to estimate standard heterogeneous ion-transfer rate constants. An encounter pre-equilibrium model for the ion-transfer step was used to estimate rate constants which provide values for activation energies and exponential pre-

factors for proton (or deuteron) transmission across graphene. Activation energies of 48 ± 2 kJ $mole^{-1}$ (0.50 ± 0.02 eV) and 53 ± 5 kJ $mole^{-1}$ (0.55 ± 0.05 eV) were obtained for protons and deuterons respectively, through single-layer graphene. The difference of 50 meV is in good agreement with the expected difference in vibrational zero-point energies for O-H and O-D bonds.

This work is an important harbinger for the prospects of developing graphene-based PEM electrochemical cell ion filters for fuel cells, electrolysis cells, gas separation and purification, and desalination applications.

# DEDICATION

To the glory of Almighty God and to my beloved late father, Bukola Iyiola Sulaiman.

ACKNOWLEDGMENTS

All thanks and praises are due to Almighty God for seeing me through and for the successful completion of my Ph.D. program. My unfeigned appreciation goes to Professor Stephen Creager for his thoughtful, support and guidance in directing my Ph.D. work. His genuine personality, knowledge of science, hospitality, and inclusiveness make me adore him. My advisor never gets frustrated with any student in the group but rather supports and encourages everyone. I thank the members of my Ph.D. committee; Prof. Garcia, Prof. Thrasher and Prof. Pennington for their scientific contributions to my work.

My special thanks to my wife, Fatima Adebayo Bukola; and my kids, Fahmida and Azeem for their support and endurance and for making me a better man. I must but register my appreciation to my mother, brothers and sisters for their prayers over me. I appreciate the support of our group members both the past (Dr. Iqbal Sharif, Dr. Jamie Shetzline and Ms. Yutung Chen) and present (Lakshman Ventrapragada, Kyle Beard, Bryan Bill, Cassandra Hager, Liyanage Mayura, and Luke Gormley). I also appreciate the efforts of Prof. Carol Korzeniewski of Texas Tech University and Prof. Joel M. Harris of the University of Utah for their help with the confocal Raman microscopy measurements. I thank Cao Duyen (aka Dana) and Dr. Alex Martinson from Argonne National Laboratory for their help with the atomic layer deposition works on graphene samples. I also thank George Wetzel (Clemson Electron Microscope Laboratory) for his help during the spectroscopic characterization of my samples.

Finally, I appreciate the assistantship opportunity provided by the Department of Chemistry at Clemson University for my Ph.D. program.

TABLE OF CONTENTS

Page

Table of Contents (Continued) Page

Table of Contents (Continued) Page

LIST OF TABLES

List of Tables (Continued)

Table Page

LIST OF FIGURES

List of Figures (Continued)

Figure Page

List of Figures (Continued)

Figure Page

List of Figures (Continued)

List of Figures (Continued)

Figure Page

List of Figures (Continued)

Figure Page

List of Figures (Continued)

Figure Page

List of Figures (Continued)

Figure Page

List of Figures (Continued)

Figure Page

List of Figures (Continued)

Figure Page

LIST OF SCHEMES

# CHAPTER ONE

# ION TRANSMISSION IN TWO-DIMENSIONAL MATERIALS

## 1.0 INTRODUCTION

Graphene, a two-dimensional hexagonal carbon network with a honeycomb lattice has received considerable research attention owing to its unique properties. It is one-atom thick, making it the thinnest membrane with unprecedented ultra-high carrier mobility (10000 $cm^2$ $V^{-1}$ $s^{-1}$), [1,2] high surface area (2630 $m^2$ $g^{-1}$),[3,4] electrical conductivity (104.36 S $cm^{-1}$),[3,5] chemical and thermal stability. It has a breaking strength as high as 42 N $m^{-1}$ with its' Young's modulus of about 1.0 x $10^{12}$ Pa[6] Its optical property came from its ultrathin thickness (1.0 Å) with ≈ 97 % of white light being able to be transmitted through it.[2] Graphene has become a paradigm for other 2D materials such as hexagonal boron nitride (hBN), transition metal dichalcogenides (TMDs), layered double hydroxide (LDH) and so on. These aforementioned properties of graphene and related 2D materials have been instrumental in their consideration for wide range of applications such as electronics / optoelectronics, electrode materials, batteries, sensors, and supercapacitors.[7–13]

More importantly, recently discovered high proton conductance at ambient temperature will make these materials revolutionary for energy storage devices and separation technologies.[14–16] Graphene, with its angstrom-scale thickness is impermeable to any molecules, atoms, and ions. This unique impermeability of graphene and other 2D materials is rooted in their atomic/electronic structure. For example, the hexagonal hollow graphene pore has a size of about 0.064 nm.[6,17,18] This size is far less than the van

der Waals radius of the smallest monatomic gas He (0.28 nm) and molecular hydrogen (0.314 nm).[6] The hexagonal carbon network in graphene is dominated by π electrons that form a dense electron cloud encapsulating the graphene layer making it impermeable to any known permeant species. As a result of this impermeability, graphene has previously being used as a selective barrier by intentionally creating artificial defects into the graphene sheet.

Precisely, four years following mechanical exfoliation of free-standing single-layer graphene,[1] Michael and co-workers[19] reported a successful creation of nanometer-scale pores into graphene with a controlled focused beam of a transmission electron microscope. In a similar work, Koenig et al.[20] demonstrated the use of ultraviolet-induce oxidative etching to create certain micrometer pore sizes in graphene sheets. The defective graphene sheet was then used as a molecular sieve for gas separation. In separate but related work, Du and co-workers designed a series of porous graphene of various pore sizes and shapes to separate hydrogen and nitrogen gases.[21] Surprisingly, recent experimental findings have demonstrated the possibility of thermal proton transmission through pristine graphene at ambient temperature using an electrochemical hydrogen pump method.[16,22] This experimental finding was unexpected because of the high energy barrier (> 1.0 eV)[23] predicted by computational studies for proton permeation through graphene would make such transmission impossible.

Area-normalized proton conductance values of 3-90 mS $cm^{-2}$ were obtained from prior work through single-layer graphene with proton selectivity being favored over deuteron by at least a factor of 10.[24] This range values is high compared to the

expectation of zero proton permeability through graphene sheet but however, still low when compared to the proton conductivity of PFSA membrane (12-15 S $cm^{-2}$ at ambient temperature).[16] For practical application, the graphene areal conductance for proton transport still needs further improvement before electrochemical hydrogen isotope separation can become a viable separation option. It has long been desired to have a viable hydrogen isotope separation technology. Hydrogen isotopes are useful in nuclear fission reactors, contrast agents in neutron scattering,[22] labeling agents in NMR and in many other applications.

Existing technologies for hydrogen isotope separation such as cryogenic distillation,[25,26] water-sulfide exchange,[27] and thermal cycling absorption process[28] are highly energy intensive with a selectivity factor less than 2.5.[29] An electrochemical hydrogen pump with graphene embedded within the membrane electrode assembly (MEA) may offer a cost effective alternative with a much better selectivity factor. Though such an electrochemical technique for hydrogen isotopic separation seemingly looks promising and attractive, the requirement of having pristine graphene free of defects in the MEA to achieve better selectivity on a large scale remains a greater challenge. The first demonstration of this exciting idea was done on a micrometer-size 2D graphene of highest quality.[24] The major disadvantage of this approach is that it is not scalable. A modern technique for large scale production of high-quality 2D materials (including graphene) is needed before an electrochemical technique could become the next generation hydrogen isotope separation technology.

The synthetic routes to produce 2D materials can be categorized into two: (1) the top-down approach and (2) the bottom-up method.[2,6,30] The prominent top-down method is the micromechanical exfoliation, the original approach that led to the discovery of free standing single-layer graphene. This is done by the application of a mechanical force through the use of adhesive tape to weaken the van der Waals forces of attraction between the graphite layers without disrupting the in-plane covalent bonds network of individual layer. Only a few to tens of micrometer size of 2D material can be produced with this technique and for which large scale production is not possible. Other methods in this category are oxidation-assisted liquid exfoliation[9,31,32], ion exchange-assisted liquid exfoliation, and ion intercalation-assisted liquid exfoliation.[30,31] The bottom-up category includes the chemical vapor deposition (CVD) method and wet chemical synthesis.[35–40] Large area 2D materials can be produced with the bottom-up technique but the growth may lead to defective graphene. The extent of the defects depends on the growth conditions, substrate and precursors, and expertise of the developer.

The most common methods (in the bottom-up category) of large area production of 2D materials are the epitaxial growth of 2D material on a SiC substrate[6] and CVD method on transition metal substrates using $CH_4$ as a precursor.[41–46] The CVD method remains the most effective and scalable way of growing high quality graphene and other 2D materials for large-scale application.[47,48] Two metal substrates, Ni and Cu are usually used for catalytic growth of graphene. Because it is difficult to completely suppress the precipitation of carbon on Ni as compared to Cu, Cu remains the most preferable metal

substrate for growing graphene. Carbon solubility is high on Ni (about 0.6 wt. % at 1326$^{o}$C), whereas it is relatively low on Cu (about 0.008 wt. % at 1084°C).[6,42]

Despite recent advances in growing large area graphene on Cu, CVD graphene still has some intrinsic defects. The abundance of defects and their nature depend on growing conditions. These defects may not be easily detected spectroscopically and if not properly controlled may alter the outstanding quality of these 2D materials especially for ion transmission application. The most common defects are enumerated below.

(1) Point defects: These include the "*Stone-Wales defect"* in which the rotation of two π-bonded carbon atoms by 90° creates two pentagons and two heptagons. This modification to the perfect hexagonal crystal structure in graphene still retains the pristine number of carbon atoms and does not lead to any dangling bonds. The other is called the "*Vacancy defect"* in which the rotation leads to a missing number of carbon atoms at lattice sites. [50–52] Such a defect might lead to creation of dangling bonds especially, if it involves an odd number of carbon atoms.

(2) Line defects: These defects include *"Gain boundary"* which are normally described as topological defects that can arise as a result of the occurrence of concurrent nucleations at different lattices during the growth of 2D materials by the CVD method. The other line defect is called the *"edge defect"* as is the result of the way 2D crystals end with a dangling bond.[53] The common edge structures in graphene are usually zigzag and armchair.

These types of defects in graphene will affect the quality of graphene and other 2D materials for their application toward hydrogen isotopes separation. Such a defect

could occur during the growth of the 2D crystals on substrates or during the transferring of graphene to another substrate for experimental studies.

## 1.1 Scope of the Dissertation

The overall objective of the research described in this dissertation was to study the effect of incorporating 2D materials in a membrane electrode assembly of a polymer electrolyte membrane electrolysis cell with the aim to increase the separation factor of hydrogen isotopes separation. Another objective was to investigate the mechanism by which a proton or deuteron traverses a 2D material with a focus on studying the temperature dependence of isotopic selectivity in crossing rates. By carefully positioning a 2D material within the ionomer membranes of an MEA, the isotopic ion filtering functionality of graphene and related 2D material was enhanced, and proton transmission through graphene occurred at a very high rate with a selectivity ratio of 14 when compared to deuteron transmission.

This dissertation is written in the following sequence:

**Chapter 1** is an overview of the work with a discussion on the general background of 2D materials.

**Chapter 2** includes a discussion on the development of a small-scale electrochemical cell for fuel cell exploratory research.

**Chapter 3** is a discussion on the modification of the miniature cell to be adaptable for studying hydrogen isotope selectivity through a layer of graphene in an MEA in both asymmetric and symmetric electrochemical hydrogen pump modes.

**Chapter 4** includes a discussion on efforts to gain fundamental knowledge on the mechanism by which protons traverse a 2D energy barrier. The concept, which is based on the Arrhenius analysis for a thermally-activated process, involves measurement of proton and deuteron transmission rates across single-layer graphene as a function of temperature.

**Chapter 5** includes a discussion on measurement of alkali cation including ammonium ion transport in aqueous electrolytes to understand the nature of defects in a CVD graphene.

**Chapter 6** includes a discussion on a comparative study of proton and deuteron transport in single-layer vs multi-layer graphene.

**Chapter 7** includes a discussion on the use of the atomic layer deposition technique to seal the defect in CVD graphene. The latter part of this Chapter covered a discussion on other 2D materials (*i.e*. hexagonal boron nitride) and related pyrochlore oxide materials.

**Chapter 8** is a discussion on the author's perspective on the future work on 2D material for ion transmission and potential applications of this class of materials in separation technologies. The readers are referred to the list of publications in the appendices and also the papers appended at the end of this dissertation for further technical discussion on this work.

# CHAPTER TWO

# A MINIATURIZED ELECTROCHEMICAL CELL FOR FUEL CELL EXPLORATORY RESEARCH

## 2.0 SYNOPSIS

The work described in this chapter has been published with the following bibliographical details, *Journal of Electroanalytical Chemistry* (2017) 797, p. 8-15. It describes a miniaturized electrochemical cell that allows replicating studies on a very small amount of materials. This is particularly useful for studies on new ionomer and electrode materials that may be available only in small quantities from new research. It is a complete revision from the prior work of a former student. This work addresses the key challenges of prior cell design and fabrication including reproducibility, better performance, and control of cell geometric area.

## 2.1 INTRODUCTION

Proton exchange membrane (PEM) fuel cell technology has been envisioned to be an energy source target, especially for the automotive application as an alternative to the internal combustion engine (ICE) that uses fossil fuel.[54,55,64, 65,56–63] A fuel cell generally is similar to a battery; both fuel cells and batteries covert chemical energy into electrical energy.[66,67] Unlike a battery, that needs to be discarded when chemical fuels are exhausted (e.g. primary battery, except dry cell) or recharged using an external source of power (e.g. secondary battery), a fuel cell can supply electricity indefinitely when there is a fuel (hydrogen) and an oxidant (oxygen or air).[68–71]

In a typical PEM fuel cell device, the major component is the membrane electrode assembly (MEA) that comprises (1) the anode, where the fuel (hydrogen gas) is oxidized by the catalyst layer to generate proton ($H_2 \longrightarrow 2H^+ + 2e^-$), (2) the perfluorosulfonic ionomer membrane (a cation conductor) that allows proton through it to the cathode compartment and (3) the cathode, where the fuel combines with the oxidant (air or oxygen gas) to produce electricity and water ($O_2 + 4H^+ + 4e^- \longrightarrow 2H_2O$). The beauty of a fuel cell is that the end product of the electrochemical reaction between the oxidant and fuel is water making it a zero-emission and environmentally friendly source of energy.[72–75]

Research in PEM fuel cells has been very active during the last few decades as a result of efforts to address the key challenges impeding the full commercialization of this technology.[76] These challenges include developing active electrocatalysts with the high kinetic facility to address the issues of slow oxygen reduction reaction, replacing precious metal catalysts (platinum group metals) with cost-effective and earth-abundant electrocatalysts. While the last two decades of research has led to a significant understanding of materials properties and device behavior, current research efforts focus on the development of cost-effective new ionomer materials and electrocatalysts.[77–81] These materials are usually synthesized in small quantities from early research and need to be appropriately characterized in order to understand how they will behave in real application testing. Real application testing involves preparing the catalyst supports and the ionomer material as an MEA. The MEA is then subjected to proper gas

humidification (to avoid drying out) as a function of temperature while evaluating material properties and behavior in a fuel cell device.

MEA fabrication for real fuel cell application is intricate, time-consuming and requires a very large amount of both ionomer material and electrocatalyst for a single measurement.[66] More importantly, PEM fuel cell testing requires special training and skills in addition to the fact that the testing is usually done on a specialized instrument that is not generally available in most electrochemical labs. As a result, a fast catalyst-screening technique is desirable especially for characterization of new ionomer materials and newly developed catalysts from early research. To circumvent the aforementioned challenges, the thin-film rotating ring-disk electrode (TF-RRDE) was developed as a fast and convenient electrochemical technique to characterize supported catalysts for fuel cell applications in an aqueous electrolyte.[82–85] The technique, which was developed in the early 1950s by Alexander Frumkin and Benjamin Levich, is still widely used today to characterize catalyst support for fuel cell applications.[86]

In RRDE, usually, catalyst powders are dispersed in a mixture of water and alcohol with a binder (Nafion® solution) by sonication to form a homogeneous ink. The ink is then prepared as a catalyst film by deposition on a glassy-carbon electrode using micropipette or other similar methods. As powerful as this technique is, and its advancements in testing PEM fuel cell catalysts, only very few catalysts demonstrate identical behavior when tested in real fuel cell conditions. The real fuel cell testing requires an aqueous-free electrolyte whereas TF-RRDE is a flooded electrochemical technique. Some critical issues that are pertinent to fuel cell devices such as flooding in

the electrodes, drying out of the membrane (humidification effect), mixed electron / proton conduction through the ionomer membrane are far beyond practical understanding with the TF-RRDE technique.

The contribution from this work involves the development of a small-scale test platform that utilizes a small amount of catalyst support similar to TF-RRDE while allowing catalyst evaluation in an environment that will exist in a real fuel cell. The supported catalysts together with the ionomer membrane are prepared as MEA identical to the standard protocol of fabricating conventional MEA. The key advantage of this miniature test platform is that material utilization for both the electrode and ionomer membrane requires just a few tens of micrograms. For example, the amount of ionomer membrane material required to fabricate a conventional MEA of size 8.0 x 8.0 $cm^2$ for a single measurement would be adequate enough to fabricate at least 50 MEAs for this miniature cell. Other advantages of this small-scale test platform are as follow: (1) MEA assembly and fabrication are uncomplicated and require little training. (2) Compatibility with the most common electrochemical workstation and thus save cost. (3) Reproducibility of measurements can be achieved easily with little or no variation from different independently prepared MEAs, and (4) enables very small quantities new ionomers and electrode materials to be screened for fuel cell application. This miniature cell is complimentary to the TF-RRDE but in an aqueous free electrolyte, where a solid ionomer membrane is in direct contact with the electrode catalyst support as is expected in a real fuel cell testing.

The overall objective of developing a miniature cell for any application is to reduce material utilization, which will allow replicate studies with a better understanding of material properties.[87] Miniature cells are usually developed either to scale down the traditional large device or to incorporate new technologies such as nanoimprint lithography technology,[88] ink-jet printing,[89] and micro-electro-mechanical systems[90] Lohoff and co-workers[88] fabricated the first miniature cell for PEM water electrolysis using metal flanges for the anode and cathode components of the cell with an active area of 1.2 $cm^2$. Although this is considered as a miniature cell, it is still very large when compared to a TF-RRDE that has an active area of 0.196 $cm^2$ or less. The miniature test platform that we have developed during this work allows for PEM fuel cell testing with good reproducibility over an area less than 0.1 $cm^2$. The cell design operates with an efficient gas delivery with proper humidification over an electrode area for efficient catalysts utilization.

## 2.2 MATERIALS AND METHODS

### 2.2.1 Cell Design, Fabrication and Assembly

The miniature cell body used for the fabrication of this test platform is a commercial plastic tube fitting made from perfluoroalkoxy alkane (PFA) resin. The dimensions of this straight union compression fitting are 1.5" x 0.79" (3.8 cm x 2.0 cm) with an internal diameter of 0.5" (1.27 cm). Other cell components are:

(1) **The graphite rods**: These serves as current collectors in the anode and cathode compartments. Each of these has a length of 1.97" (5 cm) with a diameter of 0.375"

(0.953 cm). A hole of 0.125" (0.318 cm) diameter was bored through the rod to allow gas delivery from a humidifier bottle to the MEA. To allow for the gas exit, three grooves were incised onto the external part of the graphite rods.

(2) **The PTFE sleeves**: These accommodate the graphite rods. They are made from poly(tetrafluoroethylene) otherwise known as PTFE. The sleeve has a length of 1.46" (3.7 cm) with an internal diameter of 0.375" (0.953 cm) and outer diameter 0.5" (1.27 cm), and fit comfortably into the main cell body.

(3) **Butyl rubber O-rings**: The O-ring on each side of the cell provides cushion support for the MEA against the hard contact of the sleeve and current collector. It also serves a vital role of securing a gas-tight seal. The O-ring has an internal diameter of 0.375" (0.953 cm) and outer diameter of 0.5" (1.27 cm).

(4) **Nickel foam and carbon paper**: Both nickel foam gas diffuser element and carbon paper serve as gas diffusion layers (GDLs). They primarily permeate the diffusion of gases to the active area of the catalyst layer in the MEA. They also facilitate current collection by providing an electronic path between the graphite rod current collectors and catalyst supports in the MEA. Both are 0.375" (0.953 cm) in diameter. Figure 2.1 shows the graphical representation of the cell, disassembled cell parts and assembled cell showing gas tubing and electrical connections.

The assembly of the cell components is aided with the use of PTFE rod having 0.5" diameter. First, the rod is pushed through the center of the straight union compression fitting and clamped at the cathode side. The MEA is carefully inserted through the anode side into the cell body using tweezer with the cathode side of the MEA

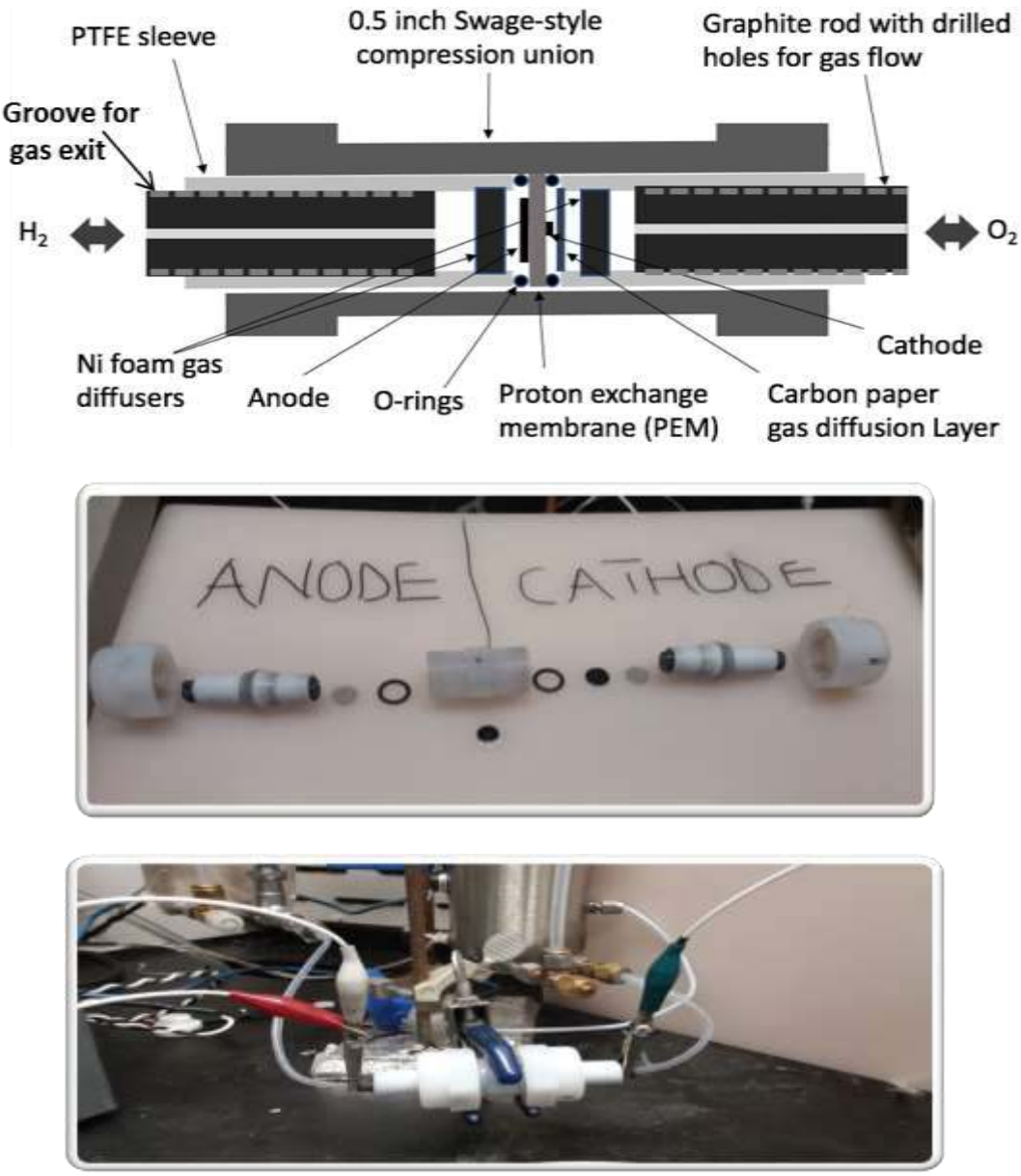


Figure 2.1. Top: Graphical representation of the miniature cell; middle: photomicrograph of disassembled parts of the cell; bottom: the photomicrograph of assembled cell in operation.

facing the PTFE rod. This is followed by the introduction of an O-ring, and a piece of nickel foam. The anode graphite rod inside the sleeve is pushed gently to make contact with the nickel foam and MEA and then clamped tightly to the cell body. The PTFE rod is then removed and similar procedures are repeated for the cathode side with the addition of a piece of carbon paper. The cell is then connected to humidified bottles of oxygen and hydrogen using gas tubing as well as electrode leads as shown in Figure 2.1 above.

### 2.2.2 Small-Scale MEA Fabrication

The small-scale MEAs used during this work in the miniaturized cell were fabricated from commercial platinum-decorated carbon cloth (Fuel Cell Store) and Nafion®-212 ionomer membranes (Fuel Cell Store). The cathode was 0.09375" (0.238 cm) diameter with 0.3 mg $cm^{-2}$ Pt on 40 % Vulcan carbon was cut from a large piece using an arch punch. One microliter of Nafion® solution (from 5 wt. % Nafion® solution) was deposited onto it and allowed to dry at ambient conditions. The anode was 0.3125" (0.794 cm) diameter with 4 mg $cm^{-2}$ Pt catalyst loading cut from Pt carbon black carbon cloth. Seven microliters of Nafion® solution again, was deposited on it and allowed to dry.

Higher catalyst loading on the anode than the cathode was chosen to ensure adequate proton flux from anode to cathode and also to avoid a well-known edge effect. Prior to the hot press step, the electrodes (anode and cathode catalysts) and a Nafion®-212 ionomer membrane, 0.5" diameter (1.27 cm) were assembled in a silicone rubber template and a fiberglass sample holder. The assembly was hot pressed at 140°C, 100 $lb_f$

(445 N) for 5 min on a Carver hot press (model 3851-0). Figure 2.2 shows the fabricated MEA for a miniature cell used in this work.

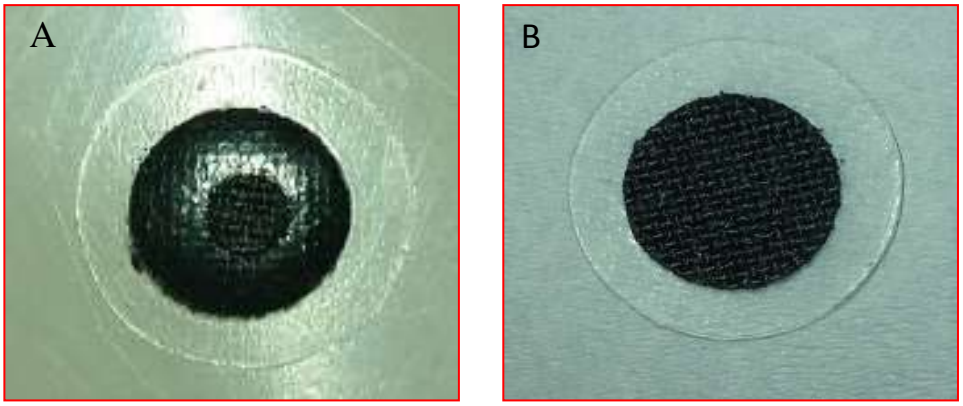


Figure 2.2. Photomicrographs of MEA prepared for a miniature PEM fuel cell: (A) Cathode side and (B) Anode side. See the text for the detailed description of the MEA dimensions.

2.2.3 Large-Scale MEA Fabrication

A large-scale MEA was fabricated for use in a conventional fuel cell test station (Scribner Fuel Cell test station model 850C) in order to compare with the results from a similar experiment using our in-house developed miniature test platform. For a fair comparison, similar catalyst loadings on both the anode and cathode electrodes were used for the large MEA as it was for the small-scale MEA. Pt catalyst loading on the cathode was 0.3 mg $cm^{-2}$ while it was 4.0 mg $cm^{-2}$ on the anode albeit on a large catalyst surface area. The large-scale MEA was also fabricated from a Nafion®-212 with a total membrane area of 7.5 cm x 7.5 cm (56.25 $cm^2$). The geometric electrode area was 2.5 cm

x 2.5 cm (6.25 $cm^2$) on anode and cathode. Then, 139 μL of a 5 wt. % Nafion® solution was added to each side of the electrodes, which were dried under ambient conditions. The electrodes and the Nafion® ionomer membrane were assembled in a similar silicone rubber / fiberglass template used for the small-scale MEA. The assembly was again hot pressed at 140°C, 400 $lb_f$ (1180 N) for 5 min on a Carver hot press. Figure 2.3 shows the fabricated large-scale MEA.

Figure 2.3. Photomicrograph of the large-scale MEA fabricated for a conventional fuel cell station. The MEA has been used on a Scribner model 850C fuel cell test station. See detailed description of the MEA dimension in the text.

## 2.3 RESULTS AND DISCUSSION

### 2.3.1 SEM and EDS Analyses of Platinized Electrode Surface

Figures 2.4 and 2.5 show the scanning electron microscope (SEM; model TM3000 Tabletop Hitachi) images and SEM mapping that shows a homogenous

distribution of elements on the surface of Nafion® coated platinum-on-carbon electrode and uncoated samples, respectively. Elemental analysis was conducted on Pt-on-carbon

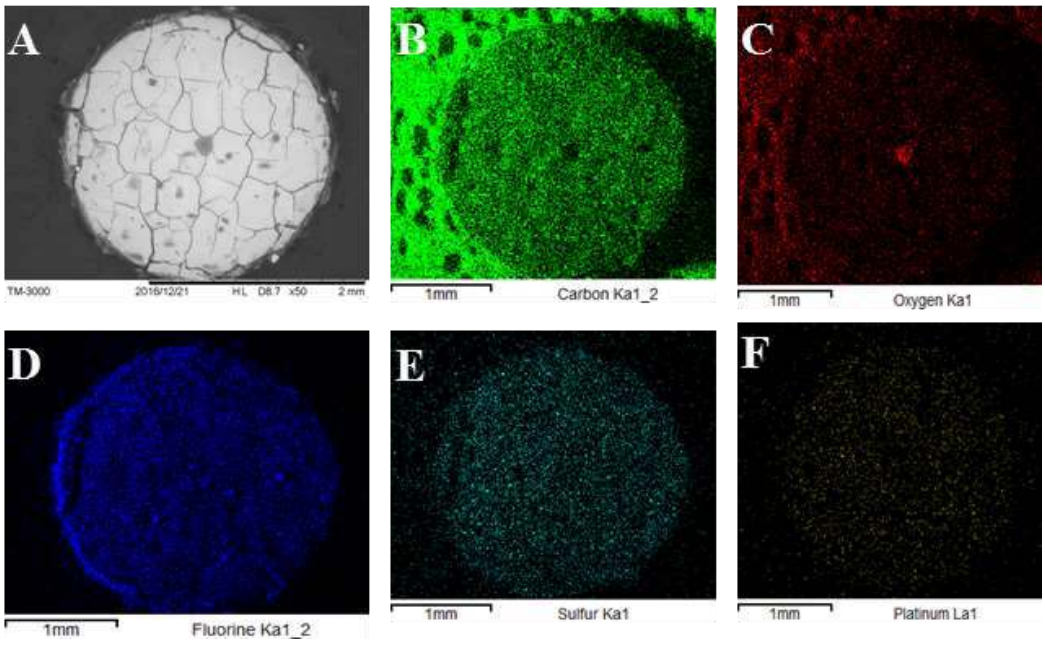


Figure 2.4. (A) SEM micrograph of Nafion® coated Pt-on-carbon electrode used in a miniature cell. SEM elemental mapping showing (B) carbon, (C) oxygen, (D) fluorine, (E) sulfur, and (F) platinum.

electrode with and without the addition of the Nafion® solution using energy dispersive X-ray spectroscopy (EDS, Oxford Instruments). The spectra obtained are shown in Figures 2.6. The elemental compositions from the spectra are presented in Table 2.1. Addition of Nafion® solution to the catalyst layer on the electrode helps to bind the electrode to the ionomer membrane and to provide intimate contact between the catalyst support and the membrane, which helps to promote faster ionic transport

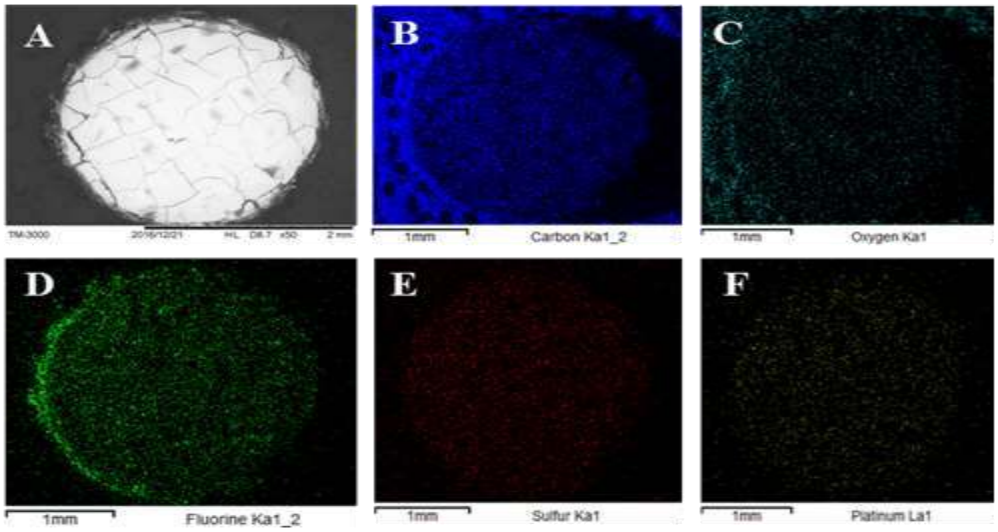


Figure 2.5. (A) SEM micrograph of a Pt-on-carbon electrode without Nafion® solution. SEM elemental mapping showing (B) carbon, (C) oxygen, (D) fluorine (E) sulfur, and (F) platinum.

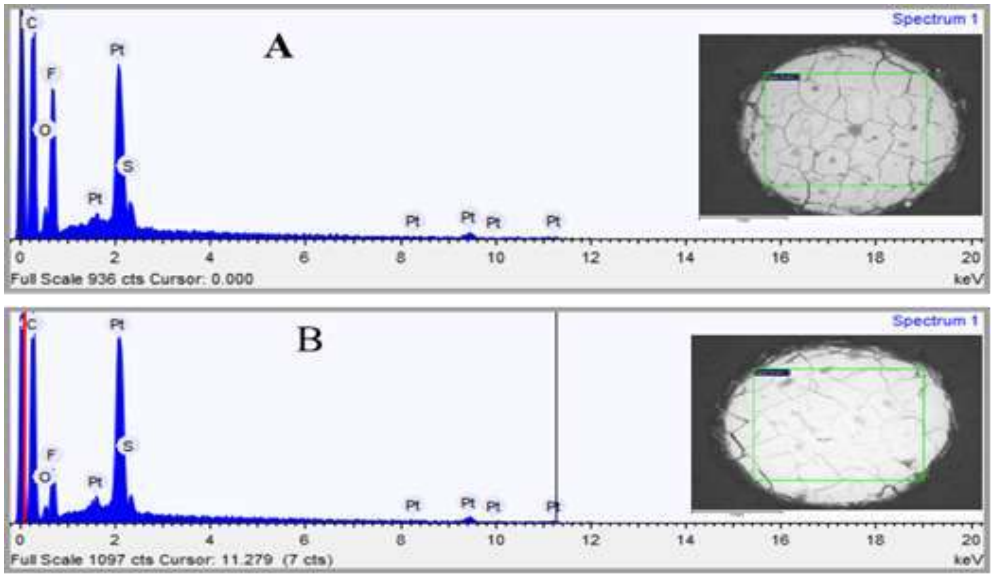


Figure 2.6. Energy dispersive x-ray spectra for platinum-on-carbon cloth electrode (A) with addition of 1.0 µL 5 wt. % Nafion® solution and (B) without Nafion® solution

Table 2.1 EDS elemental composition of platinum-on-carbon electrode

| Element | Wt. % | |
|---|---|---|
| | With Nafion® solution | Without Nafion® solution |
| Carbon | 46.1 | 52.9 |
| Oxygen | 4.9 | 4.1 |
| Fluorine | 28.0 | 13.5 |
| Sulfur | 1.2 | 1.0 |
| Platinum | 19.9 | 28.5 |

2.3.2 Open Cell Voltage (OCV) Measurement

The OCV (potential of the cell when no load is applied) of the assembled miniature cell as described in Section 2.2.1 was determined by flowing humidified oxygen gas at the cathode and hydrogen gas at the anode. Prior to the evaluation of the fuel cell performance on the miniature cell, the OCV of the cell as shown in Figure 2.7 was established to ensure proper cell assembly, no fuel crossover or pinhole in the MEA. The cell voltage was almost constant for a duration of 2 min. The obtained value of ≈ 0.975 V is reasonable and is close to the theoretical prediction of ≈ 1.0 V for PEM fuel cell.

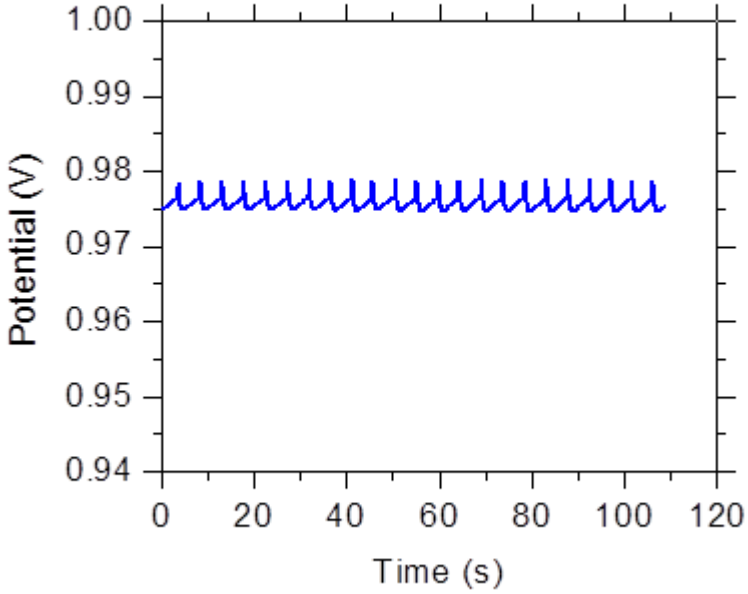


Figure 2.7. OCV of miniature PEM fuel cell; gas feed at the cathode is oxygen gas and at the anode is hydrogen gas, humidified at 30°C.

### 2.3.3 *In-situ* Voltammetry

In-situ voltammetry provides a reliable way to diagnose intrinsic electrocatalyst performance in the electrodes (anode or cathode) of an MEA. One way to understand how an electrocatalyst may catalyze a specific electrochemical reaction, is to examine the three-phase boundary otherwise known as 'triple region". This triple region consists of reactant molecules, the active sites on the electrocatalyst and the ionic conducting material (here, Nafion® ionomer membrane). It is important that the three boundaries remain in close contact. One way to diagnose this intimate contact and overall active sites in an MEA is to determine the ECSA.

To characterize the electrochemical surface area (ECSA) of the electrocatalyst layer in an MEA of a miniature cell, *in-situ* voltammetry was used in a two-electrode configuration. The anode of the miniaturized cell was used as a pseudo-reference electrode and counter electrode (CE / RE), and the cathode was used as the working electrode (WE). The two-electrode system was connected to a potentiostat (CHI 1140B electrochemical analyzer). The cathode of the miniature cell was bathed with humidified argon gas supplied through tubing connected to the humidifier bottle held at 30°C. The anode, on the other hand, was fed with humidified hydrogen gas from humidifier bottle similarly held at 30°C to maintain ≈ 100 % relative humidity.

Figure 2.8 shows the *in-situ* cyclic voltammogram obtained for one of the three MEAs prepared as described in section 2.2.2. The cyclic voltammogram was obtained by sweeping the potential between 0.05 to 0.60 V at a scan rate of 50 mV $s^{-1}$. In the forward scan (anodic direction; more positive potential), the adsorbed hydrogen on Pt electrocatalyst undergoes oxidation to form $H^+$ as represented by equation 2.1. This portion of the cyclic voltammogram is represented as the hydrogen adsorption peak ($H_{ads}$). In the reverse scan, the electrochemical reduction of protons ($H^+$) occurs on the Pt surface as indicated in equation 2.2. This portion again is represented as the hydrogen desorption peak ($H_{des}$). This cycle ($H_{ads}$-$H_{des}$) is repeated until a stable cyclic voltammogram is obtained from which the ECSA is determined.

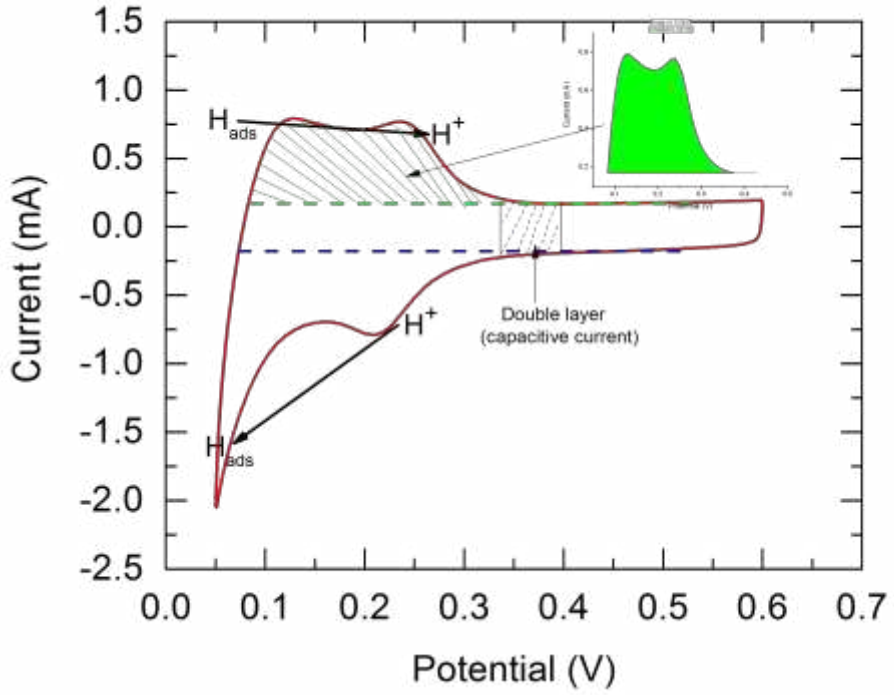


Figure 2.8. *In-situ* cyclic voltammogram of representative MEA used in a miniaturized cell. Gas feed at the anode is humidified $H_2$ and at the cathode is Ar at 100 % RH. Geometric active area of MEA is 0.045 $cm^2$ with Pt catalyst loading of 0.3 mg $cm^{-2}$.

$$Pt\ldots H_{ads} \longrightarrow Pt + H^+ + e^- \qquad \text{eqn 2.1}$$

$$Pt + H^+ + e^- \longrightarrow Pt\ldots H_{ads} \qquad \text{eqn 2.2}$$

From Figure 2.8 the area marked green can be integrated to estimate the ECSA. The charge density associated with the $H_{ads}$ peak can be obtained from the integrated region (green; inset) following correction from the capacitive current arising from the double layer charging by setting appropriate baseline as indicated in Figure 2.8. The

obtained hydrogen adsorption charge density can then be used to estimate ECSA using equation 2.3 below

$$ECSA\ (m^2\ g^{-1}\cdot Pt) = Q / (\Gamma .\ L_{catalyst}) \qquad \text{eqn 2.3}$$

where Q = hydrogen adsorption charge density, Γ = literature value (210 μC $cm^{-2}$) for the charge required to reduce a monolayer of protons on the surface of Pt, $L_{catalyst}$ = Pt electrocatalyst loading obtained from 0.3 mg $cm^{-2}$ Pt carbon cloth and MEA geometric area (0.045 $cm^2$).

In addition to estimating ECSA using the $H_{ads\text{-}des}$ technique, electrochemical CO oxidation otherwise known as "CO stripping" is another alternative to quantify the active sites on the Pt catalyst in the MEA. The CO stripping method is similar to the $H_{ads\text{-}des}$ method with regards to cell configuration for *in-situ* voltammetry. However, while humidified hydrogen gas is being fed to the anode, argon gas is being interrupted with a brief flow of CO gas through the cathode. The CO adsorbed on the surface of the Pt catalyst and the excess of it is purged out using Ar gas. Electrochemical oxidation of the adsorbed CO on the surface of Pt is observed by scanning the potential of the working electrode from 0.0 to 1.1 V at a scan rate of 50 mV $s^{-1}$. The obtained CV is shown in Figure 2.9. The CV shows interesting features. In the first forward scan (towards 0.0 V) as indicated by the blue arrow, the usual characteristics shapes of Pt disappear. This is expected due to CO adsorption on Pt surface, as CO deactivates Pt active sites. Interestingly, in the reverse scan, the adsorbed CO was stripped off by oxidation in the

potential window between 0.7-1.0 V giving rise to a large oxidation peak. Also, the characteristics features of Pt became apparent in the second forward scan indicating the complete removal of adsorbed CO by stripping.

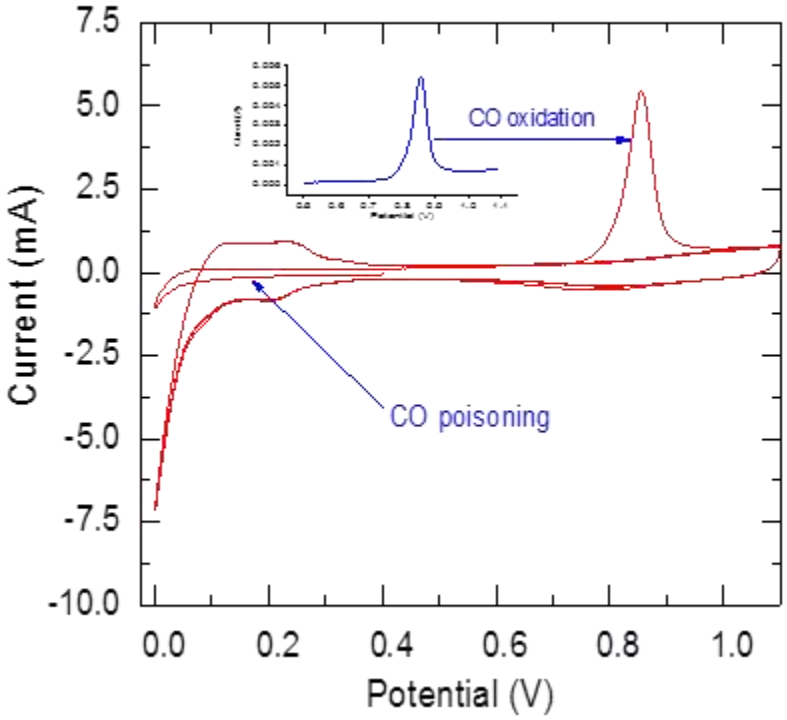


Figure 2.9. CO stripping cyclic voltammogram of representative MEA used in a miniaturized cell. Gas feed at the anode is humidified $H_2$ and at the cathode is Ar with an interruption by CO gas exposure at 100 % RH. Geometric active area of MEA is 0.045 $cm^2$ with Pt catalyst loading of 0.3 mg $cm^{-2}$.

Similar to $H_{ads\text{-}des}$, the CO oxidation peak can be integrated to estimate the associated charge density. ECSA can be determined from equation 2.3 above with the valid assumption that $\Gamma$ = literature value (420 $\mu C\ cm^{-2}$); the charge required to oxidize

adsorbed CO on Pt surface. Table 2.2 summarizes the obtained ECSA for both $H_{ads\text{-}des}$ and CO techniques using a miniaturized electrochemical cell for three MEAs. The highly reproducible data from both techniques for the three independently prepared MEA validate the use of the miniature cell developed during this work for fuel cell catalysis. Higher ECSA values from CO stripping compared to $H_{ads\text{-}des}$ might suggest difficulty in setting an appropriate baseline, to remove the double layer contribution which may eventually lead to underestimation.

Table 2.2 ECSA determination by *in-situ* CV in miniaturized PEM cell

| Samples | ECSA ($H_{ads\text{-}des}$) ($m^2\ g^{-1}Pt$) | ECSA (CO-stripping) ($m^2\ g^{-1}Pt$) |
|---|---|---|
| MEA-1 | 37.28 | 59.10 |
| MEA-2 | 38.97 | 59.22 |
| MEA-3 | 39.09 | 59.52 |

2.3.4 *Ex-situ* Voltammetry

In ex-situ voltammetry, the proton conducting medium is the liquid electrolyte. During this work, the carbon cloth electrode with 0.3 mg $cm^{-2}Pt$ was mounted onto a glassy carbon electrode by using a binder (1.0 μL 5 wt. % Nafion® solution). The electrode was immersed in 0.5 M $H_2SO_4$ in a three-electrode cell. This is in contrary to miniature PEM fuel cell testing where the catalyst is in contact with Nafion® membrane (a solid proton-conducting material). ECSA was determined using $H_{ads\text{-}des}$ technique and

CO stripping method as described under Section 2.3.3. Figures 2.10 and 2.11 show the obtained cyclic voltammograms for $H_{ads-des}$ and CO stripping respectively. The characteristic features of Pt are similar to what we observed in *in-situ* voltammetry. The ECSA values for $H_{ads-des}$ and CO stripping methods are 74.1 $m^2$ $g^{-1}$Pt and 87.3 $m^2$ $g^{-1}$Pt, respectively.

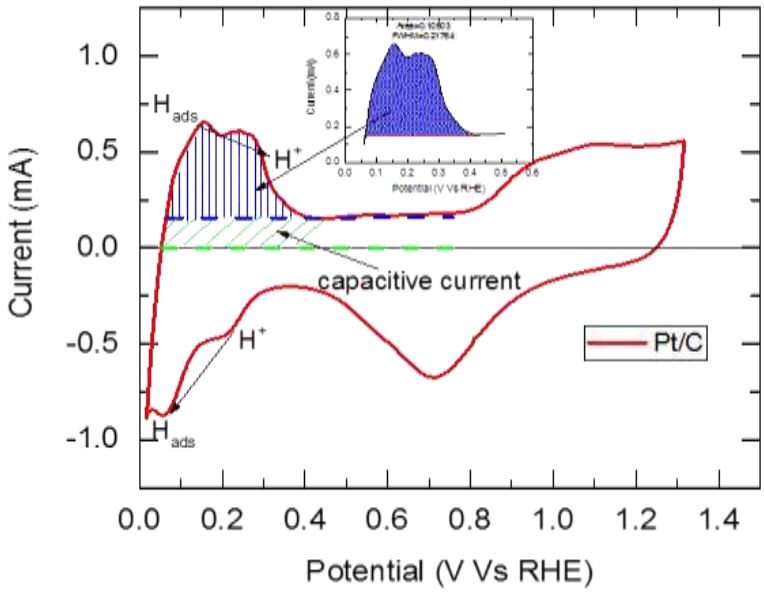


Figure 2.10. *Ex-situ* cyclic voltammogram for ECSA determination using $H_{ads-des}$ method in 0.5 M $H_2SO_4$. A scan rate of 50 mV $s^{-1}$ was used during the potential scan. The electrolyte was purged with Ar prior to measurement.

It should be noted that the ECSA determination in ex-situ was somewhat higher than that of in-situ using miniature PEM fuel cell. The discrepancy may be as a result of how the electrocatalyst was in contact with the proton-conducting medium (liquid Vs solid electrolyte). In a miniature cell, only a fraction of electrocatalyst that has contact

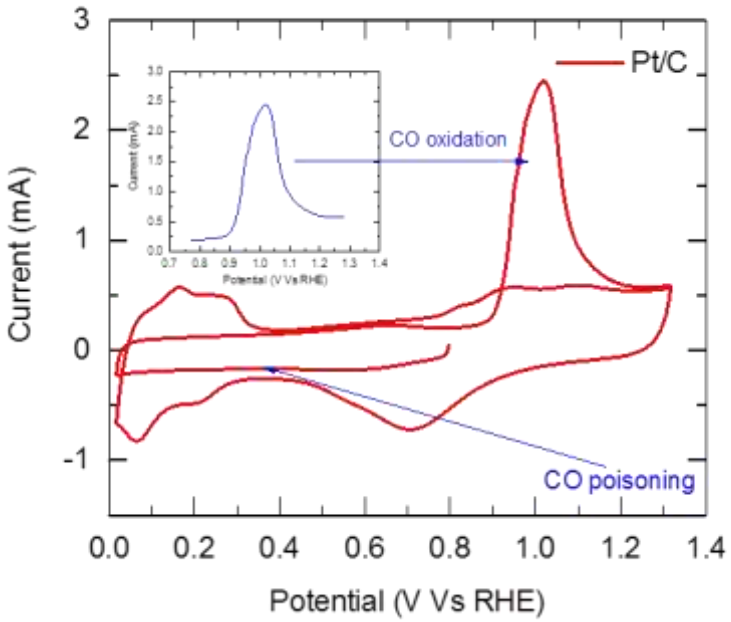


Figure 2.11. *Ex-situ* cyclic voltammogram for ECSA determination using CO stripping method in 0.5 M $H_2SO_4$ with Ar and CO purging. A scan rate of 50 mV $s^{-1}$ was used during the potential scan.

with the ionomer membrane in the MEA may be accessible. The importance of this work is the demonstration of a simple way of conducting PEM fuel cell testing in the absence of liquid electrolyte using very small quantities electrode and electrolyte materials. The ECSA determination can be improved, and the active sites can be made more accessible by proper impregnation of proton conducting electrolyte into the catalyst.

2.3.5 Oxygen Reduction Reaction (ORR) Testing

In a PEM fuel cell device, the two most impotant electrochemical reactions are hydrogen oxidation at the anode and oxygen reduction reaction (ORR) at the cathode as discussed in Section 2.1. ORR is the reaction of interest at the cathode because of its sluggish kinetics. To characterize the performance of the miniature PEM fuel cell, polarization curves for the oxygen reduction reaction were acquired while humidified $O_2$ gas is being fed to the cathode and $H_2$ gas to the anode. Both gases are maintained at ≈ 100 % RH by passing the gases over humidifier bottles kept at 30°C. A break-in experiment (from 1.0 to 0.5 V) was first conducted to prepare the MEA for a polarization experiment. This is a series of repeated potential cycling within the potential window for polarization experiment (0.3 to 1.0 V) to ensure performance stabilization for a duration of 1-3 hr.

To demonstrate reproducibility, polarization curves were recorded on each of the three independently prepared MEAs as shown in Figure 2.12. The results show a very slight variation in the three MEAs indicating how efficient the cell is for fuel cell studies. The above polarization curves in Figure 2.12 show the expected current-voltage (I-V) characteristics similar to the polarization curve obtained from a conventional fuel cell test station. In order to further evaluate the performance of the MEA, one of the polarization curves from the three MEAs above was recreated alongside its power density curve as shown in Figure 2.13. The maximum power density can be extrapolated from the curve and was estimated to be 0.71 W $cm^{-2}$ at 0.45 V.

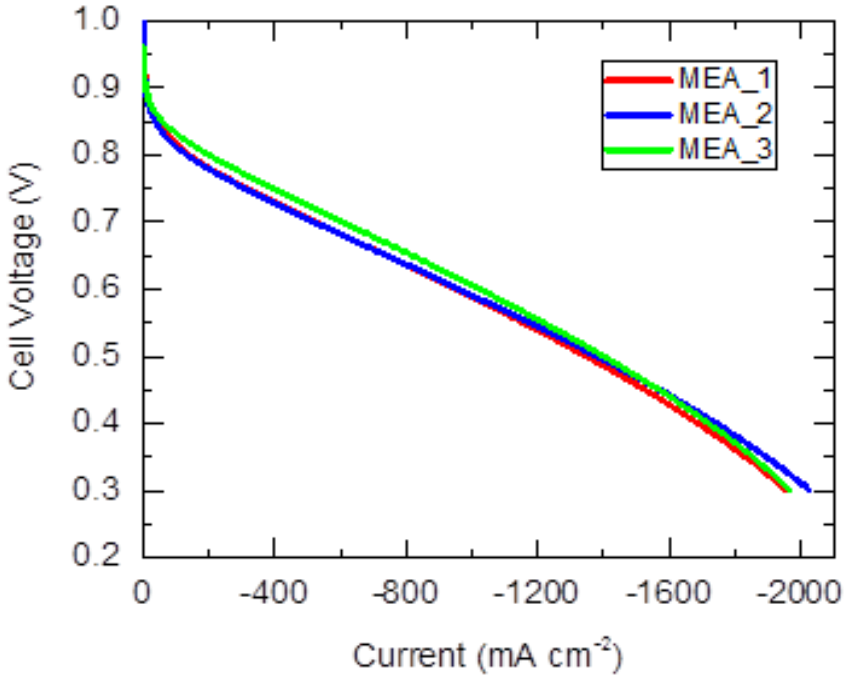


Figure 2.12. Polarization curves for three MEAs (0.3 mg $cm^{-2}$ Pt) btw 1.0 V and 0.30V; scan rate 1 mV $s^{-1}$; Cell temp of 30 °C; gas feeds are humidified (~100 % RH) $H_2$ at anode and $O_2$ at the cathode.

Similarly, the same electrode material albeit on a large carbon cloth as described in Section 2.2.3 was tested on a conventional single PEM fuel cell hardware (Scribner 850C compact fuel cell test station). Figure 2.14 shows the obtained polarization curve. Although the current density obtained is relatively lower in the conventional cell when compared to a miniature cell, this might reflect the gas flow pattern design in a miniature

cell vs conventional cell. The flow pattern in the miniature cell is uniform with circular gas delivery to and from the cell, whereas, in the large-scale cell, the gas flow pattern

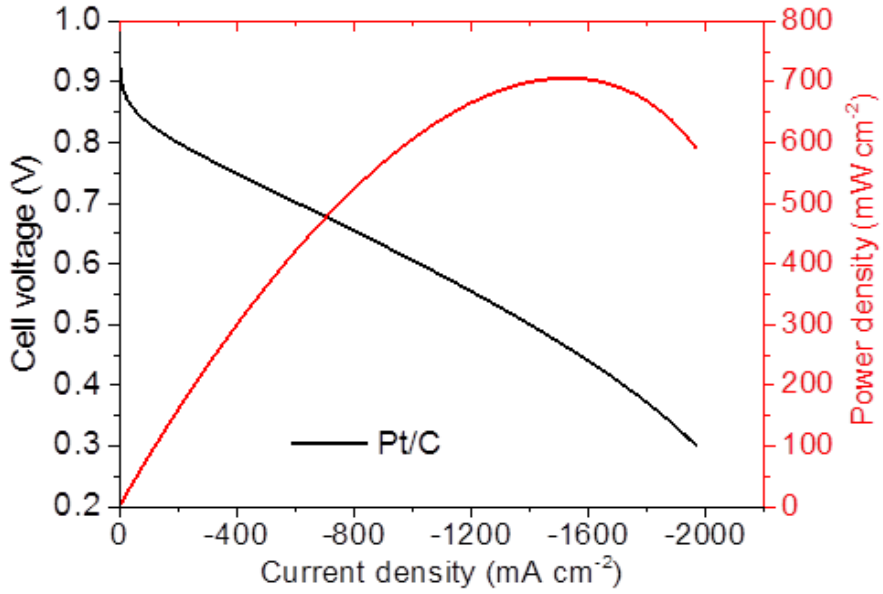


Figure 2.13. Polarization curve (black) and power density curve (red) for miniature PEM fuel cell testing.

has a serpentine design. This kind of serpentine flow pattern might result in an uneven gas distribution thus creating an inefficient catalyst utilization of active sites in the MEA.

*In-situ* ECSA on the large-scale MEA was also determined. The obtained voltammogram shown in Figure 2.15 reveal lower ECSA value of 34.25 $m^2$ $g^{-1}$ Pt than those obtained in the miniaturized cells. The unexpected lower ECSA value might reflect the difficulty in the background subtraction of the appropriate double layer charging through baseline correction. It may also indicate inaccessibility of all active sites on the

large MEA to the reactant molecules or contact between the catalyst and the ionomer membrane.

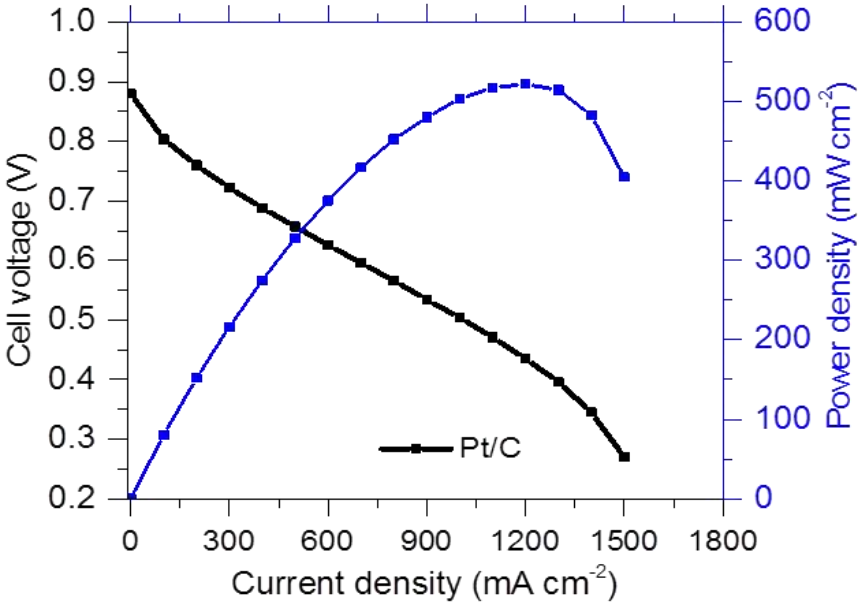


Figure 2.14. Polarization curve (black) and power density curve (blue) obtained from large-scale MEA conducted with conventional 850C compact fuel cell station. See section 2.2.3 for MEA fabrication.

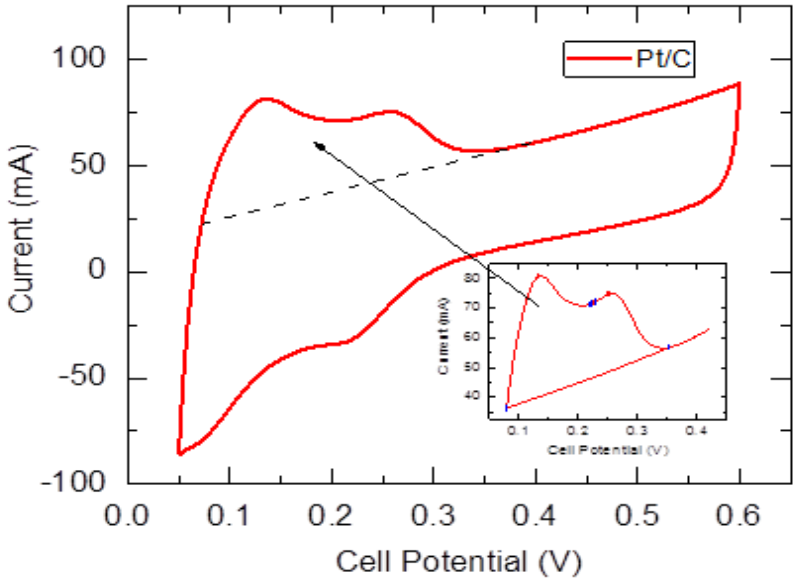


Figure 2.15. *In-situ* cyclic voltammogram on large-scale MEA used in conventional hardware. Gas feed at the anode is humidified $H_2$ and at the cathode is Ar at 100 % RH. Geometric active area of MEA is 6.25 $cm^2$ with Pt catalyst loading of 0.3 mg $cm^{-2}$.

### 2.3.6 Multi-Potential Step Testing

The polarization curves presented in Figures 2.12 and 2.13 can be deconvoluted to understand how the cell performance fluctuates with time. The multi-potential step experiment enables examination of steady-state behavior during the oxygen reduction reaction in a miniature PEM fuel cell. The potential step was applied in descending order from 1.0 to 0.3 V by 50 mV while the potential was held for a duration of 20 s. This type of fuel cell performance monitoring as a function of time offers a deep understanding of what is happening in the fuel cell device during the electrochemical oxygen reduction reaction. It is well-known that water formation from ORR can lead to device flooding.

The formation of such flooding and its overall effect on the current response can be traced using multi-potential step experiment. This is an additional diagnostic tool for the evaluation of PEM fuel cell performance that may be difficult to study in the flooded electrode system.

Figure 2.16 shows the potential step response (current vs. time) from three independently prepared MEAs. A closer look of the staircase waveform responses from the three MEAs reveals steady-state behavior for the first 100 s for the three MEAs. Slight fluctuation with time can be observed at higher current densities (from 40- 80 mA). Overall, this shows a good steady-state behavior indicating efficient gas transport and water management owing to a well-designed test platform.

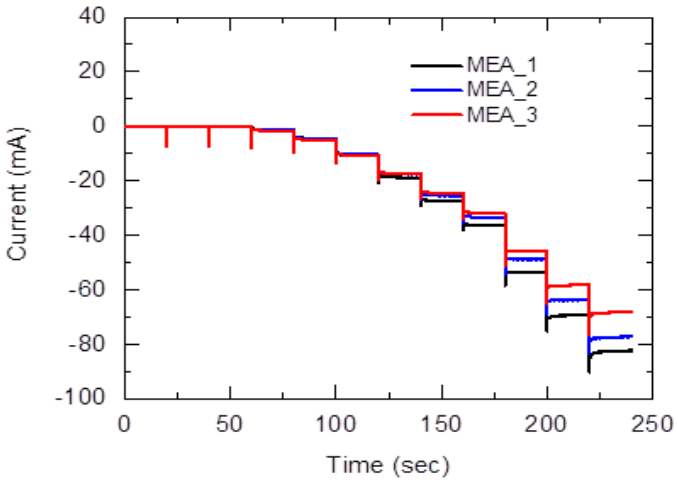


Figure 2.16 Multi-potential step curves in miniature PEM fuel cell on three MEAs from 1.0 to 0.3 V with potential held for 20 s at each potential adjusted by 0.05 V; cell temperature 30 °C; cathode: $O_2$; anode: $H_2$; 100 % RH.

## 2.4 CONCLUSIONS

In summary, a novel miniature electrochemical cell was developed for fuel cell performance testing. The key advantage of this test platform is that it utilizes small amounts of new ionomer membranes, new electrocatalysts, and catalyst supports. The small membrane electrode assembly (MEA) for this cell (1.27 $cm^2$) behaves similarly to large MEAs (56.25 $cm^2$) tested in conventional test hardware, albeit with the amount of material utilization less than a tenth to hundredth in the miniature cell as compared to the conventional cell. Cell design and MEA fabrication are quite straightforward, and it is compatible with a common electrochemical workstation. It is highly indispensable to have a test platform that utilizes smaller quantities of materials while still allowing fuel cell testing in an environment that will exist in a real fuel cell. This miniature cell will be beneficial to further the development of the fuel cell because new ionomer materials and newly developed electrocatalysts from early research, which are usually obtained at small quantity, can be screened and their properties evaluated for fuel cell application.

# CHAPTER THREE

# PROTON AND DEUTERON TRANSPORT THROUGH SINGLE-LAYER GRAPHENE

## 3.0 SYNOPSIS

The work described in this chapter has been published in the *Journal of the American Chemical Society* (JACS) with the following bibliographical details, *J. Am. Chem. Soc.* 2018, 140, p.17438-1752. It involves selective separation of hydrons (proton and deuteron) by single-layer graphene embedded in MEA in an electrochemical hydrogen pump cell. Proton transmission through graphene occurs at a high rate (with a current density of about 1.0 A $cm^{-2}$ at a potential bias less than 200 mV) with a selectivity over deuteron by a factor of 14.

## 3.1 INTRODUCTION

A growing interest exists in developing a viable technological process that can efficiently and effectively separate hydrogen isotopes.[16,22,50,91–93] Hydrogen isotopes (protium, deuterium and tritium) are of particular interest in analytical and tracing technologies. For example, deuterium oxide is used as a solvent and as a labeling agent in NMR. It is also used as a contrast agent in neutron scattering, and also as a label in drug metabolism. Hydrogen isotopes are also useful in nuclear fission reactors. Deuterium oxide ($D_2O$) is used in nuclear fission reactors as a neutron capturing agent.[22] Tritium is used as an autoradiography label in medical imaging and pharmacology.

Existing technologies to achieving the isotopic separation, such as cryogenic distillation, $H_2O$-sulfide exchange, and thermal cycling absorption process have been characteristically marked as extremely energy intensive with significant low separation factor.[25–28] A promising alternative that offers remarkable separation and selectivity is the use of 2D crystalline material such as graphene for electrochemical hydrogen isotope separation.

The micromechanical exfoliation of graphite to produce a monolayer of one atom-thick 2D crystal (*i.e.,* graphene) with unique properties has opened opportunity for 2D graphene-based and non-graphene based materials to be considered for the next generation separation technologies.[50,94,95] Earlier work that involved the use of 2D graphene for transport phenomenon was focused on deliberate creation of defects into the graphene crystal in order to act as size-selective membrane.[96] Following the discovery of free standing graphene, experimental findings from Michael et al.[97] showed successful creation of nanopores into graphene sheet using the controlled focused beam of a transmission electron microscope.

Since then, significant efforts have been made to develop a porous graphene for use as a selective membrane in separation technology. Koenig and co-workers were able to employ ultraviolet-induce oxidative etching to perforate graphene sheet with a micrometer pore-size.[20] The perforated graphene was then used as a selective molecular sieve for gas separation. Similar work was also demonstrated by H. Du et al.[21] by designing a series of porous graphene of various pore sizes and shapes to separate hydrogen and nitrogen gases.

The rationale behind having a porous graphene for separation was because graphene (with each hexagonal lattice geometric area of approximately 5 $Å^2$) at the time was known to be impermeable to atoms and molecules even the smallest ones (He and $H_2$) because of the enormous repulsive interactions between the electron cloud of graphene and that of the permeant.[6,98,107–109,99–106] It has been recently demonstrated that defect-free monolayers of 2D crystalline materials (graphene and hexagonal boron nitride <hBN>) that are impermeable to molecules and most atoms can be used to separate thermal hydrogen isotopes (i.e., protium, deuterium, and tritium).[24,29]

To accomplish this separation, usually a bias voltage is applied across the electrochemical cell that consists of anode and cathode electrodes and a polymer electrolyte membrane (PEM) as an ionic conductor together with the 2D material embedded within the cell. The anode side is fed with feed sample (either gases or water containing hydrogen isotopes of varying composition). The hydrons (proton, deuteron, or triton) are transported through the 2D crystalline material and membrane where they undergo selective separation based on their zero point energies. At the cathode end, the evolved gases are analyzed to estimate the selectivity and separation factor.

The transport of hydrogen isotopes through graphene is a thermally activated process[110], so the selectivity was thought to reflect the difference in energy barriers for $H^+$ and $D^+$ posed by the 2D crystalline materials. This exciting discovery might be an important path to an industrial-scale electrochemical hydrogen isotopes separation technology over the existing technologies. The early work by Geim and co-workers,[24] which described the phenomenon of hydrogen isotope separation by electrochemical

means utilized microfabricated devices of less than 50 μm in size. While the transmission of protons through graphene was favored over deuterons by a factor of 11, the reported proton conductance value of 3 mS $cm^{-2}$, at ambient temperature, through graphene, would be considered very low when compared to area normalized proton conductance of the well-known Nafion® membrane.

More recently, the same group reported a higher area normalized proton conductance of 90 mS $cm^{-2}$ through graphene than their earlier work (3 mS $cm^{-2}$). Fundamentally, this reported value is still significantly low for proton transport through 2D crystalline material, if this approach would be considered for practical applications for hydrogen isotopes separation technology. As an example, a typical Nafion® membrane (say 25 μm thick) has an area normalized proton conductance of about 10-15 S $cm^{-2}$. [111,112] Thus, incorporating a 2D crystalline material into a Nafion® membrane would suppress the proton conductance of Nafion® and would eventually lead to overall poor efficiency and selectivity for hydrogen isotopes transport across the 2D materials. Thus, much research attention is needed to make the electrochemical hydrogen isotope separation using 2D crystalline materials (graphene and related 2D materials) a viable technology for the next generation hydrogen isotopes separation.

In this work, proton and deuteron transmission through single-layer graphene embedded in an MEA were studied using the miniaturized electrochemical cell discussed in details in Chapter One of this dissertation. The MEA fabrication and cell design were reconfigured to allow for efficient hydrogen evolution and deuterium evolution reactions in a PEM hydrogen / deuterium pump cells. Single-layer graphene made by the chemical

vapor deposition (CVD) method was obtained from a commercial source (ACS Materials LLC.). The CVD single-layer graphene was then transferred onto Nafion® membrane via hot pressing and chemical oxidative etching. The MEAs in proton-form and deuteron-form with and without single layer graphene were characterized using electrochemical hydrogen pump cells. Areal-normalized proton and deuteron conductances though single-layer graphene were estimated following corrections from contributions to the ionic conductance by electronic resistances and ionomer membrane resistance. Butler-Volmer theory was invoked to develop an electrochemical model to provide rate constants for proton and deuteron transmission through hexagonal graphene hollow sites.

## 3.2 RESULTS AND DISCUSSION

### 3.2.1 Electrochemical Hydrogen / Deuterium Pump Cell in Asymmetric Mode

A modified miniature cell (see method section for the discussion on the modifications made to the previous version) was used to accomplish hydrogen evolution and deuterium evolution reactions in asymmetric mode. An electrochemical hydrogen pump cell in an asymmetric mode was achieved by feeding the anode compartment of the cell with the humidified hydrogen gas from humidifier bottle and the cathode with the humidified Ar gas. The pseudo-reference / counter electrode (anode) oxidizes hydrogen gas to protons and then the protons move through the Nafion® membrane to undergo hydrogen evolution reaction as illustrate in equations 3.1 and 3.2 below.

Anode: $H_2 \longrightarrow 2H^+ + 2e^-$ eqn 3.1

Cathode: $2H^+ + 2e^- \longrightarrow H_2$ eqn 3.2

The MEA is also made in asymmetric mode such that the hydrogen evolving electrode is made relatively smaller (0.094 inch diameter) than the hydrogen source electrode (0.31 inch diameter). The smaller electrodes were used to ensure small amount of evolving gas can be produced within the limitation of current output of an ordinary electrochemical workstation. Figure 3.1 shows the modified version of the miniature cell and schematic representation of the cell in asymmetric mode.

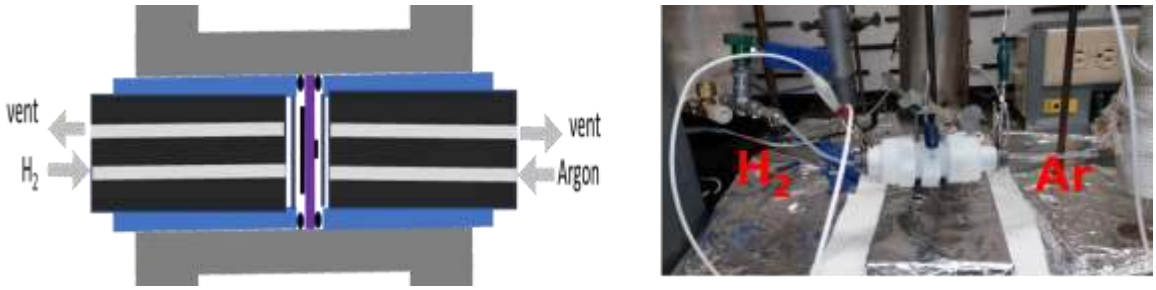


Figure 3.1. Schematic representation of miniature cell in an asymmetric mode (left) and photomicrograph of the miniature cell in operation (right).

To show reproducibility with the MEA fabrication and this miniature cell, three independently prepared MEAs were fabricated. The MEAs were made without single layer graphene with two Nafion®-211 membranes discs sandwiched together with the electrodes using the hot press technique and were tested for hydrogen evolution reaction in asymmetric hydrogen pump cell. Figure 3.2 shows the polarization curves for the hydrogen evolution reaction (HER) for the three MEAs.

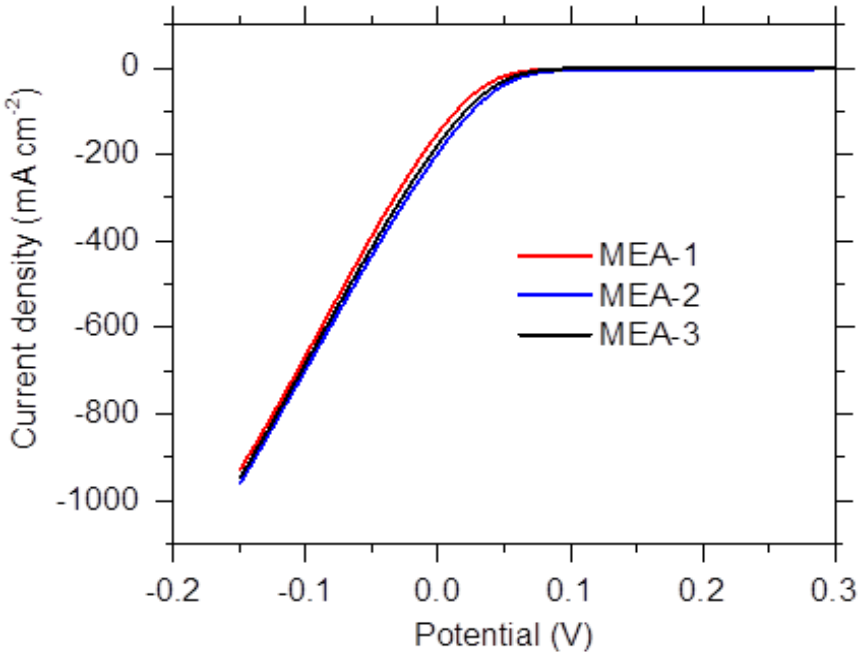


Figure 3.2 Polarization curves for HER for three independently prepared MEAs.

The cathode catalyst in the MEA was 0.03 mg $cm^{-2}$ Pt on a microporous layer carbon cloth with 0.5 µL of 5 wt. % Nafion® solution and 4 mg $cm^{-2}$ Pt on the anode with the addition of 3.5 µL of 5 wt. % Nafion® solution. Polarization curves were acquired at a scan rate of 20 mV $s^{-1}$ between 0.3 to -0.15 V. The gases were humidified at both the anode and cathode at 30 °C (≈ 100 % RH). Figure 3.2 shows expected polarization curve with near zero baseline at potential positive of zero and a rising cathodic current at potential negative of zero. The polarization curves for the three MEAs show high level of reproducibility achievable by this miniature cell. It also indicates good reproducibility of the MEAs, validating a good MEA fabrication technique. The onset potential for the

three curves is somewhat identical at ≈ 0.05 V. It is interesting that the current density approaches 1.0 A $cm^{-2}$ at modest bias voltage of just -150 mV.

Similarly, for comparison, two MEAs were prepared one from Nafion®-212 membrane (nominal thickness of 50.8 μm) and the other from two Nafion®-211 membranes (each has nominal thickness of 25.4 μm). The results are presented in Figure 3.3 for the hydrogen evolution reaction with very slight variation. The indistinguishable nature of the polarization curves from both MEAs indicates that the hot press technique produces a sandwich structures in which MEA made from one Nafion® membrane of certain nominal thickness is similar to the MEA made from two Nafion® membrane discs

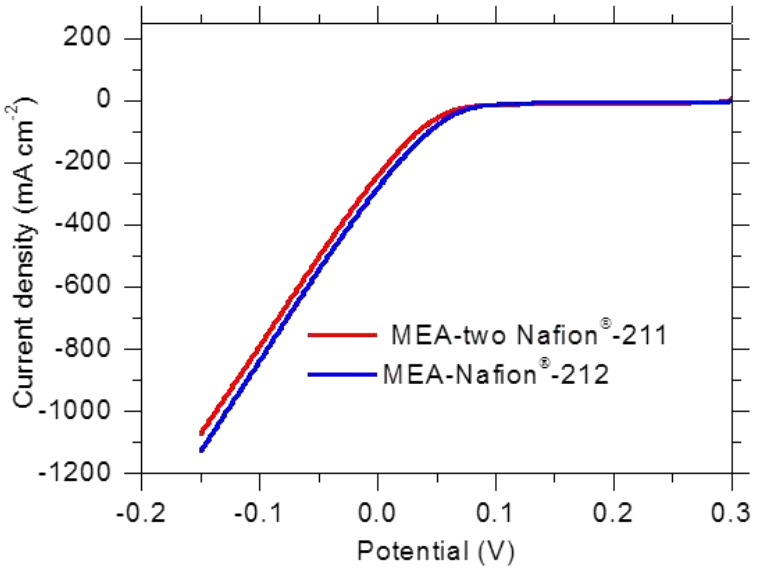


Figure 3.3. Polarization curves for HER on MEAs comparing effect of Nafion® nominal thickness.

of identical nominal thickness.

This was done by boiling the membrane in 1.0 M $H_2SO_4$ and 1M $D_2SO_4$ for 1 hr and subsequently boiling in DI $H_2O$ and $D_2O$ with proper rinse to remove excess acid, respectively. Figure 3.4 presents results for a comparison of proton and deuteron transmission through an MEA without layer of graphene in an asymmetric mode configuration. Humidified hydrogen gas or deuterium gas was fed to the anode side from different humidifier bottles connected from the gas main line and humidified Ar gas was fed to the cathode at 30 °C, ≈ 100% RH. It is quite interesting to see that the I-V curves for the hydrogen evolution reaction (HER) and the deuterium evolution reaction (DER) are similar with slight variation though. The current density of the HER approaches 1.0 A $cm^{-2}$ whereas DER is around 0.9 A $cm^{-2}$ at a similar bias of -150 mV.

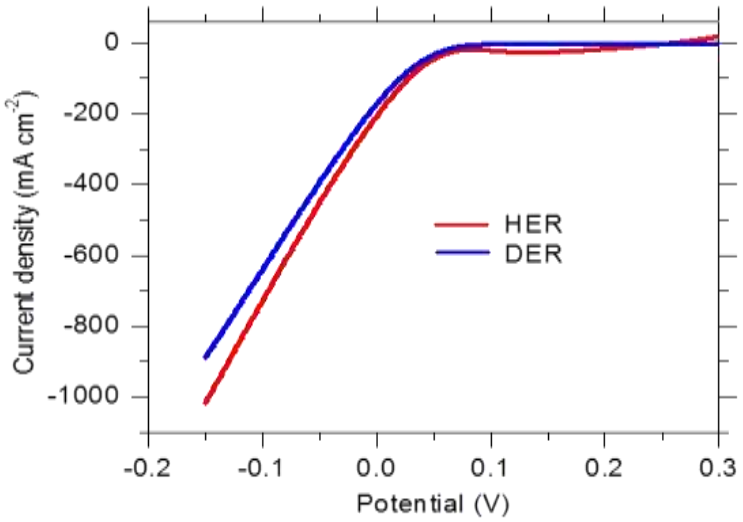


Figure 3.4. Polarization curves for HER and DER in two similar MEAs but in different cationic forms (proton vs deuteron).

The similar polarization curves are expected owing to the fact that the solvated proton ($H_3O^+$) and deuteron ($D_3O^+$) have similar ionic conductivity and not very different masses. The MEAs were pretreated to ensure they are in full proton form and deuteron form.

More importantly, the high kinetic facility for HER and DER through a Nafion® membrane with current density near 1.0 A $cm^{-2}$ suggests proton / deuteron transmission through the Nafion® membrane may be occurring through the well-known Grotthuss mechanism[113–122] otherwise known as "hopping mechanism" as represented in Scheme 3.1 below. In the Grotthuss mechanism, the protons (or deuterons) traverse the membrane through the formation of hydrogen-bonded clusters. A Proton (deuteron) hops from one water molecule to another through the water network formed by hydrogen bonding.

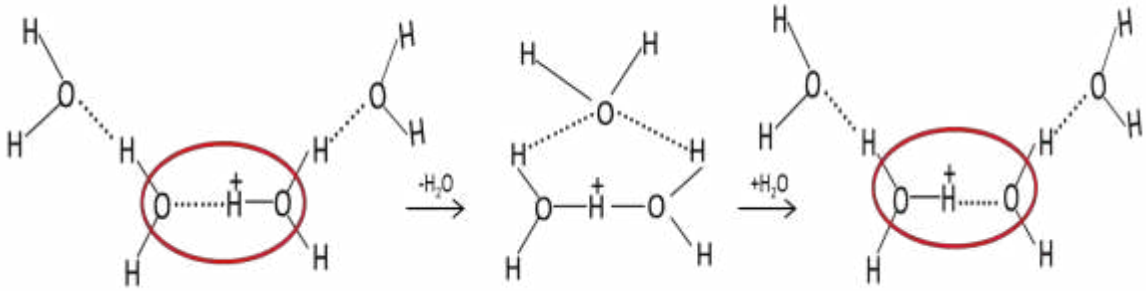


Scheme 3.1. Models of Grotthuss mechanism for $H^+$ (or $D^+$) transport through Nafion® membrane in MEAs without graphene.

This hydrogen bond creates a path that shortens the distance between two oxygen atoms (O···O) in the clusters and allows high proton mobility and thus enhances its

migration through the Nafion® membrane matrix. The exchange of a hydrogen bond with a covalent bond in a solvated proton is the basis of the Grotthuss mechanism that facilitates high proton diffusion through an ionomer membrane. Although another mechanism such as the vehicle mechanism is possible for proton transport, this mechanism is thought to only occur when the membrane is becoming dehydrated.

Figure 3.5 shows very interesting results, in which the HER and DER were compared on MEAs with and without single-layer graphene. It is obvious from Figure 3.5A that single-layer graphene has very little effect on proton transmission. On the other hand, in the Figure 3.5B, the deuteron transmission was significantly attenuated by single-layer graphene. This description of higher proton transmission through graphene than deuteron is represented in Figure 3.6. It is also important to mention that the proton transmission across single-layer graphene occurs at a very high rate (≈1.0 A $cm^{-2}$) than was previously reported on a similar phenomenon but different device architecture and design.[22,24] The bias voltage (-0.15 V) to obtain a rate of ≈1.0 A $cm^{-2}$ is also smaller than the previously reported voltage.[29] This finding is very important for applications that might benefit from using graphene as an ion filter such as a PEM fuel cell device or water electrolyser. The improved performance uncovered here might be due to how our device was fabricated in which single-layer graphene was positioned in between two Nafion® membrane disks. Previous studies have had cells in which the hydrogen evolving catalyst was decorated on the graphene layer placed on the surface of a Nafion® membrane.

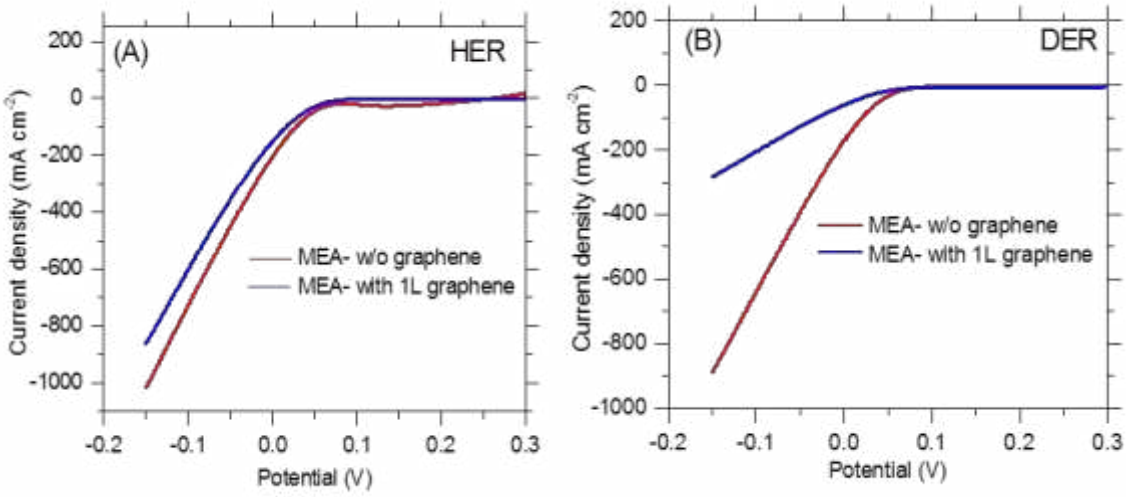


Figure 3.5. Polarization curves on MEAs with and without single-layer graphene (A) HER and (B) DER

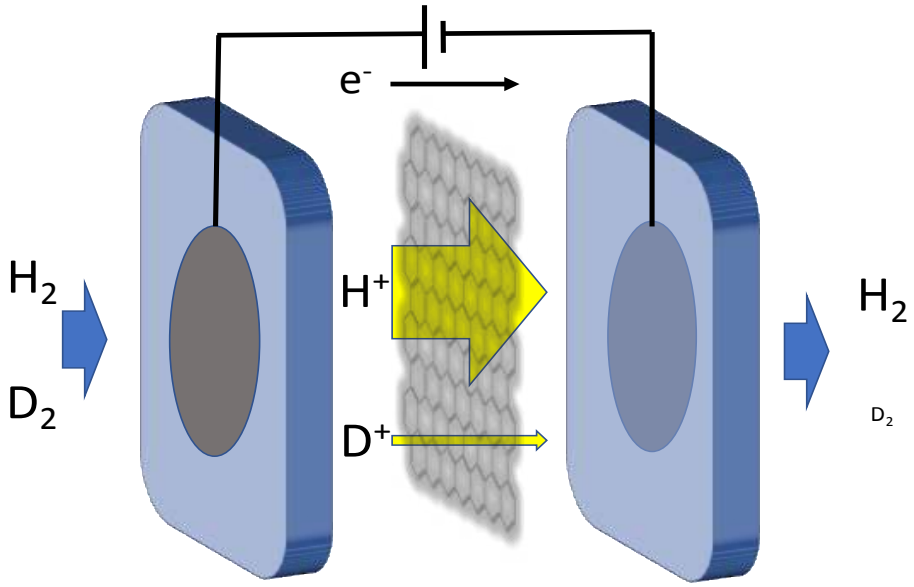


Figure 3.6. Schematic representation of attenuation of deuteron and proton through graphene.

3.2.2 Electrochemical Hydrogen / Deuterium Pump Cell in Symmetric Mode

To better quantify the transport phenomenon of proton/ deuteron through single-layer graphene, an electrochemical hydrogen / deuterium pump cell was configured in the symmetric mode from our miniature cell as shown in the Figure 3.7. The cell is symmetric such that humidified hydrogen gas or deuterium gas (at 30°C; ≈ 100% RH) is supplied to both the anode and the cathode. The MEA was also symmetric in which both the anode

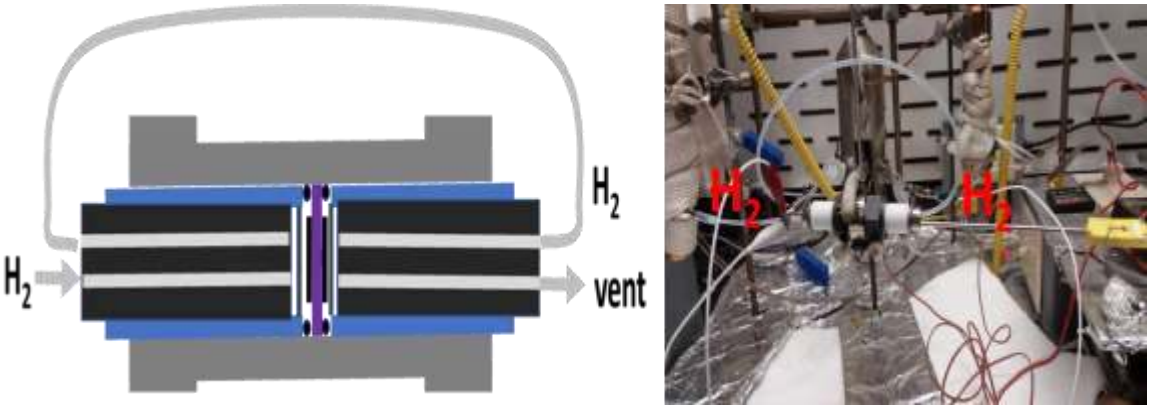


Figure 3.7. Schematic representation of miniature cell in symmetric mode (left) and photomicrograph of the miniature cell in operation with the heat tape (right).

and the cathode have equal geometric size of 0.1875 inch diameter (0.4763 cm) and similar catalyst loading. The cathode and anode catalyst loading in the MEA was 0.3 mg $cm^{-2}$ Pt on microporous layer carbon cloth respectively. An amount of one microliter of 5 wt. % Nafion® solution was added to each of the electrodes which were allowed to dry at ambient conditions. Polarization curves were acquired at a scan rate of 1 mV $s^{-1}$ at a ±

0.07 V bias. The miniature cell in this mode is the classic hydrogen / deuterium pump configuration.[123] The overall cell potential in this configuration is zero. The response from such a cell gives linear current-voltage curve with zero current at zero potential from which ohmic resistance can be obtained.

Unlike the asymmetric hydrogen pump cell that involves non-linear I-V curves (Figure 3.5), the linear I-V curve in symmetric hydrogen pump cell makes estimation of resistance due to just graphene easy as it can be computed from the slope of the I-V curve. This determination is somewhat complicated in case of asymmetric hydrogen pump cell because the rising portion (close to the onset potential) of the curve contains contributions of membrane resistance and graphene ionic resistance and also from reduction of proton / deuteron charge-transfer resistance on the supported catalyst. Figures 3.8 and 3.9 present polarization curves from hydrogen / deuterium pump cell in a symmetric configuration from two sets of MEAs. The first set of MEAs are those where the Nafion® membranes have been converted to the fully protonated form (Figure 3.8), whereas the second set are MEAs in the deuterated form (Figure 3.9). From the I-V curves in Figure 3.8, the green linear curve is the electronic resistance (*i.e.* cell without MEA), the black curve represents the MEA with single Nafion®-211 membrane, and the red I-V curve represents the MEA with two Nafion®-211 membrane disks. The MEA with two Nafion®-211 membranes in which single-layer graphene has been sandwiched between these Nafion® disks is the blue color. The I-V curves for the deuterated MEAs in Figure 3.9 are similarly represented as discussed above.

It is obvious from Figure 3.8 and 3.9 that the effect of doubling Nafion® membrane can be seen clearly (from black to red). However, the effect of graphene is more significant in the deuterium cell than in the hydrogen cell (from red curve to blue). This observation is in agreement with the asymmetric cell measurements (Figure 3.5). To estimate the ion transport resistance rate, quantitative data obtained from Figure 3.8 and 3.9 are summarized in Table 3.1. The resistances obtained from the slopes of the curves were normalized to the geometric area of the electrode. The area-normalized resistances for both protons and deuterons were corrected by subtraction of the electronic resistance (i.e. cell without MEA that includes resistance due to graphite rod, O-ring, gas diffusion

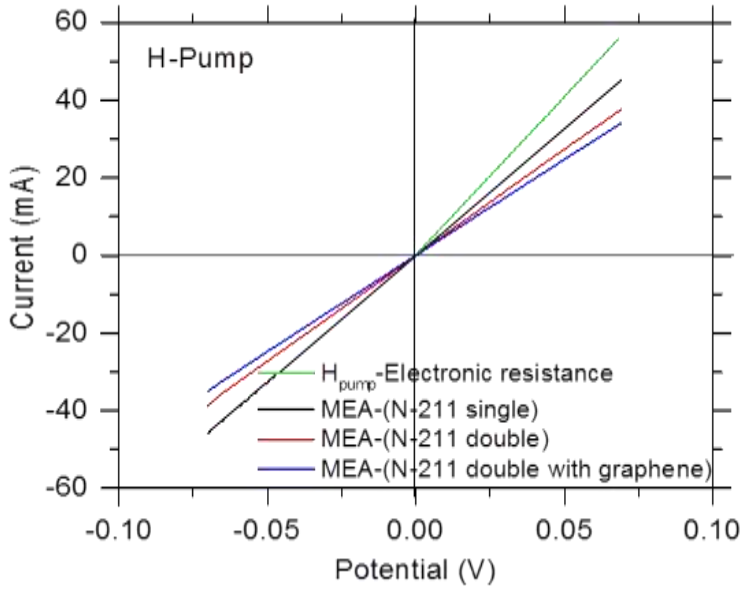


Figure 3.8. Symmetric hydrogen pump polarization curves

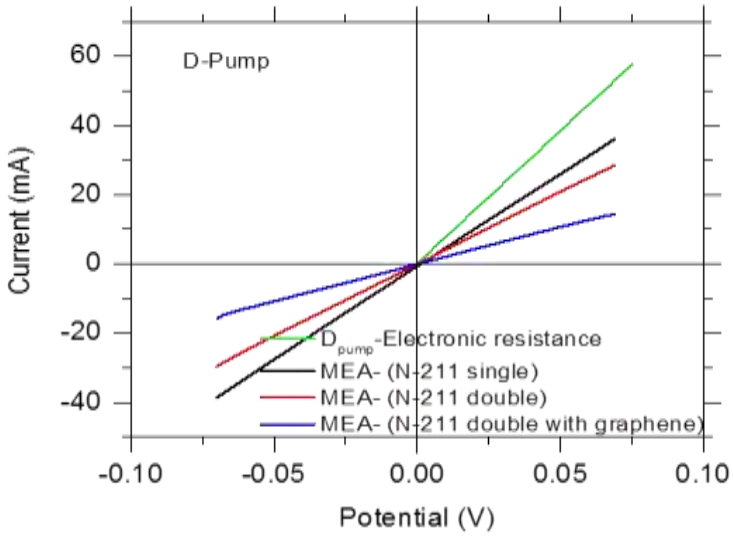


Figure 3.9. Symmetric deuterium pump polarization curves

layer, and compression cell body). Following this correction, the area-normalized resistance due to just graphene can be obtained by simple subtraction of the resistance from the MEA with and without graphene as represented in Table 3.1.

The graphene area-normalized resistances for the two ions ($H^+$ and $D^+$) were converted to graphene areal conductance by taking the reciprocal of the former. The obtained values for proton and deuteron transmission through graphene are 29 S $cm^{-2}$ and 2.1 S $cm^{-2}$, respectively. The graphene areal conductance values for protons and deuterons obtained during this study shows that proton transmission across single-layer graphene is favorable over deuteron by a factor of 14. This value is similar to the reported value of ratio 1:11 in the literature but somewhat slightly larger than prior studies on related cells. It is also important to mention that the graphene areal conductance for

proton obtained in this work is 10,000 times larger than what was reported in the prior work studying similar phenomenon.[24]

Table 3.1 Cell resistances from symmetric H/D pump experiments

| Sample | Resistance, | Corrected Resistance | MEA area resistance | Graphene area resistance |
|---|---|---|---|---|
| | Ω | Ω | mΩ cm$^2$ | mΩ cm$^2$ |
| Proton form | | | | |
| Zero Nafion 211 | 1.266 | -- | -- | -- |
| One Nafion 211 | 1.5295 | 0.264 | 47 | -- |
| Two Nafion 211 | 1.8276 | 0.562 | 100 | -- |
| Two Nafion 211 + graphene | 2.0175 | 0.752 | 134 | 34 |
| Deuteron form | | | | |
| Zero Nafion 211 | 1.266 | -- | -- | -- |
| One Nafion 211 | 1.8634 | 0.598 | 106 | -- |
| Two Nafion 211 | 2.3980 | 1.133 | 202 | -- |
| Two Nafion 211 + graphene | 5.0191 | 3.754 | 668 | 467 |

3.2.3 Confocal Raman Microscopy on Nafion | graphene | Nafion Composite

Raman spectroscopy is a powerful technique for the characterization of graphene signatures.[124,125,134–143,126,144–153,127,154–163,128,164–167,129–133] The confocal Raman microscopy facility at the University of Utah was used to investigate the quality of graphene transferred onto Nafion® membrane. The as-prepared Nafion® | graphene | Nafion® composites were probed for the buried graphene layers. Descriptions of the samples, measurements, and spectrometer are discussed in details in the methods section.

Figure 3.10 shows the confocal Raman spectra obtained for the Nafion® | graphene | Nafion® sandwich structure before the hot press step of the anode and the cathode electrodes to make the MEA.

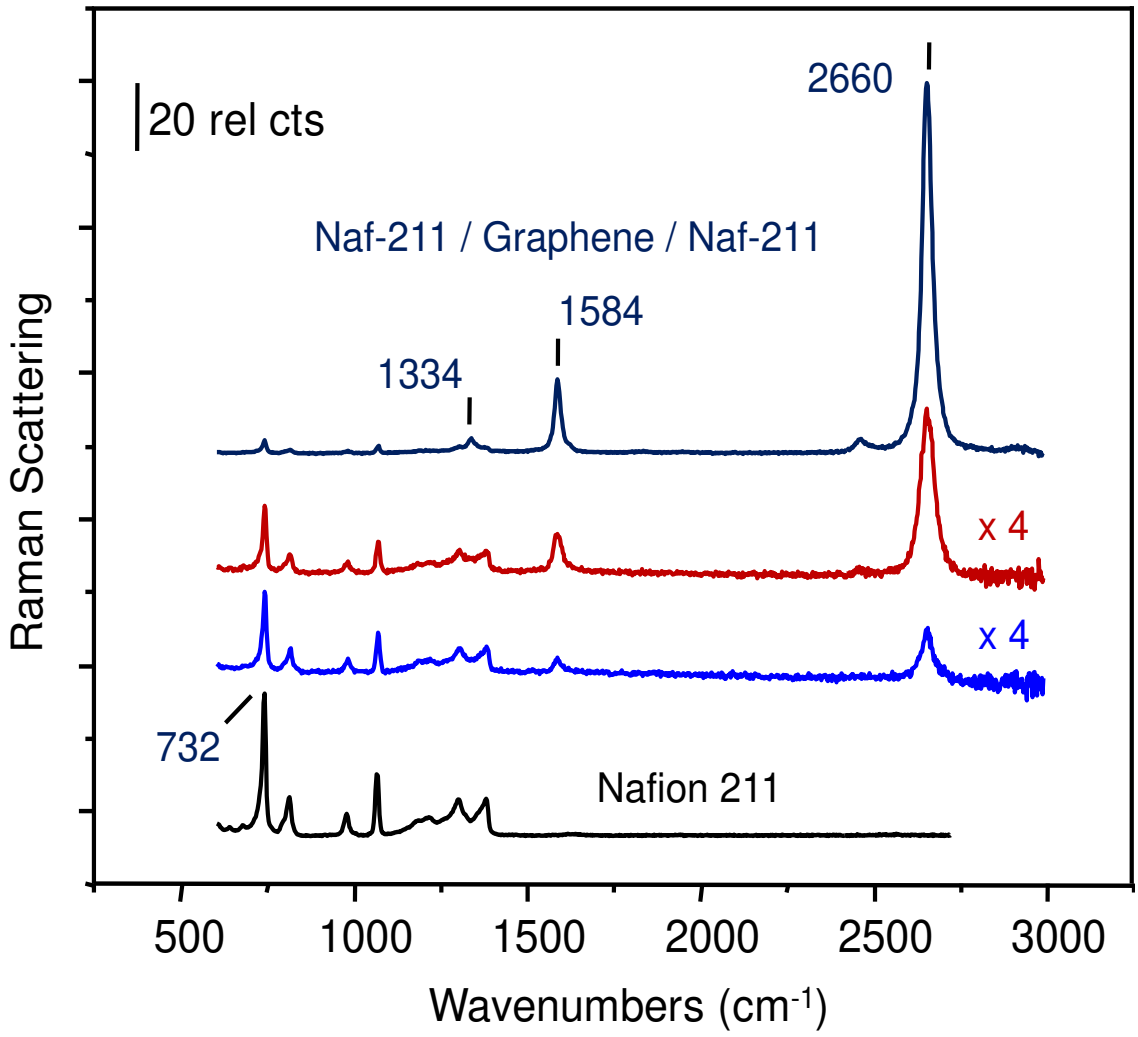


Figure 3.10 Confocal Raman spectra of a Nafion® | graphene | Nafion® structure.

In Raman spectroscopy, graphene usually shows two most important principle bands. The first band is designated as the G-band (1584 $cm^{-1}$),[168,169] which is an in-plane vibrational mode, and it involves the $sp^2$ hybridized carbon atoms in graphene. The second band is the 2D band (2660 $cm^{-1}$), which is an overtone of the D-band.[136,170,171] These two bands (G-band and 2D-band) are extremely indicative of the graphene layer. The presence of a third band, denoted as the D-band (around 1334 $cm^{-1}$), indicates a ring breathing mode, which suggests a disorder or defect in graphene.[172–175] The D-band is usually a weak signal in high-quality graphene. In Figure 3.10, the bottom spectrum (black color) represensts Raman signature of just Nafion® membrane which has no peak above 1400 $cm^{-1}$. The blue, red, and navy-blue spectra represent various stages as the interrogation volume was stepped towards the graphene. The expected G and 2D peaks match well with the literature for single-layer graphene. The full width height maximum (fwhm) of the 2D peak as indicated in Figure 3.10 was estimated to be 31 $cm^{-1}$. Also, the ratio of the intensities of G peak to 2D peak in the uppermost spectrum (navy-blue color) was $\approx$ 0.2. These values are in agreement with the literature for single-layer graphene.[126,176,177]

With a closer look of Figure 3.10, it is reasonable to conclude that the graphene prepared in this sandwich structure is relatively free of defect. Although, this must not be over-emphasized because the Nafion® membrane also has peaks in this region (D-peak). However, absence of a strong D-peak is indicative of the absence of macroscopic defects in graphene, which would have resulted into a large D-peak. Thus, the graphene survived

the hot press technique used to make this Nafion® | graphene | Nafion® sandwich structure.

### 3.2.4 Confocal Raman Microscopy on Electrolyzed MEAs

It is instructive to examine graphene Raman spectra after electrochemical characterization, i.e., when an ample of currents (well above 1.0 A $cm^{-2}$) has been passed through it. Taking a heuristic approach, a special MEA was fabricated that incorporated the use of fiberglass as a guard to protect the graphene sandwiched between two Nafion®-211 discs, as shown in the Figure 3.11. The use of fiberglass enabled easy separation of the anode and the cathode electrodes from the Nafion | graphene | Nafion sandwich structure. The graphene sample was analyzed for its Raman signature as described in Section 3.2.3.

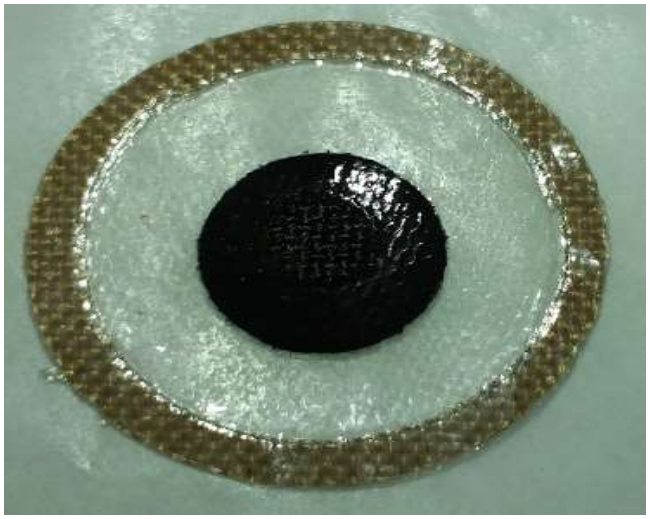

Figure 3.11 MEA fabricated for Raman spectroscopy analysis following electrolysis experiment.

Figure 3.12 shows the acquired confocal Raman spectra of the electrolyzed sampled compared to the sample before electrolysis (see also uppermost spectrum of Figure 3.10). It should be noted that the peaks below 1400 $cm^{-1}$ are typical of Nafion® membrane's Raman signature and should be carefully interpreted for the presence of defects (*i.e.*, D-peak). The observed peaks below 1400 $cm^{-1}$ in an electrolyzed sample are similar to those obtained for Nafion® membrane alone (see bottom spectrum of Figure 3.10, black color). It is obvious however that the peak positions (both G-peak and 2D-peak) shifted when compared to the sample before electrolysis. For example, the G-peak shifted from 1584 $cm^{-1}$ to 1603 $cm^{-1}$ (hypsochromic shift) and the 2D-peak shifted from 2660 $cm^{-1}$ to 2654 $cm^{-1}$ (bathochromic shift).

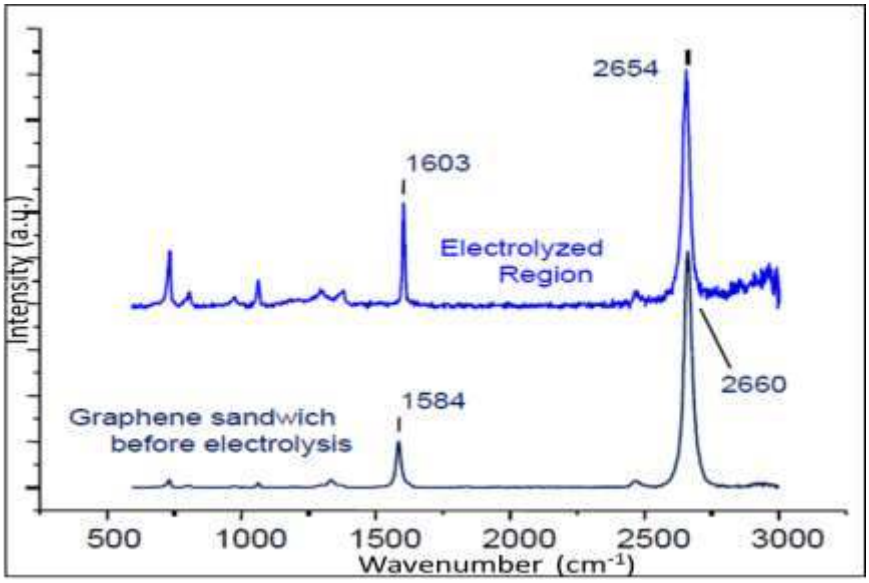


Figure 3.12 Confocal Raman spectra of a Nafion® | graphene | Nafion® sanwich structure before and after electrolysis experiment.

The shifting of peak positions could be a result of passage of ionic currents through the MEA through the graphene sheet. It is however interesting that the peaks of 2D and G are consistent with the expectation for a single-layer graphene and that the passage of ionic currents did not create additional defect in graphene. For a more detailed comparison, Figure 3.13 shows the Raman spectra of the electrolyzed MEA in two different spots. The first spot was at the center of the MEA within the electrode area where high ion flux passed through the graphene sheet. The second spot was outside the electrode area but still within the area covered by the graphene sheet around the edge of MEA. Little or no ion flux is expected through this region. Interestingly, the graphene Raman spectra from both areas are almost identical which suggest that ion flux through graphene did not create additional defect and that the ion transmission through graphene must be occuring through hexagonal graphene hollow sites.

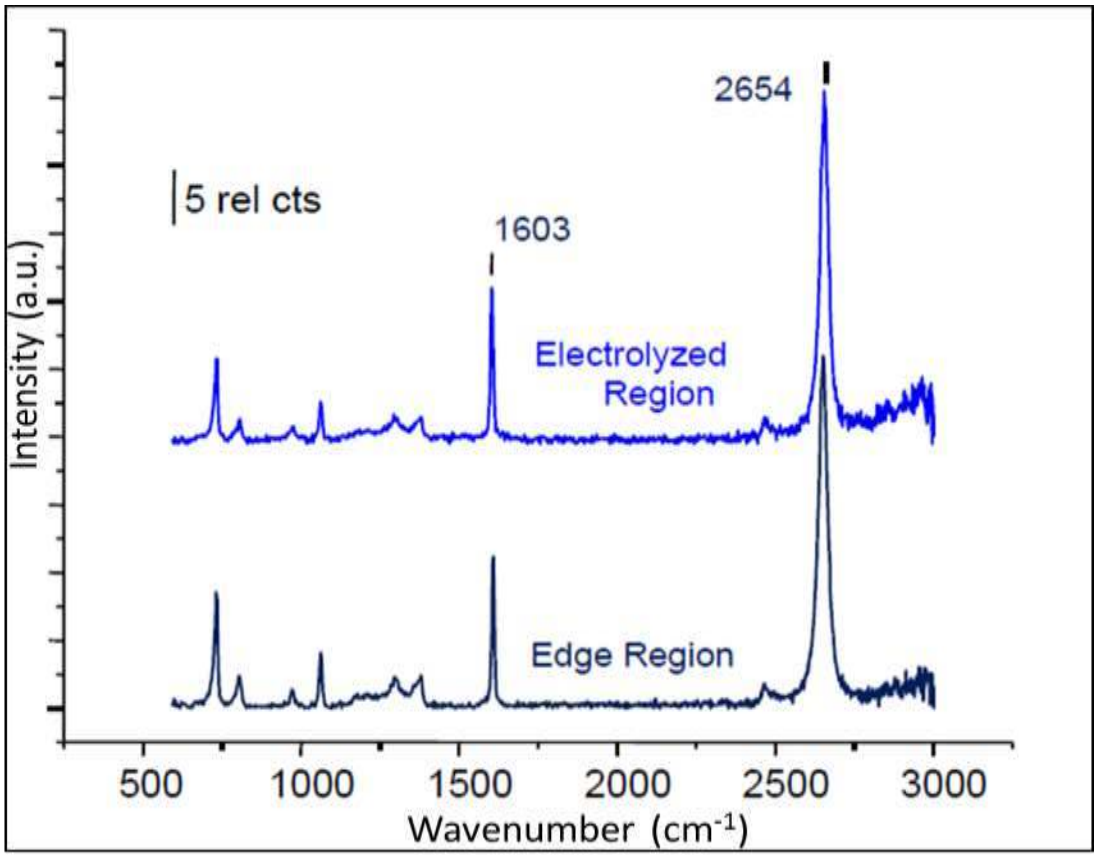


Figure 3.13. Confocal Raman spectra of Nafion® | graphene | Nafion® structure on electrolyzed MEA at different regions.

### 3.2.5 Silver/ Silver-Chloride Cells

Conventional knowledge suggests that single-layer of pristine graphene should block the transport of all ions, molecules, and even atoms except thermal protons due to the high energy barrier required for such transmission to occcur. The graphene used during this work was prepared through the CVD method on a metal substrate (Cu). Investigating how ions other than protons traverse a graphene sheet is important to understand the origin of high proton transmission observed in this study for the HER. The

miniature PEM cell used was re-modified to study the transport of other cationst as shown in Figure 3.14. The graphite rod was attached to a Ag disk electrode and the surface was converted to Ag-AgCl by a brief anodization in a solution of 0.1 M HCl. The Nafion® | graphene | Nafion® sandwich structures were converted to each ion studied and were placed within microporous filter papers. The microporous filter papers were soaked in their respective electrolytes prior to use.

From Figures 3.15A (for potassium ion) and 3.15B (for proton), it can be seen that proton and potassium ions transmit through the Nafion® membrane with no pronounced observable selectivity. However, with single-layer graphene in the MEAs, potassium ions were a lot more attenuated as compared to protons which are similar either with or without graphene. Single-layer graphene almost completely blocks the transport of $K^+$ while allowing high proton transmission through it.

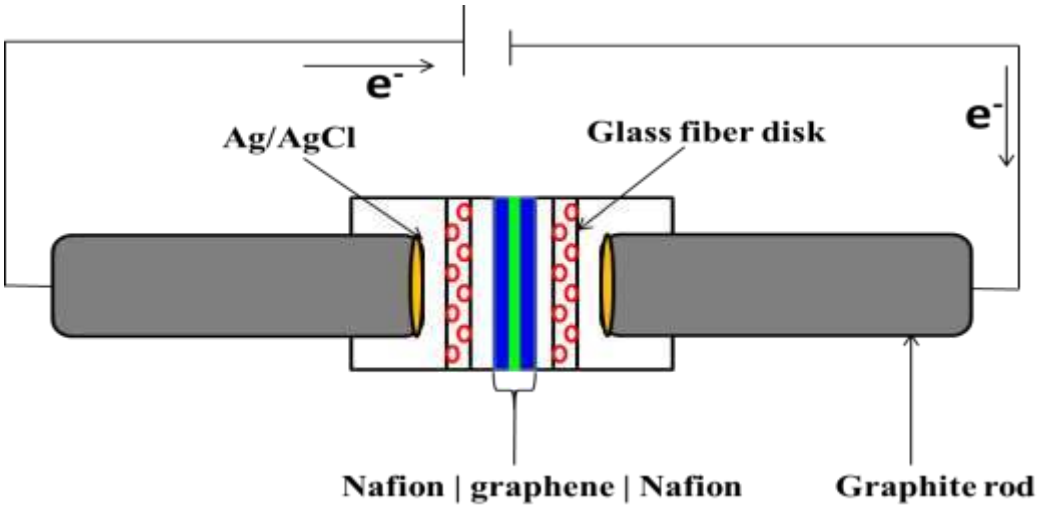


Figure 3.14. Cell representation used for cation measurement in Nafion®/graphene sample

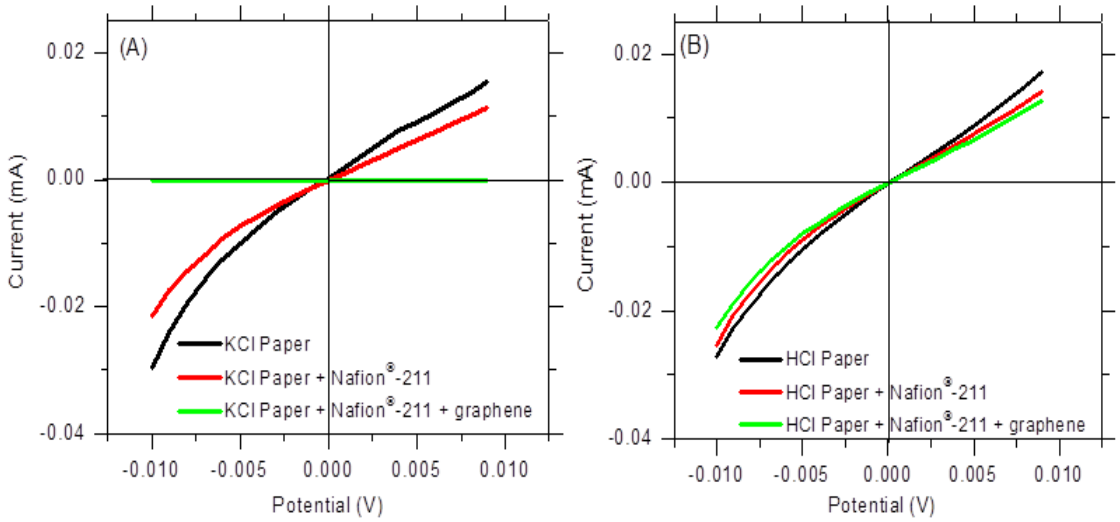


Figure 3.15 Polarization curves for aqueous solution of ion transport in Ag-AgCl PEM style cell (A) $K^+$ and (B) $H^+$

Similarly, other ions ($Na^+$, $Li^+$ and $NH_4^+$) were investigated as shown in Figure 3.16 below. Again, $Na^+$, $Li^+$, and $NH_4^+$ were largely attenuated by graphene, although not totally blocked.This shows that CVD graphene may not be a perfect barrier. But, it is interesting to see that transport of ions other than the proton through graphene is infinitesimal, which indicates that rare defects may be resposnible for the observed very low ion transport in other cations.

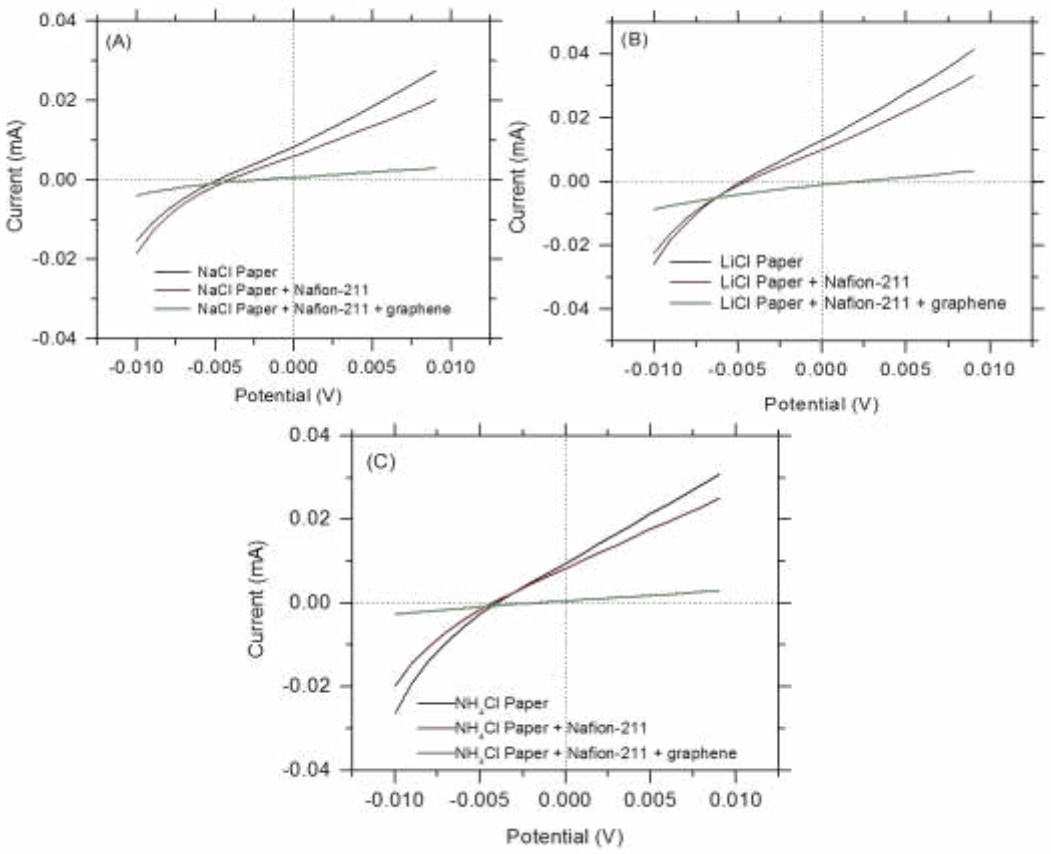


Figure 3.16. Polarization curves for aqueous ion transport in Ag-AgCl PEM style cell: (A) $Na^+$, (B) $Li^+$, and (C) $NH_4^+$

### 3.2.6 The Electrochemical Model for Proton Transport

The observed high proton transmission through graphene could mean that protons traverse the hexagonal hollow graphene structure. An electrochemical model was proposed that accounts for the observed proton transport rate through the graphene sites. Such a model is useful in understanding the role of activation energy on the rate of proton/deuteron transport across graphene sandwich structures. A regular hexagonal

graphene structure with a carbon-carbon bond distance of 0.142 nm, will have a geometric area of 5.24 $Å^2$ (5.24 x $10^{-16}$ $cm^2$) in each hollow site. The graphene area-normalized resistances for protons (34 mΩ $cm^2$) and deuterons (467 mΩ $cm^2$) in Table 3.1 correspond to a per site proton-/ deuteron- transfer resistance of 65 x $10^{12}$ Ω and 891 x $10^{12}$ Ω respectively. The obtained per site transfer resistances for both the proton and the deuteron can be considered as charge-transfer resistances using the well-known Butler-Volmer equation below.

$$i = i_0 \left[e^{-\alpha f \eta} - e^{(1-\alpha) f \eta}\right] \qquad \text{eqn 3.3}$$

where i = the net current, $i_0$ = the exchange current, α = transfer coefficient, f is a term that corresponds to F/RT (F = Faraday's constant, R = gas constant and T = absolute temperature), and η = overpotential.

From the above equation 3.3, if the overpotential (η) is sufficiently small and it was the case for the electrode kinetics that involves hydrogen oxidation and reduction reactions. The electrode process for hydrogen oxidation / reduction is usually facile and the activation overpotential is always small. Hence, the equation 3.3 above can be approximated to give equation 3.4 below:

$$i = -i_0 \ (f\eta) \qquad \text{eqn 3.4}$$

This equation shows that the net current is related linearly to the overpotential, which is usually observed in the symmetric experiment described above. The ratio (-η/i) has the

same unit as resistance and is usually called charge transfer resistance ($R_{ct}$). By re-writing the equation 3.4 above, one can obtain the equation 3.5 below:

$$R_{ct} = \frac{RT}{Fi_0} \qquad \text{eqn 3.5}$$

Parameter $R_{ct}$ is an index that illustrates the kinetic facility of electrode process. Equation 3.5 can then be expressed as equation 3.6 below. Recall, that Q (charge) = current (i) x time (s),

$$R_{CT} = \frac{RT}{Fi_0} = \frac{RT}{F\ e\ k_{rxn}} \qquad \text{eqn 3.6}$$

where e = charge on proton per site, and $k_{rxn}$ = first-order rate constant for proton transfer per site (that has unit per second). By substituting proton (or deuteron) per site transfer resistance into equation 3.5, charge-transfer resistance ($R_{ct}$) can be obtained. Consequently, equation 3.6 can be solved to determine the first-order rate constant for both the proton and the deuteron which are ≈ 2500 and ≈ 180 $s^{-1}$, respectively.

## 3.3 MATERIALS AND METHODS

### 3.3.1 Materials

Chemical vapor deposition (CVD) single-layer graphene on Cu was purchased from ACS Material LLC. Nafion®-211, carbon cloth electrodes, and gas diffusion layer (GDL) were purchased from The Fuel Cell Store. High purity hydrogen gas and research grade deuterium gas were provided from large cylinders and connected to the test station through humidifier bottles. Ammonium persulfate was purchased from Beantown Chemical. Deionized water was used throughout the experiment.

3.3.2 Fabrication and Transfer Technique of Single-Layer Graphene onto Membrane

Figure 3.17 shows various stages of transfer of single-layer graphene onto Nafion® membrane. First, the CVD graphene on Cu substrate was hot pressed onto Nafion® membrane supported with PTFE reinforced fiberglass (Figure 3.17A). This was

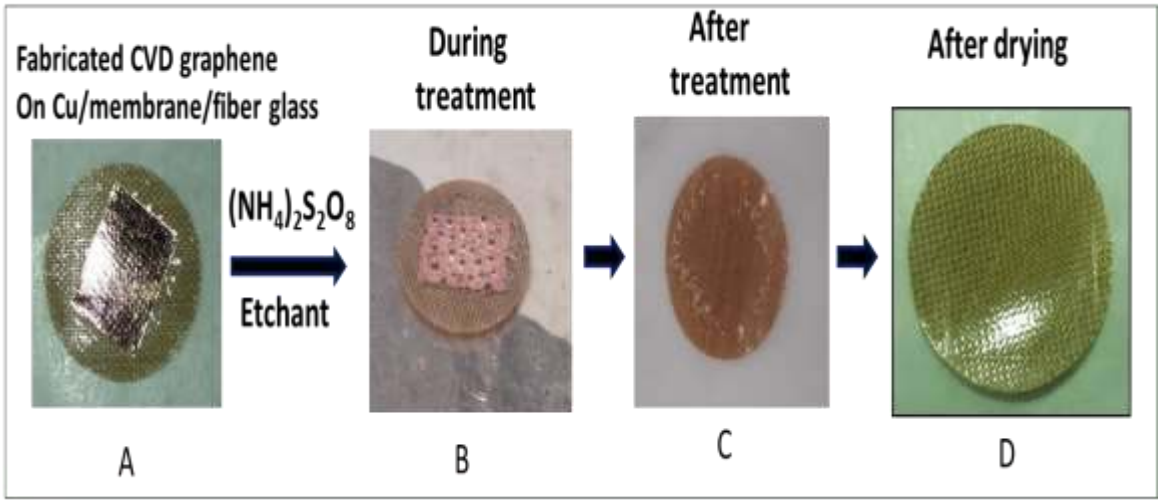


Figure 3.17. Photomicrographs of various stages of single layer graphene transfer onto Nafion® disk

followed by immersion in a solution of 0.3 M ammonium persulfate (etchant) . Figure 3.17B shows the bubbles as the etchant removes the adlayer Cu. The graphene that had been transferred onto Nafion® disk is unaffected by this treatment. Figure 3.17C shows clearly the region of graphene on Nafion® membrane with wrinkles due to absorbed moiture. A dried sample obtained afterwards is shown in the Figure 3.17D prior to making the MEA.

3.3.3 Fabrication of Nafion® | graphene | Nafion® Sandwich Structure MEAs

Figure 3.18 presents the schematic representation of the transfer and making of Nafion® | graphene | Nafion® sandwich structures and the application of carbon-cloth electrodes.

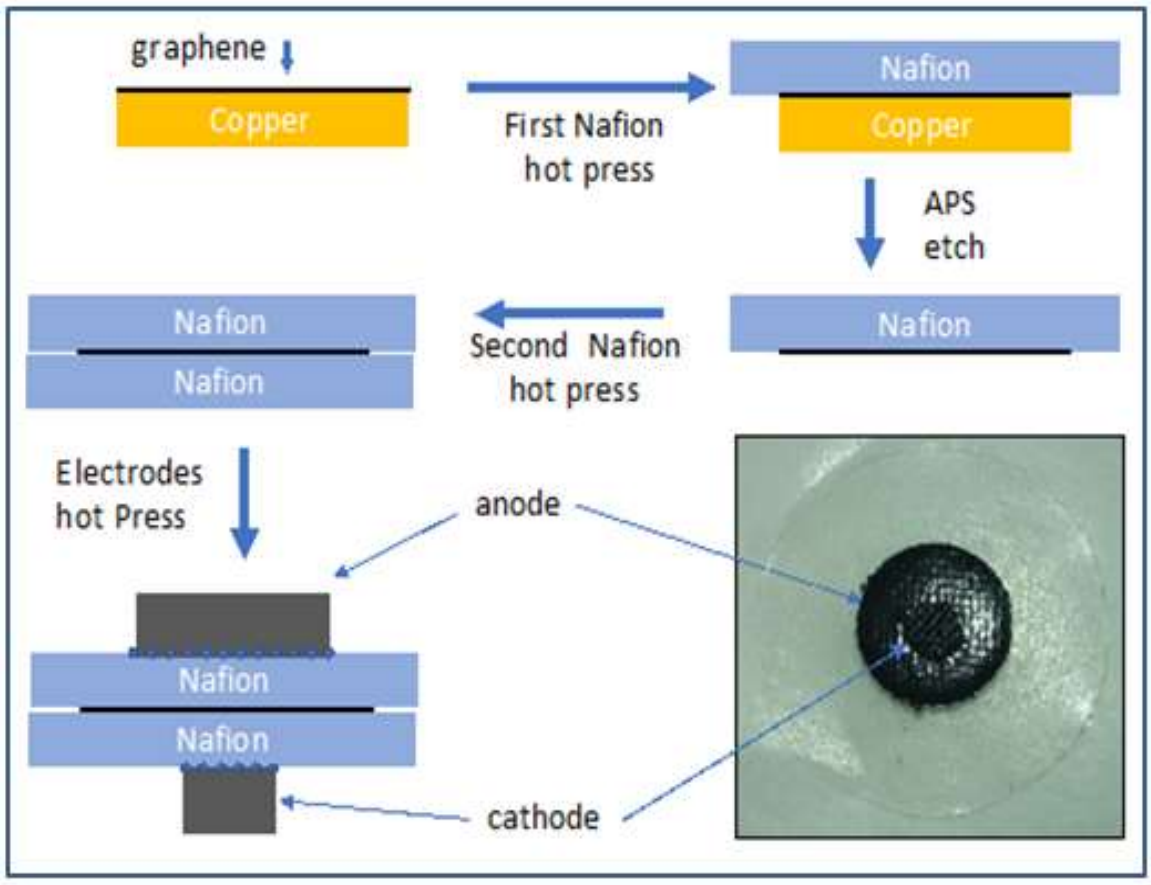


Figure 3.18. Making of Nafion® | graphene | Nafion® sandwich structures MEA.

The first three steps in Figure 3.18 illustrate what was described in Section 3.3.2. Moving from that step, a second piece of Nafion® disk was hot pressed to make the sandwich structure together with Pt on carbon-cloth electrodes. For the asymmetric

electrochemical hydrogen pump (HER and DER), the anode catalyst was 5/16 inch diameter carbon cloth containing 4 mg $cm^{-2}$ Pt and the cathode was 3/32 inch diameter carbon cloth containing 0.03 mg $cm^{-2}$ Pt. Prior to hot pressing the carbon-cloth electrodes, 0.5 μL of Nafion® solution 5 wt. % was coated on the cathode catalyst surface and 3.5 μL of the same solution on the anode electrode. This was necessary to ensure proper interfacial contact between the electrode catalyst layers and the Nafion® membrane. The cathode in the MEA is smaller than the anode electrode to avoid edge effect during electrochemical measurements. The size of the Nafion®-211 membrane used was 3/4 inch diameter. For the symmetric electrochemical hydrogen pump experiments, the anode and cathode electrodes were of the same size, 3/16 inch diameter carbon cloth electrode containing 1 μL Nafion® solution (taken from 5 wt. % Nafion® solution bottle). The whole assembly was hot pressed together as shown in the Figure 3.18 using the Carver hot press (model No 3851-0) for 5 min at 140 °C, 600 $lb_f$ (2.67 kN).

### 3.3.3 Cell Assembly and Testing

The cell assembly and components are similar to the miniaturized cell described in Section 2.2.1. The major different is the cell body is ¾ inch diameter. Also, the graphite rods are 5/8 inch diameter with two holes (1/8 inch diameter) bored through the rods. The cell testing was conducted in two modes. The first mode is the asymmetric configuration in which the anode was bathed with humidified hydrogen or deuterium gas, while the cathode was bathed argon gas. For the symmetric hydrogen / deuterium pump mode, both the anode and the cathode compartments were bathed with humidified

hydrogen or deuterium gas. All gases were humidified at 30 $^{o}$C. The polarization curves were acquired using cyclic voltammetry (scan rate 5 mV $s^{-1}$) in asymmetric mode and linear sweep voltammetry (scan rate 1 mV $s^{-1}$) in symmetric mode. All electrochemical experiments were performed on electrochemical analyzer CH Instruments (model No CHI 1140B).

### 3.3.4 Raman microscopy/spectroscopy

Confocal Raman microscopy experiments were performed using a facility at the University of Utah. The details of operation are given in the reference [178]. In brief, Raman scattering excitation was acquired using a monochromatic diode laser at 638 nm (Innovative Photonic Solutions, Monmouth Junction, NJ). The optical power of the laser was filtered and was allowed to fill an oil immersion objective (Nikon, Plan APO VC). The oil immersion objective was mounted on an inverted fluorescence microscopy frame (Nikon Eclipse TE-200). From this objective, the laser beam was directed through an immersion-oil coupled coverslip and was made to focus within the Nafion® membrane sandwich structure just a little below where the graphene was located at the center of the membrane sandwich (ca. 20 μm above the coverslip). The probe volume was scanned slowly until the graphene peaks became evident.

## 3.4 CONCLUSIONS

In summary, proton transmission through single-layer CVD graphene was demonstrated to occur at a high rate in a Nafion® | graphene | Nafion® sandwich structure. The proton

transmission through graphene was much faster than deuteron with a selectivity factor of 14. The higher proton transmission observed in this study might reflect better cell assembly, design and improved interfacial contact between the graphene carbon network and protogenic group of the perfluorosulfonic acid (PFSA) ionomer membrane. This exciting observation might suggest good prospects for electrochemical devices such as fuel cells and electrolyzers that operate at higher current densities that will make use of the exciting properties of graphene's subatomic selectivity.

# CHAPTER FOUR

# ARRHENIUS ANALYSIS FOR PROTON / DEUTERON TRANSMISSION THROUGH GRAPHENE

## 4.0 SYNOPSIS

The work described in this chapter has been published in Elsevier Journal of the *Electrochimica Acta* with the following bibliographical details, *Electrochimica Acta* Volume 296, 10 February 2019, Pages 1-7. It involves measurement of proton and deuteron transmission rates across single-layer graphene as a function of temperature. An electrochemical model based on charge-transfer resistance was invoked to estimate standard heterogeneous ion-transfer rate constants. An encounter pre-equilibrium model for ion-transfer step was used to estimate rate constants which provide values for activation energies and exponential pre-factors for proton (or deuteron) transmission across graphene.

## 4.1 INTRODUCTION

Micro-mechanically exfoliated graphene in its pristine form has long been described as an impermeable 2D material.[17,179–181] The smallest molecule such as hydrogen and monatomic helium gas with Van der Waal radii of 0.314 and 0.28 nm respectively cannot traverse pristine graphene huge electron cloud. Hu and co-workers[24] in their work demonstrated a lack of detection of helium when a positive bias or no bias was applied to Pt decorated graphene electrode that faces vacuum chamber equipped with

a mass spectrometer. Proton however, being a nuclear particle with no accompanied electron cloud may at least pierce through the dense graphene electron cloud.

Recent experimental findings have established high proton transmission across single-layer graphene despite this conventional understanding of impermeability of graphene electron cloud.[15,16,22,24,182–185] It is important to mention also, that deuteron transmission does occur but at a much slower rate when compared to that of proton. The theoretical prediction of activation energy (1.2-2.2 eV) from computational studies[186–193] would mean near-zero proton transmission across single-layer graphene at room temperature, otherwise, the activation energy must be smaller than the predicted value for such transmission to occur. One possibility for such occurrence is proton transmission through graphene hexagonal hollow site. Another possibility is the transmission through rare scale-atomic defect sites that are undetected by spectroscopic methods.[194,195] If the latter is the case, the defects must be rare enough that will support high proton transmission with pronounced selectivity to deuteron and at the same prevent other large ion species from going through it.

Hydrogenated defect or hydroxylated defect sites were also reported by Achtyl and co-workers[183] for possible high proton transmission through graphene. Other atoms placement defects that are equally observed that can contribute to ion transmission across graphene are the point defects (such as Stone-Wales defect or vacancy defect) or line defects (such as gain boundary or edge defect).[158,196,197] The actual mechanism of high proton transmission across graphene will continue to be a topic of debate and will require further research efforts. The aforenoted notion that proton transmission occurs through

graphene without any structural defect will be fascinating. This is because it will change the previous understanding that the graphene and related 2D materials are impenetrable materials.

In order to understand the mechanism by which high proton flux occurs through single-layer graphene, we used our miniaturized electrochemical cell in a symmetric hydrogen pump configuration. Electrochemical symmetric hydrogen pump has been discussed in chapter three of this dissertation.[16] It generally, consists of platinum catalysts layer on carbon cloth electrode for both the anode and the cathode of the same size and catalyst loading. The electrodes are then hot pressed with perflourosulfonic acid ionomer membranes with and without single-layer graphene. Hydrogen oxidation occurs at the anode and reduction reaction takes place at the cathode using a slow scan linear sweep voltammetry. From the slope of the I-V curves, the resistance due to ion transport is then estimated. It was demonstrated in chapter three that high proton transmission (in excess of 1.0 A $cm^{-2}$) through graphene occurs at very small applied bias (< 200 mV). This observed high proton transmission requires estimation of activation energy to understand the fundamental ion transmission step across the graphene.

As a result, variable temperature measurements were conducted in a thermal cell version of electrochemical miniaturized cell for proton and deuteron transmission through single-layer graphene. The graphene-based MEAs were prepared as sandwich composites. The obtained symmetric I-V curves were analyzed to estimate the ion transfer resistance and interpreted through a model that considers proton (or deuteron) transport through graphene as an interfacial charge-transfer resistance. This charge-

transfer resistance may be described as heterogeneous rate constant and first-order rate constant by the application of this electrochemical model. Overall, the analysis provides values for activation energies and exponential pre-factors for both proton and deuteron across single-layer graphene. The treatment described here provides mechanistic insights into which reaction pathways are involved for hydrons transmission through single-layer graphene.

## 4.2 EXPERIMENTAL

### 4.2.1 Materials

Nafion®-211 (25.4 μm) PFSA membrane was purchased from Fuel Cell Store and were converted to proton or deuteron form before use. CVD Single-layer graphene on Cu was purchased from ACS Materials LLC. The anode and the cathode electrode catalysts (0.3 mg $cm^{-2}$Pt on carbon cloth) were obtained from Fuel Cell Store. Ammonium peroxydisulfate (APS) was purchased from Beantown Chemicals. Deuterium gas (research grade) and hydrogen gas (Ultra high purity-200) were purchased from Air gas in small cylinder and large cylinder respectively, and then connected through the gas line to the flow meter (from Dwyer). Gas humidification was achieved by connecting the gas from the Dwyer rotameter to humidifier bottles maintained at set temperature (30-60$^{o}$C).

### 4.2.2 Cell Design and Fabrication

The cell design is similar to the miniaturized cell described in chapter three. The major differences are illustrated below. The cell body used for variable temperature studies was

made from stainless steel. The cell body is ¾ inch diameter. The current collectors are made from titanium rods of size 5/8 inch diameter. Two holes (1/8 inch diameter each) were bored through the center of the rods for gas entry and exit. The gas diffusion layers are platinized and unplatinized titanium mesh. A thermocouple was mounted onto the cell body which was wrapped around with the heat tape to control and monitor the cell temperature. Another thermocouple is occasionally inserted into the inner cell body to monitor the temperature where MEA is located. Humidified hydrogen or deuterium gas is supplied to the cell at different set temperature (30-60$^{o}$C). Figure 4.1 shows the description of the cell and the cell in operation in a symmetric mode.

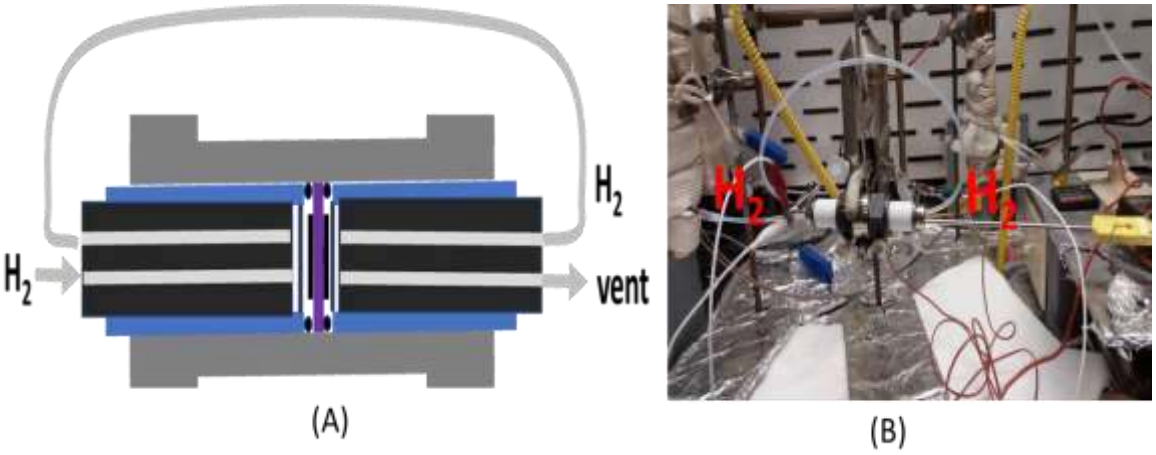


Figure 4.1. (A) Schematic representation and (B) cell in operation for variable temperature in symmetric mode.

4.2.3 Membrane Electrode Assembly Fabrication

Prior to making MEA, single-layer graphene was transferred to Nafion® membrane similar to the transfer technique described in chapter 3 and as shown in the Figure 4.2. First, 4.0 $cm^2$ CVD graphene on Cu was cut from a large CVD graphene sample, a thin layer of Nafion® solution (3.5 µL from 5 wt. % Nafion® solution) was coated on the surface of graphene on Cu and was allowed to dry at ambient condition. Thereafter, the CVD graphene was placed on Nafion® -211 membrane supported by a fiberglass and hot pressed for 2 min at 600 $lb_f$, 140 $^oC$. 0.3 M $(NH_4)_2S_2O_8$ was used to etch out the underlying Cu overnight. The second disk of Nafion® membrane was then hot pressed at the same condition as above. This step may sometime be combined with the application of 0.3 mg $cm^{-2}$ Pt carbon cloth electrodes to make the MEA at the said hot press conditions but over a period of 5 min.

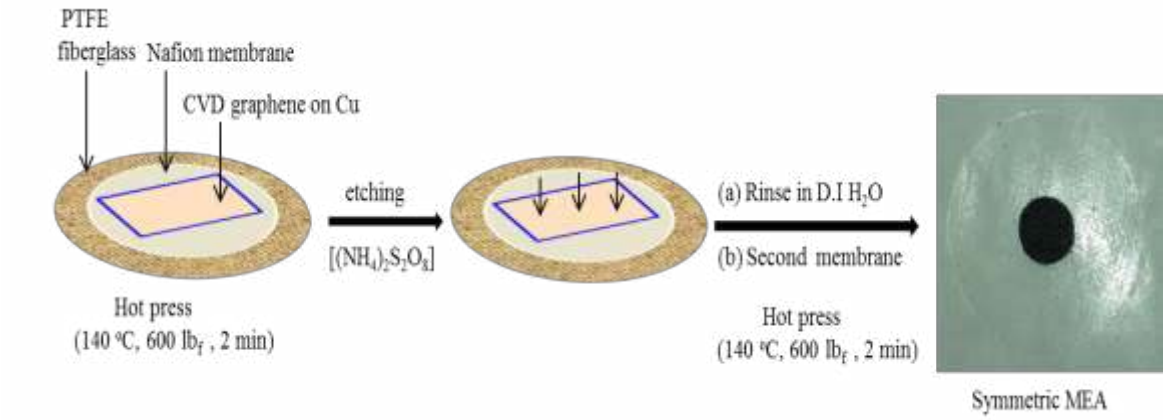


Figure 4.2. Fabrication of Nafion® | graphene | Nafion® sandwich and the making of MEA.

### 4.2.4 Electrochemical characterization

Variable temperature measurements were performed in a symmetric mode where both the anode and the cathode were bathed with humidified hydrogen or deuterium gas. The temperatures of the cell and humidifier bottle were varied from 30 to 60$^{o}$C. The MEAs were converted to their respective ionic forms ($H^+$ or $D^+$) by boiling in $H_2SO_4$ / $H_2O$ and $D_2SO_4$ / $D_2O$. Two independently prepared MEAs were tested at each set temperature for both proton and deuteron. The polarization curves were acquired using a linear sweep voltammetry with a scan rate of 1 mV $s^{-1}$.

## 4.3 RESULTS AND DISCUSSION

### 4.3.1 Variable Temperature Measurement

The polarization curves for proton and deuteron transmission through graphene at variable temperature are presented in the Figures 4.3 and 4.4 respectively. All the polarization curves for MEAs with no graphene for proton and deuteron were characterized in duplicate runs on independently prepared MEAs. This was also the case for MEAs with graphene as indicated in the figure at the indicated temperature. As can be seen from the Figures 4.3 (A, B) and 4.4 (A, B) for MEAs with no graphene, the proton and deuteron transmission through Nafion® membranes are quite similar on the current axes though deuteron being slightly lower as compared to proton. This observation is consistent to the fact that proton and deuteron are solvated and are transported through the water clusters channel as discussed in Chapter Three.[198,199] Also, the molar masses of

both are quite similar compare $H_3O^+$ to $D_3O^+$. Deuteron being heavier would be expected to transmit slower as compared to proton.

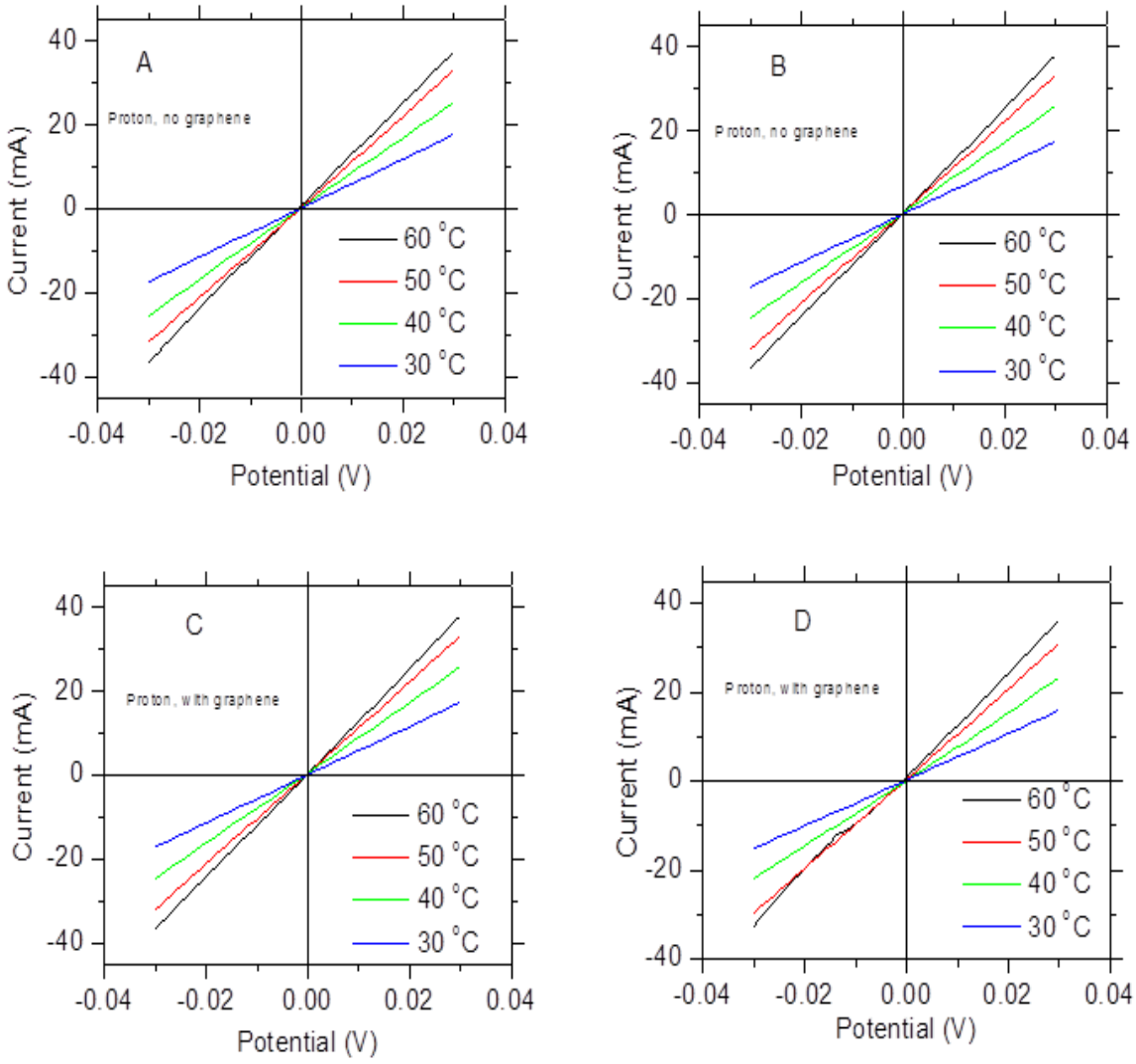


Figure 4.3. I-V curves for proton transmission in symmetric cell at variable temperature (A, B) MEAs with no graphene and (C, D) MEAs with graphene

More importantly, proton transmission occurs at a high rate considering the absolute current of ≈ 40 mA at just bias of ± 30.0 mV.

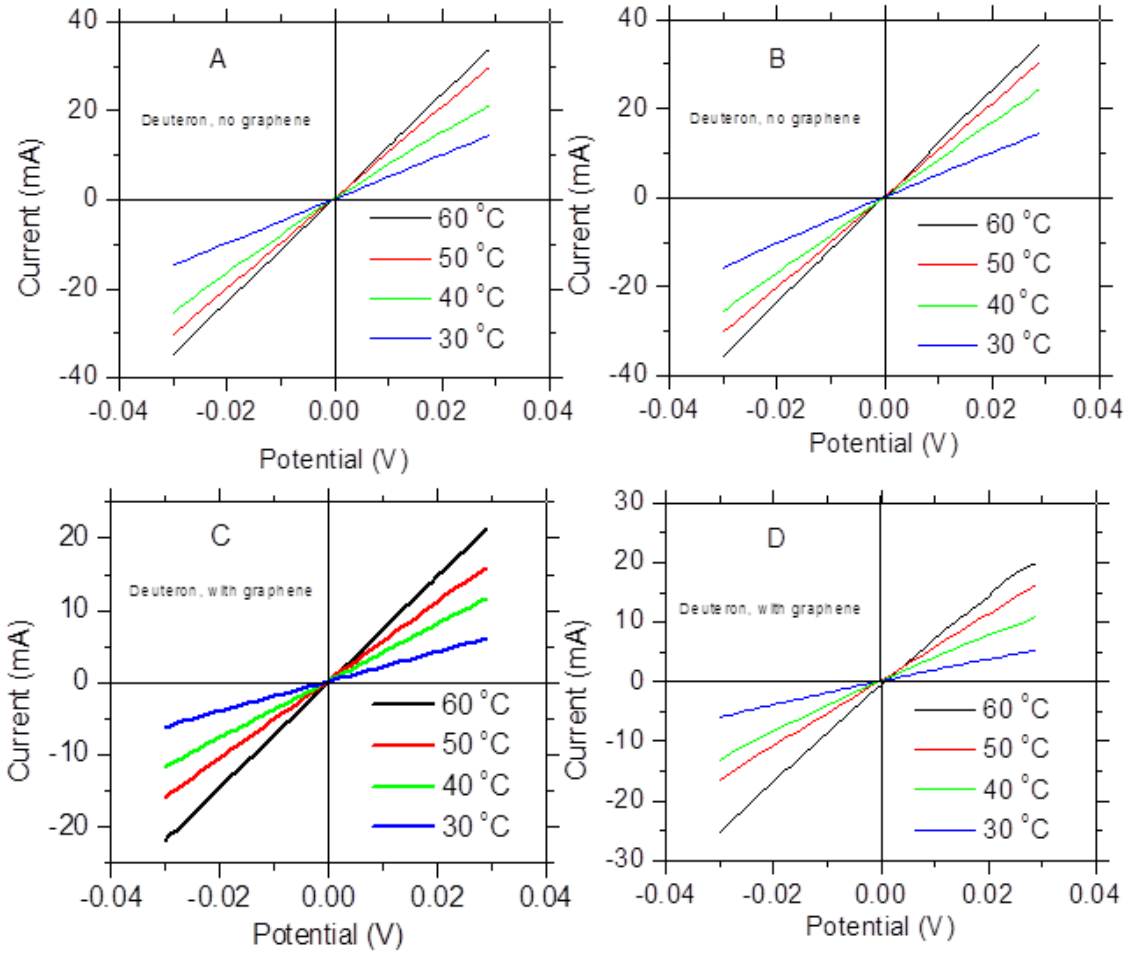


Figure 4.4. I-V curves for deuteron transmission in symmetric cell at variable temperature (A, B) MEAs with no graphene and (C, D) MEAs with graphene

Interestingly, when compared the same Figures 4.3 (C, D) and 4.4 (C, D) for MEAs with graphene, it is easy to see that the I-V curves increase with increase in

temperature consistent with the notion that proton transmission through graphene is a thermally activated process.[24,200,201] More striking though is the fact that deuteron is a lot attenuated when compared to proton at each temperature. This can be seen from the comparison of the absolute current axes of Figures 4.3 and 4.4. From the slopes of all of these curves, the resistance due to proton or deuteron transmission can be computed as presented in Table 4.1 and 4.2, respectively.

Table 4.1 Resistances due to proton transmission in symmetric experiment

| Temp | R without graphene (Ω) | | | R with graphene (Ω) | | |
|---|---|---|---|---|---|---|
| (°C) | MEA-1 | MEA-2 | Average | MEA-1 | MEA-2 | Average |
| 30 | 1.7168 | 1.7361 | 1.7265 | 1.9322 | 1.9665 | 1.9494 |
| 40 | 1.1839 | 1.1919 | 1.1879 | 1.3365 | 1.3044 | 1.3205 |
| 50 | 0.9259 | 0.9228 | 0.9244 | 0.9929 | 1.0159 | 1.0044 |
| 60 | 0.8143 | 0.8069 | 0.8106 | 0.853 | 0.8544 | 0.8537 |

Table 4.2 Resistances due to deuteron transmission in symmetric experiment

| Temp | R without graphene (Ω) | | | R with graphene (Ω) | | |
|---|---|---|---|---|---|---|
| (°C) | MEA 1 | MEA 2 | Average | MEA 1 | MEA 2 | Average |
| 30 | 2.016 | 1.9603 | 1.9882 | 4.8611 | 5.2442 | 5.0527 |
| 40 | 1.2646 | 1.1859 | 1.2253 | 2.5392 | 2.4655 | 2.5024 |
| 50 | 0.9835 | 0.971 | 0.9773 | 1.8524 | 1.8047 | 1.8286 |
| 60 | 0.8608 | 0.8407 | 0.8508 | 1.3685 | 1.2826 | 1.3256 |

4.3.2 Charge-Transfer Resistance Model

The measured resistances for proton and deuteron in MEAs with and without graphene can be further analyzed. The average resistance at each temperature for each ion with and without graphene can be subtracted to get resistance due to just graphene. The obtained resistance data can be normalized by multiplication with the geometric area of the MEA to give area normalized resistance. Uncertainties in the measurement are calculated for the MEAs with and without graphene for proton and deuteron. These uncertainties are quite low overall for proton transmission just through Nafion® membrane but a little bit more for deuteron. They are however, a bit more for MEAs with graphene regardless of the ions. This might be as a result of contamination of $D_2O$ in $H_2O$ and vice versa. Overall the relative uncertainty is quite small for MEAs in cell without graphene (less than 5%) and is less than 20 % for MEAs with graphene. Table 4.3 shows the average resistance and uncertainties in the measurements with other analyses of the measured resistance data.

Table 4.3 cell resistances and rate parameters for proton and deuteron transmission through graphene

| Proton | | | | | | | |
|---|---|---|---|---|---|---|---|
| Temp | Ravg without graphene | Ravg with graphene | Rgraphene | Rgraphene * area | $I_0$ | ko | kPT |
| $^0C$ | ohm | ohm | ohm | ohm $cm^2$ | amp $cm^{-2}$ | cm $s^{-1}$ | $s^{-1}$ |
| 30 | 1.726 ± 0.003 | 1.949 ± 0.024 | 0.215 ± 0.024 | 0.038 ± 0.004 | 0.66 | 4.2E-03 | 4.240E+05 |
| 40 | 1.188 ± 0.006 | 1.320 ± 0.023 | 0.132 ± 0.024 | 0.023 ± 0.004 | 1.15 | 7.4E-03 | 7.394E+05 |
| 50 | 0.924 ± 0.002 | 1.004 ± 0.016 | 0.080 ± 0.016 | 0.014 ± 0.003 | 1.95 | 1.3E-02 | 1.259E+06 |
| 60 | 0.811 ± 0.005 | 0.854 ± 0.001 | 0.043 ± 0.005 | 0.008 ± 0.001 | 3.75 | 2.4E-02 | 2.415E+06 |
| | | | | | | | |
| Deuteron | | | | | | | |
| 30 | 1.988 ± 0.039 | 5.05 ± 0.27 | 3.062 ± 0.273 | 0.545 ± 0.049 | 0.05 | 3.1E-04 | 3.086E+04 |
| 40 | 1.225 ± 0.056 | 2.503 ± 0.051 | 1.278 ± 0.076 | 0.227 ± 0.013 | 0.12 | 7.6E-04 | 7.637E+04 |
| 50 | 0.977 ± 0.009 | 1.829 ± 0.034 | 0.852 ± 0.035 | 0.152 ± 0.006 | 0.18 | 1.2E-03 | 1.182E+05 |
| 60 | 0.851 ± 0.014 | 1.326 ± 0.061 | 0.475 ± 0.063 | 0.085 ± 0.011 | 0.34 | 2.2E-03 | 2.186E+05 |

The calculated area normalized resistance due to just graphene for proton or deuteron can be considered as area normalized charge-transfer resistance using equation 4.1. The charge-transfer resistance can then be expressed as exchange current density using the right hand side of equation 4.1.

$$\frac{1}{R_{CT}} = \frac{\Delta i}{\Delta \eta} = i_o \frac{F}{RT} \qquad \text{eqn 4.1}$$

Where $R_{CT}$ = area normalized charge-transfer resistance, $\Delta i/\Delta \boldsymbol{\eta}$ is the slope of the symmetric curve; io= exchange current density; F= Faraday constant, R= Gas constant and T= Temperature. From the equation 4.2, the exchange current density can be conveniently expressed as the standard heterogeneous ion-transfer rate constant ($k^o$, cm $s^{-1}$), which is a measure of kinetic facility of electrochemical reaction [202].

$$i_o = Fk^o C_H^+ \qquad \text{eqn 4.2}$$

Where $C_H^+$ = concentration of proton or deuteron of the ionic group of Nafion® membrane at the interface between graphene and membrane. This value can be obtained by considering the ion-exchange capacity of Nafion® membrane (0.91 meq/g for 1100 EW series) and then multiplied with the specific gravity of Nafion membrane taken from the literature value (1.77 g $cm^{-3}$).[198,199] The obtained $k^o$ in Table 4.3 for both proton and deuteron can be further expressed as the first-order rate constant ($k_{PT}$, $s^{-1}$) using the equation 4.3 below.[204–209]

$$k^o = K_P K_{PT} = \delta \exp\left(\frac{-WP}{RT}\right) K_{PT} \qquad \text{eqn 4.3}$$

where $K_P$ = equilibrium constant for the precursor complex where ion transfer occur at the interface between the Nafion membrane and graphene, $\delta$ = the thickness of the layer at the interface of Nafion and graphene where reaction occurs (taken to be 1.0 Å), $W_P$ = average energy required to transfer ion (proton or deuteron) from the bulk of Nafion® membrane to the interface between the Nafion® membrane and the graphene (this is taken be zero). Applying this equation yields values for first-order ion-exchange rate constants for proton and deuteron listed in the last column of Table 4.3.

### 4.3.3 Arrhenius Analysis of ion transmission

Further analysis of variable temperature data in Table 4.3, by plotting the natural logarithm of first-order rate constant against the inverse of temperature yielded Arrhenius plots presented in Figures 4.5 for proton and 4.6 for deuteron transmission across single-layer graphene. These plots are linear over the range of temperature studied indicating that proton and deuteron transmission through graphene is a thermally-activated process. Activation energies and pre-exponential frequency factors for proton and deuteron can be computed from the slope of the curves from Figure 4.5 and 4.6 respectively. These values are presented in Table 4.4. The activation energy values obtained during this work are somewhat lower than those reported in the literature on a similar phenomenon for proton and deuteron (0.78 ± 0.03 eV) [24]. The lower activation energy values we obtained are in agreement with our observation of high proton transmission across single-layer graphene at near ambient temperature and are much lower than the values (above 1.0 eV) predicted theoretically by computational studies.[100,195,218–224,210–217] The disagreement between the

theory and the experimental data at this time remains unsolved and will continue to be the topic of debate and further research.

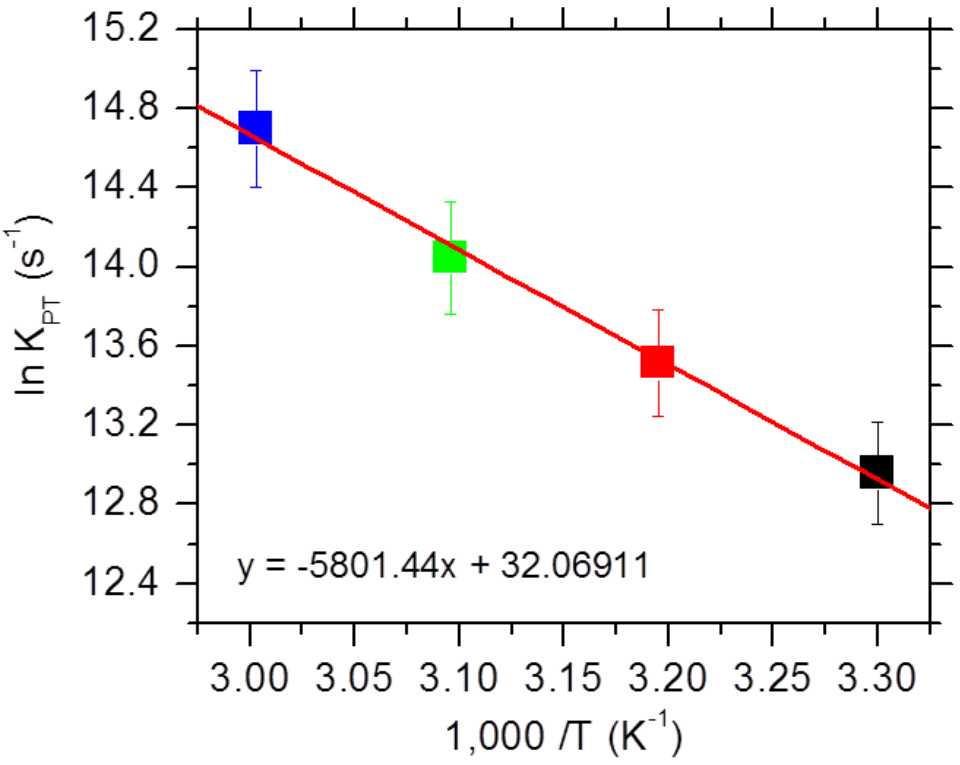


Figure 4.5. Arrhenius plot for proton transport through single-layer graphene

The difference in calculated activation energy values between proton and deuteron was 50 meV (5 kJ $mol^{-1}$). This value is reasonable compared to the expectation of 50-60 meV for the difference in vibrational zero-point energy which is responsible for kinetic isotope effect usually observed between proton and deuteron in chemical reactions.[214–218] The observed difference in transmission rates for proton and deuteron across single-layer graphene is caused as a result of difference in activation energy. The

obtained 50 meV during this work is in agreement with the literature value (60 meV) reported on a similar studies on a micro-fabricated devices [24].

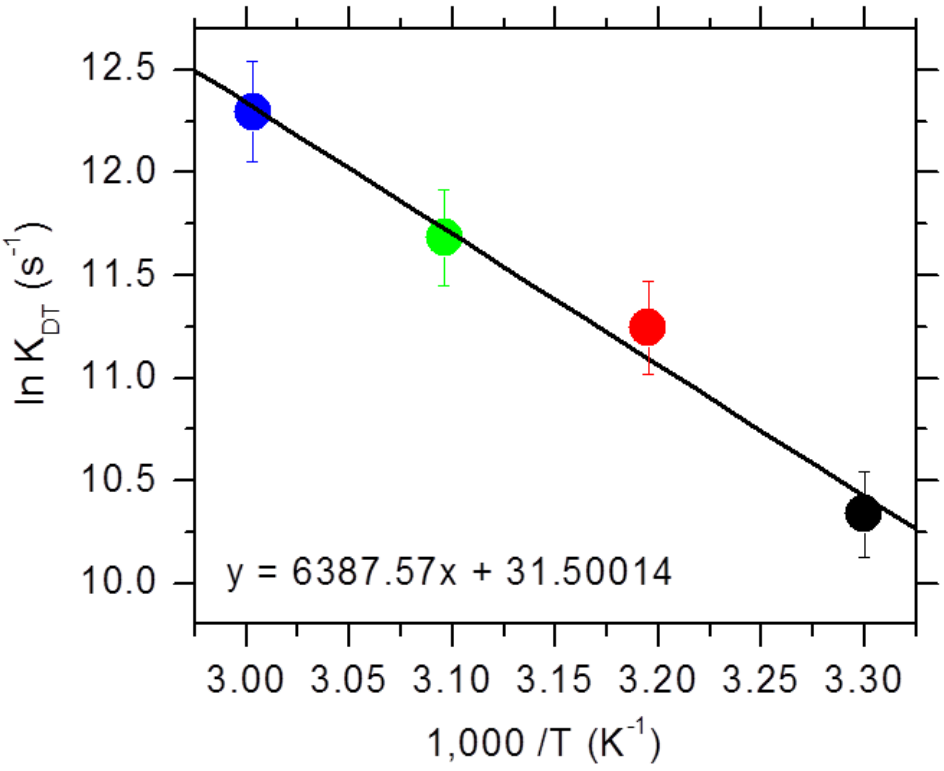


Figure 4.6 Arrhenius plot for deuteron transport through single-layer graphene

Table 4.4 Activation energy and pre-factors values for proton and deuteron transmission through single-layer graphene

| Ion | Activation energy KJ mol$^{-1}$ (eV) | Pre-factors ($s^{-1}$) |
|---|---|---|
| Proton | 48 ± 2 (0.5 ± 0.05 eV) | 8.3 ± 0.4 x $10^{13}$ |
| Deuteron | 53 ± 5 ( 0.55 ± 0.05 eV) | 4.7 ± 0.5 x $10^{13}$ |

The pre-exponential factors given in the Table 4.4 are reasonable for proton and deuteron transmission through single-layer graphene based on the rate model adopted for the interpretation of areal normalized resistances obtained from symmetric H/D pump experiments. In theory, Eyring-Polanyi equation predicted that the pre-factor for a thermally-activated process should be on the order of $kk_BT/h$.[230–232] In this term, k is the transmission coefficient, $k_B$ Boltzmann constant, h Planck's constant which relates the energy carried by a photon to its frequency and T is temperature. At ambient temperature, the value predicted by Eyring-Polanyi for the pre-factor should be $6.2 \times 10^{12}$ $s^{-1}$. Although, the values in the Table 4.4 are somewhat higher than the value predicted by theory which may suggest that the thermally activated process for proton and deuteron transmission through single-layer graphene may assume transmission coefficient near unity and may be adiabatic. This means at the activated complex, the reacting species at the intermediate cross the energy barrier to form product with a high probability.

The difference in frequency factors between proton and deuteron was not predicted by Eyring equation. However, the vibrational frequencies for oxygen-hydrogen and oxygen-deuterium bonds may be considered to gain insights into the difference of two pre-factors. Both the symmetric and asymmetric O-H stretching and symmetric and asymmetric O-D stretching of the vibrational modes (which are infrared active) occur at 3400-3600 $cm^{-1}$ and 2500-2600 $cm^{-1}$ respectively.[233–239] By converting these vibrational frequencies in units of $s^{-1}$ by multiplying it with the speed of light ($c = 3.0 \times 10^{10}$ cm $s^{-1}$) yields $1.0 \times 10^{14}$ $s^{-1}$ for O-H bond and $7.5 \times 10^{13}$ $s^{-1}$ for O-D bond. These obtained vibrational frequencies are similar in order of magnitude to those estimated from

symmetric H / D pump experimental data presented as pre-factors in Table 4.4. This result may suggest that the proton and deuteron transmission across single-layer graphene may proceed with reaction pathway such that bond stretching (O-H or O-D) is strongly involved. The slight higher value of the vibrational frequencies for O-H and O-D bonds than those values of pre-exponential factors might indicate contribution of other modes of vibration to the former aside bond stretching (such as rotation or bending). The ratio of O-H and O-D vibrational frequencies of 1.3 and that of pre-factors of 1.8 are in good agreement for proton and deuteron transmission through single-layer graphene.[240]

Figure 4.7 presents the proposed reaction coordinates for proton and deuteron transmission through single-layer graphene. Nearly the same activated complex for both proton and deuteron suggest that O-H and O-D bond breaking is the determining factor for the observed difference in the activation energy and must be broken before transmission occurs. This bond breaking along the reaction coordinates at the transition state has been the root cause for the well-known kinetic isotope effect.

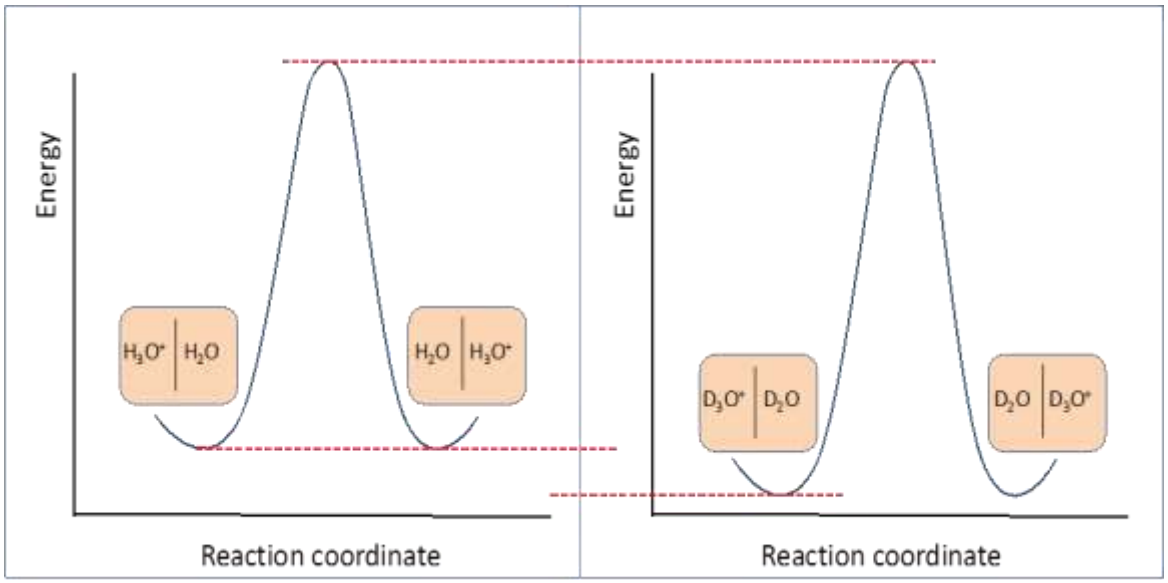


Figure 4.7 Reaction coordinates for proton/deuteron transmission across graphene

## 4.4 Conclusions

In summary, we have demonstrated through variable temperature measurement in a symmetric cell the estimation of activation energy and pre-factors for proton and deuteron transmission through single-layer graphene. The work described here will provide input into an ongoing computational and experimental research efforts in understanding the mechanism and nature of active sites by which proton transmit through graphene. The obtained activation energy values are relatively low which may suggest high proton transmission confirming prior work. Overall, the data support a model that proton and deuteron transmission through single-layer graphene are largely adiabatic and that the selectivity between proton and deuteron is due to the difference in activation energies

# CHAPTER FIVE

# AQUEOUS ION TRANSPORT THROUGH GRAPHENE

## 5.0 SYNOPSIS

The work described in this chapter has been published in American Chemical Society (ACS) Journal with the following bibliographical details *ACS Appl. Nano Mater.*, Volume 2, issue. 2, (2019), Pg. 964-974. It involves measurement of proton, deuteron transmission and other alkali cations including $NH_4^+$ in aqueous electrolytes through graphene using a DC technique in four-point probe configuration and electrochemical impedance spectroscopy. Proton transmission through graphene was found to be at least more than 100 times faster than for any other cation. Detailed characterization studies including confocal Raman spectroscopy, X-ray photoelectron spectroscopy for graphene on Nafion membrane, and defect visualization on chemical vapor deposition graphene on Cu were studied.

## 5.1 INTRODUCTION

Monolayer 2D graphene initially conceived to be impermeable to atoms, molecules, and ions was recently demonstrated to show ionic conductance for thermal proton and deuteron.[14,16,22,24] Latest research finding has shown that not only is this phenomenon possible but it can occur at a rate higher than we previously thought.[16,185,241] These exciting research findings suggest that 2D graphene-based and non-graphene based 2D materials may be considered for the next generation separation technologies. The prevention of fuel crossover in fuel cell technologies,[242–251] hydrogen isotope

fractionation in nuclear waste treatment, gas purification, wastewater treatment, desalination, and salt splitting are a few examples of fast-growing research areas that would benefit immensely from graphene.

Since in real application, a large area of graphene will be in contact with the electrolyte solution containing different ions,[252] it is essential to investigate the permselectivity of graphene toward other aqueous ions in addition to proton and deuteron, as well as to assess the overall quality of graphene. 2D materials are atomically thin and their selectivity comes from the active sites where permeation through the electron cloud occurs.[241] They are however different from the conventional polymer-based separators in which their selectivity is only a thin bulk of polymer layer accessible to permeant ions (e.g. Nafion® membrane, membrane for reverse osmosis for water desalination). These polymers do support low ion flux especially for the relatively thick membrane. Much higher flux will be beneficial to the state-of-the-art devices that require membrane to achieve better ionic separation. The ultra-thin 2D material such as graphene will be suitable to provide much needed higher flux with improved selectivity. Some recent findings on the application of graphene for such purpose have been demonstrated at the laboratory scale. [14,188, 241]

The use of graphene for ion transmission when driven by a bias (electrical potential) is of great importance to several applications highlighted above.[91,253,262, 254–261] Previous studies conducted on graphene and related 2D materials were often involved free-standing graphene suspended over a nanopore (e.g. nanofabricated SiN).[263] Transmembrane potential difference is sensed when electrical potential is applied across

the layer of graphene separating aqueous electrolytes containing cations of interest. Ion flux can be improved by artificially creating nanosize defects into graphene such as the use of ion plasma, electron or ion beams. Study on proton transmission through graphene unlike other ions is unique because in an aqueous environment, proton is highly solvated. Exceptionally high proton transmission occurs through the extended water clusters through a channel that involves hydrogen bonding via a well-known Grotthuss mechanism or vehicular mechanism.[117,119,120,264–267] This is in contrary to other ions that transmit through vehicle mechanisms (see chapter three for the discussion on the mechanism).[268–270] Although, high proton transmission through single-layer graphene has been experimentally demonstrated, the actual mechanism for which that takes place is still uncertain. This will require further research work. Possibilities include transmission through the graphene hexagonal hollow structure, or through defects sites that are rare enough which are not easily detectable spectroscopically. Proton tunneling is another possibility.

Unlike electrochemical hydrogen pumping or deuterium pumping that studies transport phenomenon of only proton or deuteron in a gas-adapted cell,[16,123,185] the method described here is a convenient technique to study the proton or deuteron transport, and also transport of alkali cations and ammonium ion. In this work, we have studied a wide range of ions transmission through graphene, all studied in a similar test environment. This will particularly be useful because it would show the selectivity of graphene for ion transport without unnecessary limitation from the cell design and testing that might affect one measurement from the other. All membrane composites, with and

without graphene, were characterized using two-probe electrochemical impedance spectroscopy (EIS) and a customized Devanathan-Stachurski electrochemical cell (D-S cell) in a four-probe electrode configuration measurement.

We have elected to study the transport phenomenon of aqueous ions ($H^+$, $D^+$, $Li^+$, $Na^+$, $K^+$, $Rb^+$, $Cs^+$, and $NH_4^+$) through graphene transferred onto a perfluorinated sulfonic-acid (PFSA) ionomer membrane in a Nafion® | graphene | Nafion® composite. Following the same transfer protocol to make Nafion® | graphene | Nafion®, we modified the composite to include polyethylene terephthalate with the aim to rule out the contribution of the Nafion® membrane towards the ionic transport. This research study was undertaken to investigate how aqueous ions traverse the energy barrier posed by CVD graphene. In four point-probe (DC) measurement, a pair of platinum electrodes (drives electrodes) drive ions through graphene and a pair of Ag-AgCl reference electrodes (sense electrodes) in Luggin-capillaries sense the transmembrane potential difference induced by the ion flow. This method is attractive because it does not involve any electrode reactions. So any membrane and any electrolyte can be used to accomplish measurement. Ion concentration was kept low to avoid contribution from counter ions or Donnan failure.[271–274]

Similarly, electrochemical impedance spectroscopy (EIS) in two point-probe configuration was also used to examine ion transport through graphene in samples prepared as MEAs. Research studies over the last few decades have been conducted using high-frequency AC impedance to study the proton transport / conductivity in PFSA membranes.[252,275,284–286,276–283] The unambiguity and good reproducibility of estimating

membrane proton conductivity from the real part of impedance, $Z_{real}$ (ohms) at high frequency when a small amplitude voltage, AC modulation is applied to the cell makes this technique attractive. Both the EIS and DC techniques[276, 287–295] have been explored for proton and few alkali cations ($Li^+$, $Na^+$, and $K^+$) conductivities measurements in PFSA membranes. While these two methods (AC impedance and DC) are reliable techniques to study ions transport phenomenon in PFSA membranes, wide variations in the reported conductivities, even for proton, have been attributed to factors that have direct influences on the membrane.[287] These factors include but are not limited to water uptake of the membrane, temperature, membrane handling, and pretreatment, electrolyte concentration (counter-ion effect), experimental technique and cell design.[284] The use of DC technique using linear sweep voltammetry (LSV) to measure through-thickness resistances of ions transport in membranes with and without graphene reveals high selectivity factor between a proton and a deuteron. The transmission rate for protons is also significantly higher as compared to other alkali cations and ammonium ion. Following correction from the contribution of background resistances, proton transport through single-layer graphene occurs at a high rate, in agreement with the previous report. The proton transmission rate was however significantly higher as compared to other alkali cations ($Li^+$, $Na^+$, $K^+$, $Rb^+$, and $Cs^+$), and $NH_4^+$. Also, the ratio of proton conductance to deuteron in aqueous electrolytes through single-layer graphene was ca. 12:1. This value is in good agreement with values reported for gas-phase studies for similar ions.[16,22,185] Proton transmission rate through graphene was about 150-350 times larger than for any other alkali cations and ammonium ion.

The data from EIS showed much lower resistances for ion transmission as compared to DC technique. This finding might reflect a situation in which there is a capacitive coupling of mobile ions with graphene layer during amplitude perturbation at such high frequency. It thus shows that near steady-state DC technique is indispensable in measuring true ionic resistance through graphene.

## 5.2 RESULTS AND DISCUSSION

### 5.2.1 Electrochemical Impedance Measurements in a Miniaturized Cell

EIS was used to measure ion transport through ionomer membranes prepared as MEA. The PFSA membrane is regarded as a resistor representing ion motion in series with two capacitors represented by the interface between the two conductive-carbon cloth electrodes and the ionomer membrane. Applying an AC signal over the range of frequencies will yield Nyquist and Bode plots. In the Nyquist plot, from the real vs. imaginary components of the impedance, resistance at high frequency can be obtained by extrapolation to the real impedance axis.

Details of the miniaturized cell used for AC impedance measurements have been discussed in previous chapters. Figures 5.1A and 5.1B show the exploded cell components and photomicrograph of the miniature cell. In brief, the cell consists of a plastic commercial compression fitting made from perfluoroalkoxy alkane (PFA) and PTFE sleeves. The other major parts are: (1) the graphite rod current collector of length 2.24 inches (5.7 cm), (2) the sleeve made from poly(tetraflluoroethylene) to hold the

graphite rod current collector, (3) the butyl rubber "O-ring" to ensure proper seal between the PTFE sleeve and the MEA, and (4) the P50T carbon gas diffusion layer.

Nafion® | graphene | Nafion® composites are prepared in form of MEAs in which electrodes are in direct contact with the Nafion® membranes (Figures 5.2A and 5.2B). See method section for the details sample preparation. The area covered by the graphene is visible to the eye. To establish measurement accuracy, AC impedance measurements were conducted on two standard resistors (10 Ω and 20 Ω). Figure 5.3 shows the expected spectra and values from the Nyquist plots for the two resistors.

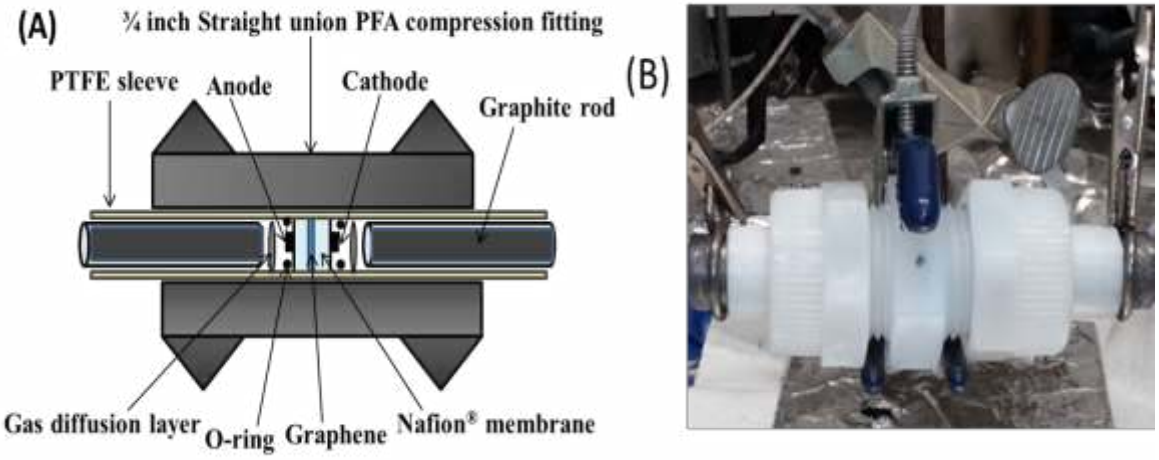


Figure 5.1 Miniature cell for EIS measurement (A) Exploded diagram (B) photomicrograph of the cell

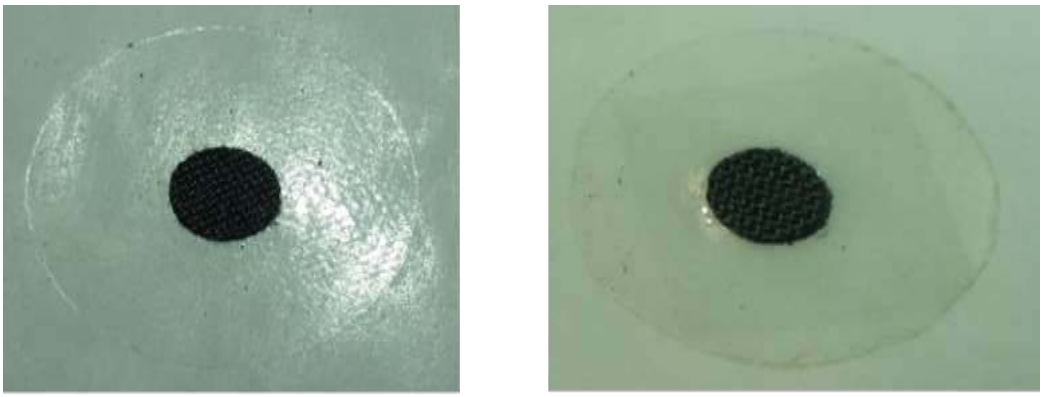


Figure 5.2 MEA for EIS measurement (A) without graphene (B) with graphene

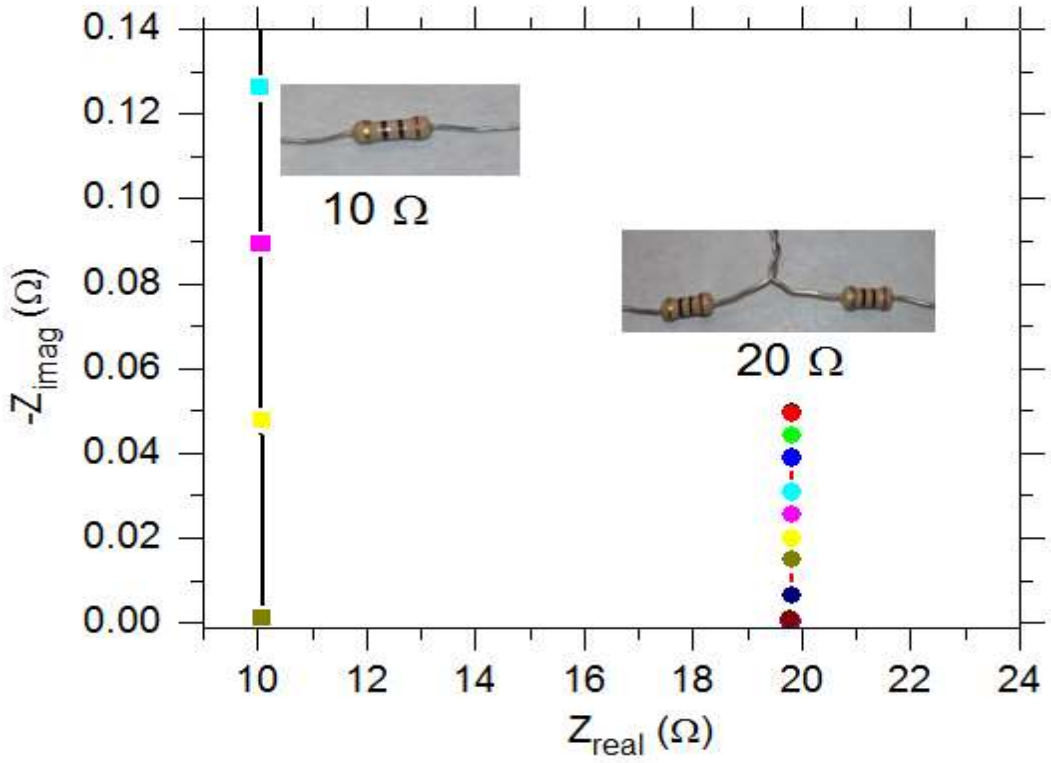


Figure 5.3 Nyquist plot showing the Rs values at high frequency obtained for standard resistors (10 and 20 Ω)

Figure 5.4 presents the Nyquist plots at high frequency for the MEAs in different cationic forms ($H^+$, $D^+$, $Li^+$, $Na^+$, $K^+$, $Rb^+$, $Cs^+$, and $NH_4^+$) that contain no graphene. Impedance measurements were taken on two independently prepared MEAs for each ion. An AC amplitude of 50 mV was used during data acquisition between 1 kHz and 100 kHz at 0V DC voltage. The electronic resistance (cell resistance with no MEA) = 0.12 Ω; MEA area = 0.178 $cm^2$. The inset shows the Nyquist plot for the indicated cations ($H^+$, $D^+$, $Li^+$, $Na^+$, and $NH_4^+$) as a result of spectra overlapped. Ionic resistances (R, ohm) can be obtained from where the spectra intercept the real axis ($Z_{real}$, ohm) from the complex plane plots. The Measured average resistances, area normalized average resistances and MEA conductivity of each ion are presented in Table 5.1.

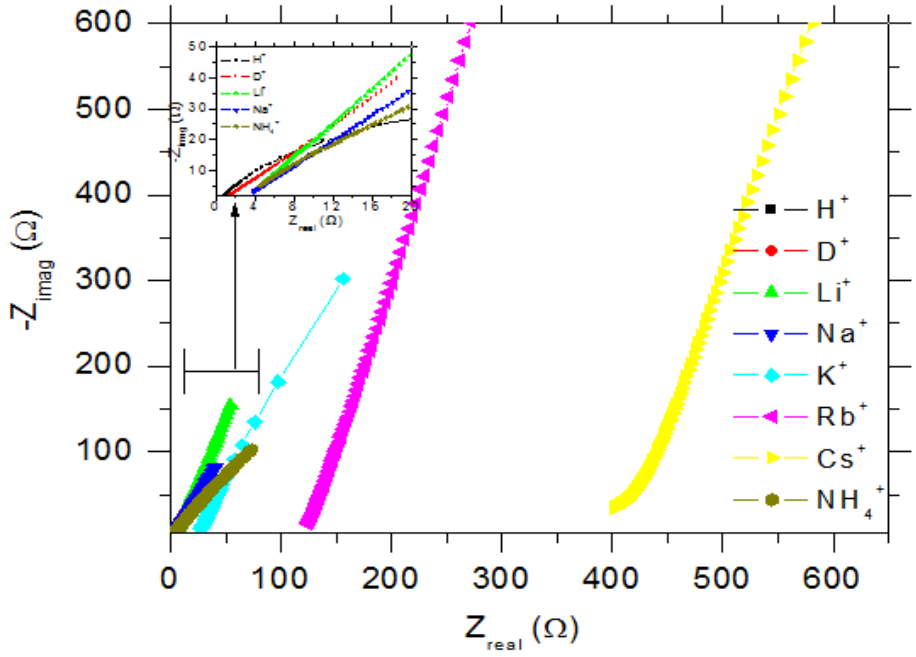


Figure 5.4 The Nyquist plot at a high frequency obtained for MEAs in different cationic forms with no graphene.

From the measured average resistances (Column 2) for all ions ($H^+$, $D^+$, $Li^+$, $Na^+$, $K^+$, $Rb^+$, $Cs^+$ and $NH_4^+$), the area normalized resistances (Column 3) can be obtained by the product of the difference between the average of measured resistances and the electronic resistance (0.12 Ω) and MEA geometric area. The electronic resistance consists of the contributions from two gas diffusion layers (P50T carbon), two current collector graphite rods, two rotor clips, carbon cloth with a microporous layer, and perfluoroalkoxy alkane compression plastic cell (miniaturized cell).

Table 5.1: Resistance and conductivity values of MEAs of different ionic forms with and without graphene obtained from EIS at high frequency

| **$MEA_{(w/o\ graphene)}$** | $R_{(average)}$ | $R_{(area\ normalized)}$ | $MEA_{(conductivity}$ | Electrolyte σ | **$MEA_{(With\ graphene)}$** | $R_{(average)}$ | $R_{graphene}$ | $R_{gra\ (area\ normalized)}$ | Graphene $_{(areal\ Conductance)}$ | | |
|---|---|---|---|---|---|---|---|---|---|---|---|
| | Ω | Ω $cm^2$ | (mS $cm^{-1}$) | (mS $cm^{-1}$) | | Ω | Ω | Ω $cm^2$ | S $cm^{-2}$ | | |
| $H^+$ | 0.74 | 0.11 | 46 | 36 | $H^+$ | 1.61 | 0.87 | 0.15 | 6.5 | | |
| $D^+$ | 1.26 | 0.2 | 24.95 | 17.1 | $Li^+$ | 6.48 | 2.22 | 0.4 | 2.5 | | |
| $Li^+$ | 4.26 | 0.74 | 6.9 | 8.1 | $Na^+$ | 4.98 | 1.21 | 0.22 | 4.5 | | |
| $Na^+$ | 3.77 | 0.65 | 7.8 | 9.2 | $K^+$ | 31.71 | 4.11 | 0.73 | 1.4 | | |
| $K^+$ | 27.6 | 4.89 | 1.04 | 11.4 | | | | | | | |
| $Rb^+$ | 124.91 | 22.21 | 0.23 | 9 | | | | | | | |
| $Cs^+$ | 405.04 | 72.08 | 0.07 | 8.2 | | | | | | | |
| $NH_4^+$ | 4.31 | 0.75 | 6.8 | 10.6 | | | | | | | |

The ionic conductivities of MEAs (column 4) in different cationic forms were estimated using the equation below.

$$\sigma_{X^+}\,(\mathrm{S\ cm^{-1}}) = \frac{l(cm)}{R(\Omega) \times Area\ (cm^2)} \qquad \text{eqn 5.1}$$

σ = conductivity, l = membrane thickness (50.8 μm, obtained from two Nafion®-211 membranes), R = measured resistance from real impedance axis at high frequency; Area = geometric area of the MEA (0.178 $cm^2$), $X^+ = H^+$, $D^+$, $Li^+$, $Na^+$, $K^+$, $Rb^+$, $Cs^+$ and $NH_4^+$.

Interestingly, the proton conductivity for Nafion® membrane reported here (46 mS $cm^{-1}$) is well within the range of the reported values for ionic conductivity measurement that involves MEA in which electrodes are in contact with the membranes [288]. The obtained Nafion conductivities for other ions ($Li^+$, $Na^+$, and $K^+$) are also close to the reported values in the literature. See Table 5.2 for the comparison between the obtained data and literature values. A slight variation in the measured data when compared to the literature data reflects some of the earlier noted factors. Similarly, the measured electrolytes conductivities (column 5), 0.1 M HCl, 0.1M DCl and 0.1M XCl ($X^+$ = $Li^+$, $Na^+$, $K^+$, $Rb^+$, $Cs^+$ and $NH_4^+$) used during this work at 22 $^oC$ are in good agreement with the work reported by Xie and co-workers [296].

Table 5.2 Conductivities of MEAs in different cationic forms with electrodes in contact with the membranes

| MEA form | Technique | σ (mS $cm^{-1}$) | $R_{area\ normalized}$ (Ω $cm^2$) | Temp ($^oC$) | Reference |
|---|---|---|---|---|---|
| $H^+$ | AC impedance | 46 | 0.11 | 22 | This work |
| $H^+$ | AC impedance | 34 | 0.53 | 25 | J. Membr. Sci. 185 (2001) 95 |
| $H^+$ | AC Coaxial probe | 24 | - | 22 | J. Electroanal. Chem. 449 (1998) 209 |
| $H^+$ | AC impedance | 49 | 0.375 | 25 | J. Power Sources, 134 (2004)18 |
| $H^+$ | AC impedance | 83 | 0.22 | 30 | Desalination 147 (2002) 191 |
| $Na^+$ | AC impedance | 7.8 | 0.65 | 22 | This work |
| $Li^+$ | AC impedance | 6.9 | 0.74 | 22 | This work |
| $K^+$ | AC impedance | 1.04 | 4.89 | 22 | This work |
| $Na^+$ | AC impedance | ≈10.8 | - | 20 | J. Electroanal. Chem. 428 (1997) 81 |
| $Na^+$ | AC impedance | 7 | - | 27 | J. Electroanal. Chem. 505 (2001) 24 |
| $Li^+$ | AC impedance | 6 | | | J. Electroanal. Chem. 505 (2001) 25 |
| $K^+$ | AC impedance | 4 | - | 27 | J. Electroanal. Chem. 505 (2001) 26 |

Figure 5.5 shows the Nyquist spectra and quantitative data (from Table 5.1) obtained for the selected ions ($H^+$, $Li^+$, $Na^+$, and $K^+$) transport through Nafion® | graphene | Nafion® composite using the AC impedance at high frequency on two independently prepared MEAs for each ion. The ionic resistance due to graphene ($R_{graphene}$) can be obtained by the difference between the average resistances from Nafion® / graphene

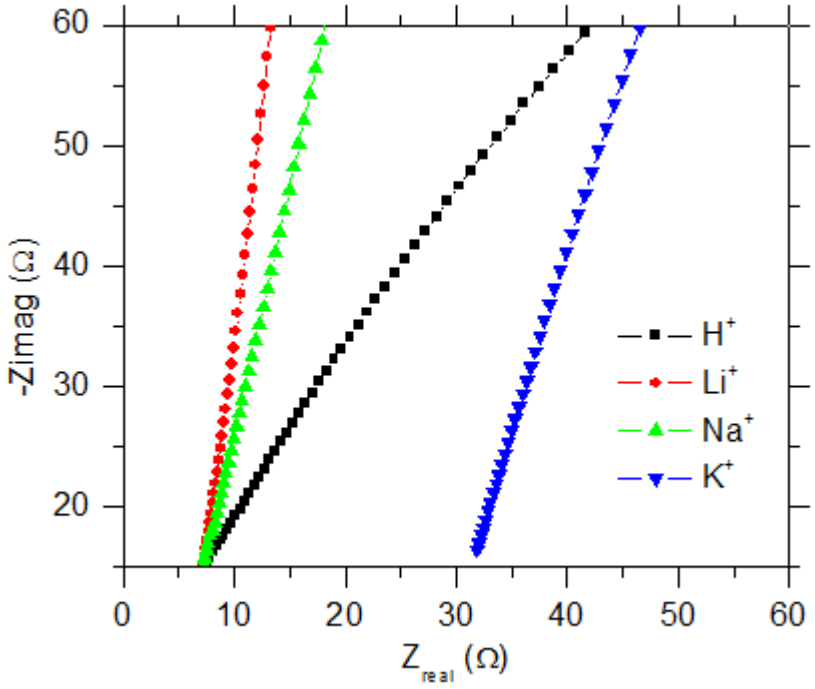


Figure 5.5. The Nyquist plot at a high frequency obtained for MEAs in different cationic forms with single-layer graphene.

sandwich (column 7) and those without graphene (column 2). From $R_{graphene}$ (column 8) data, graphene area normalized resistances (column 9) were estimated, taking into consideration the geometric area of MEA. Area normalized graphene conductance

(column 10) is the reciprocal of graphene area normalized resistance. The obtained graphene area normalized conductances for these ions ($H^+$, $Li^+$, $Na^+$, and $K^+$) through the single-layer graphene range between 6.5 to 1.4 S $cm^{-2}$. These results seem to suggest that ions ($Li^+$, $Na^+$, and $K^+$) conductances through single-layer graphene are not substantially attenuated when compared to proton. The results are unexpected, owing to the fact that ions transmission other than proton across single-layer graphene would be theoretically almost impossible considering the energy barrier required for such a transmission to occur.

To fathom the origin of such ionic conductance through graphene from $Li^+$, $Na^+$ and $K^+$ ions; a deeper analysis is required. Considering the Nafion® | graphene | Nafion® structure represented in Scheme 5.1 below, before the application of small amplitude AC voltage, the ionic group, $SO_3^-X^+$ ($X^+$ = $H^+$, $Li^+$, $Na^+$ or $K^+$ ions) at the surface of hydrophobic Nafion® membrane matrix are in close proximity to the graphene on both sides. Upon the application of AC modulation, at high frequency, since graphene has high

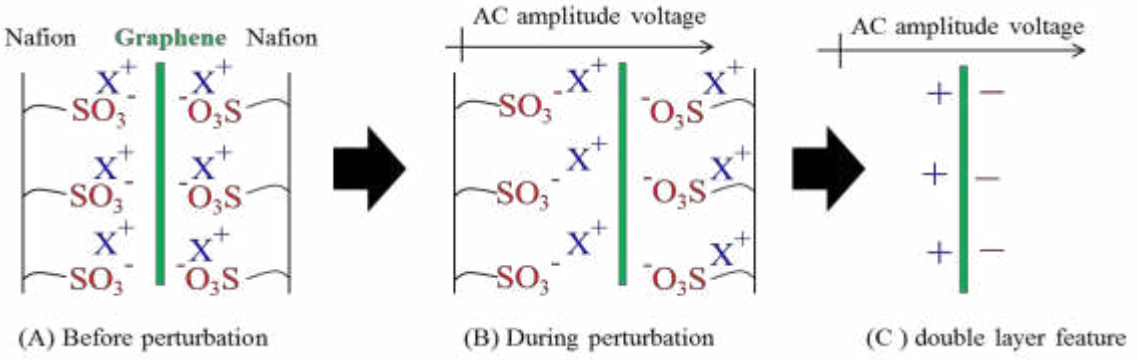


Scheme 5.1. Schematic representation of ion motion near graphene/Nafion membranes interface.

electronic conduction properties; the ionic clusters in the Nafion® membrane are reoriented. This ion motion indicates a capacitive coupling between the graphene sheet and Nafion® membranes. Thus creating a double layer feature at the Nafion® | graphene | Nafion® interface in which its impedance becomes insignificant at high frequency. As a result, the effectual attenuation of ions transport across the graphene layer becomes infinitesimal.

### 5.2.2 Four-probe Devanathan-Stachurski (D-S) Cell Measurement

To better understand the ionic transport through graphene layer, a DC technique was employed using a customized Devanathan-Stachurski electrochemical cell (D-S cell). Figure 5.6A depicts the pictorial representation of the D-S cell. Figure 5.6B shows the major components of the cell. See the method section for a detailed description of the cell. The D-S cell is an easy-to-use electrochemical cell for measuring a reproducible through-plane ionic resistance of the membrane. The four-probe electrode configuration, with the Luggin capillaries, minimizes the contribution from the ohmic drop in an aqueous electrolyte.

The as-prepared samples (Nafion® | graphene | Nafion® composite, with and without graphene) were placed in the sample holder of the cell, followed by the clamping together of the two half-cells. See method section for the fabrication and transfer of graphene onto the membrane and the making of the composite. The measurements were performed in potentiostatic mode, with a DC technique using linear sweep voltammetry (LSV). A potential bias of ± 0.1 V at a scan rate of 5 mV $s^{-1}$ was used to acquire the

current-potential (I-V) curves. Two samples were prepared for each cation studied, and the I-V curves obtained for each ion are shown in Figure 5.7 for Nafion | graphene | Nafion sandwich structure. It is evident from Figure 5.7 that aqueous proton transmission through single-layer graphene is noticeably higher as compared to deuteron. Whereas the transmission effects of other cations ($Li^+$, $Na^+$, $K^+$, $Rb^+$, $Cs^+$, and $NH_4^+$) through graphene are significantly attenuated.

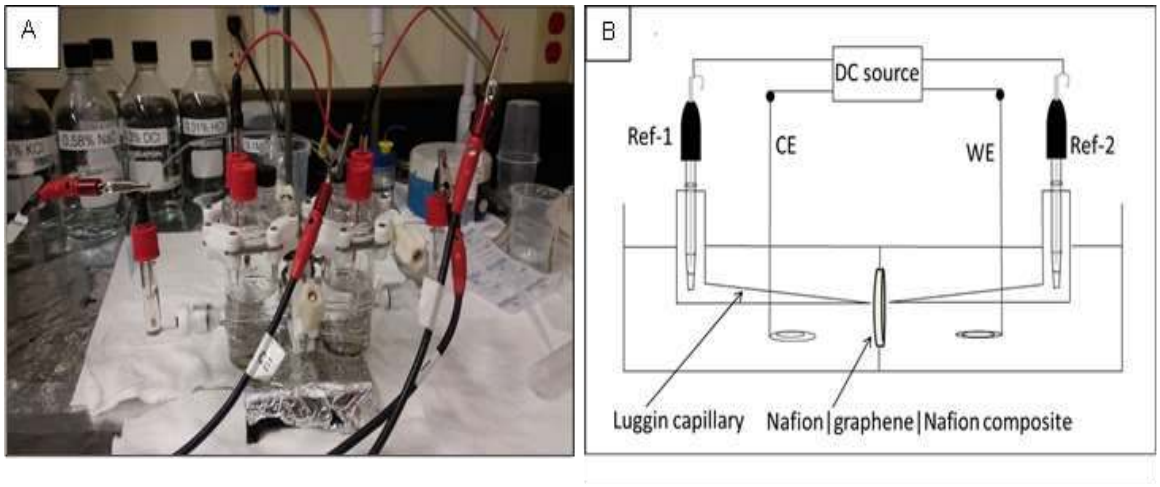


Figure 5.6. Devanathan-Stachurski (D-S) electrochemical cell (A) Pictorial representation (B) Graphical illustration of the cell components.

This observation is, in fact, consistent with the recent findings for similar studies for proton and deuteron transmission across single-layer graphene in hydrogen pump cells.[16,185] It is important to note that computational studies on ion transport through single-layer graphene, especially the pristine graphene, predicted total ion blockage, even for proton transport. Due to the theoretical calculation of the proton transmission energy

barrier 1.17-2.21 eV, proton transmission across the single-layer graphene should be almost totally prevented from occurring at ambient temperature.

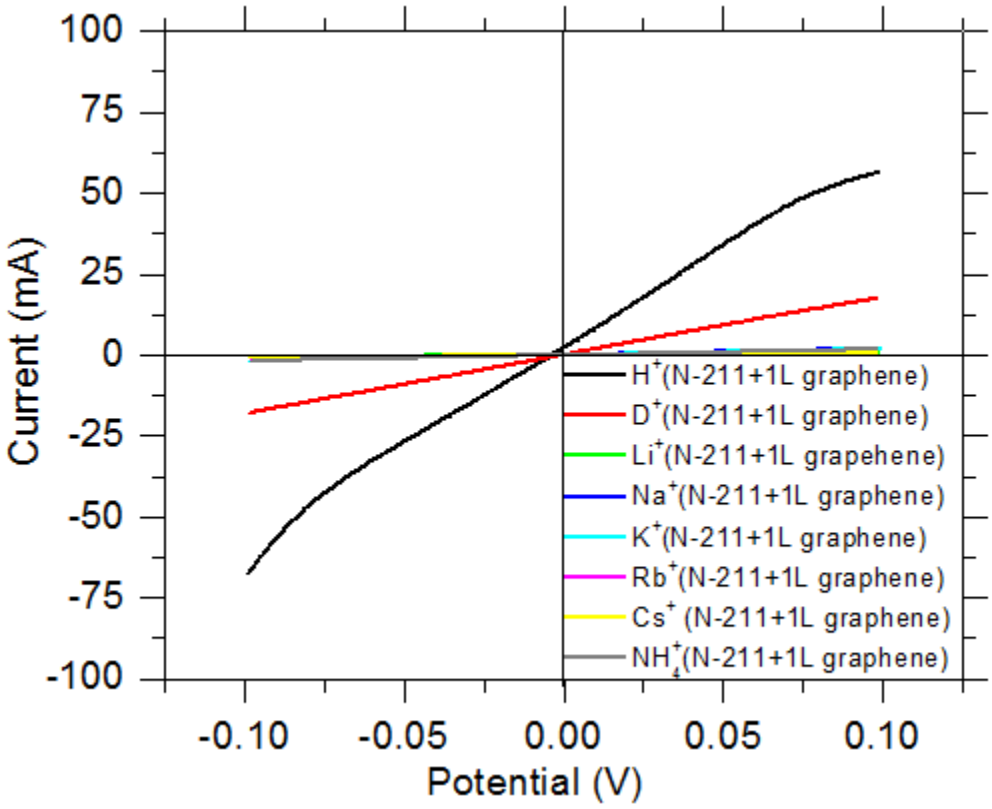


Figure 5.7 : I-V curves in D-S cell for alkali cations and ammonium ion transport through the single layer graphene

In contrary to the above theoretical prediction, S. Hu and co-workers[24] demonstrated the possibility of proton transport across monolayer graphene. Despite the fact that the results in Figure 5.7 show significantly lower ionic currents through the single-layer graphene for $Li^+$, $Na^+$, $K^+$, $Rb^+$, $Cs^+$, and $NH_4^+$; it is still not expected,

theoretically, for aqueous ions, other than protons to circumvent the graphene electron cloud that would make such transmission possible.

The results presented in Figure 5.7 are interesting for the following reasons: (1) the I-V curves for all cations except for proton and deuteron show very similar ion transport behavior across graphene; (2) it underscores the quality of CVD graphene toward ions transport; (3) it demonstrates that defects alone, in CVD graphene, cannot be responsible for high proton transmission; (4) it indicates that the CVD graphene does not contain rips, holes, cracks, and tears that would allow high flux of any ion through it; and (5) CVD graphene is not a perfect barrier that would completely block any ion through it. The origins of these low ionic currents, from other cations, across the single layer graphene will be discussed in details later in the text.

The statistical data from the I-V curves in Figure 5.7, are presented in Table 5.3, that show the areal resistances and conductances obtained for each ion transport through graphene in a Nafion® | graphene | Nafion® composite. Column 2 in Table 5.3 shows the solution resistances of each electrolyte without the membrane. Column 3 shows the obtained ionic transport resistances for both aqueous solution and Nafion® membrane. The values in parentheses for $H^+$ and $Na^+$ in Column 2 and 3 are those obtained at 1.0 M electrolyte concentration. Column 4 shows the ionic transport resistances for each ion through graphene in a Nafion® | graphene | Nafion® composite. The estimation of the ionic areal resistances, due to contributions from graphene only, for each ion can be easily obtained by subtraction of Column 3 from Column 4, and then multiplied by the geometric area of the cell 1.98 $cm^2$. The results obtained are given in Column 5 of Table

5.3. The graphene areal conductances, shown in Column 6, is the inverse of the graphene areal resistances presented in Column 5.

Table 5.3. Areal resistances and conductances for alkali cations and $NH_4^+$ in a Nafion®|graphene|Nafion® composite

| Cations | $R_{(soln)}$ | $R_{(soln+N\text{-}211)}$ | $R_{(soln+N\text{-}211+graphene)}$ | $Graphene_{(areal\ resistance)}$ | $Graphene_{(areal\ conductance)}$ |
|---|---|---|---|---|---|
| | (Ω) | (Ω) | (Ω) | (Ω $cm^2$) | (S $cm^{-2}$) |
| $H^+$ | 1.08 (0.11) | 1.32 (0.15) | 1.64 | 0.63 | 1.6 |
| $D^+$ | 1.3 | 1.59 | 5.52 | 7.78 | 0.13 |
| $Li^+$ | 4.67 | 6.67 | 118 | 220 | $4.55 \times 10^{-3}$ |
| $Na^+$ | 5.95 (0.75) | 7.68(1.09) | 53 | 90 | $1.12 \times 10^{-2}$ |
| $K^+$ | 6.57 | 9.83 | 56 | 92 | $1.09 \times 10^{-2}$ |
| $Rb^+$ | 7.04 | 47.39 | 106 | 117 | $8.56 \times 10^{-3}$ |
| $Cs^+$ | 9.85 | 48.31 | 119 | 140 | $7.14 \times 10^{-3}$ |
| $NH_4^+$ | 5.63 | 28.01 | 56 | 110 | $9.1 \times 10^{-3}$ |
| PET* | 1.08 | ($50 \times 10^6$)* | | | |

*PET is polyethylene terephthalate used as a control experiment to demonstrate the total blockage of $H^+$ transport and any other ions when incorporated into the composite

It is worth mentioning that the aqueous ion transport through the Nafion® membrane has been well studied and similar reported results can be inferred from Column 2 and Column 3 in Table 5.3. For example, at 1.0 M electrolyte concentration (values in parentheses for $H^+$ and $Na^+$ as noted above), using equation 5.1 above, the conductivity, σ (mS $cm^{-1}$) = 78 for proton and σ (mS $cm^{-1}$) = 8 for sodium ion. These values are in good agreement with the reported work. See Table 5.4, for the comparison of our work with some of the reported data. However, the values obtained at low electrolyte concentration (0.1 M) are somewhat lower, for example, σ (mS $cm^{-1}$) = 11 for

proton and σ (mS $cm^{-1}$) = 1.5 for sodium ion using the data in Column 2 and 3 in the Table 5.3.

Table 5.4 Conductivity measurements of Nafion membranes (1100 EW) in different cationic forms in aqueous electrolytes

| Ionic form | Electrolyte | Technique | σ (mS $cm^{-1}$) | $R_{area\ normalized}$ (Ω $cm^2$) | Temp (°C) | Reference |
|---|---|---|---|---|---|---|
| $H^+$ | 0.1M HCl | 4 Point probe (DC method) | 11 | 0.48 | 22 | This work |
| $H^+$ | 1M HCl | 4 Point probe (DC method) | 78 | 0.065 | 22 | This work |
| $H^+$ | 1M $H_2SO_4$ | DC Current pulse | 70 | 0.26 | 20 | J. Electrochem. Soc. 137 (1990) 3770 |
| $H^+$ | 1M $H_2SO_4$ | AC impedance | 71 | 0.259 | 25 | Desalination 147 (2002) 191 |
| $H^+$ | 1M $H_2SO_4$ | DC Current pulse | 88 | 0.26 | 20 | J. Electrochem. Soc. 139 (1992) 3421 |
| $H^+$ | 1M $H_2SO_4$ | AC impedance | 76 | 0.23 | 25 | Electrochim. Acta, 43 (1998) 3749 |
| $H^+$ | 0.1-1M $HNO_3$ | AC Impedance (Hg contact method) | 59-85 | - | 5-25 | J. Electroanal. Chem. 428 (1997) 81 |
| $Na^+$ | 0.1M NaCl | 4 Point probe (DC method) | 1.5 | 3.42 | 22 | This work |
| $Na^+$ | 1M NaCl | 4 Point probe (DC method) | 8 | 0.68 | 22 | This work |
| $Na^+$ | 0.1-1M NaCl | AC Impedance (Hg contact method) | 9.2-10.6 | - | - | Desalination 170 (2004) 49 |

Estimating ionic conductivity of Nafion® membrane using DC technique at low electrolyte concentration to measure ions conductivities might be challenging owing to the fact that Nafion membrane has ionic conductivity value similar to the electrolyte conductivity value at such low concentration. Other techniques such as AC impedance might be suitable at such low concentration as we have shown in our AC impedance measurements. We used low electrolyte concentration during ions transport studies through graphene so as to avoid the well-known Donnan effect at high electrolyte concentration in membrane conductivity measurement, where counter-ion contribution has an effect in the overall ionic conductivity values.[297–301]

Interestingly, the graphene areal conductance for proton (1.6 S $cm^{-2}$) in 0.1M HCl is high, suggesting a high rate of proton transmission across the graphene. Deuteron, on the other hand, shows much lower graphene areal conductance value of 0.13 S $cm^{-2}$ in 0.1M DCl. The proton graphene areal conductance ratio to deuteron across the graphene in an aqueous electrolyte is ca. 12:1. This value is in agreement with the previous reports.[15,16,22,24]. However, as evident from column 6 in Table 5.3, other cations show significantly lower graphene areal conductances with at least two orders of magnitude lower compared to proton transmission across single-layer graphene.

Figures 5.8 and 5.9 show the I-V curves for all the cations with and without graphene. Figures 5.10A and 5.10B show the I-V curves for the modified forms of the Nafion® | graphene | Nafion® composites for $H^+$ and $Na^+$ that incorporate polyethylene terephthalate (PET). As can be seen in Table 5.3 and Figure 5.8A, proton transport through PET was blocked entirely indicating a lack of ion transmission through this polymer matrix. The properties of this polymer were utilized to modify the Nafion® | graphene | Nafion® composite, this prevented the contribution of the ionic transport by the Nafion® membrane (see method section for a detailed description of the fabrication process).

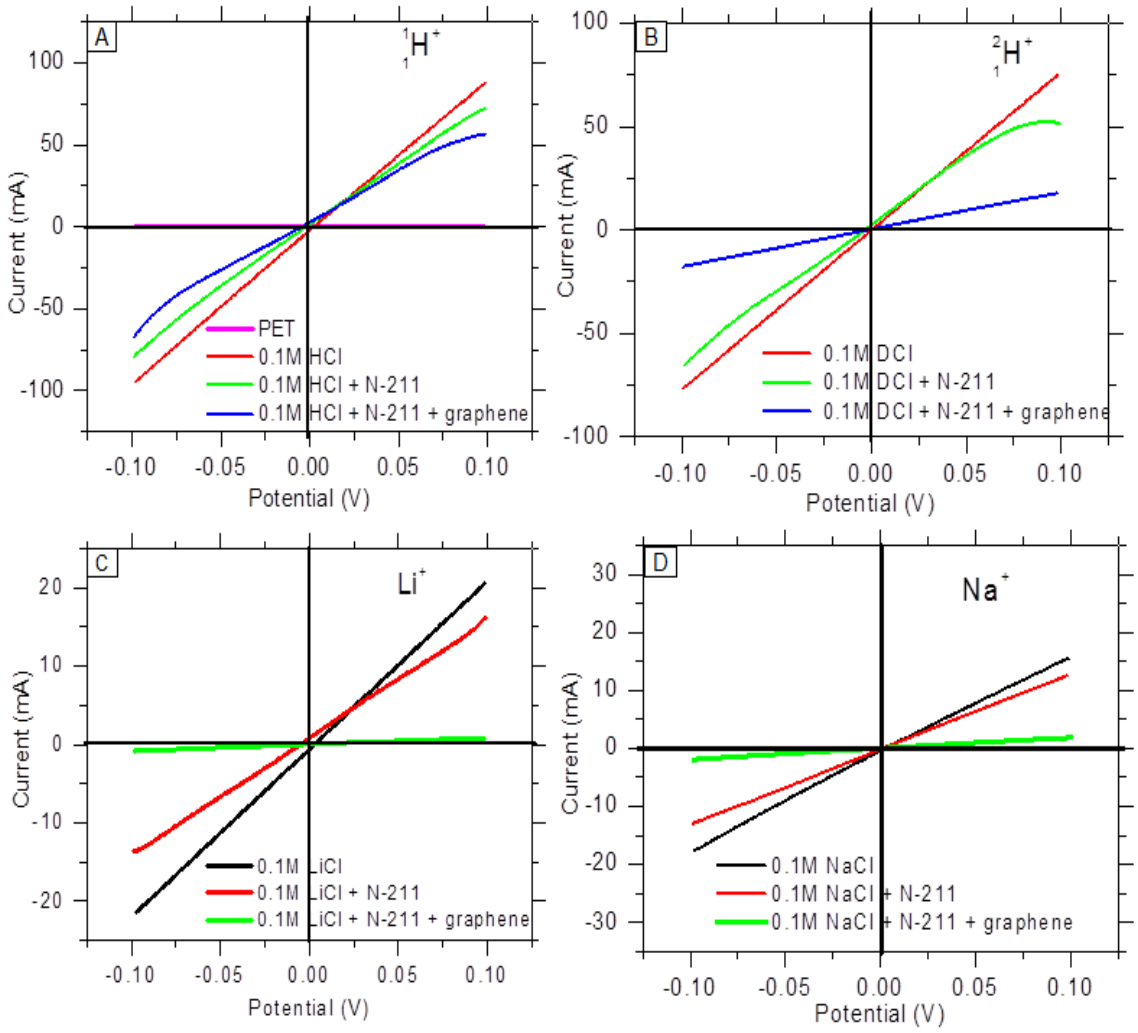


Figure 5.8 I-V curves in D-S cell with and without Nafion® /or graphene in 01. M electrolyte (A) HCl, (B) DCl, (C) LiCl, and (D) NaCl

The only exposed area to the electrolyte from the membrane that contains the single-layer graphene was just a half-inch diameter (1.27 cm). Every other part of the Nafion® membrane was completely covered with PET. In the Figure 5.10, the I-V curves are for two samples, $H^{+}$ and $Na^{+}$ respectively, in each case. The first sample is a

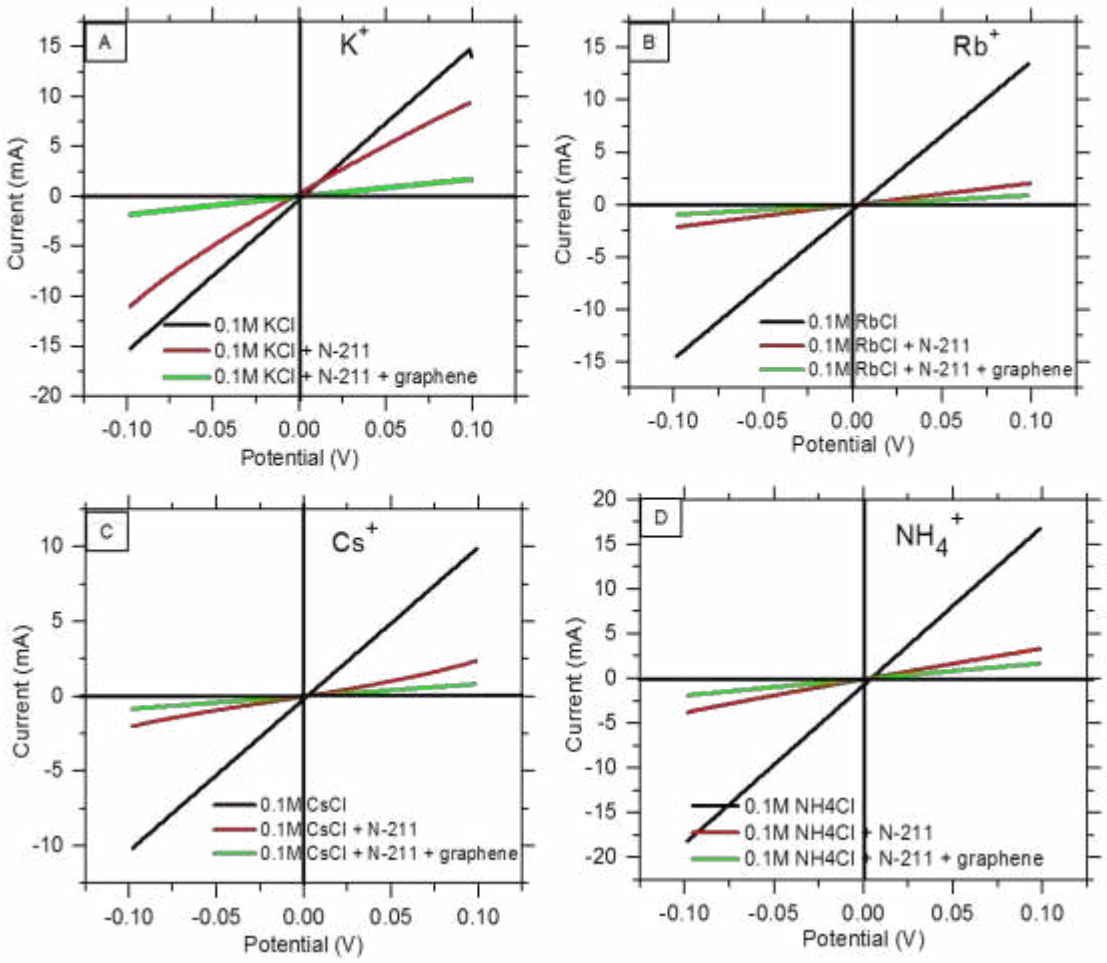


Figure 5.9. I-V curves in D-S cell with and without Nafion® /or graphene in 0.1 M electrolyte: (A) KCl, (B) RbCl, (C) CsCl, and (D) $NH_4Cl$

Nafion® | graphene | Nafion® composite with PET and the second sample is without PET. There is no significant difference for either $H^+$ or $Na^+$ in both samples. These results suggest a near zero contribution from the Nafion® membrane to ion transport. Thus, the observed high proton transmission is actually through graphene hollow sites, whereas the

low ionic currents for $Na^+$ and the other cations, maybe due to the intrinsic CVD graphene defects.

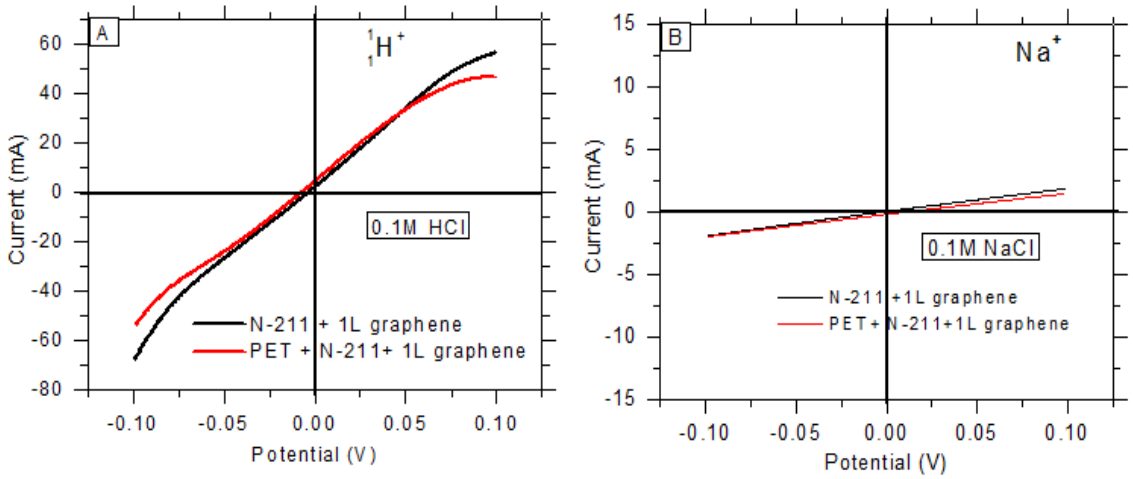


Figure 5.10 I-V curves for $H^+$ transport (A) and $Na^+$ transport (B) in a modified Nafion | graphene | Nafion composite with and without polyethylene terephthalate (PET).

To gain insight into the observed low ionic currents for the other cations, and the nature of the defects in CVD graphene, we conducted a series of comparative studies on $H^+$ transport through CVD graphene composed of the single-layer versus a double layer. Figures 5.11 presents the I-V curves obtained for the proton transport through the Nafion® | graphene | Nafion® composite, containing the single-layer graphene and the double-layer graphene, respectively. To conceptualize the proton transmission in the single- versus double-layer graphene, one might need to consider the crystallographic structures of these graphene layers. The single-layer graphene has an array of carbon atoms in a honeycomb lattice.

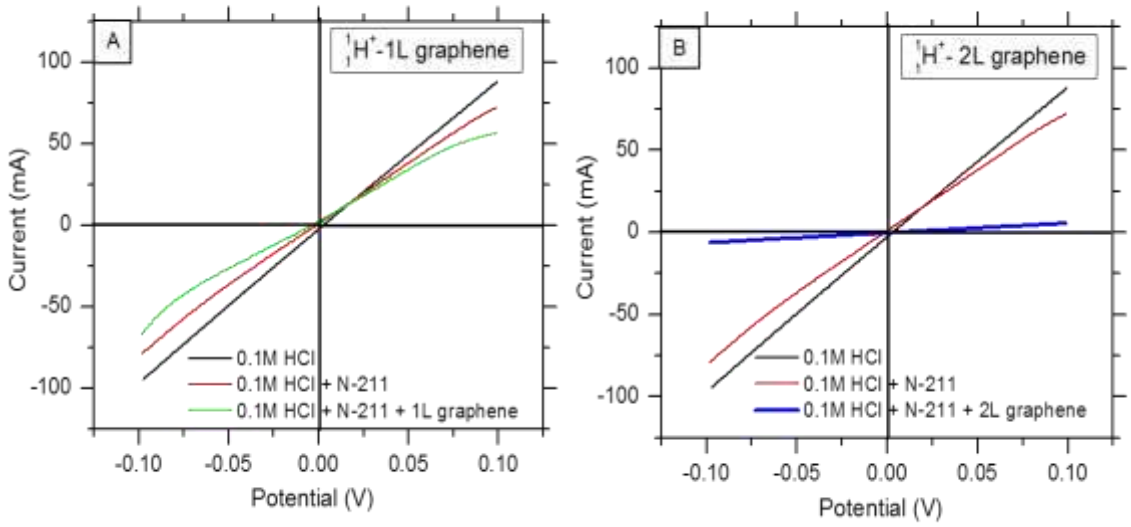


Figure 5.11. I-V responses for comparison of proton transport through (A) the single-layer graphene and (B) the double-layer graphene in 0.1M HCl electrolyte.

The double layer graphene has an AB stacking arrangement of carbon atoms, such that the hollow site of the first layer coincides with the carbon atom of the second layer. The arrangement of the carbon atoms increases the electron cloud of the double layer, and theoretically, the double layer graphene is expected to block proton transmission. Contrary to this theoretical understanding, the experimental results presented in Figure 5.11B show non-zero ionic current for proton transport through double-layer graphene. This again, strongly indicates that the same kind of intrinsic defects that are responsible for all other alkali cations and $NH_4^+$ transport in the single-layer graphene might be the same defects that are responsible for proton transmission through the double layer graphene. This result also rules out the possibility of cracks, tears, holes, or macroscopic

defects; otherwise, a large proton transmission would have been observed in the double-layer graphene.

### 5.2.3 Confocal Raman microscopy

To further investigate on the nature of active sites where ion transmission occurs in Nafion® | graphene | Nafion® composite, we used confocal Raman microscopy. Raman spectroscopy was previously discussed in the section 3.2.3 on samples for H / D electrochemical pumping. The samples characterized with this technique are fresh samples prepared for aqueous ion studies. Raman spectroscopy is a versatile spectroscopic technique for elucidating the Raman signatures of graphene. It is powerful to diagnose the presence of defect site on graphene samples.[302,303] The most important Raman peaks are D-band (around 1350 $cm^{-1}$), G-band (around 1580 $cm^{-1}$) and 2D-band (around 2650 $cm^{-1}$).[304] The D-band is an indication of defective graphitic structure which is usually considered for graphene with defect sites.[305] The G and 2D peaks have width, position and shape and intensity that are indicative of graphene layer and thickness, doping effects, and mechanical strain effects.[303,305] It is important to mention that all Raman spectra were conducted at University of Utah in Dr. Joel M. Harris's lab with the help of Dr. Korzeniewski.

Figure 5.12 shows Raman spectra acquired on single-layer graphene on a glass microscope coverslip and Nafion® | graphene | Nafion® sandwich composites. Acquisitions of spectra were achieved using oil-immersion optics to localize the detection volume on the graphene layer within the Nafion® membranes sandwich. The sample was

staged against the coverslip and the probe volume was stepped manually through the coverslip and Nafion membrane, towards the region where graphene layer is located. The summary of the graphene peaks positions from the Figure 5.12 spectra and other samples are presented in Table 5.5.

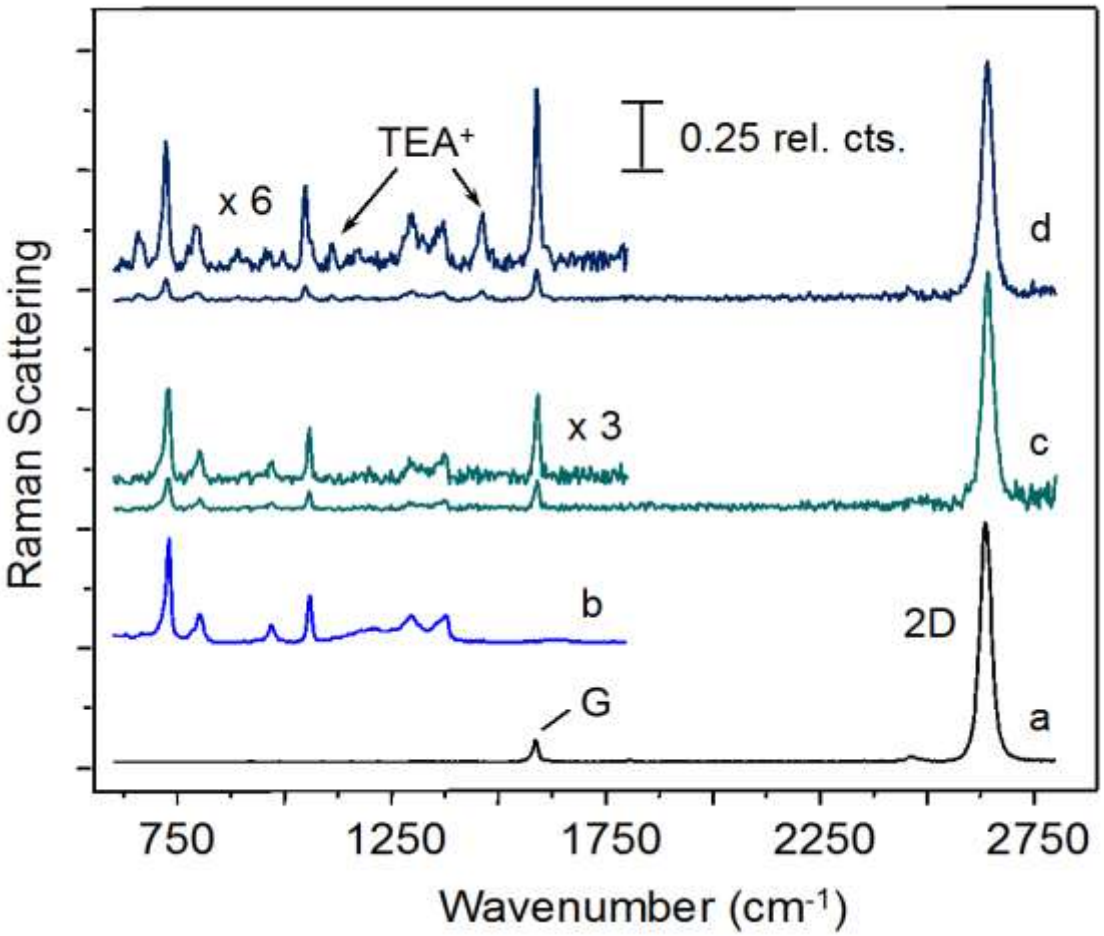


Figure 5.12 Confocal Raman spectra of single-layer graphene on microscope coverslip and Nafion® | graphene | Nafion® composites.

The Figure 5.12a and b are spectra of single-layer graphene on coverslip and Nafion-211 only without graphene. It is clear that single-layer graphene on coverslip shows no D-peak indicating lack of defect. However, the Nafion® -211 membrane Raman spectra show peaks at 1299 and 1371 $cm^{-1}$. These peaks are well within the region of D-peak. So caution must be taken while analyzing graphene spectra on Nafion® membrane. The spectra labeled (c) and (d) are for single-layer graphene in a Nafion® | graphene | Nafion® sandwich structure. Figure 5.12c is the composite in which Nafion membrane is in sodium form and Figure 5.12d is the composite in which Nafion one side is in sodium form and the other side is in tetraethylammonium (TEA) form. This conversion of Nafion form is necessary to prevent background fluorescence. The spectra show the expected G peak and 2D peak with only slight variation. The average widths are 17 $cm^{-1}$ for G peak and 33 $cm^{-1}$ for 2D peak. The ratios of the intensities of 2D peak to G peak lie between 4 and 8. The confocal Raman signatures obtained are quite consistent with the single-layer graphene.

Table 5.5 Summary of the Confocal Raman spectra for Nafion/graphene samples and graphene on coverslip

| | 1L on SiO2 | NGN Na | NGN TEA1 | NGN TEA2 | NGN TEA3 | NGN TEA4 |
|---|---|---|---|---|---|---|
| G position | 1587 | 1592 | 1590 | 1580 | 1587 | 1581 |
| G intensity | 0.089 | 0.124 | 0.127 | 0.228 | 0.159 | 0.238 |
| G width | 33 | 14 | 14 | 25 | 11 | 22 |
| | | | | | | |
| 2D position | 2631 | 2643 | 2641 | 2655 | 2638 | 2640 |
| 2D intensity | 1 | 1 | 1 | 1 | 1 | 1 |
| 2D width | 28 | 30 | 31 | 40 | 28 | 37 |
| | | | | | | |
| D position | -- | -- | -- | 1328 | -- | -- |
| D intensity | -- | -- | -- | 0.026 | -- | -- |
| G width | -- | -- | -- | -- | -- | -- |

With a closer look at the Raman data in Table 5.5, there is a clear slight variation in the graphene spectra though all are within the range that would be considered as single-layer graphene. However, Nafion® | graphene | Nafion® sandwich structure in which one side of Nafion® is in sodium form and the other side in TEA-form (*i.e.* NGN TEA2) was the only spectrum that shows very evident of D-peak as indicated in the Table 5.5. It is however difficult to establish the absence of defect in CVD graphene and also sample treatment during analysis might also be responsible for the observed variation most especially, during conversion of Nafion® membrane from one ionic form to another. This kind of treatment might give rise to electronic doping or mechanical strain. Raman imaging may be suitable to address absence or presence of defect of graphene layer on Nafion® membrane.

### 5.2.4 X-ray Photoelectron Spectroscopy

X-ray photoelectron spectroscopy (XPS) is a powerful surface-sensitive quantitative analytical tool to measure elemental composition at ppt level. Chemical environment (bonding nature) and electronic state of very near-surface region can be probed accurately [307–310]. By irradiating material with the x-ray beam, the XPS spectra can be obtained and at the same time measuring the kinetic energy and escape electrons from near-surface region (usually, 0-10 nm). Figures 5.13 and 5.14 present the XPS spectra acquired on Nafion® membrane and Nafion® membrane with a single-layer graphene respectively. The XPS surveys from the two spectra (Figures 5.13A and 5.14A)

show the expected elements in Nafion® membrane (*i.e.* carbon, oxygen, fluorine and sulfur).

The C1s region in the Figures 5.13B and 5.14B show some interesting results. For example, considering the carbon peak in Nafion®-only spectrum, the spectrum shows a large carbon peak with a high binding energy (BE) at 291 eV and a smaller peak of carbon with a low BE at 284.5 eV.[32,311] The higher BE at 291 eV is associated with carbon bonded with fluorine atoms (either $CF_2$ or $CF_3$) and this is typical of Nafion® membrane XPS signature.[312] The lower BE peak at 284.5 eV is due to adventitious carbon.

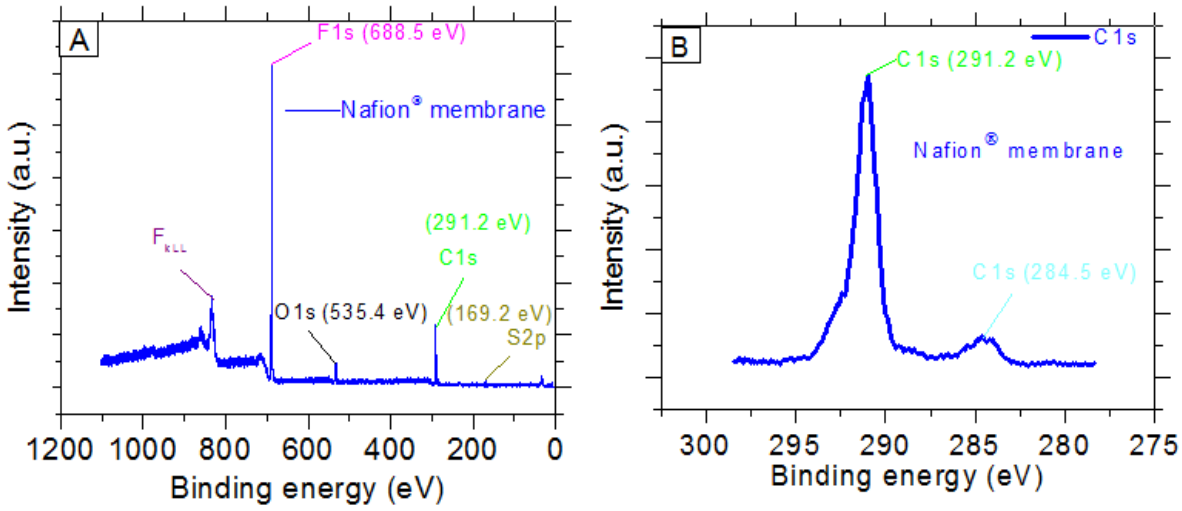


Figure 5.13 XPS survey (A) and carbon-only spectra (B) for Nafion® membrane

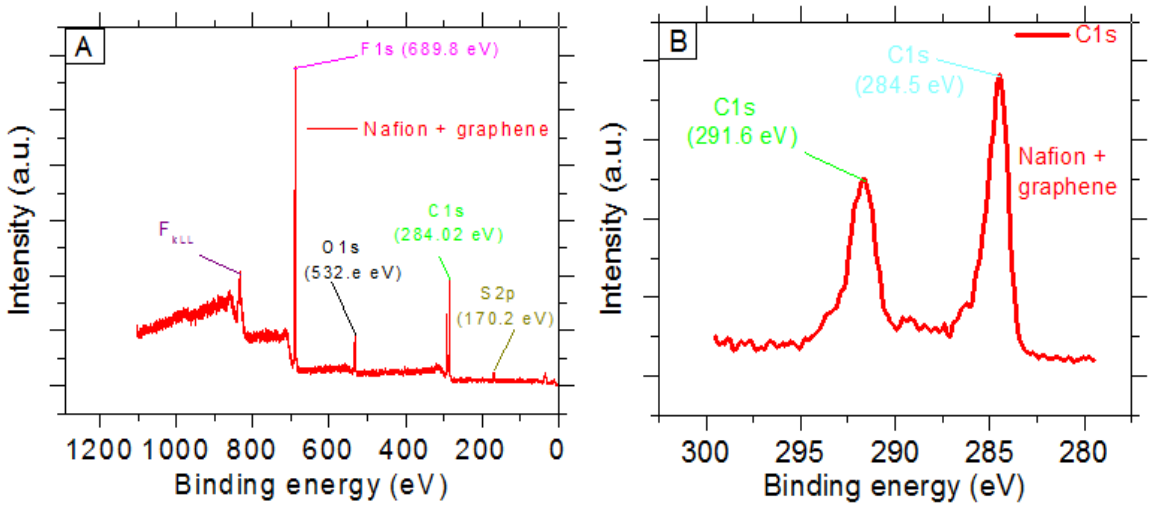


Figure 5.14. XPS survey (A) and carbon-only spectra (B) for 1L graphene on Nafion® membrane

Interestingly, the XPS spectrum of C1s from Nafion® membrane with a single-layer graphene is different from that on Nafion® membrane without graphene. In Figure 5.14B for Nafion® with single-layer graphene, the carbon peak still has two peaks at high and low binding energies. The most striking difference is the prominent peak at low BE (284.5 eV) which is larger in the sample with graphene than in the one without. This peak is definitely coming from graphene peak on the Nafion® membrane since Raman spectra confirmed the presence of graphene on Nafion® membrane. Table 5.6 presents the quantitative data from the XPS spectra from Figures 5.13 and 5.14 showing the peak intensities and elemental composition for Nafion® membrane with and without single-layer graphene.

Table 5.6 XPS peak intensities and elemental composition for Nafion® membrane with and without graphene

| | Nafion only | | | Nafion with graphene | |
|---|---|---|---|---|---|
| Element | XPS peak intensity | Atom percent | Expected Nafion atom percent* | XPS peak intensity | Atom percent |
| Carbon, high BE (291 eV) | 23600 | 33.8 | 31 | 12200 | 58.0 |
| Carbon, low BE (284 eV) | 2930 | | | 19100 | |
| Fluorine | 124000 | 57.7 | 60 | 56800 | 33.0 |
| Oxygen | 8950 | 7.5 | 7.5 | 5360 | 8.0 |
| Sulfur | 2530 | 1.0 | 1.5 | 2190 | 0.9 |
| * for Nafion 1100 EW, elemental composition C20.12 F39.24 S O5 H | | | | | |

The elemental composition as presented in Table 5.6 for Nafion® membrane are within the range expected for typical Nafion® membrane EW1100 series. It is obvious again, that there is higher atom percent of carbon in the sample that has single-layer graphene as compared to the carbon percentage from Nafion® membrane only. The diminishing content for all the elements beside carbon is reasonable because of the addition of graphene on the surface of Nafion® membrane. Exception to that is the oxygen which may be due to contamination due to exposure to the air prior to XPS measurement.

## 5.3 METHODS AND MATERIALS

### 5.3.1 Materials.

Chemical vapor deposition (CVD) Graphene on copper was obtained from ACS Materials, LLC. Nafion® 211 membrane was purchased from the Fuel Cell Store. CeTech

carbon cloth with a microporous layer (W1S1009) was purchased from Fuel Cell Store. Hydrochloric acid and deuterium chloride solution were purchased from Alfa Aesar and Sigma-Aldrich, respectively. Lithium chloride (from Alfa Aesar), sodium chloride (from Mallinckrodt Chemicals), rubidium chloride (from Beantown Chemical), cesium chloride (from Beantown Chemical), and ammonium chloride (from Acros Organics) were used as purchased. Deionized water was used throughout the experiment.

### 5.3.2 Membrane Pretreatment and Ion-Exchange Process

Prior to electrochemical measurement, all membranes used were pretreated to convert them into their respective cationic forms. For the proton-form, the membrane was immersed in 0.1 M sulfuric acid at 80 $^{o}$C for 1 h and then boiled in DI $H_2O$ for 1 hr. Thereafter, the membrane was soaked in 0.1 M HCl for 24 h. The membrane was further rinsed in DI $H_2O$ copiously to remove any impurities and air-dried at ambient temperature. For the deuteron-form, the above procedural steps were followed except, sulfuric acid was replaced with deuterated sulfuric acid, and deionized water was replaced with deuterated water ($D_2O$) and HCl was replaced with DCl.

For conversion of the membrane to the other cationic forms, the Nafion®-211 membranes were soaked in 0.1 M XCl electrolyte ($X^+$ = $Li^+$, $Na^+$, $K^+$, $Rb^+$, $Cs^+$, and $NH_4^+$) solution. The electrolyte solution was replaced with fresh solution at least three times, and the pH of the rinse solution was continuously monitored until the pH did not show the presence of $H^+$. Thereafter, the membrane was further soaked in the XCl electrolyte that had been preheated to 80 $^{o}$C for 1 h and then left in the solution for at

least 48 h. This was done to ensure complete ion-exchange of the membrane to the desired cation form and to improve the membrane's water uptake and expansion of its ion cluster that would facilitate faster ion transport. Finally, the membranes were rinsed thoroughly in DI $H_2O$ and allowed to dry at ambient temperature.

### 5.3.3 Nafion® | graphene | Nafion® Composite MEA Fabrication for Electrochemical Impedance Measurements

All the samples for EIS measurements were prepared identically to the standard protocol of making membrane electrode assembly (MEA) in which membranes are in direct contact with the electrodes. First, CVD graphene on copper was first transferred to one side of the pretreated membrane (already converted to different cationic forms as discussed above) following a fabrication / transfer technique recently reported.[16] In brief, 3/4 inch diameter (19.1 mm) size membrane was cut using an arch punch. CVD graphene on Cu of size 1.5 x 1.5 cm was cut, and hot pressed (at 140 $^oC$, 600 $lb_f$, for 2 min) on the membrane.

The Cu was removed by chemical etching using ammonium peroxydisulfate $\{(NH_4)_2S_2O_8)\}$, leaving the graphene on one side of the membrane. This was followed by a thorough rinse with deionized water and then allowed to dry under ambient condition. The two carbon cloth electrodes (CeTech MPL), 3/16 inch diameter (0.48 cm) together with the second Nafion® membrane disc were then hot pressed (at 140 $^oC$, 600 $lb_f$, for 5 min) on the first membrane that has graphene on it to form the said Nafion® | graphene | Nafion® composite. The MEA active area is ca. 0.178 $cm^2$. Prior to impedance

measurement, the MEA in different cationic forms ($H^+$, $D^+$, $Li^+$, $Na^+$, $K^+$, $Rb^+$, $Cs^+$ and $NH_4^+$) with and without single-layer graphene were soaked in DI $H_2O$ to ensure that they are in wet form.

5.3.4 Nafion® | graphene | Nafion® Membrane Fabrication for Four-Electrode Devanathan-Stachurski (D-S) Cell Measurements.

Sandwich structures containing single-layer graphene positioned between Nafion® membranes were fabricated following our previously published method, adapted for the D-S cell. First, two one-inch-diameter Nafion® membrane disks were cut from a Nafion®-211 membrane sample in the desired ionic form using an arch punch. Next, a one-inch-diameter sample of CVD graphene on copper foil was cut and hot pressed (at 140 $^oC$, 600 $lb_f$, for 2 min) onto one of the Nafion® membrane disks. The Nafion® and graphene-on-Cu-foil were placed between two sheets of PTFE-coated fiberglass during hot-pressing to avoid direct contact with the hot-press plates.

The Cu was then removed by chemical etching using a 0.3 M aqueous ammonium peroxydisulfate solution, leaving the graphene on one side of the membrane. The sample was then thoroughly rinsed with deionized water and allowed to dry under ambient conditions. Next, the second Nafion® disk was hot-pressed onto the graphene side of the first disk, using the hot-press conditions noted above. After cooling, the sample was then ready to use in electrochemical or other characterization experiments.

### 5.3.5 Polyethylene terephthalate (PET) Modified Nafion® | graphene | Nafion® Fabrication

Similar to the above procedure for Nafion® | graphene | Nafion® composite fabrication, two separate pieces of PET with a one-inch diameter (2.54 cm) were cut using an arch punch. From the center of each PET sample, exactly a half-inch diameter (1.27 cm) hole was cut out using an arch punch. The PET samples were then hot pressed together with the Nafion® | graphene | Nafion® composite leaving a half-inch diameter area (1.267 $cm^2$) of the membrane exposed to the aqueous electrolyte.

### 5.3.6 Electrochemical Measurements with Two-Electrode Electrochemical Impedance Spectroscopy (EIS) Cell

The cell used in this work is similar to that used in our recently reported work on hydrogen pump cells with Nafion® / graphene membranes. For the present work, the cell consists of two 5/8 inch diameter graphene rod current collectors fitted into ¾ inch outer diameter PTFE sleeves which are then fitted into a 3/4 inch diameter swage-style compression fitting. The MEA in appropriate ionic form with carbon electrodes on each side is placed in the center of the cell and the cell is then assembled by pressing the graphite rods against the two sides of the membrane.

EIS measurements were conducted in a two-electrode mode configuration using a Solartron 1287 electrochemical interface and Solartron 1260 impedance/gain-phase analyzer in the high-frequency range from 1 kHz to 100 kHz. AC amplitude voltage of 50 mV was applied at DC potential of zero volts to ensure accurate measurement. Each

measurement takes approximately two minutes. Membrane resistance was taken as the high-frequency intercept on the real axis of a Nyquist plot.

### 5.3.7 Electrochemical Measurements with Four-Electrode Devanathan-Stachurski (D-S) Cell

The D-S cell configuration is a four-electrode cell consisting of two platinum wire drive electrodes that drive current flow through a membrane, and two reference electrodes in Luggin capillaries the tips of which are positioned very close to the opposing surfaces of the membrane. This cell configuration is commonly used to study hydrogen permeation through metal samples, but it may also be used to study ion transmission through membranes, as long as the membrane ion transmission rates are significantly different from the ion transmission rates through the liquid electrolyte.

The cell used in this work was fabricated by Adams and Chittenden Scientific Glass (model 949838). It consists of two electrolyte chambers (approximate volume 50 mL) separated by a membrane held in a membrane mount. The membrane size is 1 inch diameter disk but the active area is a 5/8 inch (1.98 $cm^2$) diameter disk. Each compartment of the cell was filled with 50 mL of an electrolyte solution (0.1 M HCl and 0.1 M XCl where $X^+$ = $Li^+$, $Na^+$, $K^+$, $Rb^+$, $Cs^+$ and $NH_4^+$). Homemade Ag/AgCl electrodes filled with a saturated KCl solution were used as the reference electrodes. All of the four electrodes were connected to the Galvanostat / Potentiostat Solartron Instrument (Model No: 1280B). The reference electrode leads were connected to the two reference electrodes, and the working and counter electrode leads were connected to the

two drive electrodes. Ion transmission measurements were performed in potentiostatic mode using linear sweep voltammetry (LSV) at 5 mV $s^{-1}$ to measure the through-plane resistance to ion transport through membranes with and without single-layer graphene. Membrane resistance was obtained from the slope of the current-voltage curves.

5.3.8 Raman Spectroscopy/Microscopy Measurement.

Raman spectra were acquired using a confocal Raman microscope system at the University of Utah that has been previously described in detail.[16,178,313] In brief, the excitation source was a $Kr^+$ laser (Coherent, Santa Clara, CA, USA) operating at 647.1 nm and 3 mW power. The confocal probe volume, defined by the excitation beam focus (ca. 600 nm diameter) together with the collection aperture, was within a depth along the z-dimension of ±1200 nm (90 % collection efficiency). Samples containing Nafion® were ion-exchanged into the sodium ion form prior to Raman characterization. Just prior to spectral measurements, to eliminate background fluorescence, membrane samples were hydrated by brief (ca. 120 s) immersion in 0.5 M NaCl containing 0.3 % $H_2O_2$ followed by rinsing in deionized water. Both solutions were at 60 °C.

After removal from water, the membrane was set on a Kimwipe tissue to remove surface water droplets before placing the sample on a glass coverslip (BK-7 glass, No. 1.5 thickness) positioned on the microscope stage. A glass microscope slide was placed on top of the membrane to hold it firmly against the coverslip and maintain constant hydration. In some cases, one side of a sample was ion-exchanged into a

tetraethylammonium (TEA) form. This exchange had no significant effect on the spectra other than to cause appearance of some Raman peaks for TEA.

### 5.3.9 X-ray Photoelectron Spectroscopy (XPS)

XPS characterization of graphene on Nafion® samples was performed using a PHI 5000 VersaProbe III (Ulvac PHI Inc.), equipped with a monochromatic, micro-focused Al Kα X-ray source operating at 25 W, under a vacuum chamber pressure of $1 \times 10^{-8}$ Pa. The micro-focused raster X-ray beam was scanned across the sample surface. The survey scans were collected at fixed analyzer pass energy of 112 eV and quantified empirically with the sensitivity factors provided by Ulvac PHI Inc. For XPS spectroscopy of localized regions of the sample, the X-ray probe beam diameter was 100 micrometers.

### 5.3.10 XPS Imaging / Spot Analysis

Spot analysis on XPS spectra were acquired on a Nafion®-211 membrane sample for which the surface was partially coated with graphene that has been applied using the hot-press / etching procedure described in the Methods section of the paper. The X-ray spot size was approximately 100 μm. Figure 5.15 is an optical micrograph of the sample obtained from the microscope in the sample chamber of the XPS spectrometer, showing where the graphene is present, and where the spectra were acquired. Arrows point to the edge of the Nafion membrane, and the edge of the graphene deposited on Nafion. Images taken on spots 1-9, 13-22, and 24-31 are in areas where a graphene coating is present

over the Nafion. Images 11, 12, 23, and 32 are in the regions where there is no graphene coating.

The XPS spot analysis on a different sample in addition to the sample described in the main text was undertaken to show clearly the effect of single-layer graphene on the photoelectron attenuation on the elements on Nafion® membrane. The effect of graphene can be seen clearly in portions where graphene is on the membrane from where it was not. The attenuation of C1s peak at 291.2 eV (carbon bonded to fluorine atom) by graphene became evident. The C1s peak at 284.5 eV due to graphene became prominent on the spots where graphene was covered. Figures 5.16 to 5.18 show the C1s peaks for the low and high BE that show the effect of single-layer graphene on Nafion® membrane.

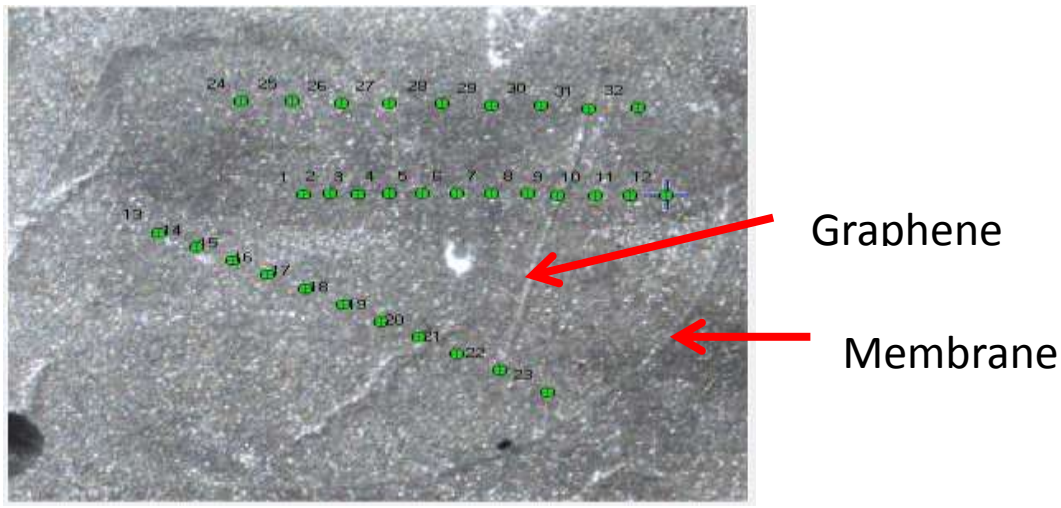


Figure 5.15**.** Optical micrograph of the Nafion® sample with graphene covering part of the sample surface.

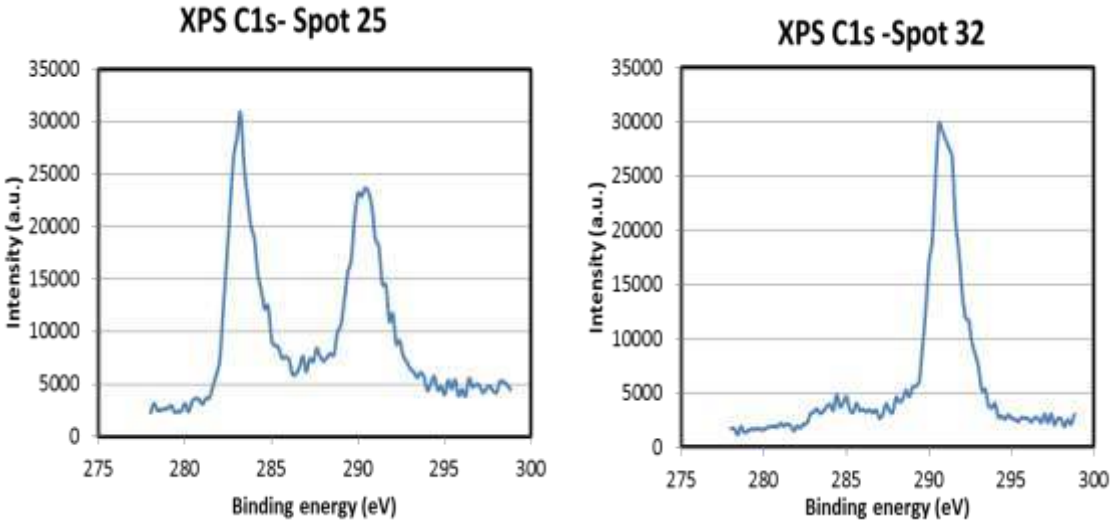


Figure 5.16 Localized C 1s XPS spectra from sample in Figure S10. Spot 25 is from the graphene area on the membrane; Spot 32 is from the area outside the graphene area i.e. on the Nafion® membrane only.

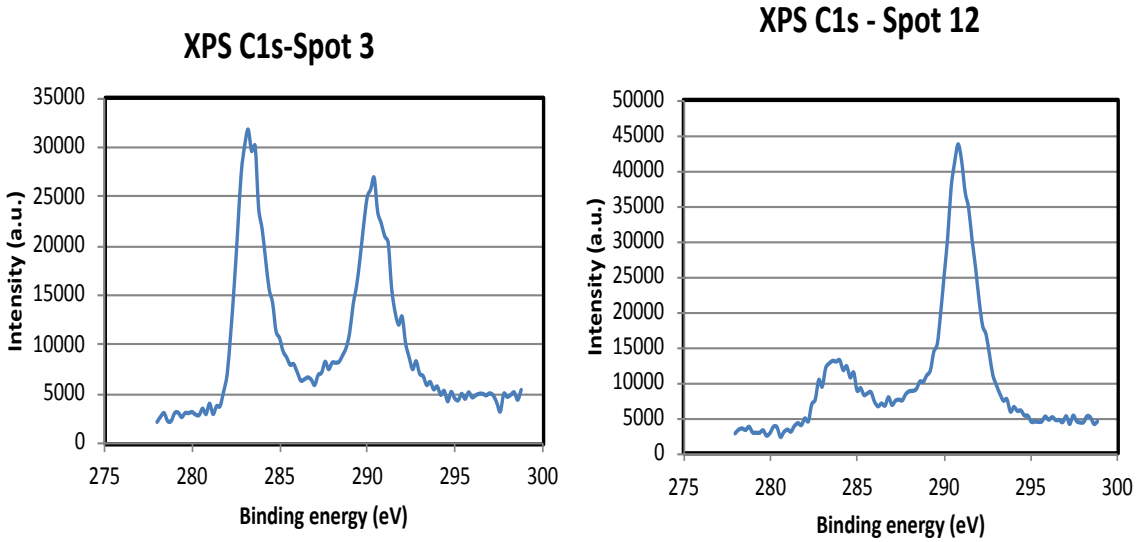


Figure 5.17 Localized C 1s XPS spectra from sample in Figure S10. Spot 3 is from the graphene area on the membrane; Spot 12 is from the area outside the graphene area i.e. on the Nafion® membrane only.

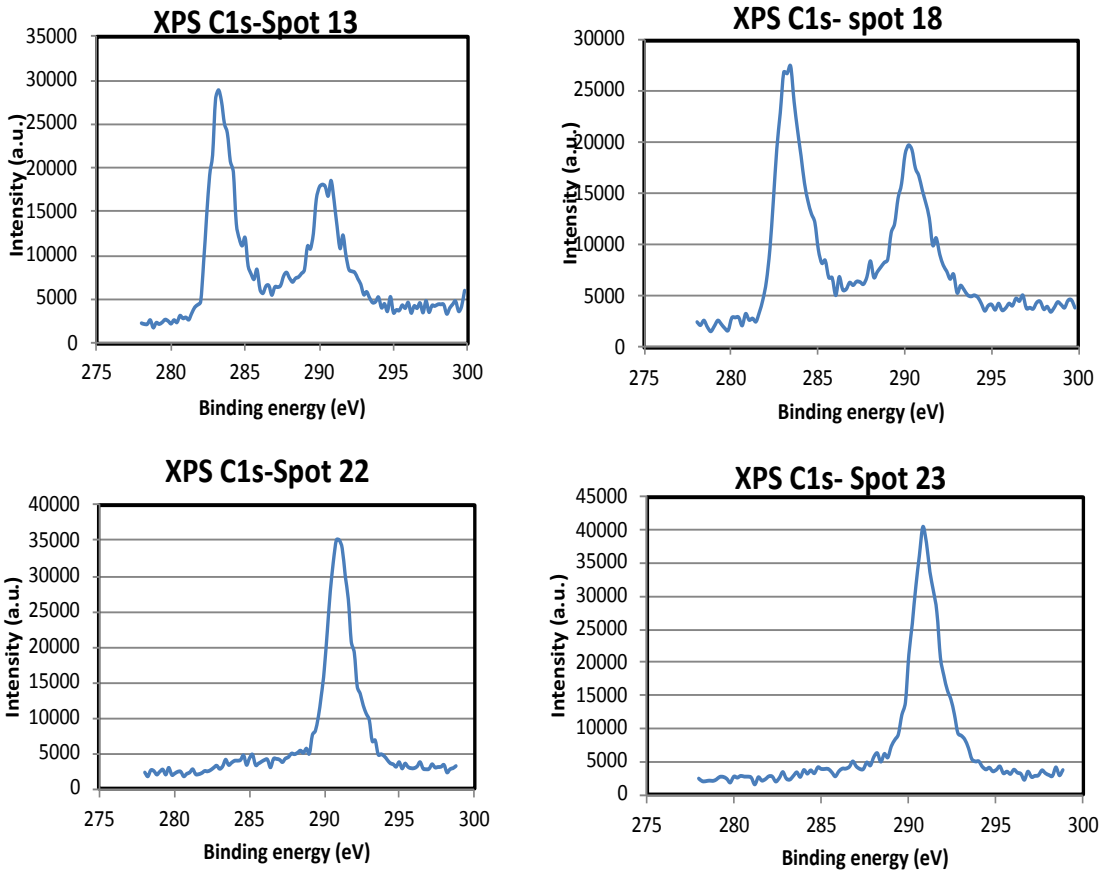


Figure 5.18 Localized C 1s XPS spectra from sample in Figure S10. Spots 13 and 18 are from the graphene area on the membrane; Spots 22 and 23 from the area outside the graphene area i.e. on the Nafion® membrane only.

## 5.4 CONCLUSIONS

In summary, we have investigated the aqueous ion transport through CVD graphene in a Nafion® | graphene | Nafion® composite. Unlike electrochemical hydrogen / deuterium pumping, exclusively used for gases, the method described here can be used for any ion. Two-probe electrochemical impedance spectroscopy (EIS) and a customized

Devanathan-Stachurski electrochemical cell (D-S cell) in a four-probe electrode configuration are easy-to-use, and allow for a reproducible through-plane resistance measurement. We have shown that the aqueous proton transmission through the single-layer graphene occurs at a higher rate than deuteron and 100 times faster than for any other cation. Both the electrochemical and spectroscopy characterization revealed that the graphene transferred onto a Nafion® membrane does not contain any macroscopic defects that could impact the selectivity of proton transport toward other aqueous cations. Although, very small defects were occasionally observed which thought might be responsible for the transmission of other cations. High-quality CVD graphene, if properly handled and transferred to a final substrate, may not contain macroscopic defects such as tears, rips, cracks, and holes that would significantly impact graphene's selectivity towards ion transport.

# CHAPTER SIX

# ELECTROCHMICAL HYDROGEN/DEUTERIUM PUMP IN SINGLE VS MULTI-LAYER GRAPHENE

## 6.0 SYNOPSIS

The work described in this chapter involves comparative studies of proton and deuteron transmission through single vs. multi-layer graphene. Proton transmission other than single-layer graphene is theoretically forbidden. However, the studies here demonstrate non-zero proton and deuteron transmission rates through bi- and multi-layer CVD graphene. All findings including spectroscopic characterization are consistent with a defect-based mechanism for ion transmission through bi-layer and tri-layer CVD graphene. The findings from this work indicate that CVD graphene is not a perfect barrier for ion transmission, although even in the presence of defects it still exhibits extraordinary subatomic selectivity. A manuscript is under preparation that will soon be submitted on this Chapter.

## 6.1 INTRODUCTION

Thermal protons have been experimentally shown to traverse single-layer graphene electron cloud at ambient temperature. Several recent experimental reports have confirmed this phenomenon with a much lower energy barrier (0.55-0.78 eV) in contrary to what was predicted (> 1.0 eV) by computational studies.[15,16,22,29,241,314] Graphene produced by the chemical vapor deposition (CVD) method has good prospects to be considered for the next separation technologies. Although the CVD method can be used

to produce graphene on a large-scale, pristine graphene is yet to be produced through this technique due to the polycrystalline nature of the metal substrate. CVD graphene is known to contain some inherent defects such as point and line defects.[196, 315–319] Even with these defects, single-layer CVD graphene has been experimentally demonstrated to be impermeable to the smallest monatomic gas, He (with Van der Waals radius of 0.28 nm).[204,320] Furthermore, it still possesses subatomic selectivity.[14]

Chapter Three of this dissertation discussed experimentally observed high proton transmission rates through single-layer CVD graphene with a selectivity factor of 14 over deuteron measured through electrochemical hydrogen pump. The story is different with bi-layer or multi-layer graphene which is expected to have an even greater energy barrier for ion transmission than what was predicted for the single-layer graphene. It thus theoretically unfavorable for proton to circumvent the huge electron cloud associated with bi-layer or multi-layer graphene.[24] This is because, multi-layer graphene has AB stacking geometry in which the hollow graphene site in one layer coincides with the carbon atom of the next layer. No experimental report is known to exist on the proton transport through bi-layer or multi-layer graphene at ambient temperature. However, only one report has demonstrated high elevated temperature proton transmission through multi-layer graphene.[320]

Daming Zhu and co-workers reported thermal proton transmission through multi-layer graphene (more than 8 layers) on nickel foil at 900 $^{o}$C using subsecond *in-situ* time-resolved grazing incidence X-ray diffraction (2D-GIXRD) technique.[320] In that work, the authors used 2D-GIXRD equipped with an *in-situ* CVD chamber to monitor the interlayer

spacing during the growth of graphene as a result of proton transmission. Under the same test conditions, argon, nitrogen, helium and their corresponding ions transport were shown to be blocked by multi-layer graphene at such elevated temperature.

Similarly, an *in-situ* transport measurement using electrochemical technique was used as complementary experiment to 2D-GIXRD to establish proton transmission at high temperature through multi-layer graphene.[320] Current-voltage measurements were conducted within potential window of 0−100 V. The gases ($CH_4$, $H_2$, Ar, $N_2$, and He) used were thermally cracked at above 600 V while monitoring from the in-situ current measurements the protonation or annealing of Ar, $N_2$, and He during the growth of CVD graphene on nickel. Again, the results indicate proton transmission through multi-layer graphene but no other ions. These experimental findings seem attractive, however, it will be practically uneconomical to separate hydrogen from other gases through the above process. It must be noted that this phenomenon is impossible theoretically at ambient temperature.

In this work, we seek to investigate the proton transmission at ambient temperature through bi-layer and multi-layer (3-5 layers) graphene produced by CVD method on Cu substrate. Study of this kind will reveal the true nature of CVD graphene defect and whether its permselectivity is still preserved. Single-, bi- and tri-layer CVD graphene on Cu was transferred to PFSA ionomer membrane using the technique discussed in Chapters 3, 4, and 5 of this dissertation. Following the transfer technique, hydrogen evolving electrodes using platinum-on-carbon cloth were hot pressed onto membranes to make the MEAs. The MEAs were studied in both symmetric and

asymmetric H / D pump mode while humidified gases were being supplied to the anode and the cathode compartments of the miniaturized cell. For the aqueous measurements in D-S cell, the graphene was prepared as a sandwich between two Nafion® membrane disks without application of electrodes. Measurements were performed according to the experimental protocols discussed in Chapter 5.[241]

Spectroscopic characterization including scanning electron microscope (SEM) and XPS findings are consistent with a defect based mechanism for ion transmission through bi-layer and multi-layer CVD graphene.

## 6.2 RESULTS AND DISCUSSION

### 6.2.1 Asymmetric H/D Evolution Reaction

The experimental procedures for the electrochemical hydrogen / deuterium pump in asymmetric configuration are similar to what was previously described in Chapter Three Section 3.2.1.[16] The MEAs were prepared asymmetrically in which the anode is somewhat larger than the cathode electrode. The anode consists of 4 mg $cm^{-2}$ Pt carbon cloth electrode (5/16 inch diameter) in which 3.5 μL of 5 wt. % Nafion® solution was coated and allowed to dry at ambient condition. The cathode electrode was 0.03 mg $cm^{-2}$ Pt carbon cloth (3/32 inch diameter) with a coating of 0.5 μL 5 wt. % Nafion® solution. Following transfer of single-, bi- and tri-layer graphene onto Nafion® membrane using the previously described fabrication and transfer technique (see Chapters 3, 4 and 5), the MEAs consisting of two Nafion® membrane disks were prepared as sandwiched structures containing single-, bi-, and tri-layer graphene and were hot pressed at 140 $^{o}$C,

600 $lb_f$ for 5 min. Nafion® membranes were pre-treated in $H_2SO_4$ / $H_2O$ and $D_2SO_4$ / $D_2O$ to put them in appropriate proton and deuteron forms.

The MEAs were then assembled in our previously described miniaturized cell (See chapters 2 and 3).[76,185] Gas humidification was achieved by connecting the gas from the gas line into a humidifier bottle set at 30 °C, at a flow rate of 0.02 SLM. The anode was bathed with humidified argon (≈ 100% RH) gas and the cathode was supplied with the humidified hydrogen/ deuterium gas (≈ 100% RH). Slow scan cyclic voltammetry (CV) experiments were conducted for the hydrogen evolution and deuterium evolution reactions between -0.15 to 0.3 V on the MEAs at a scan rate of 20 mV $s^{-1}$ or 5 mV $s^{-1}$. It should be noted that the CV behavior was independent of scan rate for the hydrogen evolution reaction when the response became stabilized after some initial forward and reverse scans.

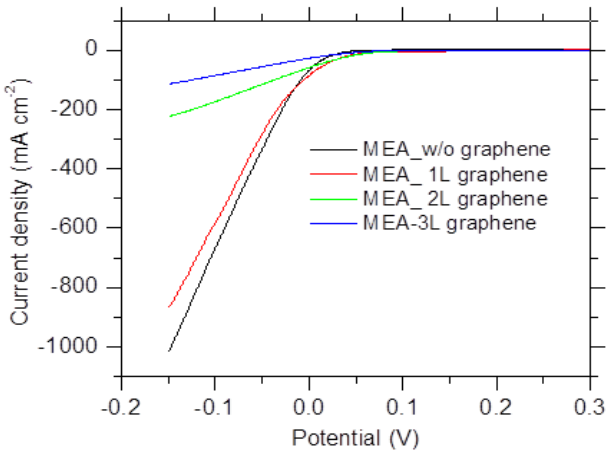


Figure 6.1. I-V curves for HER on MEAs with single-, bi- and tri-layer graphene and without graphene.

Figure 6.1 presents the I-V curves for the hydrogen evolution reaction on MEAs in proton form with and without graphene. It is interesting that proton transmission through single-layer graphene again occurs at high rate (near 1.0 A $cm^{-2}$) as it was previously observed with a little attenuation when compared to the MEA without graphene. Surprisingly, non-zero current for proton transmission was observed through double- and triple-layer graphene. The results are unexpected and might suggest intrinsic defect in CVD graphene. Although the effect of graphene layer addition is obvious, for example, proton is more attenuated by tri-layer graphene than bi-layer graphene. While high proton transmission can occur through single-layer graphene at ambient temperature, proton transmission through bi- or multi-layer graphene (3 or more layers) may not occur. The experimental data in Figure 6.1 strongly indicate that the CVD graphene is not an ideal or perfect barrier.

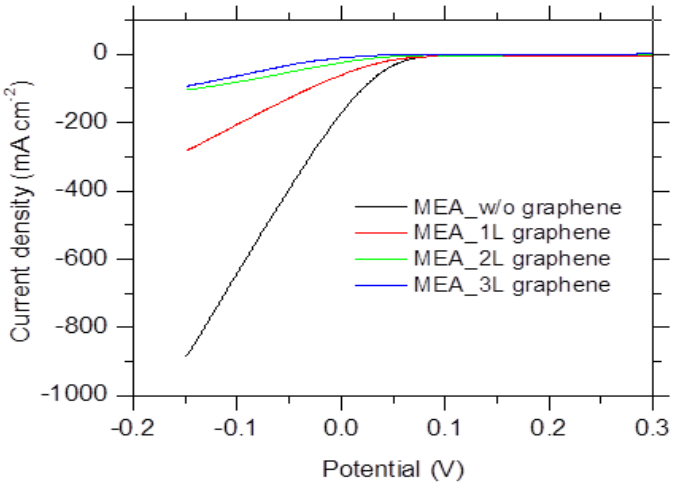


Figure 6.2. I-V curves for DER on MEAs with single-, bi- and tri-layer graphene and without graphene.

Figure 6.2 on the other hand, presents the I-V curves for the deuterium evolution reaction on MEAs in deuteron form. The data also confirmed non-zero current for the deuteron transmission across bi- and tri-layer graphene. With closer look at the Figures 6.1 and 6.2 reveals some interesting facts about the nature of CVD graphene and ion transmission through it. It thus reveals again that graphene made through CVD method is not a perfect barrier especially for proton transmission regardless of the layers of the graphene. More important though is the fact that even in the presence of these defects, it still shows selectivity between hydrogen isotopes. For example, irrespective of the graphene layer, deuteron is more attenuated than proton. This finding suggests that the nature of defect in CVD graphene is not macroscopic defect such as tears, rips or cracks that would allow any ion through it. The nature of this defect would be properly examined under spectroscopic characterization later in the Chapter.

### 6.2.2 Symmetric H / D Evolution Reaction

The I-V curves for hydrogen evolution reaction and deuterium evolution reaction are generally used to see the trend and the overpotential required for such reaction to occur. The rising part of the curves (See Figures 6.1 and 6.2) at the onset potential includes contributions from activation resistance due to both electron transfer for the reduction process and membrane / graphene ionic resistance. To better quantify the proton and deuteron transport through graphene layers, a symmetric experiment was conducted. See Chapter Three for discussion on the fundamentals of symmetric

experiment. Both the anode and the cathode electrodes were made symmetrical with the catalyst loading of 0.3 mg $cm^{-2}$ Pt on carbon cloth.

The MEAs are 3/16 inch diameter and consist of two Nafion®-211 membrane disks with graphene layer(s) sandwiched in-between. Humidified hydrogen / deuterium gas (≈ 100 RH) was fed to both the anode and the cathode so that the cell voltage would be zero. This will in turn give rise to a linear I-V curves from which the resistance due to ion transport can be computed from the slope of the curves.

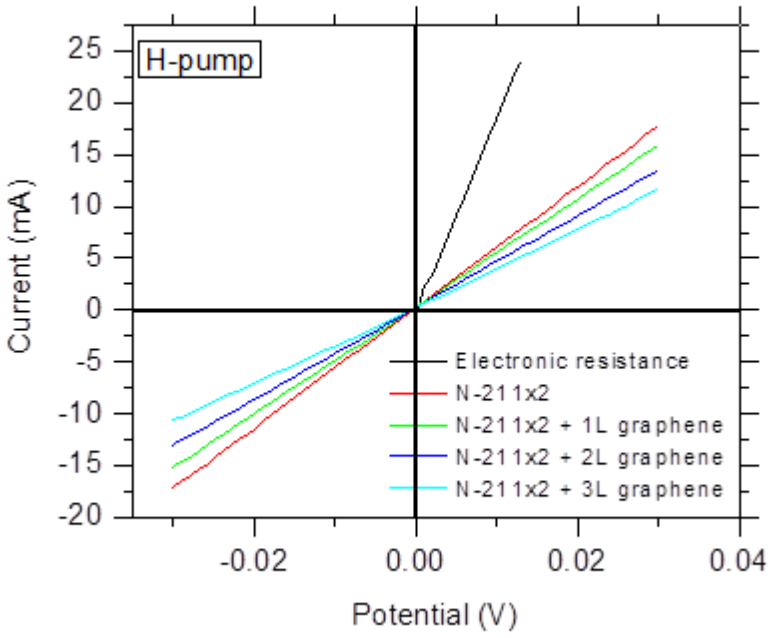


Figure 6.3. I-V curves for proton transport in symmetric cell for MEAs with layer(s) of graphene.

Linear sweep voltammetry (LSV) was used to acquire I-V curves at ± 0.03 V, at a scan rate of 1.0 mV $s^{-1}$. Figure 6.3 presents I-V curves for the symmetric hydrogen pump for MEAs with single-, double- and triple-layer graphene and electronic resistance. The electronic resistance is the resistance due to just the cell and its components (graphite rods, rotor clips, gas diffusion layers, and O-rings) without the MEA. This resistance must be subtracted from the overall cell resistance to estimate ionic resistance due to just the membrane and the graphene layer(s). The effect of graphene can be seen with decrease in the slope as more graphene layers are being added to the MEA. Similar effects were seen for deuteron (see Figure 6.4) but with a large attenuation effect for deuteron transport when compared to that of proton which strongly indicates selectivity of graphene toward hydrons.

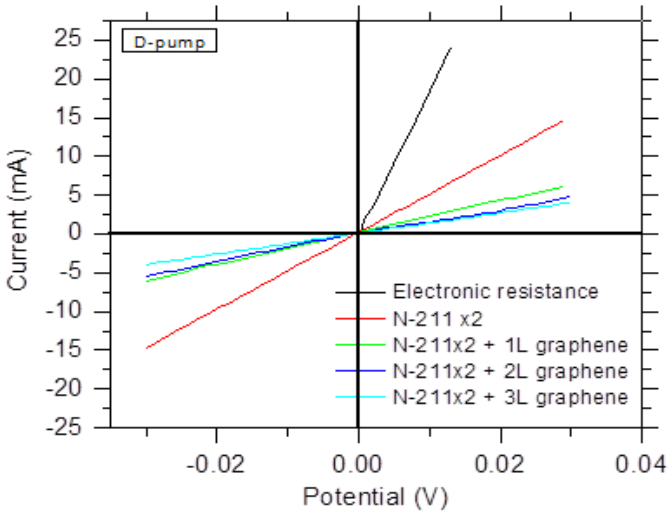


Figure 6.4 I-V curves for deuteron transport in symmetric cell for MEAs with layer(s) of graphene.

The estimated resistances and conductances for proton and deuteron transport through single-, bi-, and tri-layer graphene are presented in the Table 6.1. After subtraction of electronic resistance from the measured resistance, it is then normalized to the geometric area of the electrode to give MEA area normalized resistances. The resistance due to graphene layer(s) can be easily obtained by subtracting the area normalized resistances of the MEA with and without graphene to give just graphene areal resistance alone. By taking the inverse of graphene areal resistance gives graphene areal conductances for proton and deuteron transport across single-, bi-, and tri-layer graphene. Ratio of at least 10 between proton and deuteron can be established which confirms prior report regarding subatomic selectivity of graphene toward hydrons.[16,22,185]

Table 6.1 Resistances and Conductances for H/D transmission through graphene

| Sample | Resistance, R | Corrected R | MEA areal R | Graphene areal R | Graphene areal G |
|---|---|---|---|---|---|
| | Ω | Ω | $m\Omega\ cm^2$ | $m\Omega\ cm^2$ | $S\ cm^{-1}$ |
| **$H^+$** | | | | | |
| Electronic resistance | 0.576 | -- | -- | -- | |
| Nafion®-211 x2 | 1.7168 | 1.1408 | 203.1 | -- | |
| Nafion®-211 x2 + 1L graphene | 1.9322 | 1.3562 | 241.4 | 38.3 | 26 |
| Nafion®-211 x2 + 2L graphene | 2.2608 | 1.6848 | 299.9 | 96.8 | 10.3 |
| Nafion®-211 x2 + 3L graphene | 2.704 | 2.128 | 378.8 | 175.7 | 5.7 |
| **$D^+$** | | | | | |
| Electronic resistance | 0.576 | -- | -- | -- | |
| Nafion®-211 x2 | 2.016 | 1.44 | 256.3 | -- | |
| Nafion®-211 x2 + 1L graphene | 4.8611 | 4.2851 | 762.7 | 506.4 | 1.9 |
| Nafion®-211 x2 + 2L graphene | 5.9654 | 5.3894 | 959.3 | 703 | 1.4 |
| Nafion®-211 x2 + 3L graphene | 7.5324 | 6.9564 | 1238.2 | 981.9 | 1 |

6.2.3 Selectivity Studies through the Position of Graphene in MEA

The placement of graphene in the MEA may have an effect on the overall selectivity of H / D fractionation. It is important to investigate how the placement of graphene within the MEA influences selectivity and to see which configuration leads to higher flux and maximum isotopic separation. To test this hypothesis, two single-layer graphene placements were compared to the placement of bi-layer graphene placement within the MEAs. The MEA consists of three Nafion® membrane disks. The components are represented as A (1 = Nafion® membrane disk, 2 = graphene layer, 3 = carbon cloth electrode) and B represents the fabricated MEA. The MEAs were prepared as asymmetric with cathode being 0.03 mg $cm^{-2}$ Pt carbon cloth (3/32 inch diameter) and the anode being 4 mg $cm^{-2}$ Pt carbon cloth electrode (5/16 inch diameter).

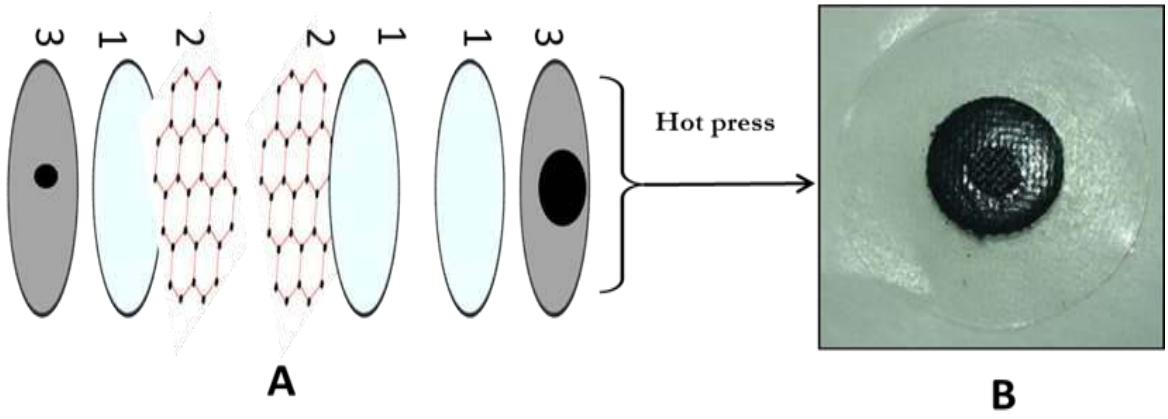


Figure 6.5. Schematic representation of MEA fabrication for graphene placement effect-Configuration I

In the first configuration represented in Figure 6.5, for the MEA made from two single-layer graphene, the graphene was transferred to two out of the three membrane disks. Whereas for the MEA made from bi-layer, the graphene was transferred to one out of the three Nafion® membrane disks. Essentially, this is done to compare the effect of having two single-layer graphene as compared to just bi-layer graphene. Both hydrogen evolution reaction and deuterium evolution reaction were compared to see if two single-

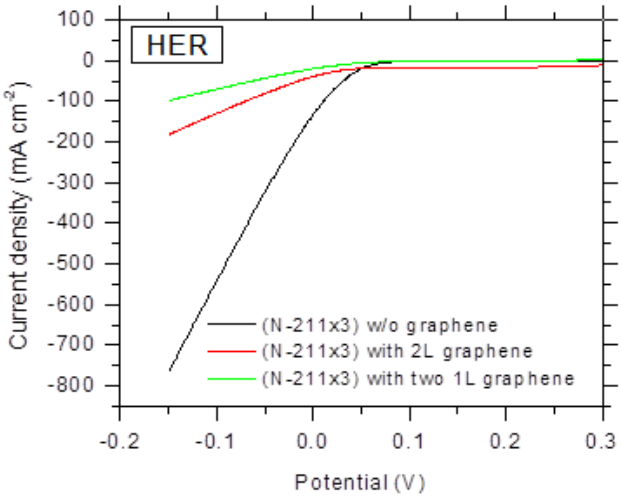


Figure 6.6. HER polarization curves from MEAs comparing two single-layer graphene (in contact with each other) with bi-layer graphene

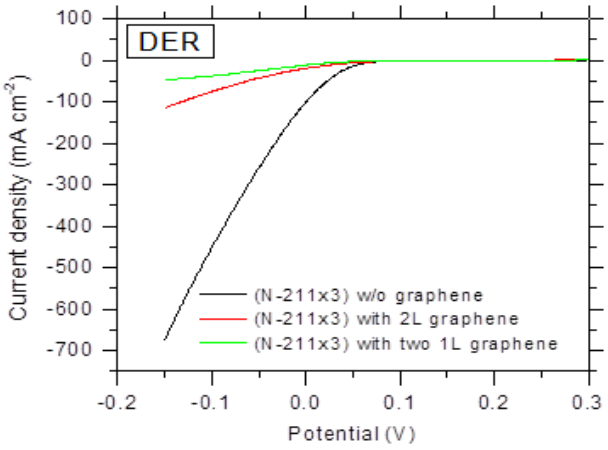


Figure 6.7 DER Polarization curves from MEAs comparing two single-layer graphene (in contact with each other) with bi-layer graphene.

layer graphene produces the same structure and selectivity as compared to the bi-layer graphene. Figures 6.6 and 6.7 present the polarization curves for HER and DER respectively, with the placement of graphene in the MEA as discussed above. It is interesting to see how two single-layer graphene sandwiched together attenuates proton and deuteron transport more than bi-layer graphene. The reason for the observed improved attenuation for two single-layer graphene over the bi-layer graphene might be as a result of the overall defect density in these samples. The defects in two single-layer CVD graphene may not align over each other and thus leading to a lower defect density than bi-layer graphene which makes ion transmission more difficult through the defect sites.

The second configuration for the placement of graphene in the MEA is represented in Figure 6.8. Unlike Figure 6.5 in which two single-layer graphene were

placed in contact with each other that otherwise mimics bi-layer graphene, here two single-layer graphene were placed within the three Nafion® membrane disks such that the graphene layers are not in contact with each other. Two MEAs were prepared, one in proton form and the other in deuteron form. Figure 6.9 presents the polarization curves for the HER on MEAs with and without two single-layer CVD graphene. This is interesting because it thus confirms previous observation of high proton transmission through single-layer graphene. It is important to emphasize that it would not matter for

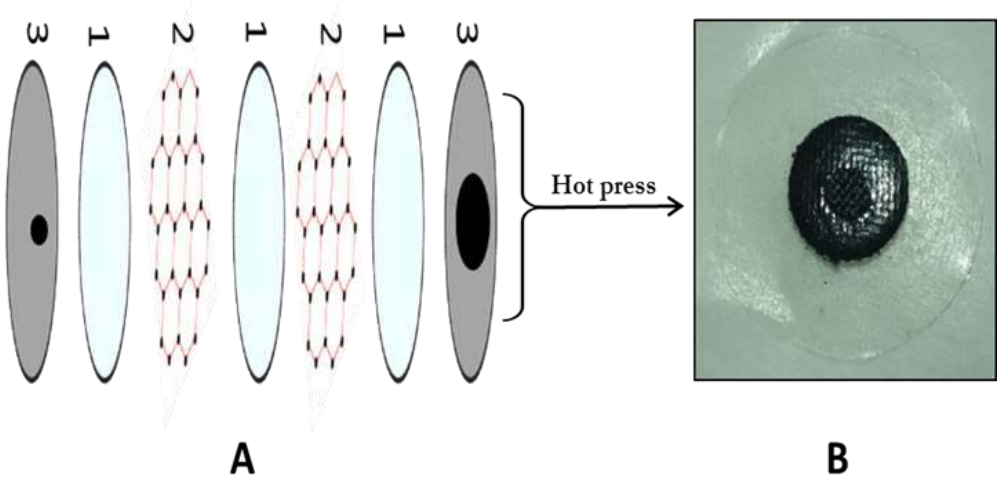


Figure 6.8. Schematic representation of MEA fabrication for graphene placement effect-Configuration II

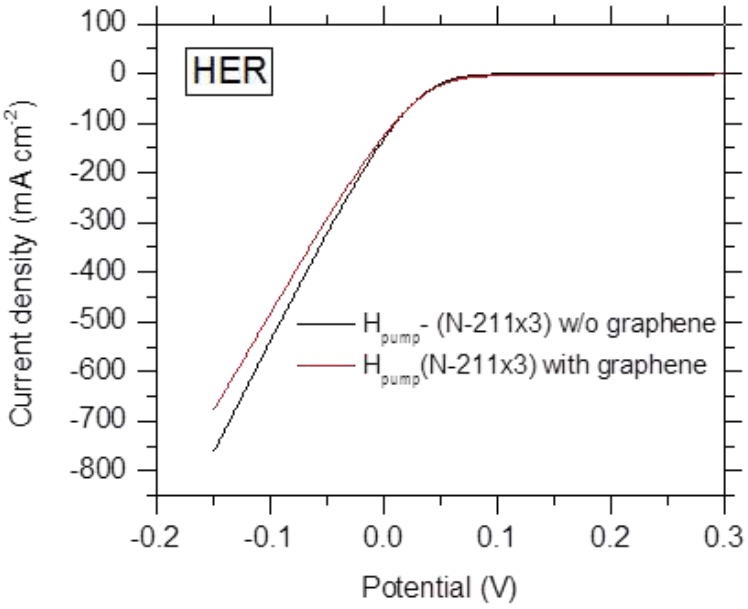


Figure 6.9. HER polarization curves for MEA with two single-layer graphene (not in contact with each other).

the proton transmission through single-layer graphene regardless of the number of graphene layers in MEA as long as they are not in contact with each other.

Similarly, Figure 6.10 presents the DER for MEAs with and without two single-layer graphene. The results from the Figures 6.10 reveal very important information on the selectivity for proton and deuteron transmission through single-layer graphene. For

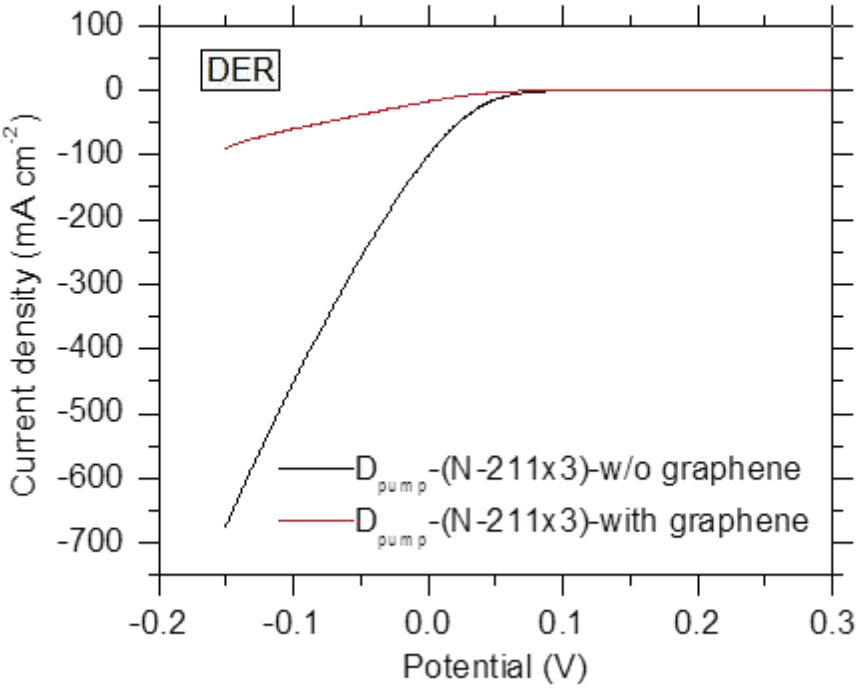


Figure 6.10. DER polarization curves for MEA with two single-layer graphene (not in contact with each other).

example, from Figure 6.10, deuteron transmission through graphene was much attenuated with the placement of two single-layer graphene in between Nafion® membranes as compared to proton. This suggests that optimum proton / deuteron selectivity can be achieved by integrating more single-layer graphene within the MEA, since such many layers have no significant effect on proton transmission but much attenuation on deuteron transmission.

### 6.2.4 SEM Defect Visualization of Graphene on Copper

It is important that the structural defects in CVD graphene must be accounted for while exploring mass transport phenomenon on macroscopic graphene samples. This is necessary to understand the role of defect and being able to quantify it in the overall ion transmission through CVD graphene. As a result, we conducted a defect visualization experiment on as-purchased CVD graphene. The technique was reported by Kidambi and co-workers,[321] in which aqueous ferric chloride chemical etchant is briefly exposed to the CVD graphene and then rinse carefully, followed by examination under scanning electron microscope. This is based on the fact that ferric ion can pass through the defect sites, which in turn can create etch pits in the underlying copper substrate.

In brief, small pieces of CVD graphene samples (single-, bi-, and tri-layer) were rinsed in DI $H_2O$ and then a drop of 0.1 M $FeCl_3$ was placed on it for a period of 5 s, followed by a proper rinse in DI $H_2O$. The samples were then subsequently examined on SEM (Hitachi model S-3400N Variable Pressure Scanning Electron Microscope). Figures 6.11, 6.12, and 6.13 present the SEM images of single-, bi- and triple-layer graphene respectively.

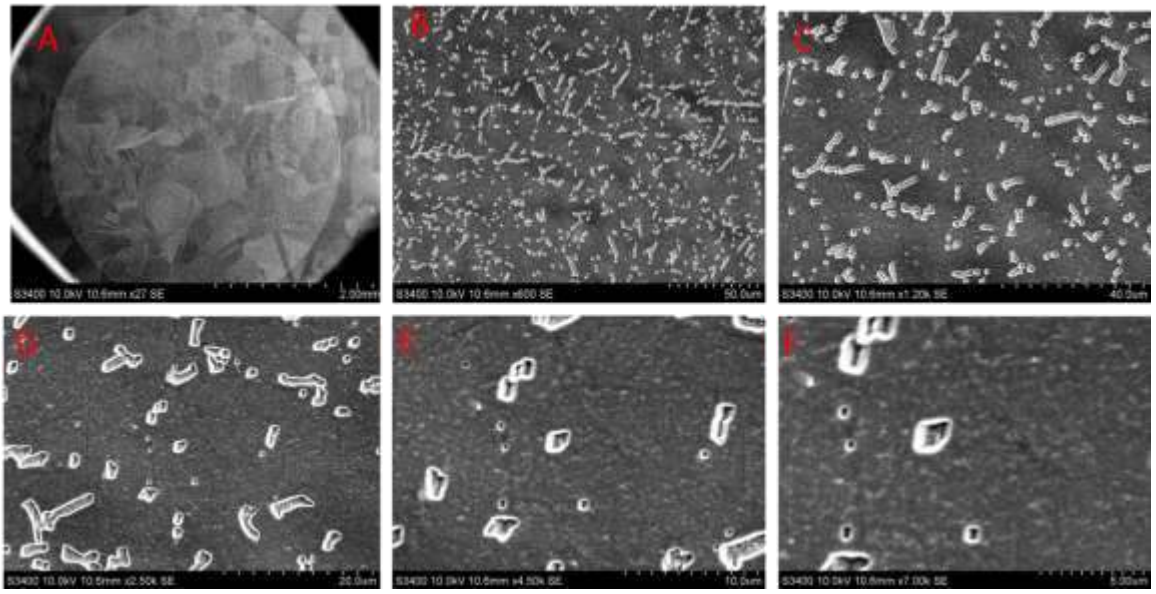

Figure 6.11. SEM images of defect visualization of single-layer CVD graphene (A) 2 mm, (B) 50 µm, (C) 40 µm, (D) 20 µm, (E) 10 µm, and (F) 5 µm scale bars

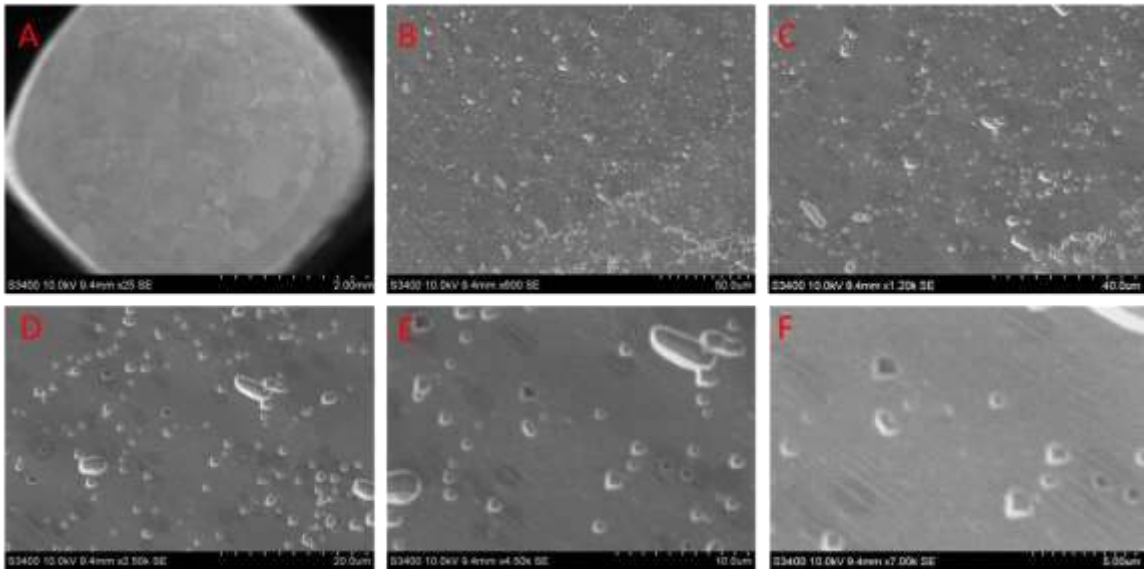

Figure 6.12. SEM images of defect visualization of bi-layer CVD graphene (A) 2 mm, (B) 50 µm, (C) 40 µm, (D) 20 µm, (E) 10 µm, and (F) 5 µm scale bars

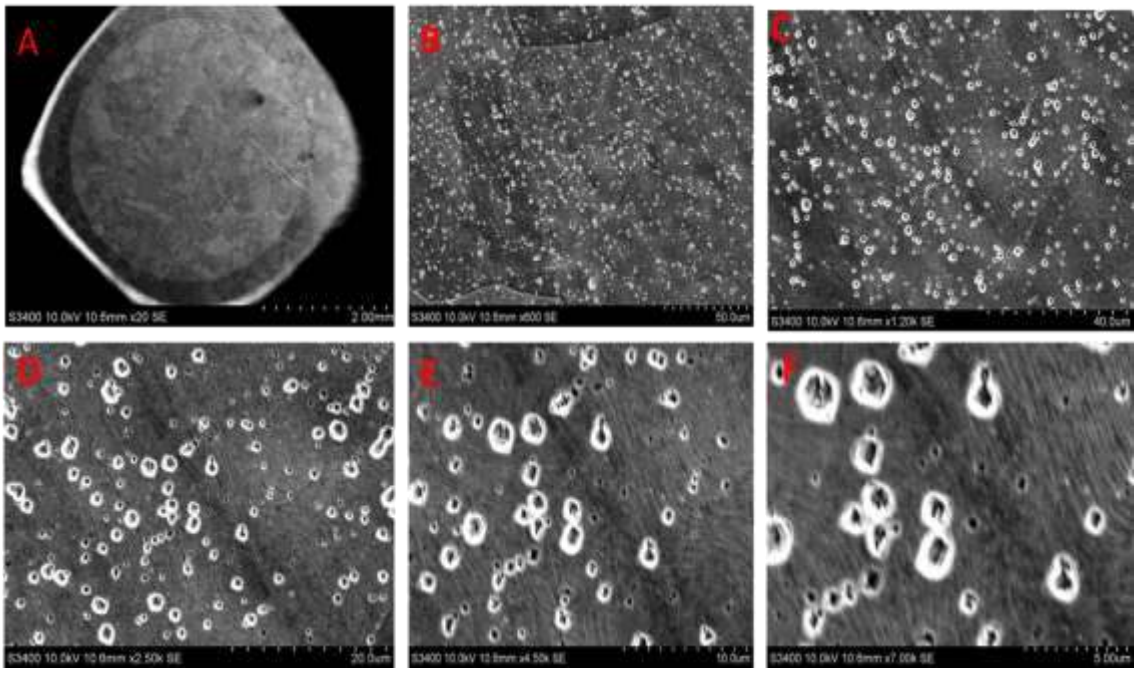

Figure 6.13. SEM images of defect visualization of tri-layer CVD graphene (A) 2 mm, (B) 50 µm, (C) 40 µm, (D) 20 µm, (E) 10 µm, and (F) 5 µm scale bars

Low magnification of Figures 6.11A, 6.12A, and 6.13A clearly shows the grain structure of the underline copper substrate and on top of that is the circular area where the etchant solution was dropped on CVD graphene. Higher magnification clearly reveals formation of etch pits. The formation of these etch pits suggest that CVD graphene is not a perfect barrier. It is obvious the etch pits can be seen across the CVD graphene surface. These etch pits are either points or short lines of less than 1 µm in widths. Interestingly, the absence of large etch pits in any of these graphene samples strongly indicate the lack of macroscopic defects that would have allowed high flux of other ions through it. With close look of the spatial distribution of these etch pits, it can be observed in some regions

were etch pits are clearly absent. These regions extend to many micrometers in extent and clearly indicate where graphene is pristine that are impenetrable to the ferric ion. Figure 6.14 shows the defect counting using ImageJ software. Analysis of several regions (40 x 40 $\mu m^2$) gives an average estimation of defect density. The average defect density on 40 x 40 $\mu m^2$ regions on the SEM images of the CVD graphene layer(s) are presented in Table 6.2.

It is reasonable to conclude that the observed very low ion transport for other cations discussed in Chapter 5 and very small proton and deuteron transmission through bi-layer and tri-layer graphene were as a result of these CVD graphene defect sites. The actual nature of the sites in which proton transmits with very high flux and selectivity as compared to other ions is still uncertain and could not be explained based on defect mechanism only. It is however certain that proton transmission is occurring through graphene at sites where other ions cannot go through.

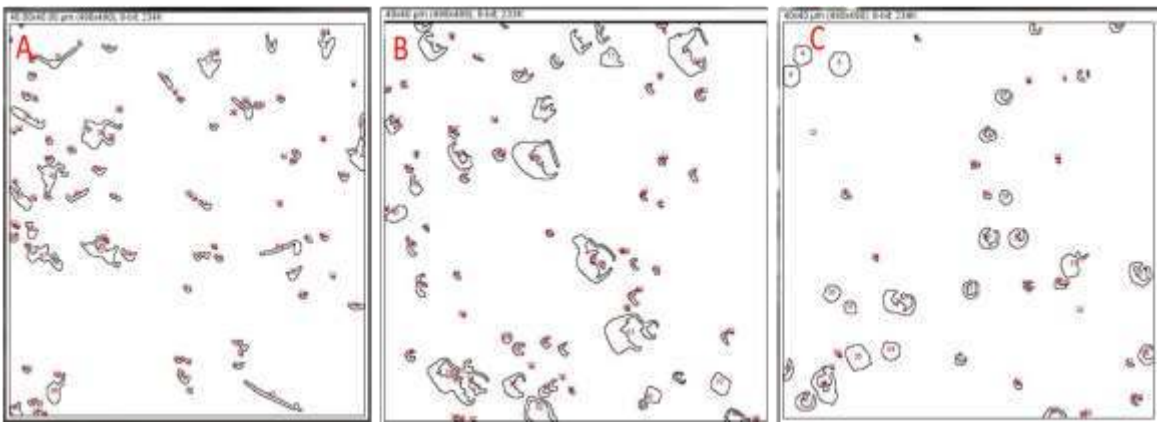


Figure 6.14. Image counting of defect sites in 40 x 40 μm graphene: (A) single-layer (B) bi-layer, and (C) tri-layer

| Table 6.2 Average defect density in graphene samples | | | |
|---|---|---|---|
| CVD graphene | Defect density | | |
| 1L graphene | 110 | | |
| 2L graphene | 87 | | |
| 3L graphene | 58 | | |

6.2.5 SEM and EDS Analyses of Graphene on Membrane

To further assess the fabrication and transfer of graphene onto Nafion® membrane, Nafion® membranes containing single-, bi-, and tri-layer graphene were subjected to SEM imaging and EDS analyses. SEM imaging was conducted using an S-3400N variable pressure scanning electron microscope (Hitachi model) at 5 kV and energy dispersive X-ray spectroscopy analysis was performed on EDX, Oxford Instrument with X-max detector to provide elemental composition on the samples. Figure 6.15 presents the SEM image and EDS spectra of single-layer graphene on Nafion®-211 membrane.

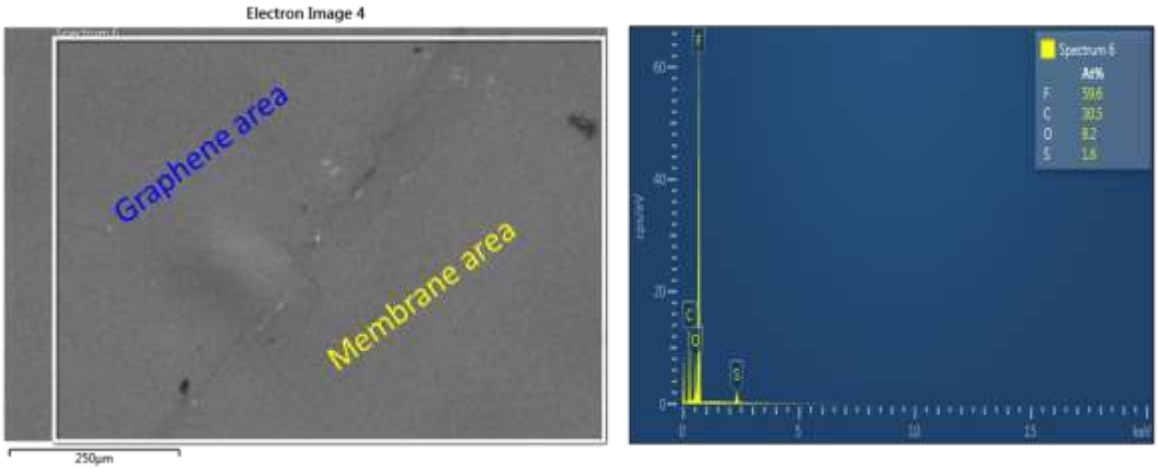


Figure 6.15. SEM and EDS spectra of single-layer graphene on Nafion® membrane

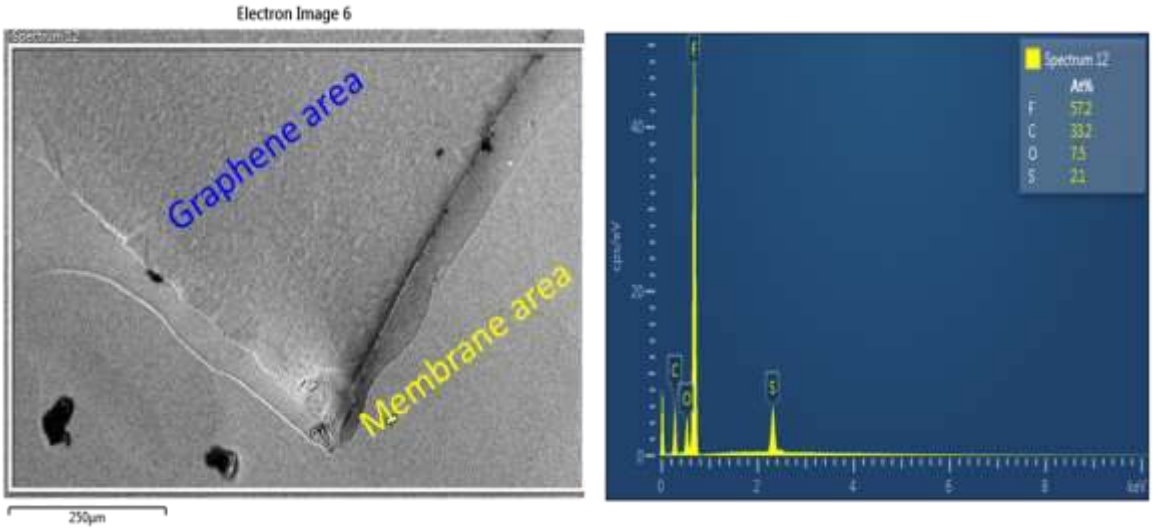


Figure 6.16. SEM and EDS spectra of bi-layer graphene on Nafion® membrane

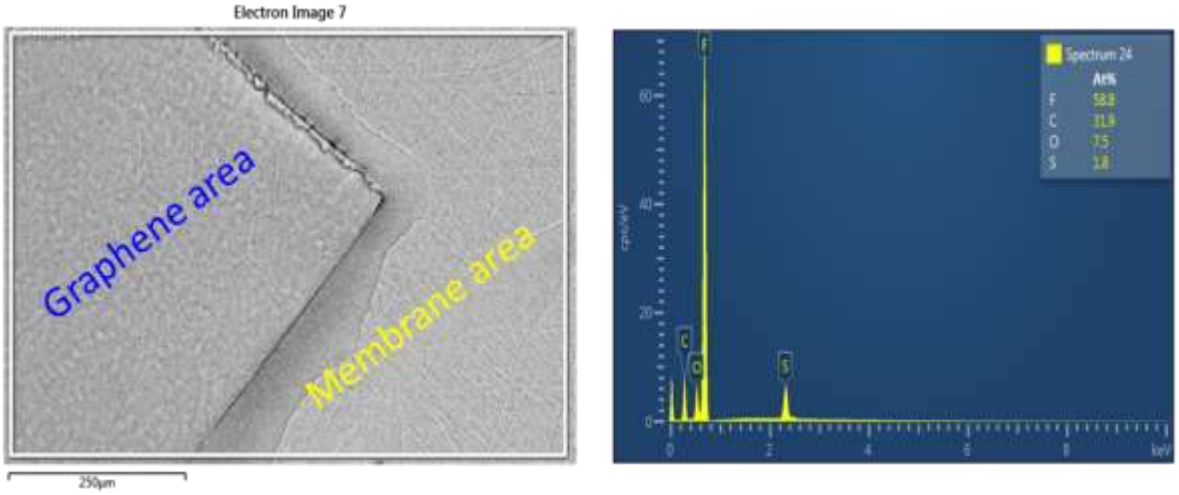


Figure 6.17. SEM and EDS spectra of tri-layer graphene on Nafion® membrane

Also Figures 6.16 and 6.17 are SEM and EDS spectra for bi- and tri-layer graphene on Nafion® membrane. For comparison SEM and EDS analyses on just Nafion® membrane were also conducted as shown in Figure 6.18. The samples were prepared by

hot pressing layer(s) of graphene onto Nafion® membrane. The graphene layer was placed on the Nafion® membrane to cover only a portion of the Nafion® membrane. The

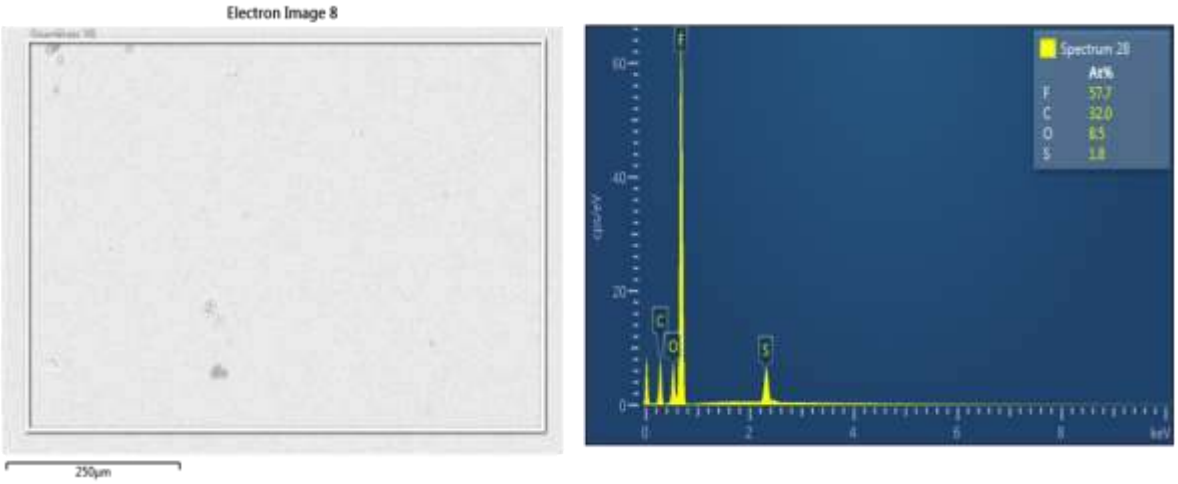


Figure 6.18. SEM and EDS spectra of Nafion®-211 membrane

SEM images clearly show the portion of the membrane that was covered and the portion that was not. Although, the SEM images of graphene on Nafion® membrane provide no useful information on the defect structure in the CVD graphene, it thus clearly indicates absence of impurities especially, from Cu substrate that was etched away from graphene.

Elemental composition analyses were also conducted on the same surface to examine the presence of any impurities that could arise as a result of etching of underlying copper. The results were compared to that obtained from Nafion® membrane without the graphene. The EDS data show no presence of any impurities which strongly suggest high efficient graphene transfer; particularly no residual copper was detected.

6.2.6 X-ray Photoelectron Spectroscopy of Graphene on Nafion® Membrane.

The basic fundamentals of XPS have been discussed in Chapter 5 (Section 5.2.4). The XPS technique was used in that section to show the effect of single-layer graphene on Nafion® membrane on the photoelectrons attenuation from the sample elements and to confirm the presence of graphene on Nafion® membrane. It was clearly shown how single-layer graphene affected the elemental composition of Nafion® membrane most especially being able to accurately differentiate adventitious carbon from graphene to the carbon bonded to fluorine atoms ($CF_2$ or $CF_3$ group).

In this section, the XPS imaging technique was extended to probe the transfer of single-, bi-, and tri-layer graphene on Nafion® membrane with a focus on the C1s signal transferred from graphene layer(s) to the Nafion® membrane. This technique is a complementary tool to traditional Raman spectroscopy, which is mostly ideal to undoubtedly probe the graphene layers and thicknesses. Figure 6.19 shows the optical micrograph of single-layer graphene on Nafion®-211 membrane. The sample was prepared in such a way that graphene layer covers a portion of the Nafion® membrane; so that XPS spot analysis can be performed on the same sample so as to simultaneously see the effect of graphene on the region that has graphene on it and the one without. This was true for the other similar samples studied (bi- and tri layer graphene).

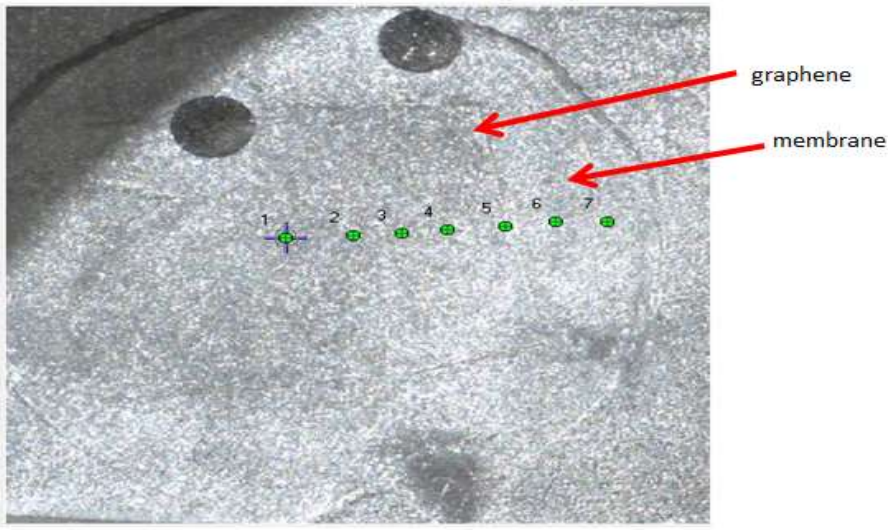


Figure 6.19. Optical micrograph of single-layer graphene on Nafion® membrane taken on the XPS spectrometer.

Figure 6.19 shows clearly region of the membrane that was covered with graphene. The spots indicated with the numbers (1-7) are the areas that were analyzed which consist a portion of graphene and a portion of membrane. Figures 6.20A and 6.20B present the representative XPS survey and C1s spectra on spot 1 (graphene region). Similarly, Figures 6.21A and 6.21B show the representative XPS survey and C1s spectra on spot 7 (membrane region) outside graphene region but still on the same sample. Both the survey spectra show the expected elements in Nafion® membrane (C, F, O, and S).

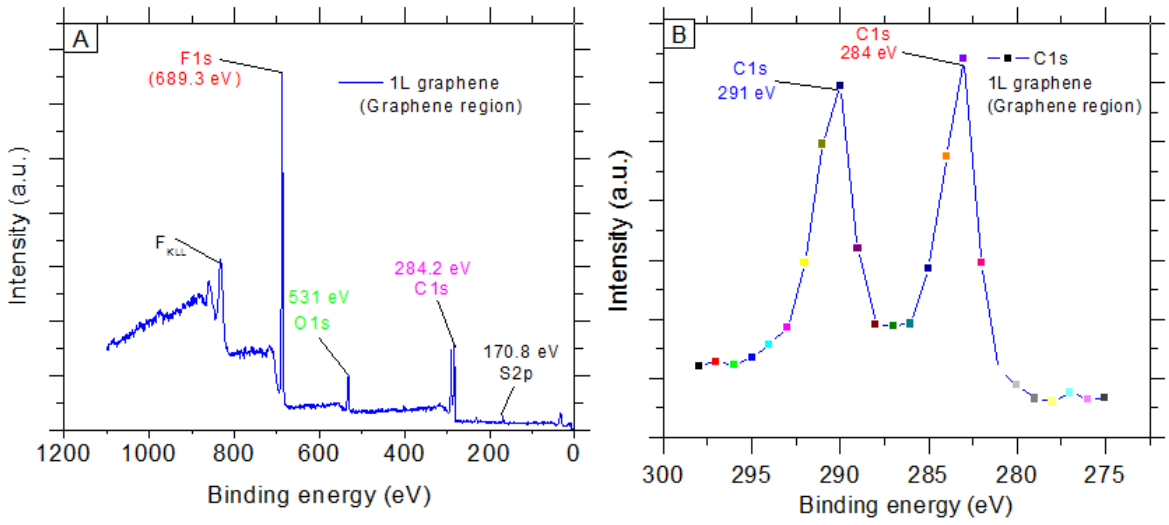


Figure 6.20. XPS spectra of single-layer graphene on Nafion® membrane (A) survey and (B) C1s spectra within the graphene region.

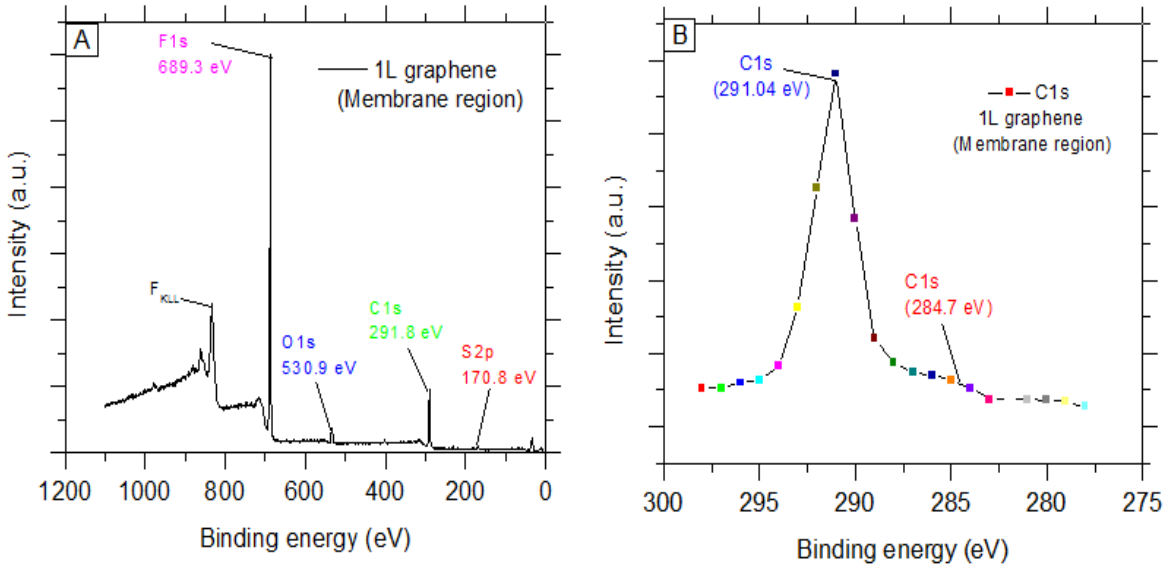


Figure 6.21. XPS spectra of single-layer graphene on Nafion® membrane: (A) survey and (B) C1s spectra on membrane region outside the graphene location.

From Figures 6.20 and 6.21, there are two important obvious C1s peaks. The first peak of C1s appears at high BE around 291 eV and the low BE C1s peak at 284.5 eV. The high BE carbon peak is associated with the carbon bonded to fluorine atom (either $CF_2$ or $CF_3$ group) of the Nafion® membrane and the low BE carbon peak is due to adventitious carbon (usually from hydrocarbon). But we are certain this is from graphene carbon because our previous work has shown no traces of hydrocarbon on Nafion® membrane following transfer of graphene with sample characterization using confocal Raman microscopy (see discussion in Chapter 3 and 5). Figures from 6.20B and 6.21B present some useful and interesting data. With close examination of the C1s peaks, it is obvious how the dominant carbon peak of high BE (Figure 6.21B) was attenuated when a single-layer graphene was added to the sample. This brought about a little more intensity of C1s low BE than high BE peak. This is no doubt due to the addition of graphene layer.

Similarly bi-layer graphene on Nafion® membrane was also analyzed. Figure 6.22 presents the optical micrograph of bi-layer graphene on Nafion®-211 membrane. Just like

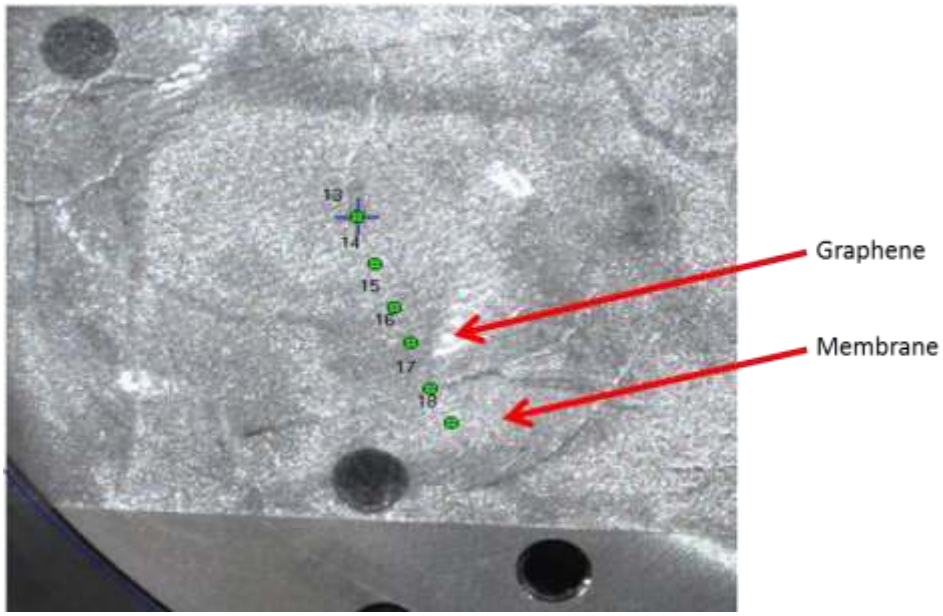


Figure 6.22. Optical micrograph of bi-layer graphene on Nafion® membrane taken on the XPS spectrometer.

the single-layer graphene, the region of graphene can be easily distinguished from the region without graphene. Figures 6.23A and 6.23B present the representative XPS survey and C1s spectra on spot 13 (graphene region). Similarly, Figures 6.24A and 6.24B show the representative XPS survey and C1s spectra on spot 18 (membrane region) outside graphene region but still within the same sample. The XPS surveys (Figures 6.23A and 6.24A) for bi-layer graphene sample on Nafion® membrane again show the expected elements on Nafion® membrane just like the single-layer graphene.

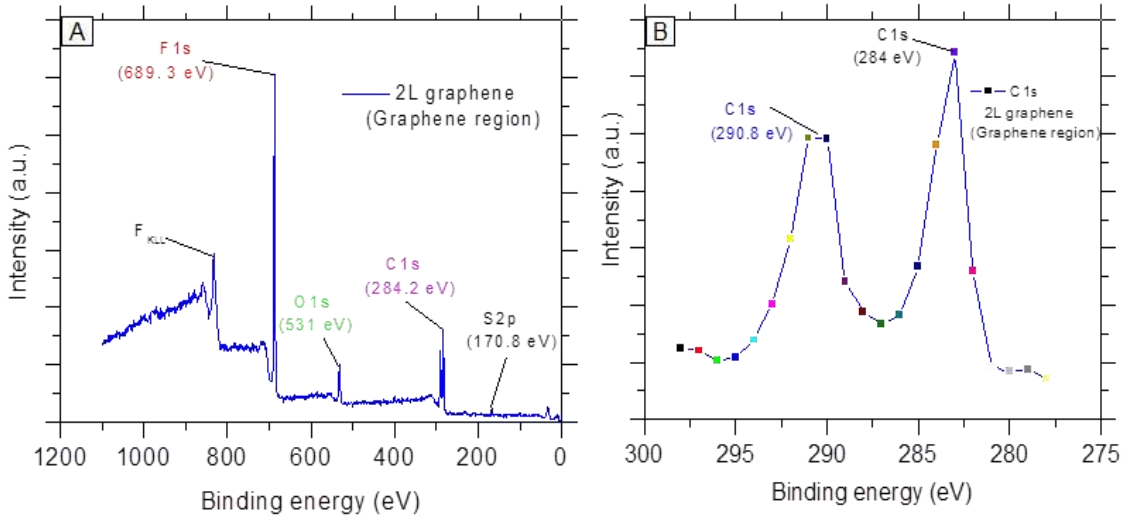


Figure 6.23. XPS spectra of bi-layer graphene on Nafion® membrane: (A) survey and (B) C1s spectra within the graphene region.

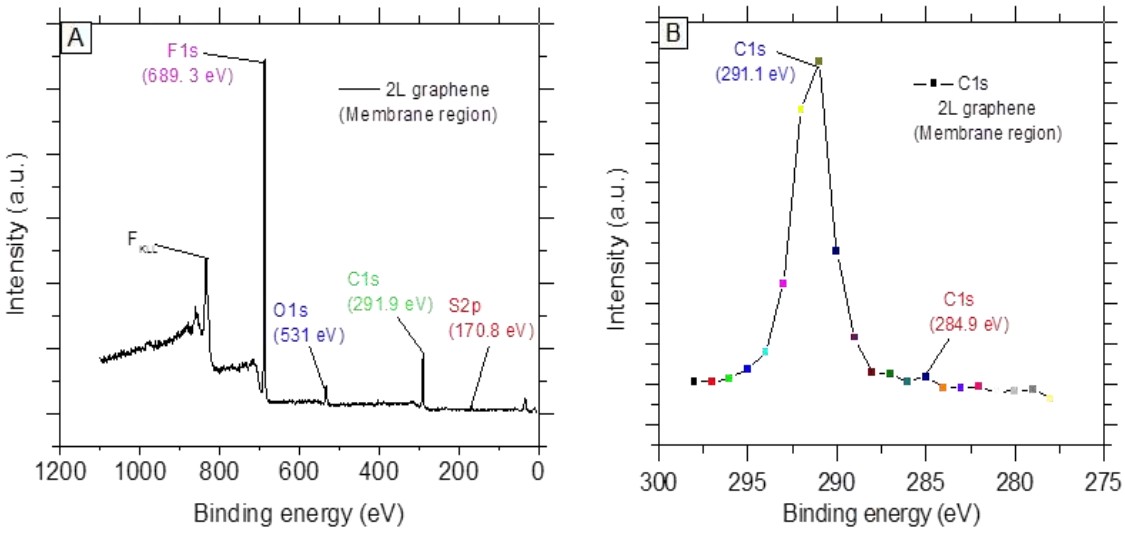


Figure 6.24 XPS spectra of bi-layer graphene on Nafion® membrane (A) survey and (B) C1s spectra on membrane region outside the graphene location.

Again, the high BE of C1s peak of Nafion® membrane was much attenuated with the addition of bi-layer graphene. This is similar to what we have seen in the case of single-layer graphene. The striking observation from the XPS spectra of single- and bi-layer graphene is the fact that the low BE C1s peak due to graphene from bi-layer graphene is more as compare to that of single-layer which means more carbon photoelectrons from bi-layer graphene carbon. A more detailed quantitative analysis will be done later in the text.

Finally, tri-layer graphene on Nafion® membrane was also examined. Figure 6.25 presents optical micrograph of triple-layer graphene on Nafion®-211 membrane.

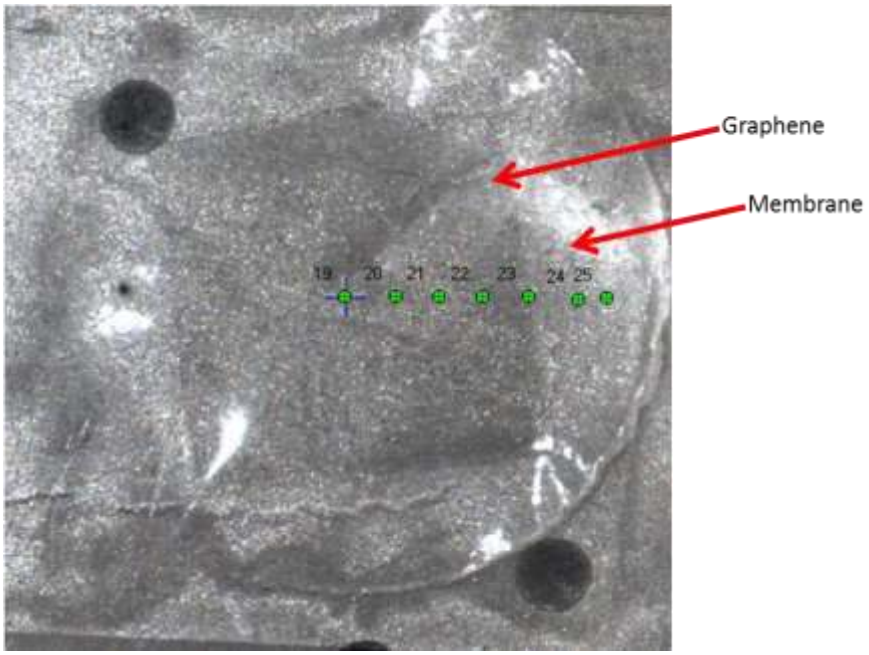


Figure 6.25 Optical micrograph of tri-layer graphene on Nafion® membrane taken on the XPS spectrometer.

Figures 6.26A and 6.26B present the representative XPS survey and C1s spectra on spot 19 (graphene region). Similarly, Figures 6.27A and 6.27B show the representative XPS survey and C1s spectra on spot 25 (membrane region) outside graphene region. The XPS surveys in both Figures again also confirm the expected elements in Nafion® membrane.

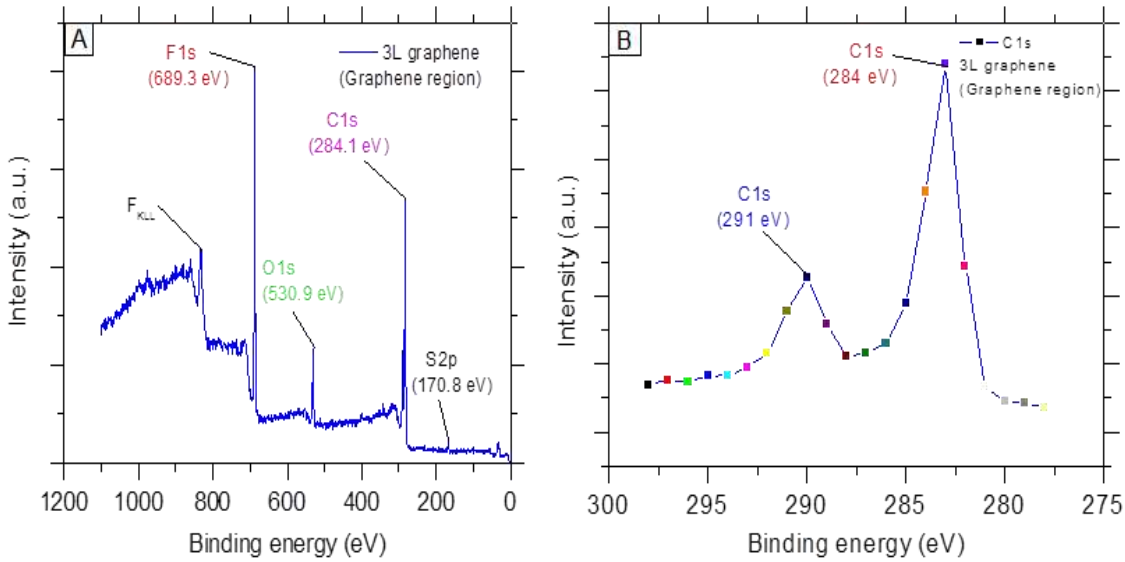


Figure 6.26. XPS spectra of bi-layer graphene on Nafion® membrane (A) survey and (B) C1s spectra within the graphene region.

When XPS C1s spectra of the Figure 6.26B (graphene region) and that of the Figure 6.27B (membrane region outside graphene area) are compared, it is interesting to see the effect of triple-layer graphene on Nafion® membrane high BE C1s peak. This observation is similar to that of single-layer and bi-layer graphene on Nafion® membrane high BE

C1s peak. However, the attenuation was much greater than that of both the single-layer graphene and bi-layer graphene.

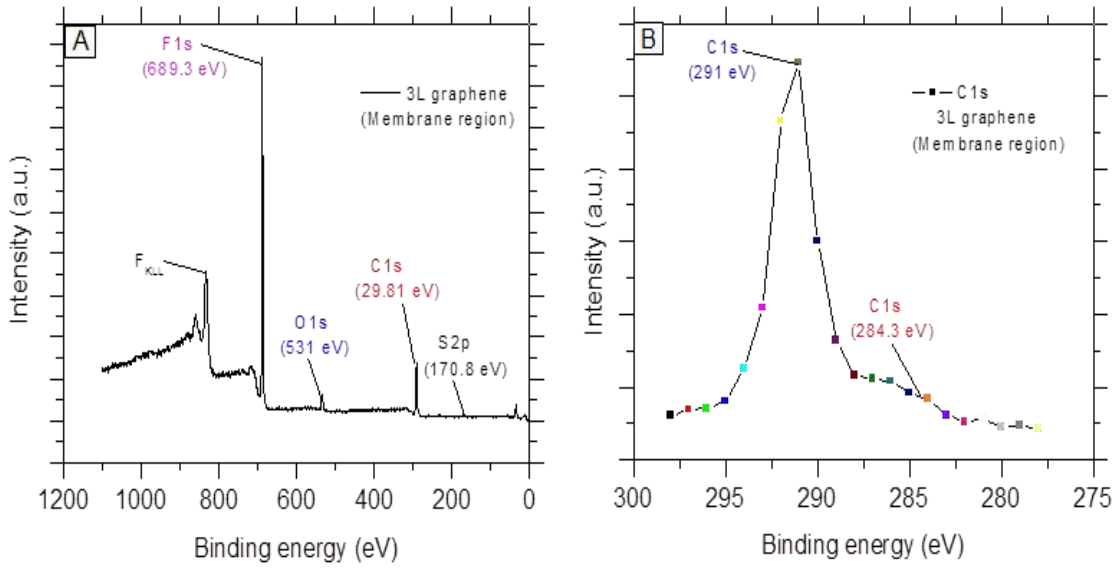


Figure 6.27. XPS spectra of tri-layer graphene on Nafion® membrane: (A) survey and (B) C1s spectra on membrane region outside the graphene location.

It is instructive to consider the quantitative data from all these spectra so as to compare their relative intensities of the sample with and without graphene. Table 6.3 presents the XPs peak intensities of C1s from graphene samples (single-, bi- and tri-layer graphene). The table includes additional spots analyzed aside from those represented in all the spectra above. As earlier noted, the focus was on C1s in order to see the effect of graphene carbon peak intensity over the carbon peak intensity of Nafion® membrane. From Table 6.3, it is obvious that the peak intensities on different spots of the same

sample for C1s regardless of whether it is in the graphene region or membrane area are quite similar. For example, the peak intensities of C1s for the single-layer graphene in the graphene region are somewhat similar. This is true for all the other graphene layers. It can be inferred that the carbon distribution from the graphene is uniform over the Nafion® membrane surface though further analysis might be needed to unequivocally establish this claim.

Table 6.3 XPS peak intensities of C1s from Nafion®/graphene samples showing effect of graphene layers

| | Single-layer graphene | | Bi-layer graphene | | Triple-layer graphene | |
|---|---|---|---|---|---|---|
| | Spot-1 (2) | Spot-7 (6) | Spot-13 (15) | Spot 18 | Spot 19 | Spot 25 (24) |
| | Graphene region | membrane region | Graphene region | membrane region | Graphene region | membrane region |
| Element | XPS Peak Intensity | XPS Peak Intensity | XPS Peak Intensity | XPS Peak Intensity | XPS Peak Intensity | XPS Peak Intensity |
| Carbon, high BE (291 eV) | 29,740 (28,700) | 48,140 (42,920) | 24,620 (24,960) | 18,020 | 22,740 (24,180) | 27,300 (34,180) |
| Carbon, low BE (284 eV) | 32,020 (35,840) | 6,380 (6,340) | 32,120 (35,140) | 2,380 | 54,000 (56,460) | 5,380 (4,460) |

It is clear from the Table 6.3 that the graphene layers did in fact increase the intensity of low BE C1s peak and attenuation of high BE C1s peak. To see the effect of graphene layers one may need to consider the relative intensities ratio between the low BE peak and that of high BE peak. The intensities of the peaks may seem for single-layer and bi-layer but the relative intensity of the peak shows clearly the effect of graphene layer. For example, in the graphene region, the ratio of low BE peak (at 284 eV) to high BE peak (at 291 eV) for single-, bi- and tri-layer graphene are (1.1-1.2), (1.3-1.4), and (2.3-2.4), respectively. The increase in the relative intensity clearly indicates addition of carbon atoms from the graphene layers. Thus, the XPS data provide valuable information

on how graphene layers transferred onto Nafion® membrane can be easily distinguished based on photoelectron intensity.

## 6.3 CONCLUSIONS

In summary, proton / deuteron transmission through single- and multi-layer CVD graphene was investigated. While the theory predicted a large energy barrier for proton transmission through single- and multi-layer graphene, non-zero ionic currents were found for proton transmission through bi- and triple-layer graphene. These findings suggest that the CVD graphene is not a perfect barrier that would completely block out any ion transmission through it. Both electrochemical and spectroscopic characterization data are consistent with a defect-based mechanism for proton transmission through bi- and triple-layer graphene. Surprisingly, even in the presence of these rare atomic scale defects, CVD graphene still shows subatomic selectivity between proton and deuteron with selectivity factor of at least 10 for single-layer graphene and 6 for both bi-layer and triple-layer graphene. A Study on graphene placement within an MEA reveals that selectivity between proton and deuteron can be increased by using two or more single-layer graphene within an MEA. It is important that these graphene layers not be in direct contact with each other in order to achieve superior selectivity.

# CHAPTER SEVEN

# ATOMIC LAYER DEPOSITION OF ALUMINA ON GRAPHENE AND RELATED MATERIALS

## 7.0 SYNOPSIS

This Chapter described a study of the effect of alumina treatment on single-layer graphene using atomic layer deposition (ALD) technique for protons and deuterons transmission in electrochemical hydrogen / deuterium pump cells. Some selected cations ($H^+$, $K^+$, and $Cs^+$) were equally studied on the ALD coated samples in liquid electrolytes using a Devanathan-Stachurski cell in a four-electrode configuration. Spectroscopic characterization including X-ray photoelectron spectroscopy and SEM defect visualization studies confirmed a continuous ALD alumina coating on the Nafion® / graphene composite. While the ALD alumina coating completely blocked the permeability of etchant species (ferric ion), it thus has a very minimal effect on the transmission of protons. It also does not completely block transmission of other cations studied in liquid D-S cell. The concluding part of this Chapter discussed the proton transmission through 2D hexagonal boron nitride (hBN) and pyrochlore oxides. A manuscript is under preparation that will soon be submitted on this Chapter.

## 7.1 INTRODUCTION

Atomic layer deposition (ALD) is a versatile technique for a continuous deposition of thin-film materials from the vapor phase.[322–330] First developed in 1977, its industrial evolution began in 1983 for the production of thin-film electroluminescent

(TFEL) displays.[323] It is a self-limiting process, its superiority over chemical vapor deposition (CVD) and physical vapor deposition (PVD) comes from the capability to produce conformal films with uniform thickness control at the atom-scale level.[324] It has found application in the manufacture of semiconductors,[328] micro-electro-mechanical systems (MEMS), nano-electro-mechanical systems (NEMS), displays, and organic light emitting diode (OLED).[331–333]

Recently, the ALD technique has been used to deposit platinum catalyst on carbon electrode for fuel cell applications.[327] Groner and co-workers[334] used ALD alumina as a barrier for the permeability of oxygen through flexible organic polymer substrate for OLED application. Toikkanen et al.[335] demonstrated the suitability of PFSA ionomer membrane for ALD alumina coating. The resulting alumina on Nafion® membrane was shown to decrease the permeability of $O_2$ by 10.0% and methanol by 30-50% through the Nafion® membrane. In a similar approach, Wang and co-workers explored a coating of ALD alumina on defect-free pristine graphene.[336] No evidence of coating was seen on the surface of pristine graphene by monitoring the growth of alumina using atomic force microscopy (AFM). This is because, ALD coating requires a chemisorption or reaction of precursor with the surface functional groups. Such surface functional groups are absent in pristine graphene and thus no ALD coating was observed. However, there were evidences of ALD coatings on the edges of graphene sheets which suggests existence of dangling bond (defect site) and also on the defect site on graphene surface.

The fundamental requirements for ALD technique are: (1) a vacuum chamber, (2) valves for alternating reactive precursor, and (3) at least two reactive precursors.[324] It is important that these reactive precursors not be present at the same time in the vacuum chamber. Also, they must also have good thermal stability at the growth temperature with high vapor pressure. They may be gases, volatile liquid, or solids. The basic processes involved in ALD technology can be summarized below:

(1) A reactive substrate in a vacuum chamber is exposed to the first gaseous precursor pulse.

(2) Chemical reaction between the substrate and the first precursor by chemisorption.

(3) Inert gas purge to ensure monolayer coating of the first reactive precursor on the substrate.

(4) Exposure of the second gaseous precursor followed by a chemical reaction that produces thin film of subnanometer or few nanometers in thickness.

(5) Final inert gas purge to remove unreactive precursors or by-products of reaction.

We elected to use ALD technique to coat the graphene layer transferred onto Nafion® membrane and also on as-purchased CVD graphene on Cu substrate. We anticipated such conformal growth of ALD alumina will selectively seal the defect sites in the CVD graphene. Such treatment should allow proton transmission but prevent other species from permeating through the ALD alumina coated samples. All the ALD alumina coating experiments on our graphene / Nafion® samples were conducted using the ALD equipment at Argonne National Laboratory (ANL) by Dr. Alex Martinson and Dr. Cao Duyen. Single-layer graphene was transferred onto Nafion®-211 membrane following

similar procedures that were previously described in the previous Chapters. Following the ALD alumina coating, hydrogen evolving platinum catalysts were applied at both the anode and cathode to make the MEAs. The MEAs were tested using PEM-based electrochemical hydrogen pump cells in an asymmetric mode to study the proton transmission through graphene with and without ALD alumina coating.

Similar to the hydrogen pump experiments, ALD coated Nafion® / graphene were equally prepared without electrodes and were tested in aqueous electrolytes for proton and other cations transmission through graphene with and without ALD alumina coating.

## 7.2 EXPERIMENTAL

### 7.2.1 Sample Preparation and MEA making

Polyethylene terephthalate (PET) was used as a template support to hold the Nafion®/ graphene sample. First, single-layer graphene was transferred onto Nafion® membrane using the hot press technique with the aid of fiberglass support. The procedures for transferring graphene onto membrane had been discussed in details in the previous Chapters. Figure 7.1 presents the stages of the fabrication processes. Figure 7.1A consists of the Nafion® disk with CVD graphene on Cu that has been hot pressed together with the fiberglass. Figure 7.1B shows the second round of hot press step. After the etching of underlying Cu substrate and successful transfer of graphene layer onto Nafion® membrane, the single-layer graphene on membrane was sandwiched between two disks of PET as shown in the Figure 7.1B. The Nafion® membrane disk has 3/4 inch diameter and the PET was also 3/4 inch diameter. The uppermost PET was used as a

spacer with a hole of 5/8 inch diameter (the area of graphene on Nafion® membrane exposed to ALD coating).

Figure 7.1C presents the PET | Nafion®-graphene | PET sandwich structure that has been subjected to ALD alumina coating with occasional change in appearance. The color change may reflect the ALD growth temperature (125 $^{o}$C) effect on PET and Nafion® membrane. Figure 7.1D shows the MEA fabricated from the ALD coated sample. The ALD coated region is obvious and visible to the eye. For the D-S cell experiment in aqueous electrolytes, similar template was used as described above with a little modification. The membranes were first converted to their respective cationic forms and also the size of the membrane disk was one-inch diameter which is the size required for

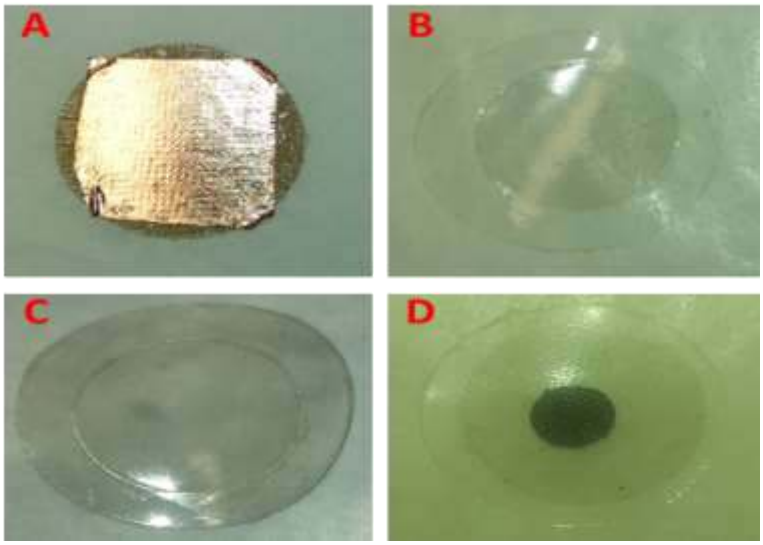


Figure 7.1. Photographs of Nafion® / graphene MEAs subjected to ALD alumina treatment at various stages.

the D-S liquid cell experiment. The center hole for ALD alumina treatment was also 5/8 inch diameter. Nafion® | graphene-ALD alumina | Nafion® composite structures were prepared for D-S cell without the application of electrodes.

7.2.2 ALD alumina coating

The coating of ALD alumina on Nafion® / graphene samples was conducted (at Argonne National Lab equipment by Dr. Cao Duyen and Dr. Alex Martinson) in a ALD vacuum chamber using trimethylaluminum (TMA) and water (steam). The ALD growth temperature was 125 $^{o}$C. The stages of coating a film of alumina are represented in the Scheme 7.1. The rectangular shape with the wavy bond attached to the sulfonic acid group represents the Nafion® structure on which single-layer graphene was attached.

Four stages are involved. The first stage (step A, Scheme 7.1) was the exposure of TMA precursor to the vacuum chamber. Aluminum was able to adsorb onto the surface of Nafion®/graphene by chemisorption with the sulfonic acid group of the Nafion membrane which are exposed as a result of defect sites on graphene layer. The second stage (step B) represents the purging of the chamber with the inert gas (usually $N_2$ or Ar) to remove the by-product (*i.e.* $CH_4$ gas). The third stage (step C) involves the exposure of the second precursor (steam). Water molecules react with the aluminum to form aluminum oxides with surface terminated hydroxyl group, which can be removed by further heat treatment.

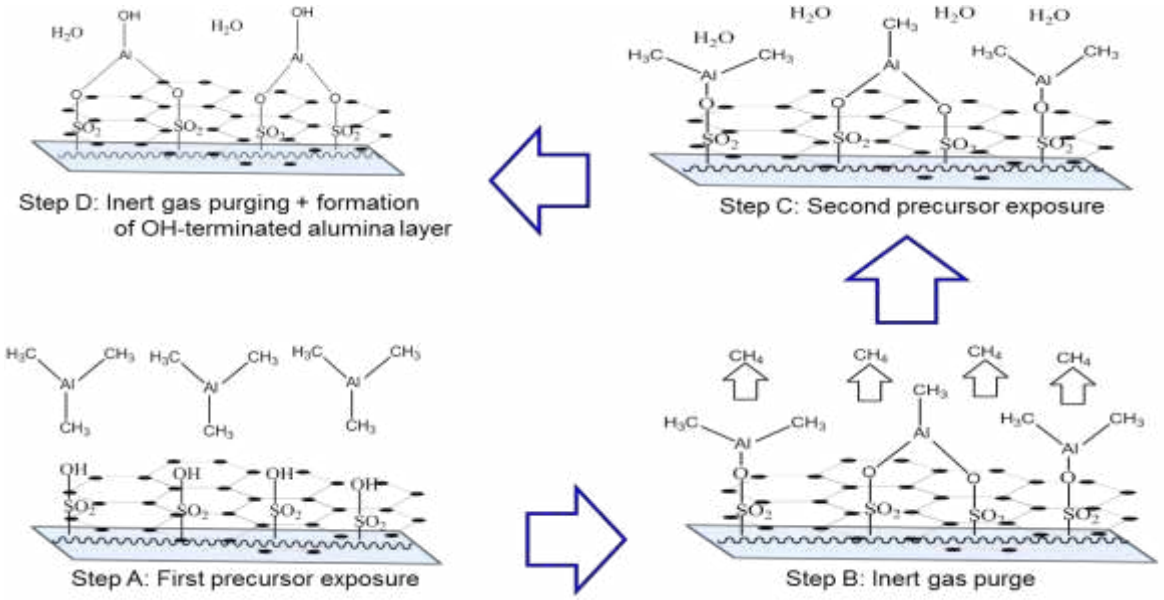


Scheme 7.1. Schematic representations of stages of ALD alumina coating of Nafion®/graphene sample.

The fourth stage (step D) is the final purging with the inert gas to remove by-products and unreacted species (such as $H_2O$ or $CH_4$). A layer of alumina is formed on the surface of Nafion®/graphene sample. This process is cyclic and several layers of alumina can be formed by repeating the steps from A to D. Fifty cycles of ALD alumina deposited was ≈ ≤ 5.0 nm (this value was provided by Dr. Alex Martinson from ANL).

## 7.3 RESULTS AND DISCUSSION

### 7.3.1 Asymmetric Hydrogen / Deuterium Pump on ALD Samples

The fundamentals of asymmetric hydrogen pump have been discussed in Chapter Three of this dissertation.[16] Here, the hydrogen and deuterium pump experiments were

conducted in PEM cell configurations represented in Figure 7.2 with single-layer graphene without ALD coating and were compared with the graphene with ALD alumina coating. The effect of ALD alumina coating on the proton/deuteron transmission can be determined by comparing the IV-curves.

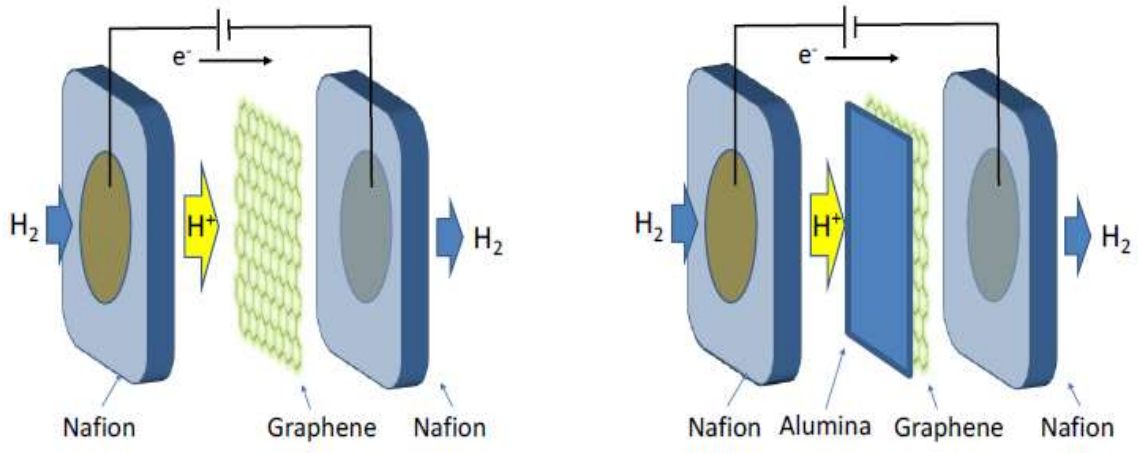


Figure 7.2. Representation of PEM-based cells for hydrogen (or deuterium) pump for studying proton transmission through Nafion® / graphene with and without ALD alumina.

Figure 7.3 presents the I-V curves for the hydrogen evolution reaction through Nafion® / graphene MEAs with and without ALD alumina. Also the I-V curves from deuterium evolution reactions studies are represented in Figure 7.4. It is obvious from the

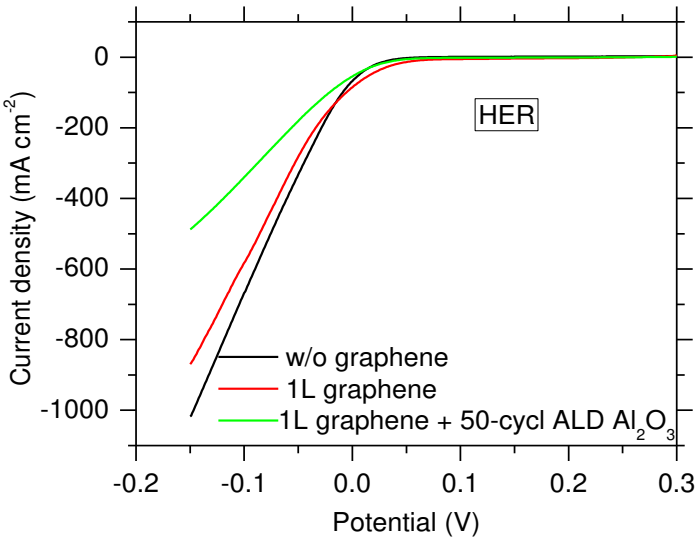


Figure 7.3. I-V curves for HER on Nafion/graphene MEAs with and without ALD alumina coating.

data shown in Figures 7.3 and 7.4 that the ALD alumina coating did not completely block the proton or deuteron transmission through graphene. It does not also show any improved selectivity between proton and deuteron when compared with the Nafion® / graphene samples without ALD alumina coating. The reduction in current responses might reflect an additional resistance from alumina to the ohmic resistance from the Nafion® membrane as a result of the ALD alumina coating. The nature of ALD coating on graphene needs further spectroscopic characterization.

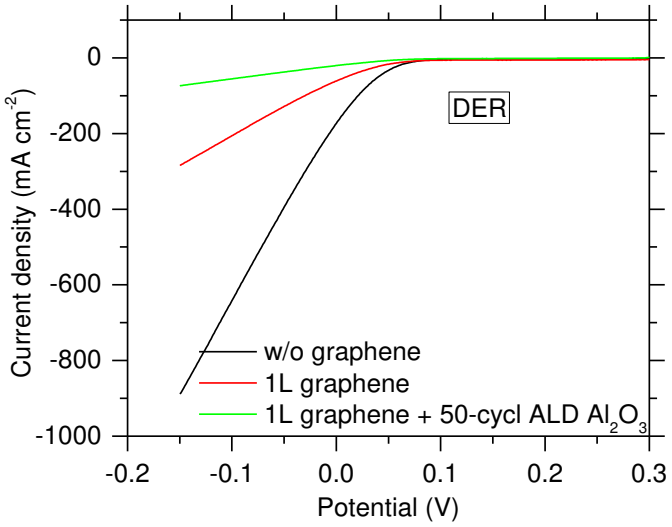


Figure 7.4. I-V curves for DER on Nafion® / graphene MEAs with and without ALD alumina coating.

Figure 7.5 presents the results from the studies on the effect of ALD alumina coating cycles on HER. The I-V responses from the effect of 50 cycles (Figure 7.5A), 5 cycles (Figure 7.5B), and 2 cycles (Figure 7.5C) of ALD alumina were compared to investigate optimum coating of ALD cycles that would result in better selectivity or total blockage of ion transmission. Unexpectedly, the results from Figure 7.5 did not show any discernible effect of ALD cycles. The number of cycle seems not to have significant effect on the HER performance.

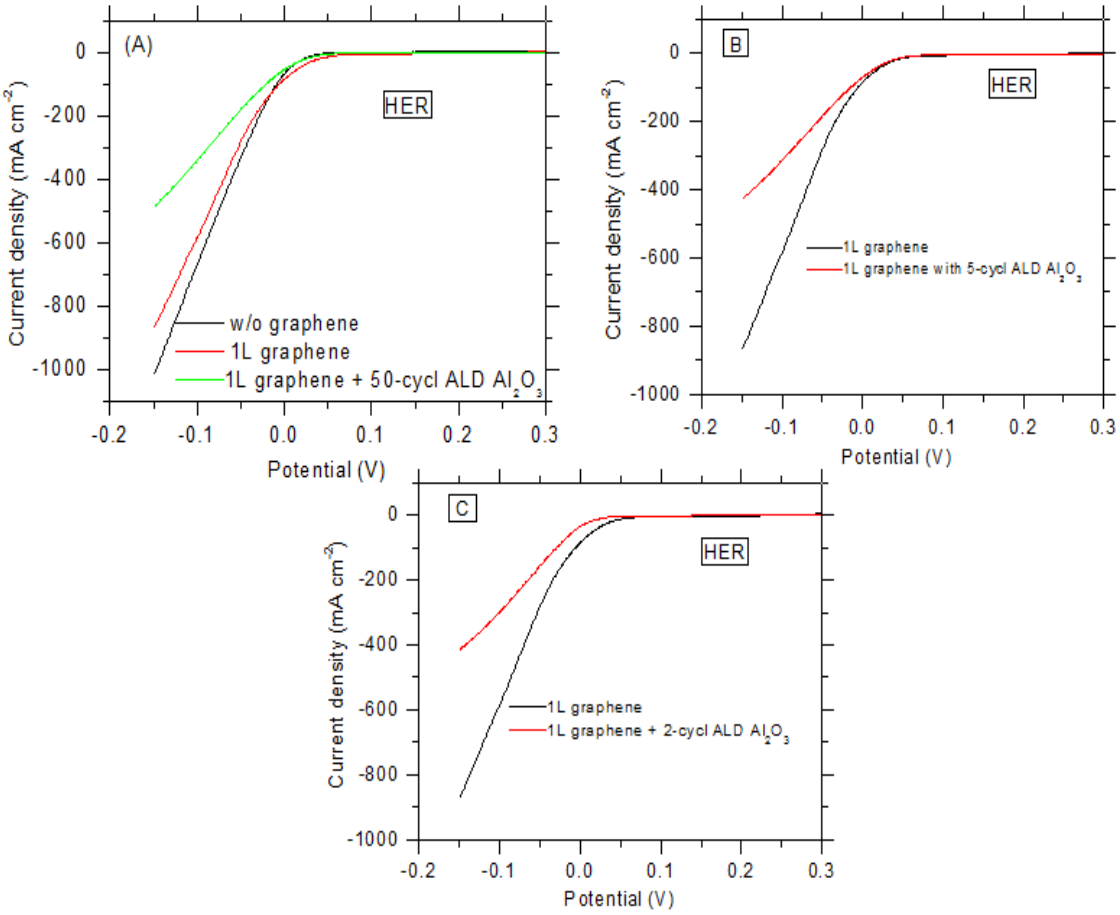


Figure 7.5. I-V curves comparing the effect of ALD alumina cycles on HER

### 7.3.2 Symmetric Hydrogen Pump on ALD Samples

In order to quantify the proton transport rate on Nafion® / graphene samples MEAs with and without ALD coating were prepared in symmetric mode with the geometric area of anode being the same with the cathode. The experimental procedures are the same as previously discussed in the previous chapters. Figure 7.6 presents the I-V curves obtained for electronic resistance (cell without MEA), two Nafion®-211 membranes, two Nafion®-211 membrane with graphene, and two Nafion®-211

membranes with graphene and ALD alumina. As can be seen from the Figure 7.6, the addition of ALD alumina only slightly attenuates proton transmission with a little drop in the absolute current. From the slopes of these curves, the resistance due to proton transmission with graphene / ALD alumina can be obtained.

Table 7.1 presents the resistance values from the I-V curves in Figure 7.6. By subtracting the electronic resistance value and the membrane resistance, one can estimate resistance due to graphene/ALD alumina. The obtained resistance values are normalized with the geometric area of the MEA (0.178 $cm^2$). The graphene areal resistance / conductance with the addition of ALD alumina caused a drop in value of less than a half. This is similar to what we observed in HER in asymmetric hydrogen pump experiment.

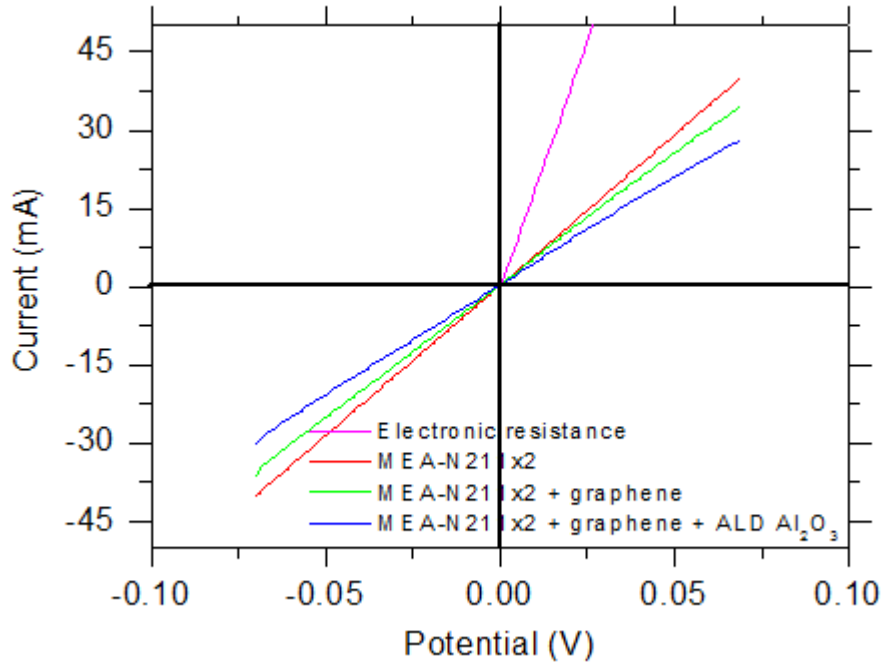


Figure 7.6. I-V curves for symmetric H-pump for Nafion® / graphene with and without ALD alumina

Table 7.1

| Areal resistances and conductances for proton transmission through graphene with and without ALD $Al_2O_3$ | | | | | |
|---|---|---|---|---|---|
| Sample | Resistance,R | Corrected R | MEA areal R | Graphene areal R | Graphene areal G |
| | Ω | Ω | $m\Omega\,cm^2$ | $m\Omega\,cm^2$ | $S\,cm^{-1}$ |
| Electronic resistance | 0.576 | -- | -- | -- | |
| N211x2 | 1.737 | 1.161 | 206.7 | -- | |
| N211x2 + 1L graphene | 1.971 | 1.395 | 248.3 | 41.6 | 24 |
| N211x2 + 1L graphene +ALD $Al_2O_3$ | 2.395 | 1.819 | 323.8 | 75.5 | 13 |

7.3.3 Aqueous ion transport through Nafion®/graphene with ALD alumina

Figure 7.7 presents both a representation and a photograph of the D-S cell used for cation transport measurement in liquid electrolytes. During the ion transport measurement, ion currents are forced through the membrane containing graphene and ALD alumina by the drive electrodes (Pt wire) and the potential difference induced as a result of the ionic current is monitored between the two luggin reference electrodes.[241]

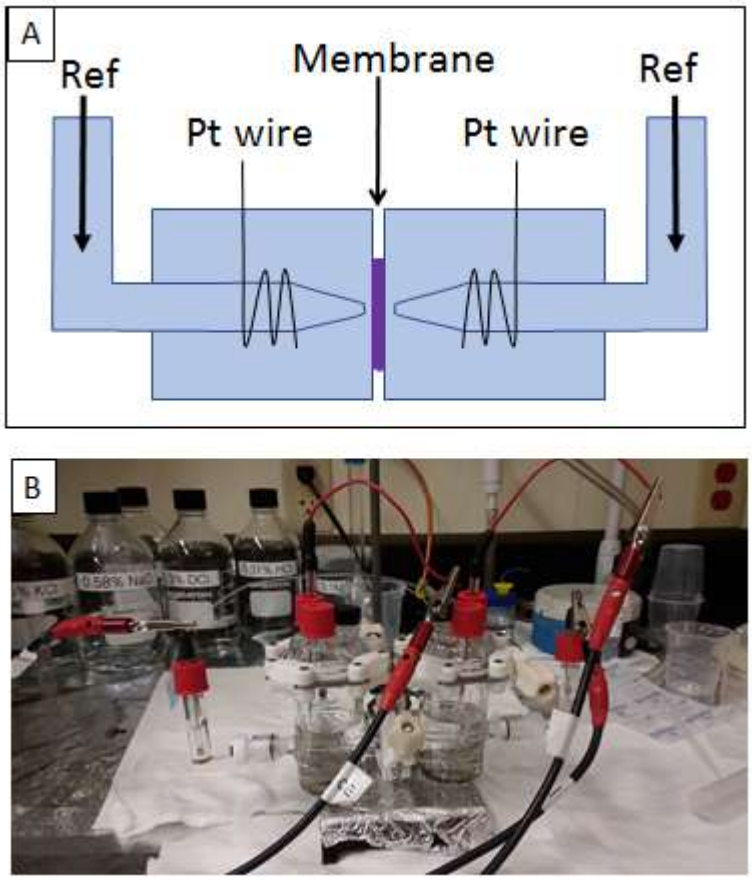


Figure 7.7. (A) Schematic representation and (B) photograph of D-S cell used for cation transport measurment through Nafion®/graphene with ALD alumina.

Figure 7.8 presents the I-V curves from D-S cell measurements in four-electrode configuration. Selected cations investigated are proton (Figure 7.8A), potassium ion (Figure 7.8B), and cesium ion (Figure 7.8C). It is evident that proton transmission occurs at a high rate with little attenuation from the ALD alumina coating, which is consistent with the previous observation in the symmetric H-pump cell. Transmission of other cations ($K^+$ and $Cs^+$) were greatly attenuated but not completely shut down by the ALD

alumina coating. The inverse of the slopes from these curves give resistance values for ion transmission, and the results are represented in Table 7.2.

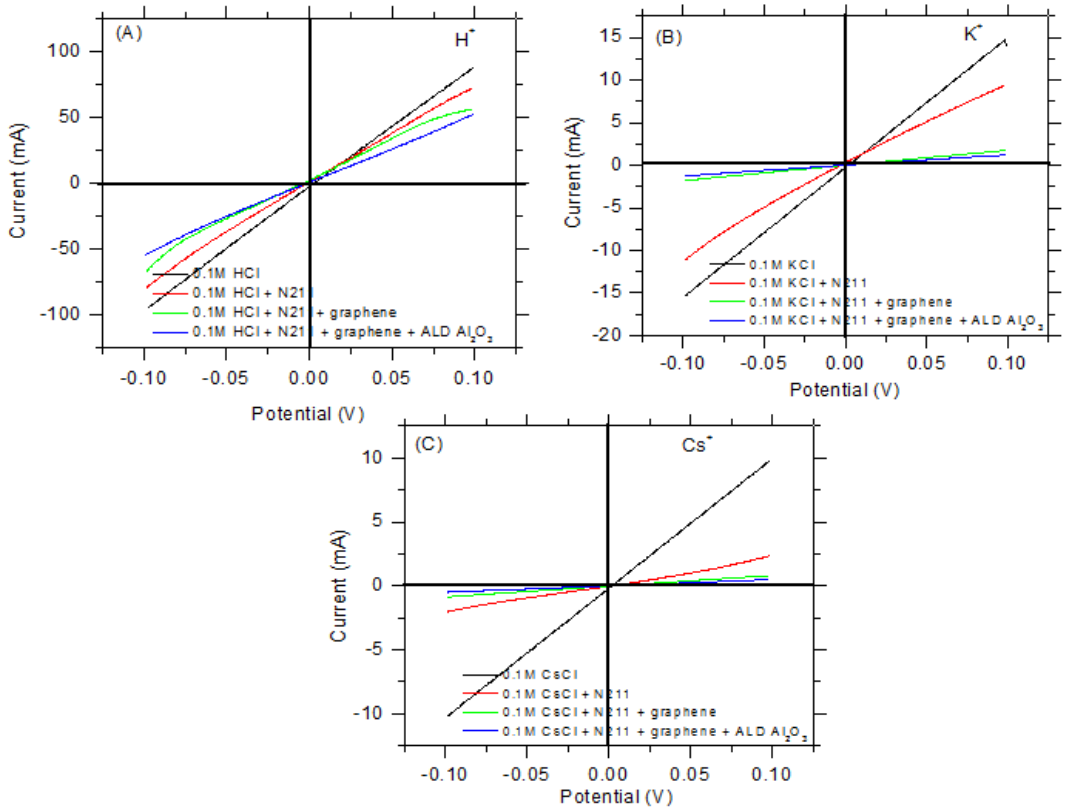


Figure 7.8. I-V curves for aqueous ion transport in D-S cell for Nafion®/graphene ALD alumina: (A) $H^+$, (B) $K^+$, and (C) $Cs^+$

As is evident from Table 7.2 the ALD alumina coating on Nafion®/ graphene samples did not show any noticeable additional selectivity as regards the ionic size of the cations studied. It only increased the resistance to ion transmission with no selectivity. For example, in Table 7.2, the graphene areal resistances with and without ALD alumina only increased from 0.6 to 1 $\Omega cm^2$ for proton. Similar effect is seen for $K^+$ and $Cs^+$. Thus,

| Table 7.2 Graphene areal resistances with ALD alumina for aqueous ion transport in D-S cell | | | | |
|---|---|---|---|---|
| Cations | Resistance (solution) (Ω) | Resistance (soln+ N211) (Ω) | Resistance (soln + N211 + graphene) (Ω) | Resistance (soln + N211 + graphene +ALD $Al_2O_3$ (Ω) |
| $H^+$ | 1.08 | 1.32 | 1.64 | 2 |
| $K^+$ | 6.57 | 9.83 | 56.18 | 81 |
| $Cs^+$ | 9.85 | 48.31 | 119.05 | 200 |
| | | | | |
| | Graphene areal resistanc | Graphene areal resistance + ALD $Al_2O_3$ | | |
| | (Ω cm2) | (Ω cm2) | | |
| $H^+$ | 0.6 | 1 | | |
| $K^+$ | 92 | 141 | | |
| $Cs^+$ | 140 | 300 | | |

the ALD coating is not effective to seal up the defect sites in graphene but rather uniformly contribute to ionic resistance regardless of the ion size.

### 7.3.4 SEM Defect Visualization of ALD modified CVD graphene

It is instructive to examine the nature of the coating of ALD alumina on CVD graphene on Cu substrate using the defect visualization method. Figure 7.9 the SEM images of the etching of CVD graphene on Cu with and without ALD alumina coating. The defect visualization test involves brief exposure of a drop of $FeCl_3$ solution to the surface of graphene on Cu sample with and without ALD alumina. The samples were then rinsed with DI $H_2O$ and examined under SEM microscope.

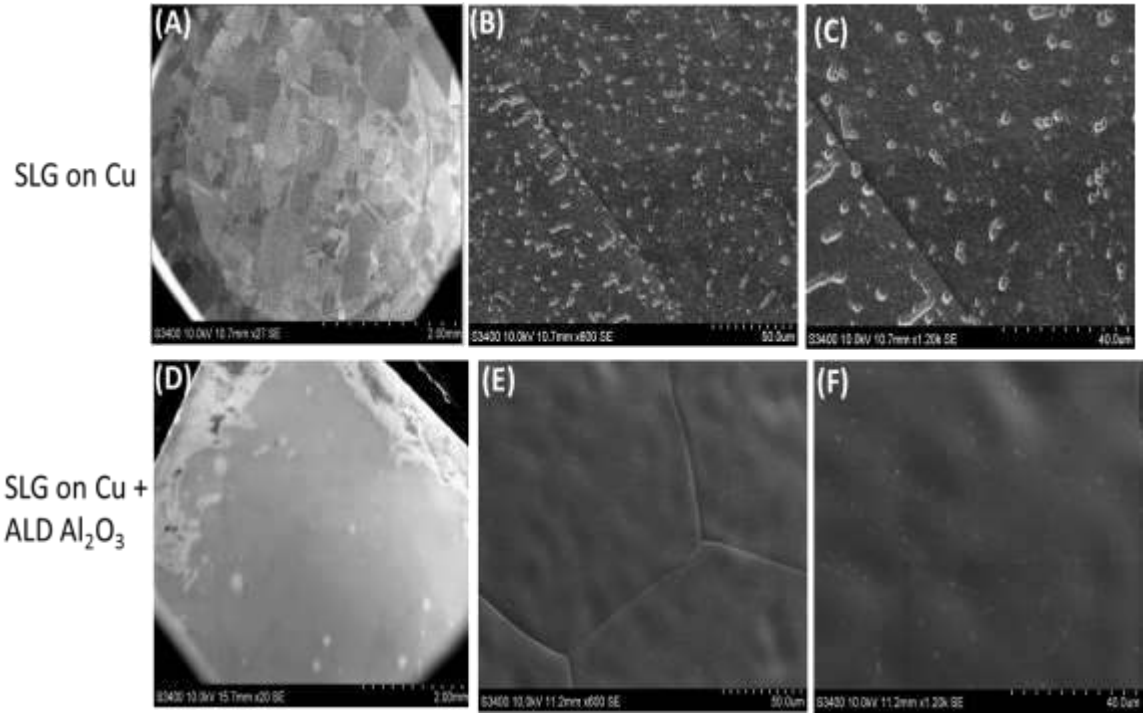


Figure 7.9. SEM images of defect visualization CVD single-layer graphene on Cu with and without ALD alumina coating at 2 mm, 50 μm, and 40 μm scale bars.

Formation of etch pits through the Cu indicate defect sites in the graphene sheet. The defect sites on graphene allow the permeation of ferric ion to attack underlying Cu to form these etch pits. By close inspection of these images, it is clear that the ALD alumina coated samples on graphene completely blocked the ferric ion from attacking the underlying Cu substrate. It is interesting that the formation of etch pits is almost abated on the ALD alumina coated samples.

7.3.5 X-ray Photoelectron Spectroscopy on ALD Modified Samples

XPS experiment was conducted on Nafion® / graphene sample with and without ALD alumina coating to understand the elemental composition and nature of the bonding environment. Fundamentals of the XPS measurement had been discussed in the previous chapter. In order to conceptualize the effect of ALD alumina coating on Nafion®/graphene samples, surveys of Nafion® membrane, Nafion® membrane with graphene, and that of Nafion® with graphene with ALD alumina were compared as presented in the Figure 7.10 survey spectra.

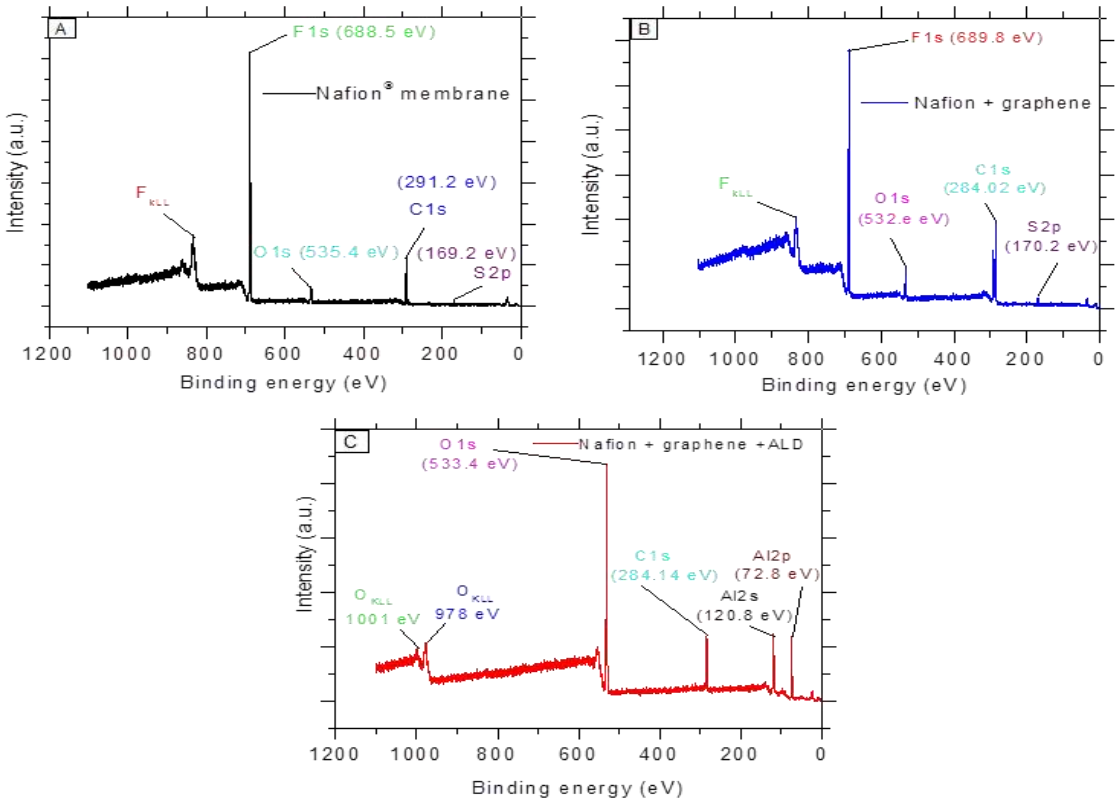


Figure 7.10. XPS survey spectra for (A) Nafion® membrane, (B) Nafion® membrane with graphene, and (C) Nafion® membrane with graphene with ALD alumina

Further analysis of the spectra revealed expected elements for Nafion® membrane (Figure 7.10A) *i.e.* C, F, O, and S. It is important to note that the prominent carbon peak of Nafion® as it can be seen from the BE is at 291 eV. This carbon high BE is associated with the carbon bonded to fluorine atoms as previously noted in the preceding chapter. However, upon addition of single-layer graphene (Figure 7.10B), all the aforementioned elements were still observed but with a little modification to the carbon peak signal. The prominent carbon peak now has changed from 291 eV (high BE) to the 284.5 eV adventitious carbon low BE peak. This low BE energy peak of carbon at 284 eV came from the graphene carbon. This is similar to what was previously observed.

Interestingly, Nafion® / graphene sample with ALD alumina XPS survey spectrum (Figure 7.10C) reveals Al, C, and O peaks. Two important things can be observed from this spectrum. First, there was no fluorine peak which suggests ALD alumina coating is continuous over the entire Nafion® / graphene sample. This observation is in agreement with the SEM defect visualization that shows complete blockage of ferric ion transmission without any noticeable formation of etch-pits. Secondly, again, the prominent carbon peak is adventitious carbon from graphene and no evidence of presence of carbon high BE peak. C1s spectra for Nafion® membrane, Nafion® / graphene and Nafion® / graphene with ALD alumina are presented side by side in the Figure 7.11. The figure clearly shows the effect of addition of single-layer graphene and subsequent treatment with ALD alumina.

XPS experiment was also conducted on CVD graphene on Cu with and without ALD alumina coating to confirm the coating of alumina on graphene. The survey spectra for CVD graphene on Cu and CVD graphene on Cu with ALD alumina are represented in

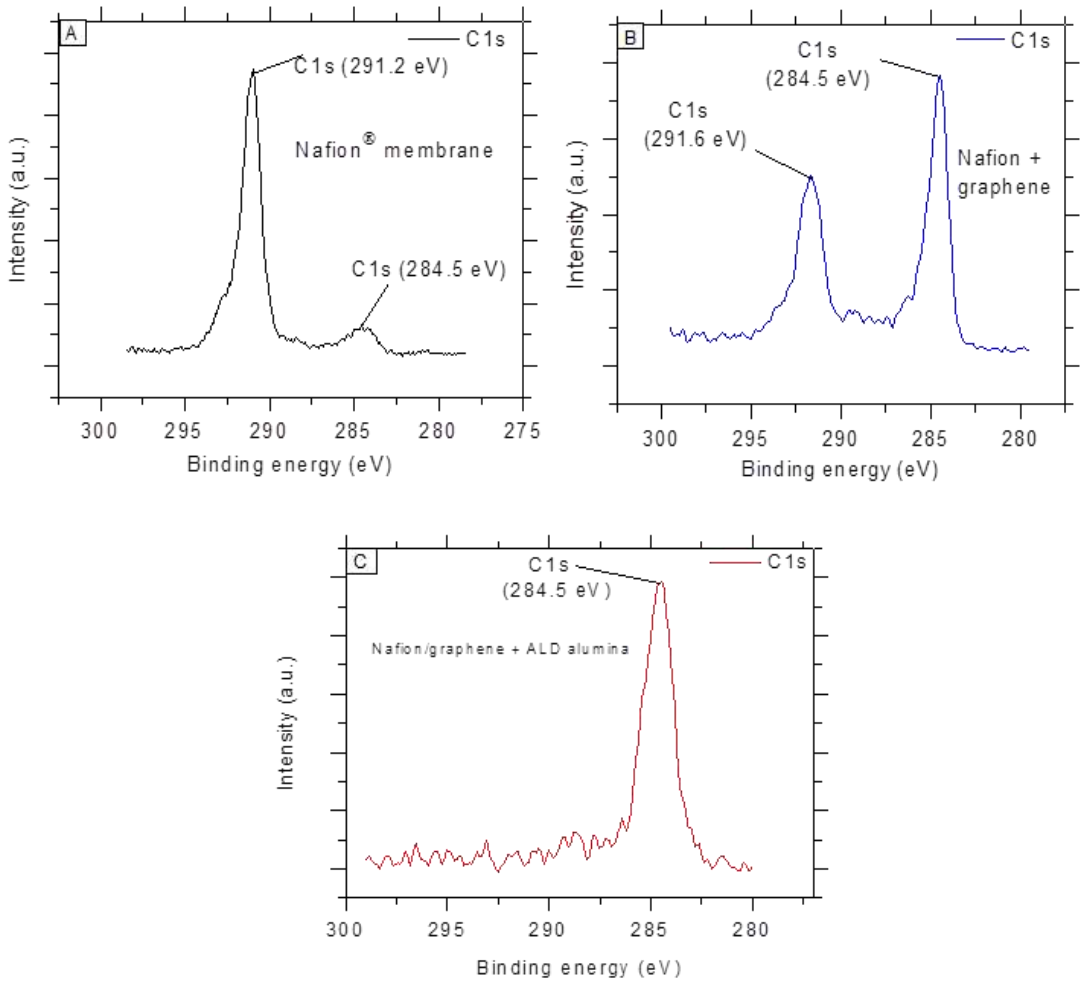


Figure 7.11 XPS C1s spectra for (A) Nafion® membrane, (B) Nafion® / graphene, and (C) Nafion® / graphene with ALD alumina

the Figure 7.12. The XPS survey spectrum (Figure 7.12A) for graphene on Cu without ALD coating shows the expected element Cu and C peaks but also with traces of O1s peak. The oxygen peak might be contamination by exposure to the air or from partially oxidized graphene carbon. Interestingly, the XPS survey spectrum (Figure 7.12B) for graphene on Cu with ALD alumina coating did not show any evidence of Cu peak and also has some pronounced oxygen peaks. These oxygen peaks must be from alumina. The fact that photoelectron of Cu was completely attenuated indicates the ALD alumina coating is uniform and continuous over the entire surface. Thus, the ALD alumina coating did not produce a selective coating only on the defect sites of the graphene sheet. This is in contrast to the conventional wisdom that ALD alumina only grows on a defect site and not on the pristine graphene.

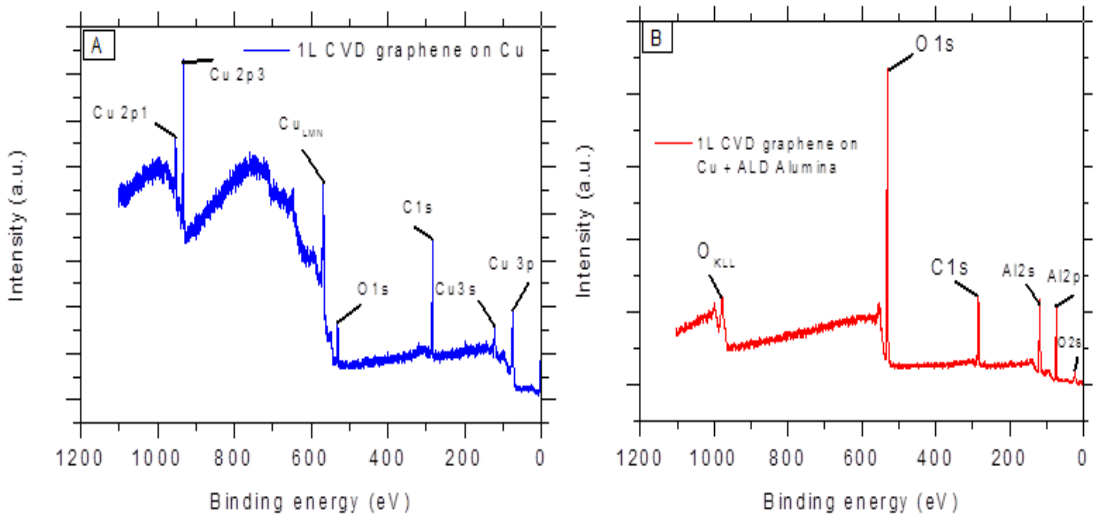


Figure 7.12. XPS survey spectra for CVD single-layer graphene on Cu (A) without ALD alumina coating and (B) with ALD alumina coating

7.4 Hexagonal Boron Nitride (hBN)

Besides graphene, a related 2D-material that has attracted research attention is the hexagonal boron nitride. Monolayer hBN shares unique properties with graphene such as its thermal proton conductivity at ambient temperature and stability, and mechanical strength.[337–344] Boron-nitride bond is polarized with lower energy barrier (0.68-1.02 eV) predicted by computational studies for room temperature proton conductivity as compared to 2D graphene (1.2-2.2 eV). Scheme 7.2 depicts the structural representations of graphene and hBN and their bond lengths.[345] These materials are known to be insulators, but surprisingly, recent research findings including this dissertation work have shown their selective proton conductivity with subatomic selectivity.[16, 24]

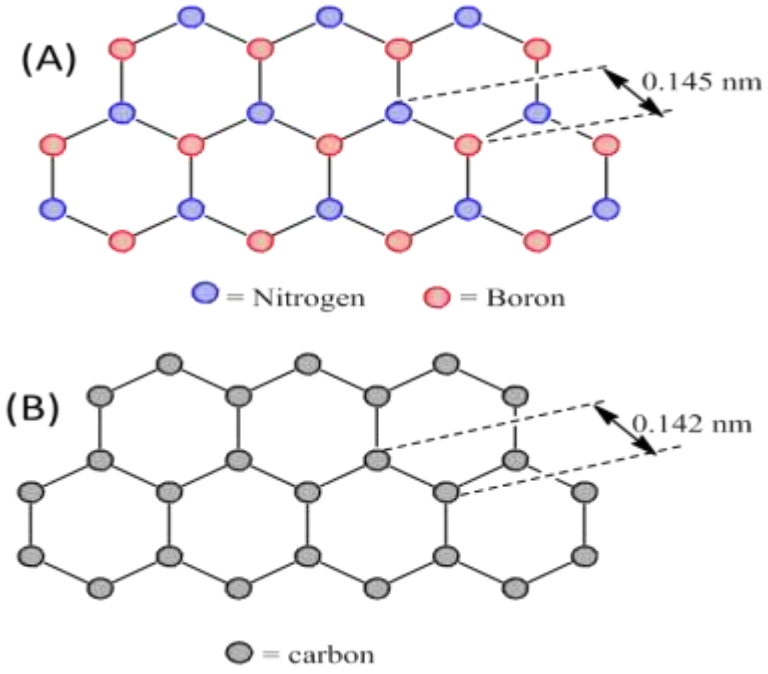


Scheme 7.2 Structural representations of graphene and hBN with their bond lengths

Like single-layer graphene, monolayer hexagonal boron nitride was obtained as CVD hBN from a commercial source (ACS Materials, LLC). Following the transfer

technique protocol previously described for graphene, hBN was transferred onto Nafion®-211 membrane, and its proton / deuteron conductivity was investigated using the electrochemical hydrogen / deuterium pump in an asymmetric mode.

7.4.1 Asymmetric H / D pump in hBN

Figures 7.13 and 7.14 present the hydrogen evolution and deuterium evolution reaction polarization curves for single-layer hBN. The results were compared to that of single-layer graphene in each case. From the two I-V curves, the effect of hBN and graphene seems similar with almost the same effect on selectivity between the proton and deuteron.

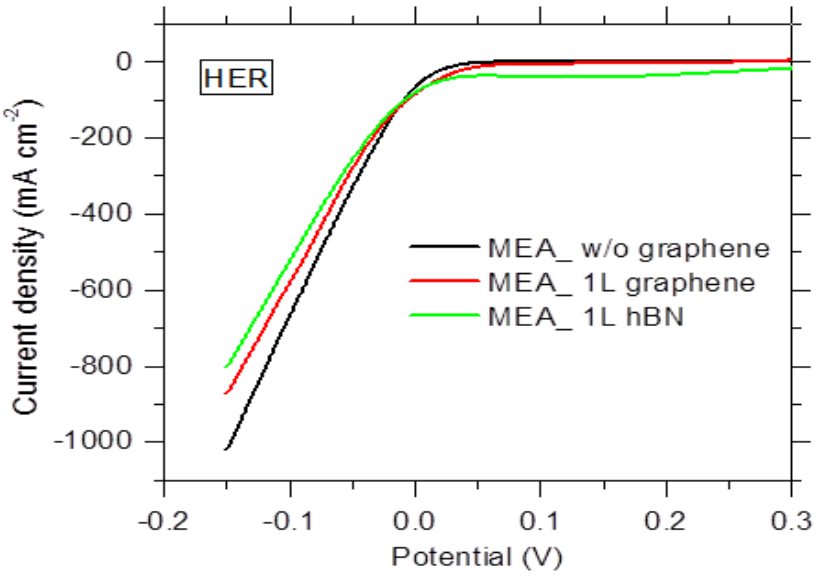


Figure 7.13 I-V curves for HER from MEA with single-layer hBN

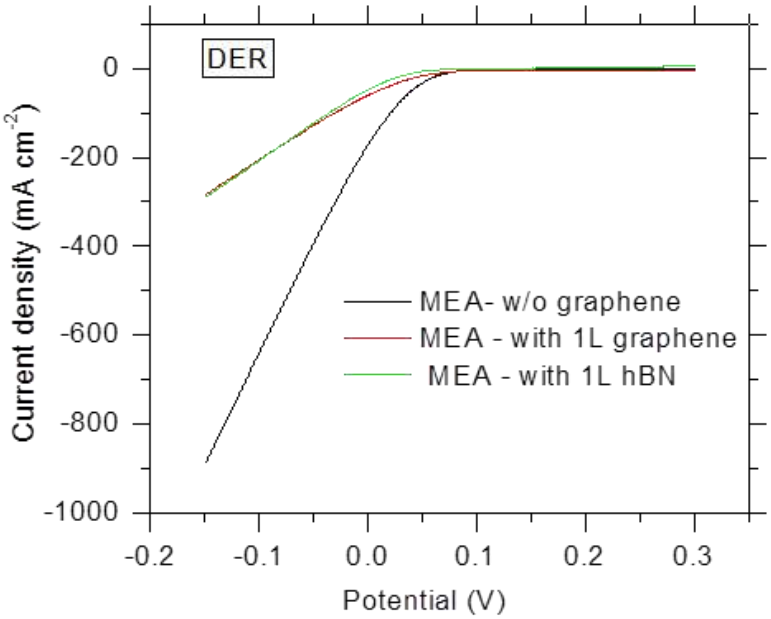


Figure 7.14. I-V curves for DER from MEA with single-layer hBN

7.4.2 X-ray Photoelectron Spectroscopy of hBN on Nafion® membrane

Figure 7.15 presents the optical micrograph of hBN on Nafion® membrane taken from the sample chamber of the XPS spectrometer. The edge of hBN is clearly visible. Spots 8, 9, and 10 are the areas of the membrane covered by hBN and also spot11 was on the boundary between the membrane and hBN. Finally, spot 12 was outside the hBN region, but on the membrane. By the placement of the hBN on the membrane described here, it was easily demonstrated the successful transferred of hBN on the membrane. Figures 7.16 and 7.17 present sets of data on the micrograph in Figure 7.15. Figure 7.16 shows the XPS survey and C1s peak on the spot 8 (*i.e.* region covered by hBN). The

survey identified the expected elements (C, F, O, and S) in Nafion® membrane just like the graphene sample but with the addition of boron and nitrogen which, are definitely

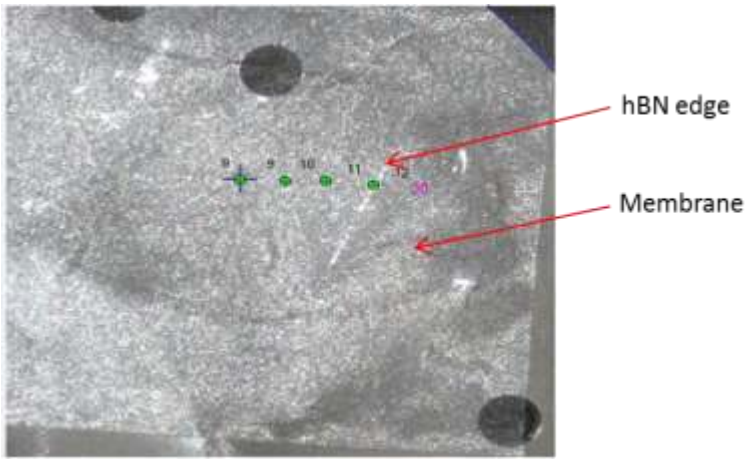


Figure 7.15. Optical micrograph of single-layer hBN on Nafion membrane taken from XPS spectrometer

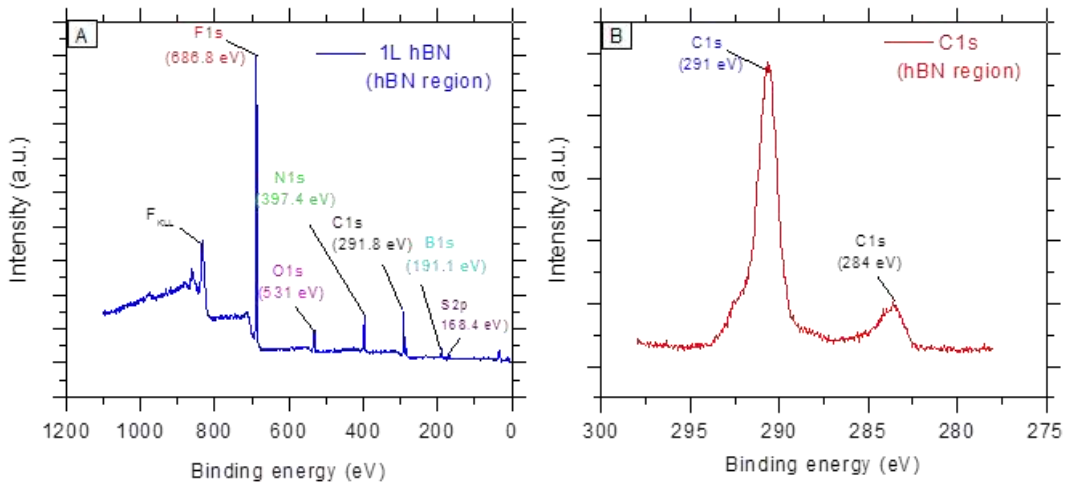


Figure 7.16. XPS spectra of single-layer hBN on Nafion® membrane (A) survey and (B) C1s spectra within the hBN region.

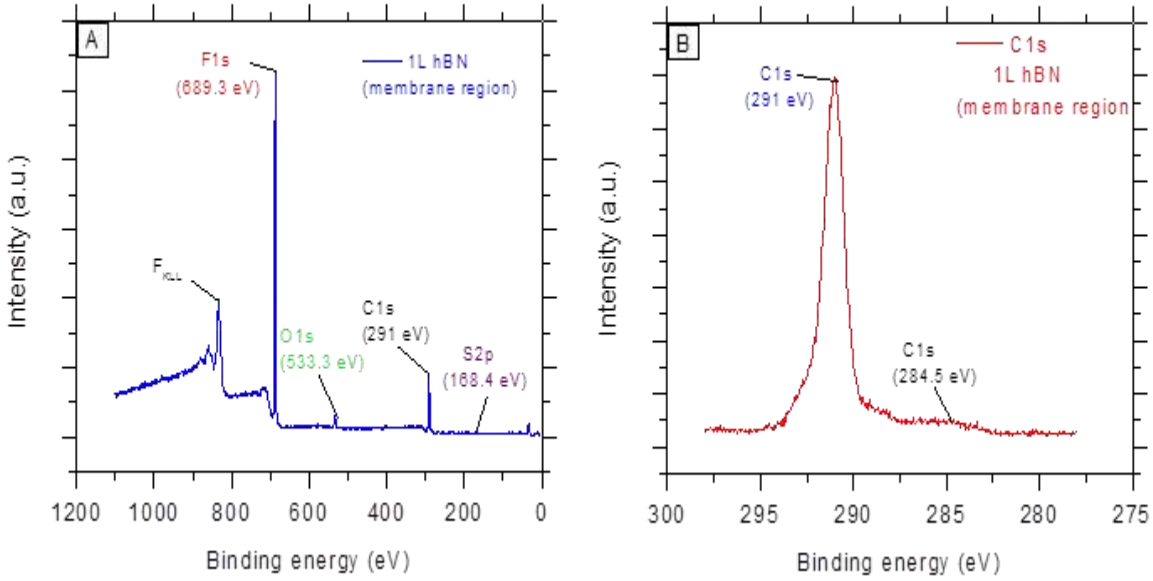


Figure 7.17. XPS spectra of single-layer hBN on Nafion® membrane (A) survey and (B) C1s spectra on membrane outside the hBN region.

elements from single-layer hBN. Conversely, Figure 7.17 presents the XPS survey and C1s spectra on the spot 12 (*i.e.,* region on the membrane outside area covered by hBN). Interestingly, the survey only identified the elements of the Nafion® membrane (C, F, O and S) without elements boron and nitrogen. This again, confirms that the boron and nitrogen peaks from Figure 7.16 are truly from hBN transferred onto Nafion® membrane.

Furthermore, the hBN XPS data are particularly interesting when C1s peaks from hBN region and that of the membrane area outside hBN region are compared. For example, the high BE C1s peak at 291 eV in Figure 7.16B still remains the dominant peak in Figure 7.17B. These are really interesting results because they corroborate our

previous observation on the XPS of Nafion® / graphene samples. In hBN sample, whether in the region of hBN or outside it, the high BE C1s peak remains the dominant peak because there is no introduction of foreign carbon that does attenuate this peak. Whereas, in graphene, the high BE of C1s at 291 eV was the dominant peak in the region outside graphene but became less dominant in the region where graphene was located. This is because low BE C1s peak at 284.5 eV coming from graphene attenuates the high BE C1s peak associated with the fluorine atoms (either in $CF_2$ or $CF_3$). It is not only that the XPS data of single-layer hBN confirm the presence of hBN but also reinforced the conclusion on Nafion® / graphene XPS data.

### 7.4.3 SEM Defect Visualization on CVD hBN

Similar to the defect visualization experiment discussed on CVD graphene on Cu substrate, the same technique was extended to study the formation of etch pits on CVD hBN on Cu. From the Figure 7.18, the circular region in which the etchant was dropped on the sample can be visualized clearly. The underlying Cu grain boundaries cannot be distinguished visibly may be due to the fact the hBN bond is partially ionic and that the Cu substrate is somewhat thinner (15-25 μm) than the Cu substrate used in the case of graphene sample (45 μm). A spot can also be identified on Figure 7.18A which was due to water droplet that adhered to the hBN surface on the Cu. Even after drying, the spot still clearly shows this adherence of water droplet as a result of polar nature of hBN bond. Other images were acquired at higher magnification with no discernible pattern of defect etch pits. The etch pits are short lines often aligned together in a well ordered layer.

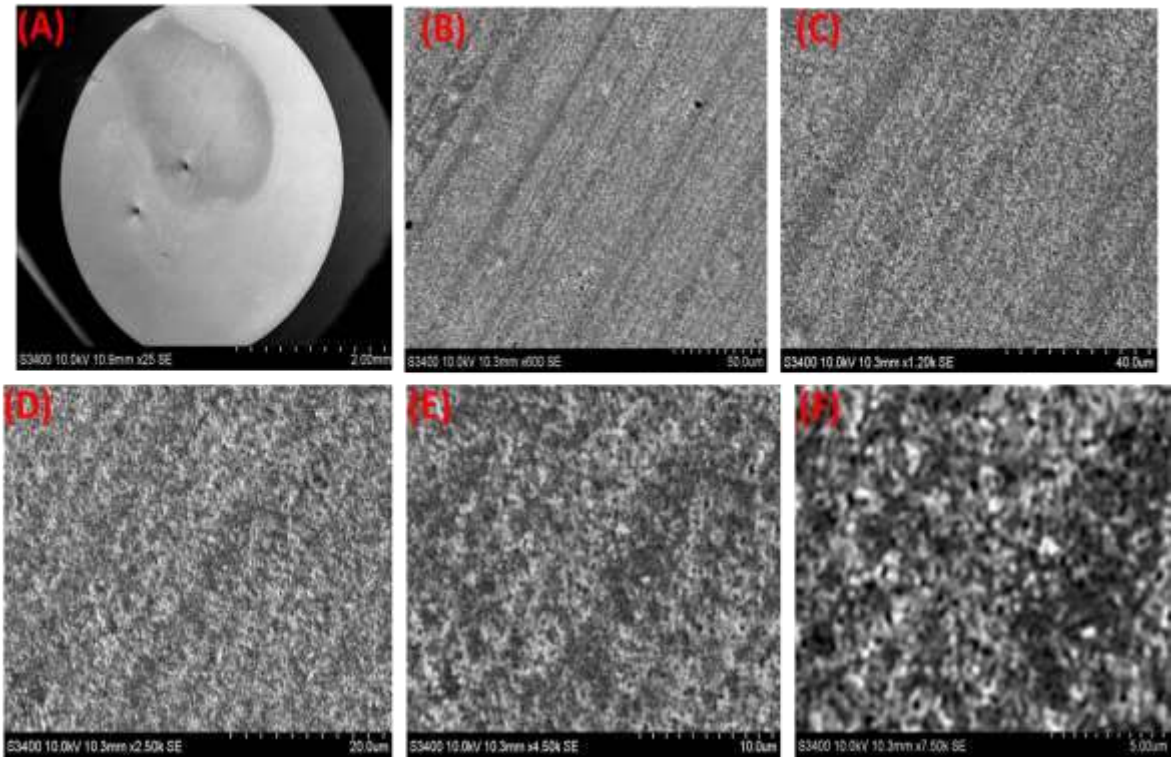


Figure 7.18. SEM images of defect visualization of single-layer CVD hBN on Cu: (A) 2 mm, (B) 50 μm, (C) 40 μm, (D) 20 μm, (E) 10 μm, and (F) 5 μm scale bars.

## 7.5 Pyrochlore Oxides Based Electronic/ Ionic Conductors

Pyrochlore crystal materials are rich inorganic compounds with exciting properties that may be tailored for the application of electrochemical hydrogen pump and as electrocatalysts. They occur naturally in pegmatites or in granite. Pyrochlore, a more generic term of crystal structure Fd-3m is described generally as $A_2B_2O_{7,}$ where A and B are "struckturbericht" symbols that represent transition metals or rare earth metals.[341–345] While the actual structure of pyrochlore still remains a topic of debate in the literature

due in part to the variation in the coordination polyhedra around cations A and B; the more established representation describes pyrochlore crystal structure as an interpenetrating cuprite $A_2O$ tetrahedral with corner sharing $BO_6$ octahedron.[351] Figure 7.19 below shows the schematic representation of the unit cell of pyrochlore crystal.[352]

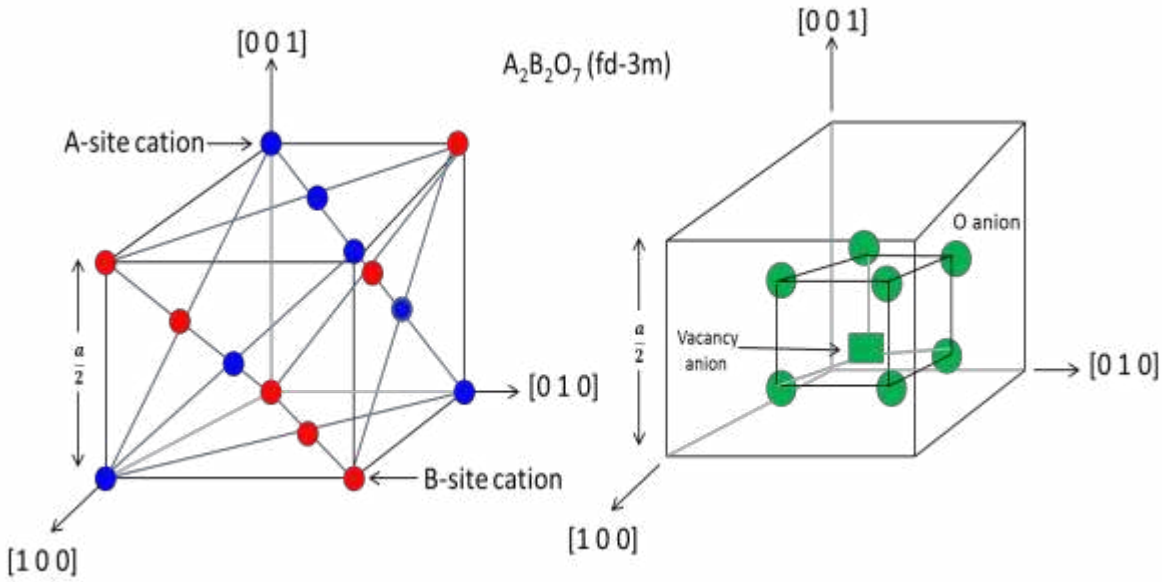


Figure 7.19. Unit cell representation of pyrochlore crystal showing (a) cation and (b) anion {Recreated from reference [344]}

The pyrochlores show varied physical properties such as insulator ($La_2Zr_2O_7$), ionic conductors ($Gd_{1.9}Ca_{0.1}Ti_2O_{6.9}$), metallic conductor ($Bi_2Ru_2O_7$ ), and some others that have mixed ionic and electronic properties Their cations basically exist in two forms: (i) (3+, 4+) (represented as $A_2^{3+}B_2^{4+}O_7$) and (ii) (2+, 5+) (represented as $A_2^{2+}B_2^{5+}O_7$). The potential transition metals and some alkali-earth metal that fit into this category that were studied in this work include: Sr, Zr, Bi, Mn, and Ce. The goal is to study the proton transmission characteristics of these pyrochlore oxides materials. Another goal is to

transform the pyrochlore oxides materials into carbide / oxycarbides by heat treatment in methane atmosphere and investigate their electrocatalytic nature for the hydrogen evolution reaction, oxygen evolution reaction, and oxygen reduction reaction.

### 7.5.1 Synthesis of Pyrochlore Oxides

There are quite a few ways to synthesize pyrochlore crystalline materials such as solvothermal process, sol-gel, and microwave sintering. These techniques are somewhat energy intensive and may be time consuming. The more appropriate technique that was employed was the wet chemistry using a co-precipitation approach. This method is more benign and environmentally friendly in which the respective salts of the metals were dissolved in appropriate solvents and precipitated in hydroxide forms using concentrated ammonium hydroxides and were subsequently pyrolyzed. Two sets of pyrochlore oxides were developed. The first is bismuth zirconate oxide intended to be used as proton conductors. The second set was cerium zirconate oxide on carbon based electrocatalysts doped with manganese.

#### 7.5.1.1 Synthesis of Bismuth Zirconate Oxide

Materials. Bismuth(III) acetate was purchased from Alfa Aesar and zirconium(IV) propoxide was obtained from Alfa Aesar. Nitric acid and ammonium hydroxide were obtained from Millipore Sigma and Fisher Scientific, respectively. Deionized water was used throughout the experiment.

In a typical experiment, 0.1 M bismuth acetate was prepared by dissolving 0.97 g in 25 mL DI $H_2O$ and was subsequently nitrated with 25 mL of 1 M $HNO_3$ until a clear solution was obtained. Zirconium(IV) propoxide (0.1 M) was hydrolyzed in 25 mL DI $H_2O$ and the mixture was nitrated again in 25 mL of 1 M $HNO_3$. The solution was left stirring for few hours. The resulting bismuth nitrate and zirconium nitrate were then mixed together and placed on a magnetic stirrer at 500 rpm for 2 hr. Thereafter, the solution mixture was then precipitated as metal hydroxide with 70 mL of 3 M $NH_4OH$. The precipitate was then subjected to vacuum filtration and was later dried in an oven at 80 $^oC$ for 4 hours.

Subsequently, the obtained dried sample was subjected to heat treatment at 700 $^oC$ using multi-programmable temperature controller furnace (Thermolyne F79300). During the heat treatment, the furnace temperature was ramped at 5 $^oC\ min^{-1}$ from RT to 100 $^oC$ and was held at 100 $^oC$ for 10 min to purge out adsorbed $H_2O$ molecules. Then, the temperature was ramped again at 10 $^oC\ min^{-1}$ from 100 $^oC$ to 700 $^oC$. The furnace temperature was held at 700 $^oC$ for 2 hours and was later cooled down at the ramping rate of 20 $^oC\ min^{-1}$ to RT. Scheme 7.3 illustrates the synthesis route and the heat treatment of bismuth zirconate.

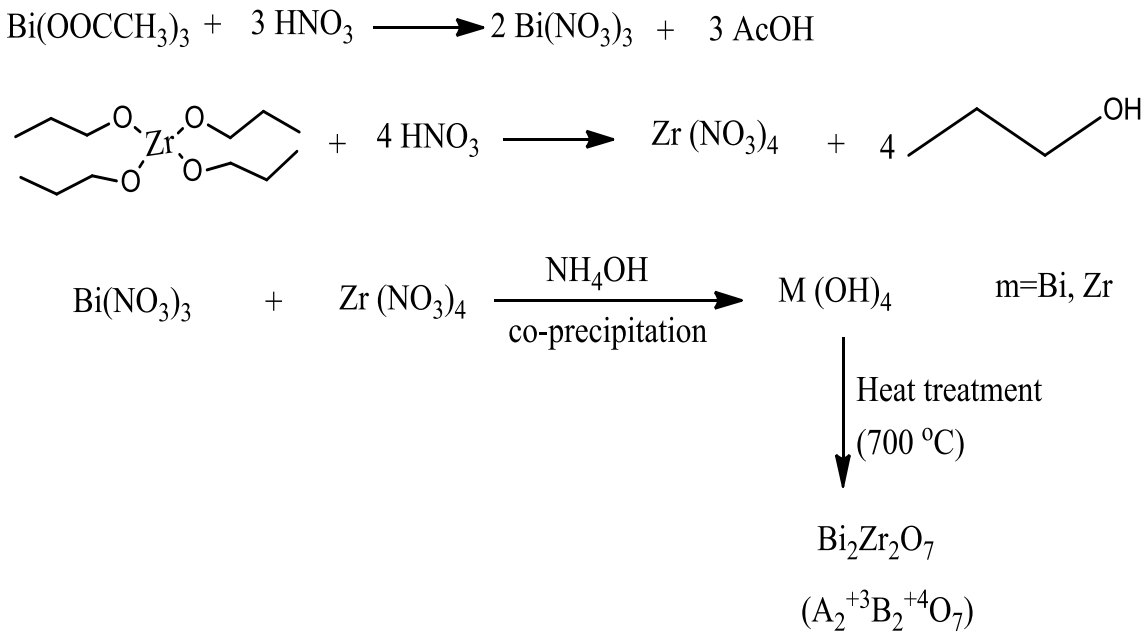


Scheme 7.3. Proposed schematic representation for the pyrochlore crystal synthesis of the form ($A_2^{+3}B_2^{+4}O_7$)

Figure 7.20 presents the stages of the sample synthesis. Figure 7.20A shows the heat treated sample and Figure 7.20B shows the sample obtained before the heat treatment. Thereafter, the obtained sample was grinded into a powder and integrated into a MEA by dissolving it in isopropanol (IPA) solvent as slurry. The sample as a slurry was sandwiched between two Nafion®-211 membranes and hot pressed together with 0.3 mg $cm^{-2}$ Pt carbon-cloth electrodes 3/16 inch diameter (0.178 $cm^2$) as anode and cathode, respectively.

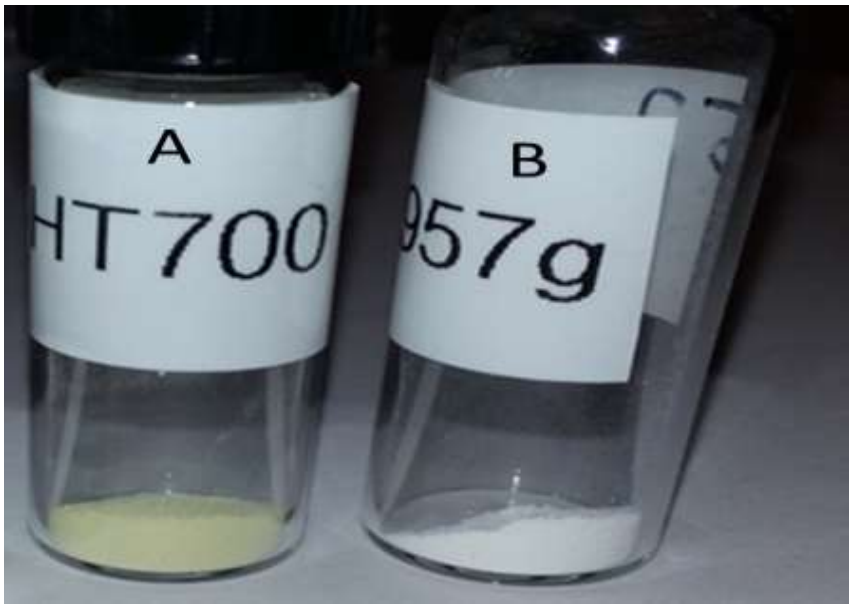


Figure 7.20. Stages of bismuth zirconate oxides synthesis: (A) sample obtained after the heat treatment at 700 $^{o}$C and (B) as-synthesized raw sample

7.5.1.2 Synthesis of Cerium Zirconate Oxide / Vulcan Carbon doped with Mn

Materials. Cerium acetate and zirconium propoxide were obtained from City Chemical Corporation and Alfa Aesar, respectively. Manganese acetate was purchased from Alfa Aesar. Vulcan XC-72R (Vu) carbon was obtained from Fuel Cell Store.

Similar procedures described above were used to prepare Mn doped cerium zirconate oxide/Vu samples. All the salts were prepared in nitrate forms from the reaction between 0.1 M salt precursors [$Ce(OOCCH_3)_3$, $Zr(OCH_2CH_2CH_3)_4$, and $Mn(OOCCH_3)_2$], and 1.0 M $HNO_3$ and were later precipitated in hydroxide form using about 70 mL of 3 M $NH_4OH$. The heat treatment was done at 800 $^{o}$C using $CH_4$ and $H_2$ gas mixture at a flow

rate of 0.33 SLM $CH_4$ and ≈ 0.1 SLM for $H_2$ to transform the sample from oxide to oxycarbides / carbide.

7.5.2 Spectroscopic characterization

Scanning electron microscopy (SEM) and energy dispersive X-ray spectroscopy (EDS) were used to examine the samples morphology and elemental composition. Figure 7.21 shows the SEM and EDS spectra for the bismuth zirconate oxide comparing the as-synthesized catalyst and the heat treated sample at 700 $^{o}$C. A dramatic change exists in the morphology from the as-synthesized sample when compared to that of the heat treated sample (Figures 7.21A and 7.21C). The particles of the sample in 7.21C are larger and sparsely distributed; whereas, the particles in Figure 7.21C for the heat treated samples were somewhat evenly distributed and contained less particle agglomeration.

As can be seen from the EDS spectra (Figures 7.21A and 7.21D), the elemental composition coincidentally seems to follow with what would be expected for pyrochlore oxide. However, one cannot be definitive in this conclusion until thorough spectroscopic characterization such as XRD (to determine the crystal structure and phase) and XPS are conducted. The electrochemical data from the samples are still preliminary and need great efforts to improve the performance as a result, further characterization on the sample was not pursued.

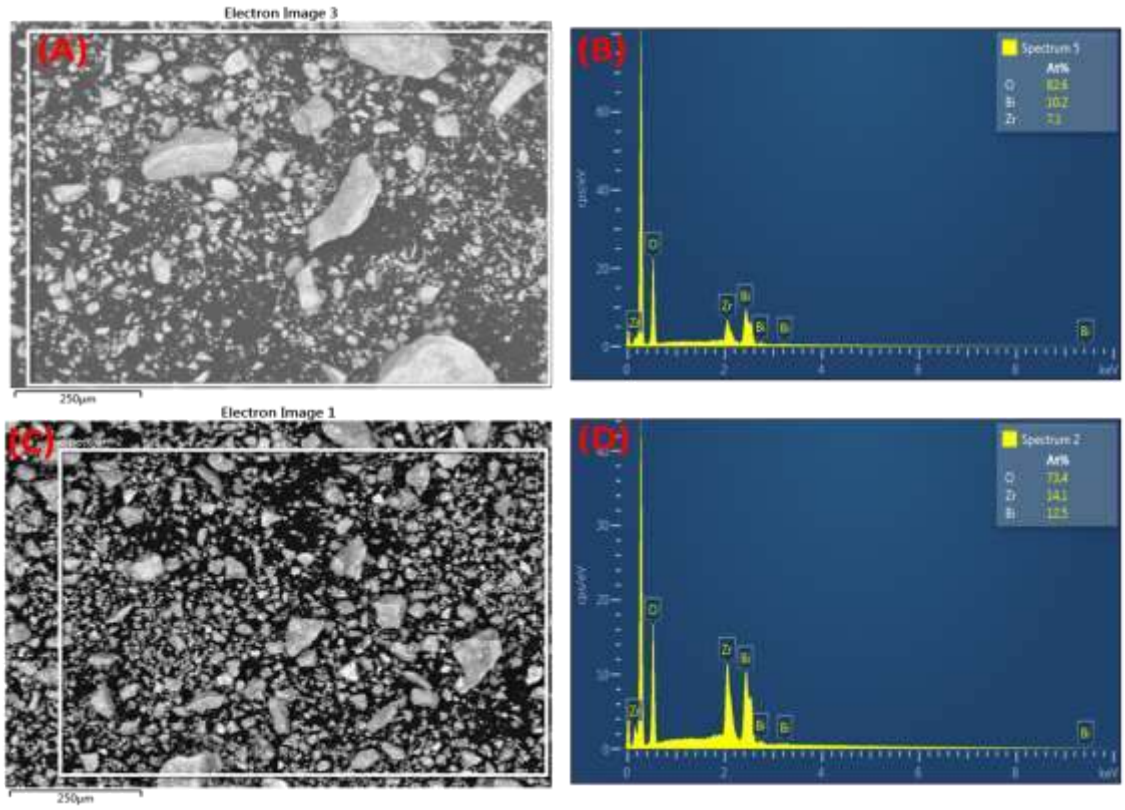


Figure 7.21. SEM images of bismuth zirconate oxide: (A) before the heat treatment, (C) after the heat treatment and EDS spectra for (B) before the heat treatment, and (D) after the heat treatment.

### 7.5.3 Electrochemical Characterization

For the bismuth zirconate oxide (BZO), the MEA was tested in a symmetric mode with the humidified hydrogen supplied to both the anode and cathode side in a miniature hydrogen pump cell. Linear sweep voltammetry (LSV) technique was applied at a potential bias of ± 0.07 V and at a scan rate of 1 mV $s^{-1}$. Figure 7.22 shows the obtained I-V curves for the symmetric experiment from the MEA of bismuth zirconate oxide. The

inverse of the slope from the curve is the resistance (911.74 Ω) due to proton transmission. By correcting the obtained resistance value from the electronic resistance (1.266 Ω) one can obtain the proton conductivity of this oxide material. Though, the proton conductivity of bismuth zirconate oxide (0.03 mS $cm^{-1}$) is significantly lower as compared to the Nafion® conductivity (50-60 mS $cm^{-1}$ at ambient temperature), however, the result suggests that the obtained oxide is not an insulator and its conductivity can be improved by optimizing the synthesis in the future work.

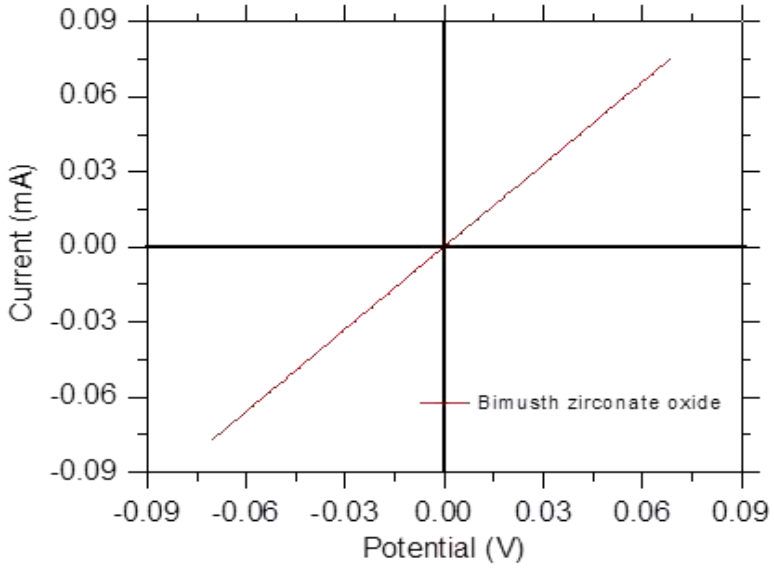


Figure 7.22. Symmetric hydrogen pump I-V curve for bismuth zirconate oxide MEA.

For the Mn doped cerium zirconate oxide / Vu electrocatalyst, the obtained catalysts were prepared as thin-film ink. In a typical procedure, 10 mg of the catalyst was dispersed in 1 mL DI $H_2O$ and 0.5 ML IPA and sonicated for 10 min. This was followed

by adding 100 µL 5 wt. % Nafion® solution and mixture was further sonicated for at least 1 hr until homogeneous well dispersed ink was obtained. Approximate 9 µL thin film ink was deposited on a glassy carbon electrode (0.0707 $cm^2$) and dried under ambient conditions. The electrodes were tested in 1.0 M KOH for the electrochemical performances. Figure 7.23 presents the three-electrode cell used for the electrochemical testing. The cell was fabricated from polytetrafluoroethylene (PTFE) polymer. The catalyst films on the glassy carbon electrode were investigated for their potential oxygen evolution reaction (water splitting), hydrogen evolution reaction, and oxygen reduction reaction using a stationary electrode.

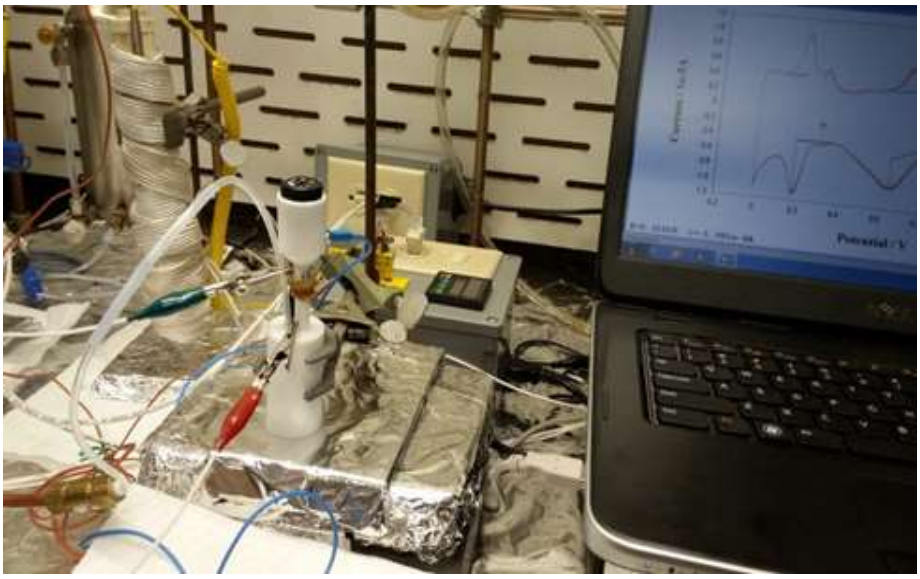

Figure 7.23. Photograph of small liquid electrolyte alkaline PTFE cell.

Figure 7.24 presents the cyclic voltammograms of cerium zirconate oxide / Vu with and without Mn, Pt bulk, and glassy carbon electrode (GCE). The as-prepared electrodes containing the catalyst films were cycled in $N_2$ saturated 1.0 M KOH between

0.0 to 1.3 V at a scan rate of 50 mV $s^{-1}$. The electrodes were continuously cycled until the CV became stabilized after at least 20 potential cycles. The CV for bulk Pt (black) and glassy carbon electrode (red) show the expected characteristics peaks. The cyclic voltammograms for Mn doped cerium zirconate oxide/Vu and undoped homologue clearly show that the catalysts have some slight redox peaks different from that of the glassy carbon electrode in which they were deposited on. Interestingly, the catalysts did not show huge capacitive behavior, which may be good for electrochemical processes.

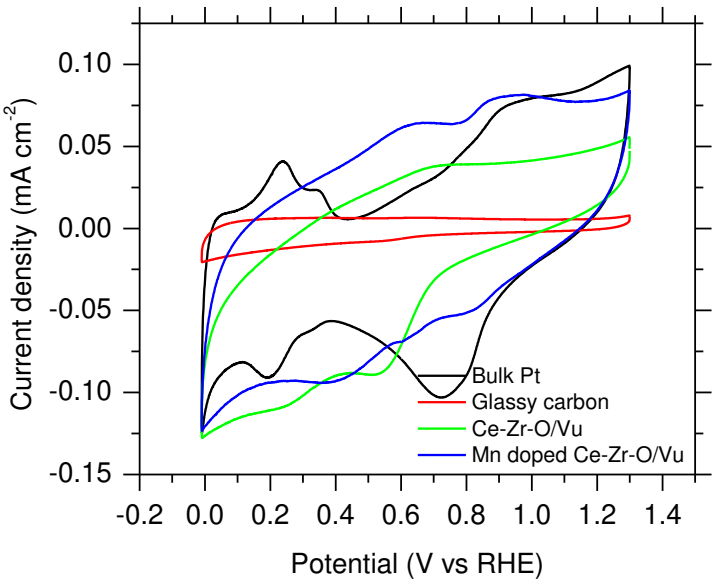


Figure 7.24 Cyclic voltammograms in $N_2$ saturated 1.0 M KOH for bulk Pt, GCE, cerium zirconate oxide / Vu and Mn doped cerium zirconate oxide / Vu.

The cyclic voltammograms in $N_2$ saturated electrolyte are generally good to have a glimpse of the redox peaks and the capacitive behavior of catalysts. To better understand the reactivity of an electrocatalyst towards a particular electrochemical reaction, experimental conditions need to be modified. The catalysts (Mn doped and undoped cerium zirconium oxide / Vu) were further investigated for their activities toward water splitting (oxygen evolution reaction), hydrogen evolution reaction (HER) and oxygen reduction reaction (ORR). Figure 7.25 shows the linear sweep voltammograms for Mn doped cerium zirconium oxide / Vu and the undoped electrocatalysts for water oxidation or water splitting (also known as oxygen evolution reaction) in 1.0 M KOH between 0.0 to 1.9 V at a scan rate of 20 mV $s^{-1}$. Despite that the performances of the two catalysts are not greatly enhanced, the LSV does show that Mn doped homologue is a better water oxidation catalyst than the undoped catalyst.

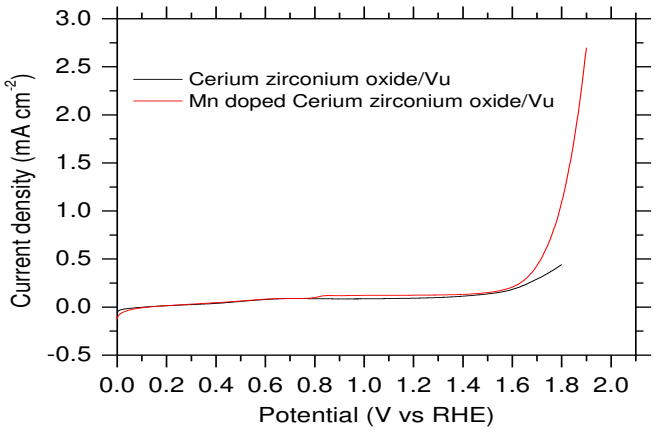


Figure 7.25. Linear sweep voltammograms for water oxidation in $N_2$ purged 1.0 M KOH, at room temperature for Mn doped cerium zirconium oxide / Vu and the undoped homologue.

Furthermore, the catalysts were equally investigated for their hydrogen evolution reaction activities. Figure 7.26 presents the cyclic voltammograms for the hydrogen evolution reactions in $N_2$ saturated 1.0 M KOH, with the scan rate of 50 mV $s^{-1}$ for the two catalysts. Again, the performances are not greatly enhanced but they do show promising potential of being active for alkaline HER. Here, the undoped cerium zirconium oxide/Vu demonstrated better HER behavior than the doped counterpart.

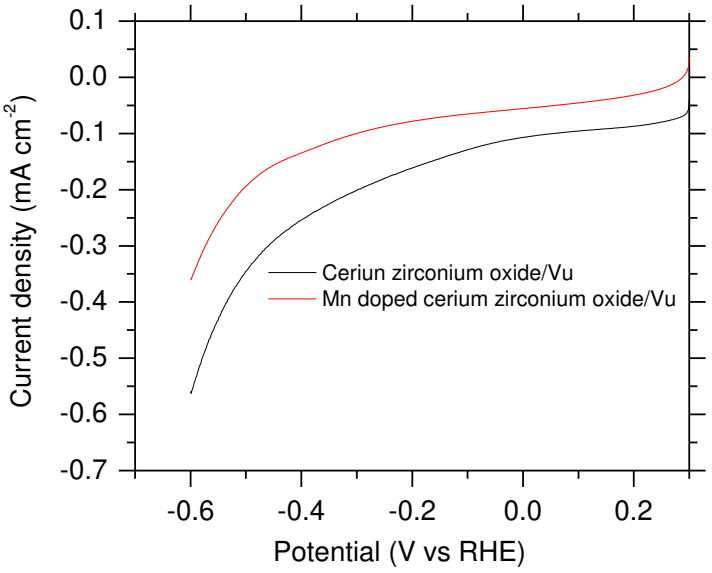


Figure 7.26. Linear sweep voltammetry for hydrogen evolution reaction in $N_2$ purged 1.0 M KOH for Mn doped and undoped cerium zirconium oxide / Vu

Finally, the catalysts were equally examined under oxygen saturated 1.0 M KOH for their oxygen reduction reaction activity. The CV-based system is a form of stationary

electrode in contrast to RDE but capable enough to reveal the catalyst activity towards ORR. The CV is recorded similar to those obtained in Figure 7.24 but in an oxygen purged electrolyte. Figure 7.27 presents the CV obtained for Mn doped cerium zirconium oxide/Vu and undoped homologue in oxygen purged 1.0 M KOH. The shape of the CV is examined for ORR characteristics peaks in ORR potential window to determine the catalyst potential of being active towards oxygen reduction reaction. Both catalysts demonstrated these properties at potential less than 0.8 V Vs reversible hydrogen electrode (RHE). Mn doped counterpart seems to be more active than the undoped catalyst. To show this behavior clearly, the CV in $N_2$ saturated was overlaid in each case.

Taken together, it is exciting to see a single catalyst demonstrate potential of being active for more than one electrochemical reaction. Mn doped cerium zirconium oxide/Vu seems to be a better option for water oxidation and oxygen reduction than the undoped homologue. Conversely, for the hydrogen evolution reaction, the undoped counterpart (cerium zirconium oxide/Vu) would be a better choice.

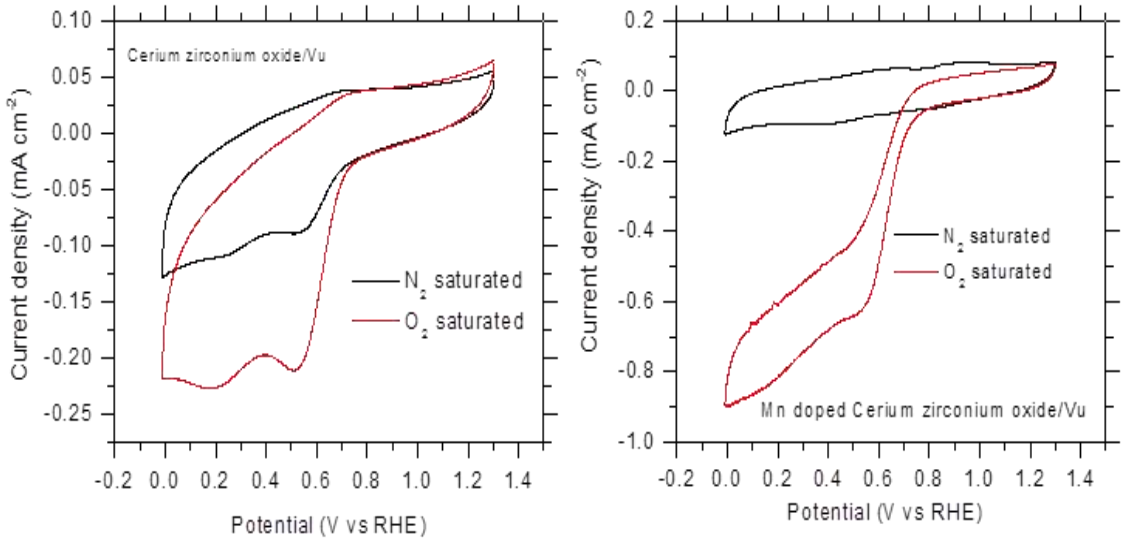


Figure 7.27. Cyclic voltammograms for Mn doped cerium zirconium oxide / Vu and undoped homologue in oxygen and nitrogen saturated 1.0 M KOH.

## 7.6 Polymer-Supported Graphene for Pressure-Driven Water Desalination

A study of water flux through polymer-supported graphene was a proof of concept to demonstrate the application of graphene for water desalination. These experiments were conducted in collaboration with Dr. A. Ladner using pressure-driven Amicon® stirred cell apparatus in his laboratory. Nafion® | graphene | Nafion® sandwich structure was prepared in an identical way to the sample used for aqueous measurement discussed in Chapter 5 in D-S cell. The Nafion®-211 / graphene structure (one inch diameter) was compared to that without graphene. Measurements were conducted on Amicon® stirred cells (model 8010) by pressuring the cell having membrane with and without graphene. A set of pressure values illustrated in the Figure 7.28 was applied to

the test samples and was held for duration of 5 min and water flux through the samples was monitored by measuring the mass of the effluent.

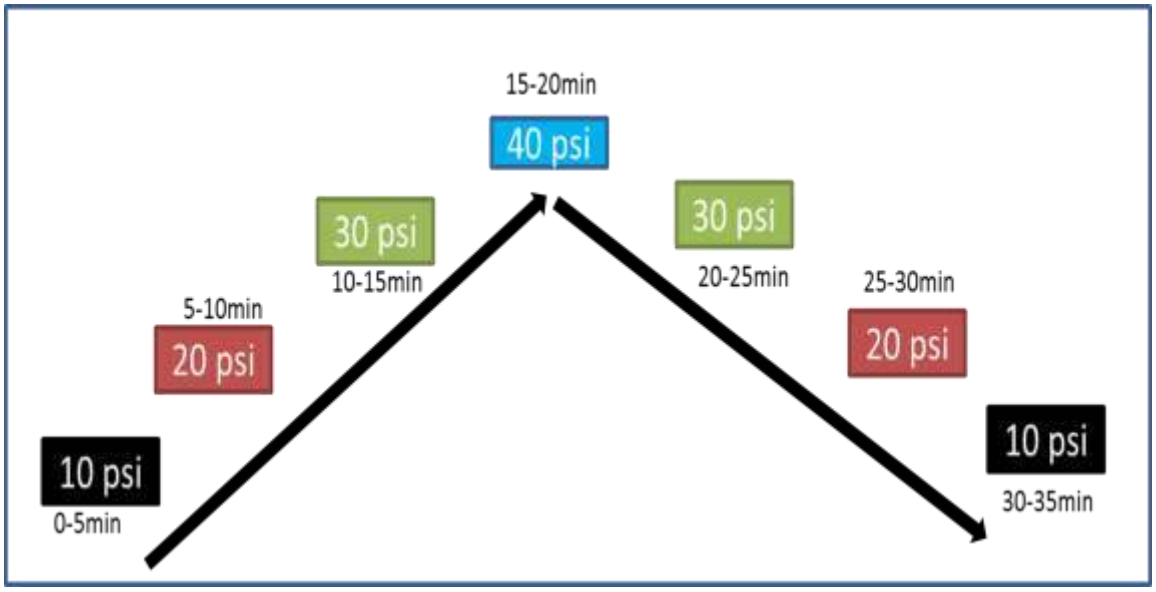


Figure 7.28. Pressure variation program used for water flux measurement

Figure 7.29 shows the results of water flux measurement against time for Nafion® membrane with and without single-layer graphene. It is obvious that the water flux through Nafion® membrane increases with increase in pressure. Interestingly, the water flux through Nafion® | graphene | Nafion® sandwich structure is invariant with pressure increase and no appreciable flux was established. This is particularly useful when considering application such as water purification and desalination in which, the use of graphene may prevent unwanted crossover contaminants.

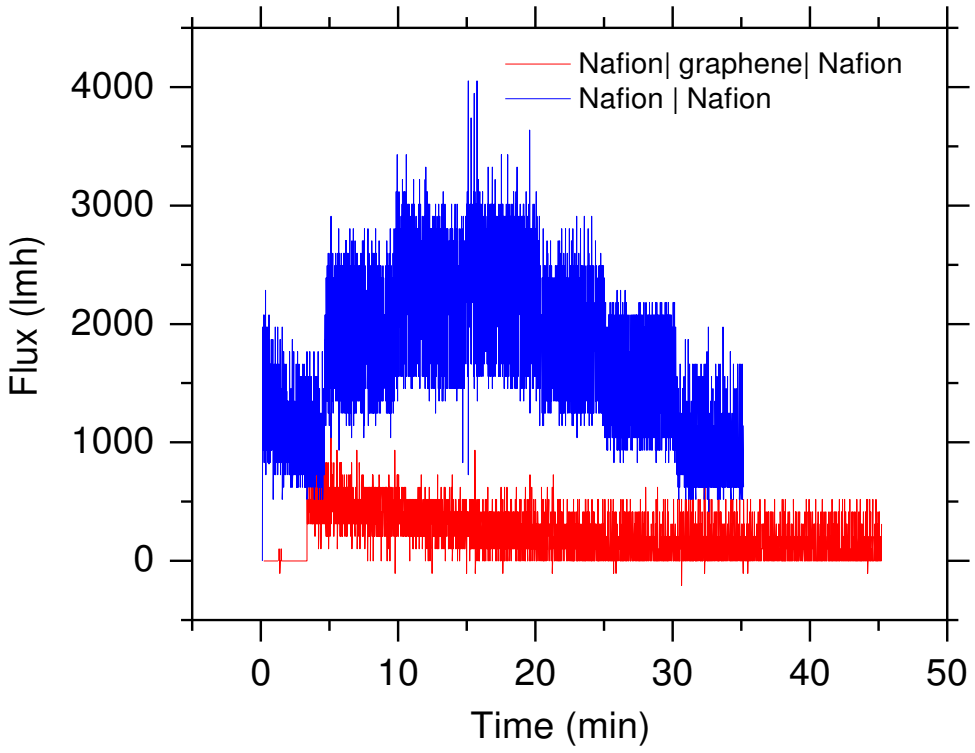


Figure 7.29. Demonstration of zero water flux through single-layer graphene in Amicon® cell

## 7.7 CONCLUSION

In summary, ALD alumina coating on a Nafion® / graphene sample showed little effect on proton transmission and did not demonstrate any special selectivity between proton and deuteron other than the selectivity from single-layer graphene and also did not completely block transmission of other cations in aqueous studies. Surprisingly, it does prevent etching of Cu through defect visualization experiment in which etchant species can transmit through the defects in CVD graphene on Cu. X-ray photoelectron

spectroscopy and SEM defect visualization studies confirm the coating of ALD alumina on both Nafion® membrane with single-layer graphene and on Cu substrate. In a separate but related study, proton and deuteron transmission through hBN was analogous to single-layer graphene with identical selectivity. Also, preliminary studies on other related material based on pyrochlore oxides electronic / ionic conductors show very low performance and can be further improved with optimization in the synthesis such as controlling the stoichiometric of the reaction. Single-layer graphene also demonstrated potential application for pressure-driven water desalination from its near zero water flux in pressurized water cell.

# CHAPTER EIGHT

# PERSPECTIVE ON ION TRANSMISSION THROUGH 2D MATERIALS

## 8.0 SYNOPSIS

This Chapter reflects my opinion based on the work that I have done in this dissertation and current research status in the literature. The first part highlights the challenges ahead that need to be addressed for better application of CVD graphene and related materials. The second part discusses the potential applications in which graphene and related 2D materials might play a key role to benefit the growing science.

## 8.1 CHALLENGES AHEAD

Pristine single-layer graphene free of defects is impermeable to atoms, molecules, ions except thermal proton. The well-known graphene that has this special characteristic is the graphene exfoliated mechanically. A disadvantage of this material is that it cannot be produced on a large scale. The only efficient way that has been greatly explored to develop large area graphene has been graphene made by chemical vapor deposition (CVD). There are two challenges associated with the CVD graphene.

First, the intrinsic defects in CVD graphene may alter its quality. This is as a result of the polycrystalline nature of the growing substrate (*i.e.,* Cu or Ni). More importantly, the conditions of growing graphene by CVD method need further optimization before it can be considered as an ideal membrane for ion transmission. Various kinds of graphene flakes have been produced with varying qualities depending on the sources of that graphene and the conditions in which it was grown. Raman

spectroscopy has been widely used to diagnose the defective graphene structure. However, there are still some atomic-scale defects that cannot be easily detected by Raman spectroscopy. Another difficulty with the Raman spectroscopy is the substrate in which graphene is being transferred onto. For example, graphene transferred onto Nafion® membrane or some other fluorinated polymers have Raman characteristics peaks in the region where D-band of graphene is usually observed. It is even more difficult for hexagonal boron nitride transferred onto PFSA membranes. The Raman peaks peculiar to hBN are exactly in the regions where PFSA membranes show Raman signatures. This makes it difficult to accurately characterize the defect of CVD graphene or hBN and other related 2D materials.

Secondly, the transfer of CVD graphene to a final substrate where it would be used is another challenge. We were lucky to have used the hot press technique to transfer CVD graphene onto PFSA membrane that proved efficient and relatively free of defects. One can unintentionally create defects into graphene by improper handling and various transfer techniques in the literature. Removal of poly(methylmetacrylate) (PMMA) usually used as a substrate to support graphene for an easy transfer of graphene to another substrate, aggressive oxidative agents (nitric acid and $FeCl_3$ / HCl) may cause major damage to the graphene and as well as the substrate (like Nafion® membrane).

## 8.2 PROSPECTS AND FUTURE WORK

The major prospects of graphene and other 2D materials as far as ion transmission is concerned would be in the area of energy conversion and storage systems. Although,

graphene has also found application in optoelectronics / electronics, solar cell, biosensors and so on, the growing field of energy storage and conversion systems is seriously in need of materials that can prevent the issues related to crossover. This material must address this challenge and at the same time not contribute to overall device resistance due to ionic transport. It must also support a high current density through it without compromising its properties in solving the contamination issues due to crossover. Almost every energy related device suffers from these issues.

For example, in fuel cell technology, fuel crossover ($H_2$ gas permeation by diffusion through membrane) is a major problem that needs urgent solution. In batteries technology (either in Li-ion battery or redox-flow battery), crossover of reactive electrolyte species (lithium ion or vanadium ion) is also a major issue. In $CO_2$ electrolysis to renewable fuel chemical (CO) or formic acid, crossover due to formate ion ($HCOO^-$) and formic acid contamination into the anode compartment had reduced the overall efficiency of this electrolyzer. In water electrolysis (PEM or AEM), crossover of evolved gases ($O_2$ and $H_2$) is also a major problem. In water desalination or salt splitting, crossover of counter ions and co-ions is a great challenge for this technology.

The prospects for graphene are high. What is really amazing about graphene even in the presence of these so-called “atomic-scale defects”, it still demonstrates superb sub-atomic selectivity. The incorporation of graphene into device architectures of these energy technologies can play a key role in addressing all issues related to crossover and expand the full commercialization of the aforementioned technological areas.

While research efforts are looking at the possibility of integrating graphene to solve the issues of crossover, we must also not forget to develop earth-abundant, highly active electrocatalysts that can replace the noble metal catalysts currently in use in most of these devices. Many research studies are ongoing in this area in developing non-precious metal catalysts for energy application.

# APPENDICES

## APPENDIX A

### Authored and Co-Authored Publications


[1] **Bukola, S**., Beard, K., Korzeniewski, C., Harris, J. M., Creager, S. E., **(2019)** Single-layer graphene sandwiched between proton-exchange membranes for selective proton transmission, **ACS Appl. Nano Mater**; Volume 2 (2) 964-974

[2] **Bukola, S**., Liang, Y., Korzeniewski, C., Harris, J., Creager, S. (**2018**) Selective proton / deuteron transport through Nafion | graphene | Nafion sandwich structures at very high current density, **J. Am. Chem. Soc.** 140 (5), 1743-1752.

[3] **Bukola, S**., Creager, S.E. (**2019**) A charge-transfer resistance model and Arrhenius activation analysis for hydrogen ion transmission across single-layer graphene, **Electrohimica Acta**, 296, p. 1-7

[4] Korzeniewski, C., Kitt, J.P., **Bukola S**., Creager, S.E., Minteer, S.D., Harris, J.M., (**2019**), Single layer graphene for estimation of axial spatial resolution in confocal Raman microscopy depth profiling, **Analytical Chemistry,** 91 (1) 1049-1055

[5] Shetzline, J.A., **Bukola, S**., Creager, S.E., (**2017**) A convenient miniature test platform for polyelectrolyte membrane fuel-cell research, **Journal of Electroanalytical Chemistry**, 797, p. 8-15.

[6] **Bukola, S**., Merzougui, B., Creager, S.E., Qamar, M., Pederson, L.R., Noui-Mehidi, M.N. (**2016**) Nanostructured cobalt-modified molybdenum carbides electrocatalysts for hydrogen evolution reaction, **International Journal of Hydrogen Energy**, 41, p. 22899-22912.

[7] **Bukola, S.,** Merzougui, B., Akinpelu, A. Zeama, M. (**2016**) Cobalt and Nitrogen Co-Doped Tungsten Carbide Catalyst for Oxygen Reduction and Hydrogen Evolution Reactions, **Electrochimica Acta**, 190, p. 1113-1123.

[8] Merzougui, B., **Bukola**, S., Zaffou, R. (**2016**) Further Understanding of Nitrogen-Doped Carbon Catalytic Property towards Oxygen Reduction Reaction (ORR), **Materials Today: Proceedings**, 4, p. 691-695

[9] Akinpelu, A. Merzougui, B. **Bukola**, S., Azad, A., Basheer, R., Swain, G.M., Shao, M., (**2015**) A Pt-free Electrocatalyst Based on Pyrolized Novel Vinazene-Carbon Composite for Oxygen Reduction Reaction (ORR) **Electrochemica Acta**, 161, p. 305-311

[10] Qamar, M., Abdalwadoud, M., Ahmed, M.I., Azad, A.-M., Merzougui, B., **Bukola**, S., Yamani, Z.H., Siddiqui, M.N., (**2015**) Single-Pot Synthesis of ⟨001⟩-Faceted N-Doped Nb2O5/ Reduced Graphene Oxide Nanocomposite for Efficient Photoelectrochemical Water Splitting, **ACS Appl. Mater. Interfaces**, 7, p. 17954–17962

[11] **Bukola**, S., Merzougui, B., Akinpelu, A., Laoui, T., Hedhili, M.N., Swain, G.M.,

Shao, M., (**2014**) Fe-N-C Electrocatalysts for Oxygen Reduction Reaction Synthesized by Using Aniline Salt and $Fe^{3+}/H_2O_2$ Catalytic System, **Electrochimica Acta**, 146, p. 809-818

[12] Merzougui, B., Hachimi, A., Akinpelu, A., **Bukola**, S., Shao, M. (**2013**) A Pt-free catalyst for Oxygen Reduction Reaction Based on Fe-N-Multiwalled Carbon Nanotube Composite, **Electrochimica Acta**, 107, p. 126-132.

## APPENDIX B

### Refereed Technical Conference Presentations

[1] **Bukola, S**., Beard, K., Korzeniewski, C., Harris, J. M., Creager, S. E., **(2019)** Selective cation transmission through single-layer graphene embedded in proton-exchange membrane, **Polymers for Fuel Cells, Energy Storage, and Conversion Systems Conference,** ACS Division of Polymer Chemistry, February 24-27, 2019; Asilomar Conference Grounds, Pacific Grove, California, USA.

[2] **Bukola, S**., Creager, S., (**2018**) Hydrogen Isotopes Separation by a 2D graphene embedded in a polymer electrolyte membrane, **Electrochemistry Gordon Research Conference**, January 7-12, 2018; Four Points Sheraton/ Holiday Inn Express, Ventura, CA, USA.

[3] Creager, S.E., **Bukola S**., Korzeniewski, C., Harris, J., Liang, Y., (**2018**) Selective proton / deuteron transfer across single-layer graphene at very high current density, **Electrochemistry Gordon Research Conference**, January 7-12, 2018; Four Points Sheraton/ Holiday Inn Express, Ventura, California, USA.

[4] Creager S.E., **Bukola S**., Korzeniewski, C., Harris, J.M., (**2018**) Electrochemical proton / deuteron separation in Nafion | graphene |Nafion hydrogen pump cells, **Electrochemical Society (ECS), AiMES 2018 Meeting**, September 30 - October 04, 2018, Cancun, Mexico

[5] Creager S.E., **Bukola S**., Korzeniewski, C., Harris, J.M., (**2018**) Proton transfer can occur at high rates through single-layer graphene in Nafion | graphene | Nafion sandwich structures, **Electrochemical Society (ECS), AiMES 2018 Meeting**, September 30 - October 04, 2018, Cancun, Mexico

[6] Creager, S., **Bukola, S**., Smith, R., (**2018**) Polyelectrolyte membrane PEM and fuel cell catalyst studies using a miniaturized PEM fuel cell test fixture, Qatar Foundation Annual Research Conference Proceedings, EEPD796, March 19-20, 2018, Doha, Qatar.

[7] Creager, S. E., **Bukola S**., (**2017**) Proton and deuteron transport through single-layer graphene sandwiched between two Nafion membranes, **69th Southeastern Regional Meeting of the American Chemical Society,** Charlotte, NC, USA, November 7-11, 2017, SERMACS-129

[8] **Bukola, S**., Creager, S.E., (2017) Hydrogen Isotope Sieving by a 2D Material Embedded in a Polymer Electrolyte Membrane, **69th Southeastern Regional Meeting of the American Chemical Society,** Charlotte, NC, USA, November 7-11, SERMACS-33

[9] **Bukola, S.,** Creager, S. E., (2016) A novel micro-electrochemical cell for PEM fuel cell catalys ts screening, **68th Southeastern Regional Meeting of the American**

**Chemical Society,** Columbia, SC, USA, October 23-26 (2016), SERMACS-203

[10] Shetzline, J. A., **Bukola, S.,** Creager, S. E., (2016) A miniaturized test platform for research on PEM fuel cell catalysts without liquid electrolyte, **68th Southeastern Regional Meeting of the American Chemical Society**, Columbia, SC, USA, October 23-26 (2016), SERMACS-748

[11] Merzougui, **B., Bukola**, S., Zaffou, R., (**2015**) Further Understanding of Nitrogen-Doped Carbon Catalytic Property towards Oxygen Reduction Reaction (ORR)" **Advances in Functional Materials International Conference,** June 29-July 3, 2015, Stony Brook, New York, USA.

[12] Merzougui, B., **Bukola, S.**, Akinpelu, A., Shao, M., (**2015**) A Pyrolized Vinazene-Carbon Nano-Composites for Oxygen Reduction Reaction" EMRS, Lille, France, May 11-15, 2015

[13] Merzougui, B. **Bukola, S**., Akinpelu, A. Hakeem, A., Laoui, T., (**2014**) Improved Activity and Stability of Nitrogen Doped Carbon as Pt-free Catalysts for Oxygen Reduction Reaction (ORR)", **Fuel Cell 2014 Science & Technology, A Grove Fuel Cell Event**, NH Grand krasnapolsky, Amsterdam, Netherlands, April, 3-4, 2014.

[14] Merzougui, B. Hachimi, A., Hakeem, A. **Bukola**, S., Akinpelu, A., Laoui, T. Atiya, M.A., Shao, M., (**2013**) Activity and Durability of Fe-N-Multiwalled Carbon Nanotubes as Nanocomposite Catalyst for ORR in Acidic and Alkaline Mediums" EMRS, Strasbourg, France, May 27-31 2013.

[15] Hachimi, A., Merzougui, B., Hakeem, A., Akinpelu, A., **Bukola S**., Laoui, T., Atiya, M.A., (**2012**) A Pt-free catalyst based on metal-nitride-carbide nanocomposites for oxygen reduction reaction (ORR), 2nd Saudi International Nanotechnology Conference (2SINC), November 11-13, 2012, Riyadh, Saudi Arabia

## APPENDIX C

### Awards and Honors

[1] Outstanding Graduate Researcher Award for the College of Science-2019

[2] 4th Annual Graduate Research and Discovery Symposium **(GRADS 2017),** Clemson University, Watt Innovation Center, USA; April 7, 2017
Emerged as First for the College of Science

[3] 2nd Annual Chemistry Research Symposium- Clemson University, Watt Innovation Center, March 4, 2017
Overall Best Research Poster Presentation Award

[4] Chemistry Graduate Student, Clemson University, SC 29634, USA
Fall 2016 Professional Enrichment Grants (PEG) Award
Fall 2017 Professional Enrichment Grants (PEG) Award

[5] First Cohort of Mandel Fellowship Award, Chemistry Department Clemson University ($4,000 cash award)

REFERENCES


1. Novoselov KS. Electric Field Effect in Atomically Thin Carbon Films. *Science (80- )*. 2004;306(5696):666-669. doi:10.1126/science.1102896
2. Tan C, Cao X, Wu X-J, et al. Recent Advances in Ultrathin Two-Dimensional Nanomaterials. *Chem Rev*. 2017;117(9):6225-6331. doi:10.1021/acs.chemrev.6b00558
3. Maria, Perez, Madhumita, Sahoo SMH. Single Layer 2D Crystals for Electrochemical Applications of Ion Exchange Membranes and Hydrogen Evolution Catalysts. *Adv Mater interfaces*.:1801838.
4. Ramdayal Yadav, Akshay Subhash, Nikhil Chemmenchery and BK. Graphene and Graphene Oxide for Fuel Cell Technology. *Ind Eng chem Res*. 2018;57:9333.
5. Balandin AA. Thermal properties of graphene and nanostructured carbon materials. *Nat Mater*. 2011;10(8):569-581. doi:10.1038/nmat3064
6. Zhao Y, Xie Y, Liu Z, Wang X, Chai Y, Yan F. Two-Dimensional Material Membranes: An Emerging Platform for Controllable Mass Transport Applications. *Small*. 2014;10(22):4521-4542. doi:10.1002/smll.201401549
7. Loh KP, Bao Q, Eda G, Chhowalla M. Graphene oxide as a chemically tunable platform for optical applications. *Nat Chem*. 2010;2(12):1015-1024. doi:10.1038/nchem.907
8. Bonaccorso F, Colombo L, Yu G, et al. Graphene, related two-dimensional crystals, and hybrid systems for energy conversion and storage. *Science (80- )*. 2015;347(6217):1246501-1246501. doi:10.1126/science.1246501

9. Zhu Y, Murali S, Cai W, et al. Graphene and Graphene Oxide: Synthesis, Properties, and Applications. *Adv Mater*. 2010;22(35):3906-3924. doi:10.1002/adma.201001068

10. Chang H, Wu H. Graphene-Based Nanomaterials: Synthesis, Properties, and Optical and Optoelectronic Applications. *Adv Funct Mater*. 2013;23(16):1984-1997. doi:10.1002/adfm.201202460

11. Stankovich S, Dikin DA, Dommett GHB, et al. Graphene-based composite materials. *Nature*. 2006;442(7100):282-286. doi:10.1038/nature04969

12. Li X, Rui M, Song J, Shen Z, Zeng H. Carbon and Graphene Quantum Dots for Optoelectronic and Energy Devices: A Review. *Adv Funct Mater*. 2015;25(31):4929-4947. doi:10.1002/adfm.201501250

13. Sun Z, Chang H. Graphene and Graphene-like Two-Dimensional Materials in Photodetection: Mechanisms and Methodology. *ACS Nano*. 2014;8(5):4133-4156. doi:10.1021/nn500508c

14. Geim AK, Wang FC, Radha B, et al. Size effect in ion transport through angstrom-scale slits. *Science (80- )*. 2017;358(6362):511-513. doi:10.1126/science.aan5275

15. Lozada-Hidalgo M, Hu S, Marshall O, et al. Sieving hydrogen isotopes through two-dimensional crystals. *Science (80- )*. 2016;351(6268):68-70. doi:10.1126/science.aac9726

16. Bukola S, Liang Y, Korzeniewski C, Harris J, Creager S. Selective Proton/Deuteron Transport through Nafion|Graphene|Nafion Sandwich Structures at High Current Density. *J Am Chem Soc*. 2018;140(5):1743-1752.

doi:10.1021/jacs.7b10853

17. Berry V. Impermeability of graphene and its applications. *Carbon N Y*. 2013;62:1-10. doi:10.1016/j.carbon.2013.05.052

18. Gass MH, Bangert U, Bleloch AL, Wang P, Nair RR, Geim AK. Free-standing graphene at atomic resolution. *Nat Nanotechnol*. 2008;3(11):676-681. doi:10.1038/nnano.2008.280

19. Fischbein MD, Drndić M. Electron beam nanosculpting of suspended graphene sheets. *Appl Phys Lett*. 2008;93(11):113107. doi:10.1063/1.2980518

20. Koenig SP, Wang L, Pellegrino J, Bunch JS. Selective molecular sieving through porous graphene. *Nat Nanotechnol*. 2012;7(11):728-732. doi:10.1038/nnano.2012.162

21. Du H, Li J, Zhang J, Su G, Li X, Zhao Y. Separation of Hydrogen and Nitrogen Gases with Porous Graphene Membrane. *J Phys Chem C*. 2011;115(47):23261-23266. doi:10.1021/jp206258u

22. Lozada-Hidalgo M, Zhang S, Hu S, Esfandiar A, Grigorieva I V., Geim AK. Scalable and efficient separation of hydrogen isotopes using graphene-based electrochemical pumping. *Nat Commun*. 2017;8:15215. doi:10.1038/ncomms15215

23. Niranji Thilini Ekanayake, Jingsong Huang , Jacek Jakowski , Bobby G. Sumpter and SG. Relevance of the Nuclear Quantum Effects on the Proton/Deuteron Transmission through Hexagonal Boron Nitride and Graphene Monolayers. *J Phys Chem C*. 2017;121(43):24335-24344.

24. Hu S, Lozada-Hidalgo M, Wang FC, et al. Proton transport through one-atom-thick crystals. *Nature*. 2014;516(7530):227-230. doi:10.1038/nature14015

25. Ellehoj MD, Steen-Larsen HC, Johnsen SJ, Madsen MB. Ice-vapor equilibrium fractionation factor of hydrogen and oxygen isotopes: Experimental investigations and implications for stable water isotope studies. *Rapid Commun Mass Spectrom*. 2013;27(19):2149-2158. doi:10.1002/rcm.6668

26. Zakrzewska-Trznadel G, Chmielewski AG, Miljević NR. Separation of protium/deuterium and oxygen-16/oxygen-18 by membrane distillation. *J Memb Sci*. 1996;113(2):337-342. doi:10.1016/0376-7388(95)00131-X

27. Andreev BM. SEPARATION OF HYDROGEN ISOTOPES IN H 2 O-H 2 S SYSTEM. *Sep Sci Technol*. 2001;36(8-9):1949-1989. doi:10.1081/SS-100104764

28. Xiao X, Heung LK, Sessions HT. Recent Advances in SRS on Hydrogen Isotope Separation Using Thermal Cycling Absorption Process. *Fusion Sci Technol*. 2015;67(3):643-646. doi:10.13182/FST14-T100

29. Lozada-Hidalgo M, Hu S, Marshall O, et al. Sieving hydrogen isotopes through two-dimensional crystals. *Science (80- )*. 2016;351(6268):68-70. doi:10.1126/science.aac9726

30. Moghadam F, Park HB. Two-dimensional materials: an emerging platform for gas separation membranes. *Curr Opin Chem Eng*. 2018;20:28-38. doi:10.1016/j.coche.2018.02.004

31. Hummers WS, Offeman RE. Preparation of Graphitic Oxide. *J Am Chem Soc*. 1958;80(6):1339-1339. doi:10.1021/ja01539a017

32. Stankovich S, Dikin DA, Piner RD, et al. Synthesis of graphene-based nanosheets via chemical reduction of exfoliated graphite oxide. *Carbon N Y*. 2007;45(7):1558-1565. doi:10.1016/j.carbon.2007.02.034

33. Niu L, Coleman JN, Zhang H, Shin H, Chhowalla M, Zheng Z. Production of Two-Dimensional Nanomaterials via Liquid-Based Direct Exfoliation. *Small*. 2016;12(3):272-293. doi:10.1002/smll.201502207

34. Nicolosi V, Chhowalla M, Kanatzidis MG, Strano MS, Coleman JN. Liquid Exfoliation of Layered Materials. *Science (80- )*. 2013;340(6139):1226419-1226419. doi:10.1126/science.1226419

35. Yu J, Li J, Zhang W, Chang H. Synthesis of high quality two-dimensional materials via chemical vapor deposition. *Chem Sci*. 2015;6(12):6705-6716. doi:10.1039/C5SC01941A

36. Jacobberger RM, Machhi R, Wroblewski J, Taylor B, Gillian-Daniel AL, Arnold MS. Simple Graphene Synthesis via Chemical Vapor Deposition. *J Chem Educ*. 2015;92(11):1903-1907. doi:10.1021/acs.jchemed.5b00126

37. Yan Z, Peng Z, Tour JM. Chemical Vapor Deposition of Graphene Single Crystals. *Acc Chem Res*. 2014;47(4):1327-1337. doi:10.1021/ar4003043

38. Hawaldar R, Merino P, Correia MR, et al. Large-area high-throughput synthesis of monolayer graphene sheet by Hot Filament Thermal Chemical Vapor Deposition. *Sci Rep*. 2012;2(1):682. doi:10.1038/srep00682

39. Li X, Cai W, An J, et al. Large-Area Synthesis of High-Quality and Uniform Graphene Films on Copper Foils. *Science (80- )*. 2009;324(5932):1312-1314.

doi:10.1126/science.1171245

40. Li X, Colombo L, Ruoff RS. Synthesis of Graphene Films on Copper Foils by Chemical Vapor Deposition. *Adv Mater*. 2016;28(29):6247-6252. doi:10.1002/adma.201504760

41. Seah C-M, Chai S-P, Mohamed AR. Mechanisms of graphene growth by chemical vapour deposition on transition metals. *Carbon N Y*. 2014;70:1-21. doi:10.1016/j.carbon.2013.12.073

42. Chen X, Zhang L, Chen S. Large area CVD growth of graphene. *Synth Met*. 2015;210:95-108. doi:10.1016/j.synthmet.2015.07.005

43. Ago H, Ogawa Y, Tsuji M, Mizuno S, Hibino H. Catalytic Growth of Graphene: Toward Large-Area Single-Crystalline Graphene. *J Phys Chem Lett*. 2012;3(16):2228-2236. doi:10.1021/jz3007029

44. Reina A, Thiele S, Jia X, et al. Growth of large-area single- and Bi-layer graphene by controlled carbon precipitation on polycrystalline Ni surfaces. *Nano Res*. 2009;2(6):509-516. doi:10.1007/s12274-009-9059-y

45. Losurdo M, Giangregorio MM, Capezzuto P, Bruno G. Graphene CVD growth on copper and nickel: role of hydrogen in kinetics and structure. *Phys Chem Chem Phys*. 2011;13(46):20836. doi:10.1039/c1cp22347j

46. Batzill M. The surface science of graphene: Metal interfaces, CVD synthesis, nanoribbons, chemical modifications, and defects. *Surf Sci Rep*. 2012;67(3-4):83-115. doi:10.1016/j.surfrep.2011.12.001

47. Liang X, Sperling BA, Calizo I, et al. Toward Clean and Crackless Transfer of

Graphene. *ACS Nano*. 2011;5(11):9144-9153. doi:10.1021/nn203377t

48. Kim KS, Zhao Y, Jang H, et al. Large-scale pattern growth of graphene films for stretchable transparent electrodes. *Nature*. 2009;457(7230):706-710. doi:10.1038/nature07719

49. Muñoz R, Gómez-Aleixandre C. Review of CVD Synthesis of Graphene. *Chem Vap Depos*. 2013;19(10-11-12):297-322. doi:10.1002/cvde.201300051

50. Li X, Tao L, Chen Z, et al. Graphene and related two-dimensional materials: Structure-property relationships for electronics and optoelectronics. *Appl Phys Rev*. 2017;4(2):021306. doi:10.1063/1.4983646

51. Fei Z, Rodin AS, Andreev GO, et al. Gate-tuning of graphene plasmons revealed by infrared nano-imaging. *Nature*. 2012;487(7405):82-85. doi:10.1038/nature11253

52. Woessner A, Lundeberg MB, Gao Y, et al. Highly confined low-loss plasmons in graphene–boron nitride heterostructures. *Nat Mater*. 2015;14(4):421-425. doi:10.1038/nmat4169

53. Huang PY, Ruiz-Vargas CS, van der Zande AM, et al. Grains and grain boundaries in single-layer graphene atomic patchwork quilts. *Nature*. 2011;469(7330):389-392. doi:10.1038/nature09718

54. Song C. Fuel processing for low-temperature and high-temperature fuel cells Challenges, and opportunities for sustainable development in the 21st century. *Catal Today*. 2002;77(1-2):17-49. doi:10.1016/S0920-5861(02)00231-6

55. Taherian R. A review of composite and metallic bipolar plates in proton exchange

membrane fuel cell: Materials, fabrication, and material selection. *J Power Sources*. 2014;265:370-390. doi:10.1016/j.jpowsour.2014.04.081

56. Mehta V, Cooper JS. Review and analysis of PEM fuel cell design and manufacturing. *J Power Sources*. 2003;114(1):32-53. doi:10.1016/S0378-7753(02)00542-6

57. Karimi S, Fraser N, Roberts B, Foulkes FR. A Review of Metallic Bipolar Plates for Proton Exchange Membrane Fuel Cells: Materials and Fabrication Methods. *Adv Mater Sci Eng*. 2012;2012:1-22. doi:10.1155/2012/828070

58. Zhou X, Gan Y, Du J, et al. A review of hollow Pt-based nanocatalysts applied in proton exchange membrane fuel cells. *J Power Sources*. 2013;232:310-322. doi:10.1016/j.jpowsour.2013.01.062

59. Peighambardoust SJ, Rowshanzamir S, Amjadi M. Review of the proton exchange membranes for fuel cell applications. *Int J Hydrogen Energy*. 2010;35(17):9349-9384. doi:10.1016/j.ijhydene.2010.05.017

60. Kim DJ, Jo MJ, Nam SY. A review of polymer–nanocomposite electrolyte membranes for fuel cell application. *J Ind Eng Chem*. 2015;21:36-52. doi:10.1016/j.jiec.2014.04.030

61. Schmittinger W, Vahidi A. A review of the main parameters influencing long-term performance and durability of PEM fuel cells. *J Power Sources*. 2008;180(1):1-14. doi:10.1016/j.jpowsour.2008.01.070

62. Park S, Lee J-W, Popov BN. A review of gas diffusion layer in PEM fuel cells: Materials and designs. *Int J Hydrogen Energy*. 2012;37(7):5850-5865.

doi:10.1016/j.ijhydene.2011.12.148

63. Authayanun S, Im-orb K, Arpornwichanop A. A review of the development of high temperature proton exchange membrane fuel cells. *Chinese J Catal*. 2015;36(4):473-483. doi:10.1016/S1872-2067(14)60272-2

64. Shao Y, Yin G, Wang Z, Gao Y. Proton exchange membrane fuel cell from low temperature to high temperature: Material challenges. *J Power Sources*. 2007;167(2):235-242. doi:10.1016/j.jpowsour.2007.02.065

65. Sutharssan T, Montalvao D, Chen YK, Wang W-C, Pisac C, Elemara H. A review on prognostics and health monitoring of proton exchange membrane fuel cell. *Renew Sustain Energy Rev*. 2017;75:440-450. doi:10.1016/j.rser.2016.11.009

66. Shao M, Chang Q, Dodelet J-P, Chenitz R. Recent Advances in Electrocatalysts for Oxygen Reduction Reaction. *Chem Rev*. 2016;116(6):3594-3657. doi:10.1021/acs.chemrev.5b00462

67. Jaouen F, Proietti E, Lefèvre M, et al. Recent advances in non-precious metal catalysis for oxygen-reduction reaction in polymer electrolyte fuelcells. *Energy Environ Sci*. 2011;4(1):114-130. doi:10.1039/C0EE00011F

68. Shao M. Palladium-based electrocatalysts for hydrogen oxidation and oxygen reduction reactions. *J Power Sources*. 2011;196(5):2433-2444. doi:10.1016/j.jpowsour.2010.10.093

69. Costamagna P, Srinivasan S. Quantum jumps in the PEMFC science and technology from the 1960s to the year 2000. *J Power Sources*. 2001;102(1-2):242-252. doi:10.1016/S0378-7753(01)00807-2

70. Weber AZ, Balasubramanian S, Das PK. Proton Exchange Membrane Fuel Cells. In: *Advances in Chemical Engineering*. ; 2012:65-144. doi:10.1016/B978-0-12-386874-9.00003-8

71. Bose S, Kuila T, Nguyen TXH, Kim NH, Lau K, Lee JH. Polymer membranes for high temperature proton exchange membrane fuel cell: Recent advances and challenges. *Prog Polym Sci*. 2011;36(6):813-843. doi:10.1016/j.progpolymsci.2011.01.003

72. Liu C-Y, Sung C-C. A review of the performance and analysis of proton exchange membrane fuel cell membrane electrode assemblies. *J Power Sources*. 2012;220:348-353. doi:10.1016/j.jpowsour.2012.07.090

73. Zhang S, Yuan X-Z, Hin JNC, Wang H, Friedrich KA, Schulze M. A review of platinum-based catalyst layer degradation in proton exchange membrane fuel cells. *J Power Sources*. 2009;194(2):588-600. doi:10.1016/j.jpowsour.2009.06.073

74. Ticianelli EA. Methods to Advance Technology of Proton Exchange Membrane Fuel Cells. *J Electrochem Soc*. 1988;135(9):2209. doi:10.1149/1.2096240

75. Stampino PG, Molina D, Omati L, et al. Surface treatments with perfluoropolyether derivatives for the hydrophobization of gas diffusion layers for PEM fuel cells. *J Power Sources*. 2011;196(18):7645-7648. doi:10.1016/j.jpowsour.2011.04.039

76. Shetzline JA, Bukola S, Creager SE. A convenient miniature test platform for polyelectrolyte membrane fuel-cell research. *J Electroanal Chem*. 2017;797:8-15. doi:10.1016/j.jelechem.2017.05.009

77. Bukola S, Merzougui B, Akinpelu A, et al. Fe-N-C Electrocatalysts for Oxygen Reduction Reaction Synthesized by Using Aniline Salt and Fe 3+ /H 2 O 2 Catalytic System. *Electrochim Acta*. 2014;146:809-818. doi:10.1016/j.electacta.2014.08.152

78. Akinpelu A, Merzougui B, Bukola S, et al. A Pt-free Electrocatalyst Based on Pyrolized Vinazene-Carbon Composite for Oxygen Reduction Reaction. *Electrochim Acta*. 2015;161:305-311. doi:10.1016/j.electacta.2015.02.072

79. Merzougui B, Bukola S, Zaffou R. Further Understanding of Nitrogen-Doped Carbon Catalytic Property towards Oxygen Reduction Reaction (ORR). *Mater Today Proc*. 2016;3(2):691-695. doi:10.1016/j.matpr.2016.01.113

80. Bukola S, Merzougui B, Akinpelu A, Zeama M. Cobalt and Nitrogen Co-Doped Tungsten Carbide Catalyst for Oxygen Reduction and Hydrogen Evolution Reactions. *Electrochim Acta*. 2016;190:1113-1123. doi:10.1016/j.electacta.2015.12.074

81. Merzougui B, Hachimi A, Akinpelu A, Bukola S, Shao M. A Pt-free catalyst for oxygen reduction reaction based on Fe–N multiwalled carbon nanotube composites. *Electrochim Acta*. 2013;107:126-132. doi:10.1016/j.electacta.2013.06.016

82. Xing W, Yin G, Zhang J. *Rotating Electrode Methods and Oxygen Reduction Electrocatalysts*. Elsevier; 2014. doi:10.1016/C2012-0-06455-1

83. Shinozaki K, Zack JW, Richards RM, Pivovar BS, Kocha SS. Oxygen Reduction Reaction Measurements on Platinum Electrocatalysts Utilizing Rotating Disk

Electrode Technique. *J Electrochem Soc*. 2015;162(10):F1144-F1158. doi:10.1149/2.1071509jes

84. Du C, Tan Q, Yin G, Zhang J. Rotating Disk Electrode Method. In: *Rotating Electrode Methods and Oxygen Reduction Electrocatalysts*. Elsevier; 2014:171-198. doi:10.1016/B978-0-444-63278-4.00005-7

85. Kocha S. Best Practices and Benchmark Activities for ORR Measurements by the Rotating Disk Electrode Technique. *DOE Annu Prog Rep*. 2014.

86. Dalton F. ECS Classics: Historical Origins of the Rotating Ring-Disk Electrode. *Interface Mag*. 2016;25(3):50-59. doi:10.1149/2.f03163if

87. Kundu A, Karan K, Peppley BA, Sahai Y. FUEL CELLS – EXPLORATORY FUEL CELLS | Micro-Fuel Cells. In: *Encyclopedia of Electrochemical Power Sources*. ; 2009. doi:10.1016/b978-044452745-5.00913-8

88. Carmo M, Stolten D, Müller M, Poggemann L, Lohoff AS. Enabling High Throughput Screening of Polymer Electrolyte Membrane (PEM) Water Electrolysis Components via Miniature Test Cells. *J Electrochem Soc*. 2016;163(11):F3153-F3157. doi:10.1149/2.0211611jes

89. Taylor AD, Kim EY, Humes VP, Kizuka J, Thompson LT. Inkjet printing of carbon supported platinum 3-D catalyst layers for use in fuel cells. *J Power Sources*. 2007;171(1):101-106. doi:10.1016/j.jpowsour.2007.01.024

90. Yamazaki Y. Application of MEMS technology to micro fuel cells. *Electrochim Acta*. 2004;50(2-3):663-666. doi:10.1016/j.electacta.2004.01.092

91. Sun P, Wang K, Zhu H. Recent Developments in Graphene-Based Membranes:

Structure, Mass-Transport Mechanism and Potential Applications. *Adv Mater*. 2016;28(12):2287-2310. doi:10.1002/adma.201502595

92. Wan X, Huang Y, Chen Y. Focusing on Energy and Optoelectronic Applications: A Journey for Graphene and Graphene Oxide at Large Scale. *Acc Chem Res*. 2012;45(4):598-607. doi:10.1021/ar200229q

93. Geim AK, Novoselov KS. The rise of graphene. *Nat Mater*. 2007;6(3):183-191. doi:10.1038/nmat1849

94. Dhakate SR, Chauhan N, Sharma S, et al. An approach to produce single and double layer graphene from re-exfoliation of expanded graphite. *Carbon N Y*. 2011;49(6):1946-1954. doi:10.1016/j.carbon.2010.12.068

95. Lin T, Tang Y, Wang Y, et al. Scotch-tape-like exfoliation of graphite assisted with elemental sulfur and graphene–sulfur composites for high-performance lithium-sulfur batteries. *Energy Environ Sci*. 2013;6(4):1283. doi:10.1039/c3ee24324a

96. Sint K, Wang B, Král P. Selective Ion Passage through Functionalized Graphene Nanopores. *J Am Chem Soc*. 2008;130(49):16448-16449. doi:10.1021/ja804409f

97. Fischbein MD, Drndić M. Electron beam nanosculpting of suspended graphene sheets. *Appl Phys Lett*. 2008;93(11):113107. doi:10.1063/1.2980518

98. Du H, Li J, Zhang J, Su G, Li X, Zhao Y. Separation of Hydrogen and Nitrogen Gases with Porous Graphene Membrane. *J Phys Chem C*. 2011;115(47):23261-23266. doi:10.1021/jp206258u

99. Bunch JS, Verbridge SS, Alden JS, et al. Impermeable Atomic Membranes from

Graphene Sheets. *Nano Lett*. 2008;8(8):2458-2462. doi:10.1021/nl801457b

100. Schrier J. Helium Separation Using Porous Graphene Membranes. *J Phys Chem Lett*. 2010;1(15):2284-2287. doi:10.1021/jz100748x

101. Tian Z, Mahurin SM, Dai S, Jiang D. Ion-Gated Gas Separation through Porous Graphene. *Nano Lett*. 2017;17(3):1802-1807. doi:10.1021/acs.nanolett.6b05121

102. Nguyen BH, Nguyen VH. Promising applications of graphene and graphene-based nanostructures. *Adv Nat Sci Nanosci Nanotechnol*. 2016;7(2):023002. doi:10.1088/2043-6262/7/2/023002

103. Li D, Hu W, Zhang J, et al. Separation of Hydrogen Gas from Coal Gas by Graphene Nanopores. *J Phys Chem C*. 2015;119(45):25559-25565. doi:10.1021/acs.jpcc.5b06165

104. Kidambi PR, Terry RA, Wang L, et al. Assessment and control of the impermeability of graphene for atomically thin membranes and barriers. *Nanoscale*. 2017;9(24):8496-8507. doi:10.1039/C7NR01921A

105. Maassen J, Ji W, Guo H. First principles study of electronic transport through a Cu(111)|graphene junction. *Appl Phys Lett*. 2010;97(14):142105. doi:10.1063/1.3496490

106. Sun C, Wen B, Bai B. Recent advances in nanoporous graphene membrane for gas separation and water purification. *Sci Bull*. 2015;60(21):1807-1823. doi:10.1007/s11434-015-0914-9

107. Ambrosetti A, Silvestrelli PL. Gas Separation in Nanoporous Graphene from First Principle Calculations. *J Phys Chem C*. 2014;118(33):19172-19179.

doi:10.1021/jp504914u

108. Tsetseris L, Pantelides ST. Graphene: An impermeable or selectively permeable membrane for atomic species? *Carbon N Y*. 2014;67:58-63. doi:10.1016/j.carbon.2013.09.055

109. Y. Cui SIK and SK. Gas barrier performance of graphene/polymer nanocomposites. *Carbon N Y*. 2016;98:313-333.

110. Maassen J, Ji W, Guo H. First principles study of electronic transport through a Cu(111)|graphene junction. *Appl Phys Lett*. 2010;97(14):142105. doi:10.1063/1.3496490

111. Mauritz KA, Moore RB. State of Understanding of Nafion. *Chem Rev*. 2004;104(10):4535-4586. doi:10.1021/cr0207123

112. Kusoglu A, Weber AZ. New Insights into Perfluorinated Sulfonic-Acid Ionomers. *Chem Rev*. 2017;117(3):987-1104. doi:10.1021/acs.chemrev.6b00159

113. Miyake T, Rolandi M. Grotthuss mechanisms: from proton transport in proton wires to bioprotonic devices. *J Phys Condens Matter*. 2016;28(2):023001. doi:10.1088/0953-8984/28/2/023001

114. Paddison SJ, Paul R. The nature of proton transport in fully hydrated Nafion®. *Phys Chem Chem Phys*. 2002;4(7):1158-1163. doi:10.1039/b109792j

115. Riccardi D, König P, Prat-Resina X, et al. "Proton Holes" in Long-Range Proton Transfer Reactions in Solution and Enzymes: A Theoretical Analysis. *J Am Chem Soc*. 2006;128(50):16302-16311. doi:10.1021/ja065451j

116. Son DN, Kasai H. Proton transport through aqueous Nafion membrane. *Eur Phys J*

*E*. 2009;29(4):351-361. doi:10.1140/epje/i2009-10500-1

117. Merte LR, Peng G, Bechstein R, et al. Water-Mediated Proton Hopping on an Iron Oxide Surface. *Science (80- )*. 2012;336(6083):889-893. doi:10.1126/science.1219468

118. Godet J, Pasquarello A. Proton Diffusion Mechanism in Amorphous <math display="inline"> <msub> <mi>SiO</mi> <mn>2</mn> </msub> </math>. *Phys Rev Lett*. 2006;97(15):155901. doi:10.1103/PhysRevLett.97.155901

119. Feng S, Voth GA. Proton Solvation and Transport in Hydrated Nafion. *J Phys Chem B*. 2011;115(19):5903-5912. doi:10.1021/jp2002194

120. Vuilleumier R, Borgis D. Hopping along hydrogen bonds. *Nat Chem*. 2012;4(6):432-433. doi:10.1038/nchem.1365

121. Hassanali A, Giberti F, Cuny J, Kühne TD, Parrinello M. Proton transfer through the water gossamer. *Proc Natl Acad Sci*. 2013;110(34):13723-13728. doi:10.1073/pnas.1306642110

122. Hoarfrost ML, Tyagi MS, Segalman RA, Reimer JA. Effect of Confinement on Proton Transport Mechanisms in Block Copolymer/Ionic Liquid Membranes. *Macromolecules*. 2012;45(7):3112-3120. doi:10.1021/ma202741g

123. Neyerlin KC, Gu W, Jorne J, Gasteiger HA. Study of the Exchange Current Density for the Hydrogen Oxidation and Evolution Reactions. *J Electrochem Soc*. 2007;154(7):B631. doi:10.1149/1.2733987

124. Ferrari AC, Meyer JC, Scardaci V, et al. Raman Spectrum of Graphene and Graphene Layers. *Phys Rev Lett*. 2006;97(18):187401.

doi:10.1103/PhysRevLett.97.187401

125. Malard LM, Pimenta MA, Dresselhaus G, Dresselhaus MS. Raman spectroscopy in graphene. *Phys Rep*. 2009;473(5-6):51-87. doi:10.1016/j.physrep.2009.02.003

126. Ferrari AC. Raman spectroscopy of graphene and graphite: Disorder, electron–phonon coupling, doping and nonadiabatic effects. *Solid State Commun*. 2007;143(1-2):47-57. doi:10.1016/j.ssc.2007.03.052

127. Kudin KN, Ozbas B, Schniepp HC, Prud'homme RK, Aksay IA, Car R. Raman Spectra of Graphite Oxide and Functionalized Graphene Sheets. *Nano Lett*. 2008;8(1):36-41. doi:10.1021/nl071822y

128. Eckmann A, Felten A, Mishchenko A, et al. Probing the Nature of Defects in Graphene by Raman Spectroscopy. *Nano Lett*. 2012;12(8):3925-3930. doi:10.1021/nl300901a

129. Casiraghi C, Pisana S, Novoselov KS, Geim AK, Ferrari AC. Raman fingerprint of charged impurities in graphene. *Appl Phys Lett*. 2007;91(23):233108. doi:10.1063/1.2818692

130. Dresselhaus MS, Jorio A, Saito R. Characterizing Graphene, Graphite, and Carbon Nanotubes by Raman Spectroscopy. *Annu Rev Condens Matter Phys*. 2010;1(1):89-108. doi:10.1146/annurev-conmatphys-070909-103919

131. Lee DS, Riedl C, Krauss B, von Klitzing K, Starke U, Smet JH. Raman Spectra of Epitaxial Graphene on SiC and of Epitaxial Graphene Transferred to SiO 2. *Nano Lett*. 2008;8(12):4320-4325. doi:10.1021/nl802156w

132. Hulman M. Raman spectroscopy of graphene. In: *Graphene*. Elsevier; 2014:156-

183. doi:10.1533/9780857099334.2.156

133. Das A, Chakraborty B, Sood AK. Raman spectroscopy of graphene on different substrates and influence of defects. *Bull Mater Sci*. 2008;31(3):579-584. doi:10.1007/s12034-008-0090-5

134. Hao Y, Wang Y, Wang L, et al. Probing Layer Number and Stacking Order of Few-Layer Graphene by Raman Spectroscopy. *Small*. 2010;6(2):195-200. doi:10.1002/smll.200901173

135. Martins Ferreira EH, Moutinho MVO, Stavale F, et al. Evolution of the Raman spectra from single-, few-, and many-layer graphene with increasing disorder. *Phys Rev B*. 2010;82(12):125429. doi:10.1103/PhysRevB.82.125429

136. Reich S, Thomsen C. Raman spectroscopy of graphite. Ferrari A, Robertson J, eds. *Philos Trans R Soc London Ser A Math Phys Eng Sci*. 2004;362(1824):2271-2288. doi:10.1098/rsta.2004.1454

137. Ferrari AC, Basko DM. Raman spectroscopy as a versatile tool for studying the properties of graphene. *Nat Nanotechnol*. 2013;8(4):235-246. doi:10.1038/nnano.2013.46

138. Ni Z, Wang Y, Yu T, Shen Z. Raman spectroscopy and imaging of graphene. *Nano Res*. 2008;1(4):273-291. doi:10.1007/s12274-008-8036-1

139. Němeček D, Thomas GJ. Raman Spectroscopy of Viruses and Viral Proteins. In: *Frontiers of Molecular Spectroscopy*. Elsevier; 2009:553-595. doi:10.1016/B978-0-444-53175-9.00016-7

140. Kaniyoor A, Ramaprabhu S. A Raman spectroscopic investigation of graphite

oxide derived graphene. *AIP Adv*. 2012;2(3):032183. doi:10.1063/1.4756995

141. Ferrari AC, Robertson J. Interpretation of Raman spectra of disordered and amorphous carbon. *Phys Rev B*. 2000;61(20):14095-14107. doi:10.1103/PhysRevB.61.14095

142. Poncharal P, Ayari A, Michel T, Sauvajol J-L. Raman spectra of misoriented bilayer graphene. *Phys Rev B*. 2008;78(11):113407. doi:10.1103/PhysRevB.78.113407

143. Schedin F, Lidorikis E, Lombardo A, et al. Surface-Enhanced Raman Spectroscopy of Graphene. *ACS Nano*. 2010;4(10):5617-5626. doi:10.1021/nn1010842

144. Wang Y ying, Ni ZH, Yu T, et al. Raman Studies of Monolayer Graphene: The Substrate Effect. *J Phys Chem C*. 2008;112(29):10637-10640. doi:10.1021/jp8008404

145. Pimenta MA, Dresselhaus G, Dresselhaus MS, Cançado LG, Jorio A, Saito R. Studying disorder in graphite-based systems by Raman spectroscopy. *Phys Chem Chem Phys*. 2007;9(11):1276-1290. doi:10.1039/B613962K

146. Calizo I, Ghosh S, Bao W, Miao F, Ning Lau C, Balandin AA. Raman nanometrology of graphene: Temperature and substrate effects. *Solid State Commun*. 2009;149(27-28):1132-1135. doi:10.1016/j.ssc.2009.01.036

147. Casiraghi C, Hartschuh A, Qian H, et al. Raman Spectroscopy of Graphene Edges. *Nano Lett*. 2009;9(4):1433-1441. doi:10.1021/nl8032697

148. Ni ZH, Yu T, Lu YH, Wang YY, Feng YP, Shen ZX. Uniaxial Strain on

Graphene: Raman Spectroscopy Study and Band-Gap Opening. *ACS Nano*. 2008;2(11):2301-2305. doi:10.1021/nn800459e

149. Ferralis N. Probing mechanical properties of graphene with Raman spectroscopy. *J Mater Sci*. 2010. doi:10.1007/s10853-010-4673-3

150. Graf D, Molitor F, Ensslin K, et al. Spatially Resolved Raman Spectroscopy of Single- and Few-Layer Graphene. *Nano Lett*. 2007;7(2):238-242. doi:10.1021/nl061702a

151. Xie L, Ling X, Fang Y, Zhang J, Liu Z. Graphene as a Substrate To Suppress Fluorescence in Resonance Raman Spectroscopy. *J Am Chem Soc*. 2009;131(29):9890-9891. doi:10.1021/ja9037593

152. Berciaud S, Ryu S, Brus LE, Heinz TF. Probing the Intrinsic Properties of Exfoliated Graphene: Raman Spectroscopy of Free-Standing Monolayers. *Nano Lett*. 2009;9(1):346-352. doi:10.1021/nl8031444

153. Röhrl J, Hundhausen M, Emtsev K V., Seyller T, Graupner R, Ley L. Raman spectra of epitaxial graphene on SiC(0001). *Appl Phys Lett*. 2008;92(20):201918. doi:10.1063/1.2929746

154. Kim K, Coh S, Tan LZ, et al. Raman Spectroscopy Study of Rotated Double-Layer Graphene: Misorientation-Angle Dependence of Electronic Structure. *Phys Rev Lett*. 2012;108(24):246103. doi:10.1103/PhysRevLett.108.246103

155. Saito R, Furukawa M, Dresselhaus G, Dresselhaus MS. Raman spectra of graphene ribbons. *J Phys Condens Matter*. 2010;22(33):334203. doi:10.1088/0953-8984/22/33/334203

156. Cuong TV, Pham VH, Tran QT, et al. Photoluminescence and Raman studies of graphene thin films prepared by reduction of graphene oxide. *Mater Lett*. 2010;64(3):399-401. doi:10.1016/j.matlet.2009.11.029

157. Graf D, Molitor F, Ensslin K, et al. Raman imaging of graphene. *Solid State Commun*. 2007. doi:10.1016/j.ssc.2007.01.050

158. Bokobza L, Bruneel J-L, Couzi M. Raman spectroscopy as a tool for the analysis of carbon-based materials (highly oriented pyrolitic graphite, multilayer graphene and multiwall carbon nanotubes) and of some of their elastomeric composites. *Vib Spectrosc*. 2014;74:57-63. doi:10.1016/j.vibspec.2014.07.009

159. Wu J-B, Lin M-L, Cong X, Liu H-N, Tan P-H. Raman spectroscopy of graphene-based materials and its applications in related devices. *Chem Soc Rev*. 2018;47(5):1822-1873. doi:10.1039/C6CS00915H

160. Sato K, Park JS, Saito R, et al. Raman spectra of out-of-plane phonons in bilayer graphene. *Phys Rev B*. 2011;84(3):035419. doi:10.1103/PhysRevB.84.035419

161. Ryu S, Maultzsch J, Han MY, Kim P, Brus LE. Raman Spectroscopy of Lithographically Patterned Graphene Nanoribbons. *ACS Nano*. 2011;5(5):4123-4130. doi:10.1021/nn200799y

162. Tuinstra F, Koenig JL. Raman Spectrum of Graphite. *J Chem Phys*. 1970;53(3):1126-1130. doi:10.1063/1.1674108

163. Popov VN, Henrard L, Lambin P. Resonant Raman spectra of graphene with point defects. *Carbon N Y*. 2009;47(10):2448-2455. doi:10.1016/j.carbon.2009.04.043

164. Beams R, Gustavo Cançado L, Novotny L. Raman characterization of defects and

dopants in graphene. *J Phys Condens Matter*. 2015;27(8):083002. doi:10.1088/0953-8984/27/8/083002

165. Yu Q, Jauregui LA, Wu W, et al. Control and characterization of individual grains and grain boundaries in graphene grown by chemical vapour deposition. *Nat Mater*. 2011;10(6):443-449. doi:10.1038/nmat3010

166. Saito R, Hofmann M, Dresselhaus G, Jorio A, Dresselhaus MS. Raman spectroscopy of graphene and carbon nanotubes. *Adv Phys*. 2011;60(3):413-550. doi:10.1080/00018732.2011.582251

167. Lee J-U, Yoon D, Cheong H. Estimation of Young's Modulus of Graphene by Raman Spectroscopy. *Nano Lett*. 2012;12(9):4444-4448. doi:10.1021/nl301073q

168. Park JS, Reina A, Saito R, Kong J, Dresselhaus G, Dresselhaus MS. G′ band Raman spectra of single, double and triple layer graphene. *Carbon N Y*. 2009. doi:10.1016/j.carbon.2009.01.009

169. Wall M. The Raman spectroscopy of graphene and the determination of layer thickness. *Thermo Sci Appl note*. 2011.

170. Frank O, Mohr M, Maultzsch J, et al. Raman 2D-Band Splitting in Graphene: Theory and Experiment. *ACS Nano*. 2011;5(3):2231-2239. doi:10.1021/nn103493g

171. Han MY, Özyilmaz B, Zhang Y, Kim P. Energy Band-Gap Engineering of Graphene Nanoribbons. *Phys Rev Lett*. 2007;98(20):206805. doi:10.1103/PhysRevLett.98.206805

172. Rao CNR, Biswas K, Subrahmanyam KS, Govindaraj A. Graphene, the new nanocarbon. *J Mater Chem*. 2009;19(17):2457. doi:10.1039/b815239j

173. Bruna M, Borini S. Raman signature of electron-electron correlation in chemically doped few-layer graphene. *Phys Rev B*. 2011;83(24):241401. doi:10.1103/PhysRevB.83.241401

174. Bukola S, Merzougui B, Akinpelu A, et al. Fe-N-C Electrocatalysts for Oxygen Reduction Reaction Synthesized by Using Aniline Salt and Fe 3+ /H 2 O 2 Catalytic System. *Electrochim Acta*. 2014;146:809-818. doi:10.1016/j.electacta.2014.08.152

175. Riedl C, Coletti C, Starke U. Structural and electronic properties of epitaxial graphene on SiC(0 0 0 1): a review of growth, characterization, transfer doping and hydrogen intercalation. *J Phys D Appl Phys*. 2010;43(37):374009. doi:10.1088/0022-3727/43/37/374009

176. Castro Neto AH, Guinea F, Peres NMR, Novoselov KS, Geim AK. The electronic properties of graphene. *Rev Mod Phys*. 2009;81(1):109-162. doi:10.1103/RevModPhys.81.109

177. Cong C, Yu T, Saito R, Dresselhaus GF, Dresselhaus MS. Second-Order Overtone and Combination Raman Modes of Graphene Layers in the Range of 1690−2150 cm −1. *ACS Nano*. 2011;5(3):1600-1605. doi:10.1021/nn200010m

178. Kitt JP, Bryce DA, Harris JM. Spatial Filtering of a Diode Laser Beam for Confocal Raman Microscopy. *Appl Spectrosc*. 2015;69(4):513-517. doi:10.1366/14-07671

179. Rodríguez-Pérez L, Herranz MÁ, Martín N. The chemistry of pristine graphene. *Chem Commun*. 2013;49(36):3721. doi:10.1039/c3cc38950b

180. Schriver M, Regan W, Gannett WJ, Zaniewski AM, Crommie MF, Zettl A. Graphene as a Long-Term Metal Oxidation Barrier: Worse Than Nothing. *ACS Nano*. 2013;7(7):5763-5768. doi:10.1021/nn4014356

181. Peres NMR. The transport properties of graphene. *J Phys Condens Matter*. 2009;21(32):323201. doi:10.1088/0953-8984/21/32/323201

182. Poltavsky I, Zheng L, Mortazavi M, Tkatchenko A. Quantum tunneling of thermal protons through pristine graphene. *J Chem Phys*. 2018;148(20):1-21. doi:10.1063/1.5024317

183. Achtyl JL, Unocic RR, Xu L, et al. Aqueous proton transfer across single-layer graphene. *Nat Commun*. 2015. doi:10.1038/ncomms7539

184. Walker MI, Braeuninger-Weimer P, Weatherup RS, Hofmann S, Keyser UF. Measuring the proton selectivity of graphene membranes. *Appl Phys Lett*. 2015;107(21):213104. doi:10.1063/1.4936335

185. Bukola S, Creager SE. A charge-transfer resistance model and Arrhenius activation analysis for hydrogen ion transmission across single-layer graphene. *Electrochim Acta*. 2019;296:1-7. doi:10.1016/j.electacta.2018.11.005

186. Jiang DE, Chen Z. *Graphene Chemistry*. (Jiang D-E, Chen Z, eds.). Chichester, UK: John Wiley & Sons, Ltd; 2013. doi:10.1002/9781118691281

187. Konatham D, Yu J, Ho TA, Striolo A. Simulation Insights for Graphene-Based Water Desalination Membranes. *Langmuir*. 2013;29(38):11884-11897. doi:10.1021/la4018695

188. Zhao S, Xue J, Kang W. Ion selection of charge-modified large nanopores in a

graphene sheet. *J Chem Phys*. 2013;139(11):114702. doi:10.1063/1.4821161

189. Qiu Y-H, Li K, Chen W-Y, Si W, Tan Q-Y, Chen Y-F. Ion and water transport in charge-modified graphene nanopores. *Chinese Phys B*. 2015;24(10):108201. doi:10.1088/1674-1056/24/10/108201

190. Shahbabaei M, Kim D. Molecular Dynamics Simulation of Water Transport Mechanisms through Nanoporous Boron Nitride and Graphene Multilayers. *J Phys Chem B*. 2017;121(16):4137-4144. doi:10.1021/acs.jpcb.6b12757

191. Yan Y, Li W, Král P. Enantioselective Molecular Transport in Multilayer Graphene Nanopores. *Nano Lett*. 2017;17(11):6742-6746. doi:10.1021/acs.nanolett.7b02846

192. Suk ME, Aluru NR. Ion transport in sub-5-nm graphene nanopores. *J Chem Phys*. 2014. doi:10.1063/1.4866643

193. Mahmoud KA, Mansoor B, Mansour A, Khraisheh M. Functional graphene nanosheets: The next generation membranes for water desalination. *Desalination*. 2015;356:208-225. doi:10.1016/j.desal.2014.10.022

194. Zhang Q, Ju M, Chen L, Zeng XC. Differential Permeability of Proton Isotopes through Graphene and Graphene Analogue Monolayer. *J Phys Chem Lett*. 2016;7(17):3395-3400. doi:10.1021/acs.jpclett.6b01507

195. Seel M, Pandey R. Proton and hydrogen transport through two-dimensional monolayers. *2D Mater*. 2016;3(2):025004. doi:10.1088/2053-1583/3/2/025004

196. Banhart F, Kotakoski J, Krasheninnikov A V. Structural Defects in Graphene. *ACS Nano*. 2011;5(1):26-41. doi:10.1021/nn102598m

197. Liu L, Qing M, Wang Y, Chen S. Defects in Graphene: Generation, Healing, and Their Effects on the Properties of Graphene: A Review. *J Mater Sci Technol*. 2015;31(6):599-606. doi:10.1016/j.jmst.2014.11.019

198. Choi P, Jalani NH, Datta R. Thermodynamics and Proton Transport in Nafion. *J Electrochem Soc*. 2005;152(3):E84. doi:10.1149/1.1855872

199. Zawodzinski TA. Water Uptake by and Transport Through Nafion® 117 Membranes. *J Electrochem Soc*. 1993;140(4):1041. doi:10.1149/1.2056194

200. Peters KS. A Theory−Experiment Conundrum for Proton Transfer. *Acc Chem Res*. 2009;42(1):89-96. doi:10.1021/ar8001156

201. Staib A, Borgis D, Hynes JT. Proton transfer in hydrogen-bonded acid–base complexes in polar solvents. *J Chem Phys*. 1995;102(6):2487-2505. doi:10.1063/1.468678

202. Bard A, Faulkner L. Allen J. Bard and Larry R. Faulkner, Electrochemical Methods: Fundamentals and Applications, New York: Wiley, 2001. *Russ J Electrochem*. 2002. doi:10.1023/A:1021637209564

203. Aziz M, Ismail AF. X-Ray Photoelectron Spectroscopy (XPS). In: *Membrane Characterization*. ; 2017. doi:10.1016/B978-0-444-63776-5.00005-X

204. Leenaerts O, Partoens B, Peeters FM. Graphene: A perfect nanoballoon. *Appl Phys Lett*. 2008;93(19):193107. doi:10.1063/1.3021413

205. Marcus RA. On the theory of ion transfer rates across the interface of two immiscible liquids. *J Chem Phys*. 2000;113(4):1618-1629. doi:10.1063/1.481950

206. Benjamin l. Mechanism and Dynamics of Ion Transfer Across a Liquid-Liquid

Interface. *Science (80- ).* 1993;261(5128):1558-1560. doi:10.1126/science.261.5128.1558

207. Benjamin I. Dynamics of ion transfer across a liquid-liquid interface: A comparison between molecular dynamics and a diffusion model. *J Chem Phys*. 1992. doi:10.1063/1.462496

208. Samec Z, Mareček V, Koryta J, Khalil MW. Investigation of ion transfer across the interface between two immiscible electrolyte solutions by cyclic voltammetry. *J Electroanal Chem Interfacial Electrochem*. 1977;83(2):393-397. doi:10.1016/S0022-0728(77)80186-1

209. Hupp JT, Weaver MJ. The frequency factor for outer-sphere electrochemical reactions. *J Electroanal Chem*. 1983. doi:10.1016/S0022-0728(83)80028-X

210. Aydin H, Bacaksiz C, Yagmurcukardes N, et al. Experimental and computational investigation of graphene/SAMs/n-Si Schottky diodes. *Appl Surf Sci*. 2018;428:1010-1017. doi:10.1016/j.apsusc.2017.09.204

211. Li Y, Yuan H, von dem Bussche A, et al. Graphene microsheets enter cells through spontaneous membrane penetration at edge asperities and corner sites. *Proc Natl Acad Sci*. 2013;110(30):12295-12300. doi:10.1073/pnas.1222276110

212. Haghighatpanah S, Börjesson A, Amara H, Bichara C, Bolton K. Computational studies of graphene growth mechanisms. *Phys Rev B*. 2012;85(20):205448. doi:10.1103/PhysRevB.85.205448

213. Yoon K, Ostadhossein A, van Duin ACT. Atomistic-scale simulations of the chemomechanical behavior of graphene under nanoprojectile impact. *Carbon N Y*.

2016;99:58-64. doi:10.1016/j.carbon.2015.11.052

214. Miao M, Nardelli MB, Wang Q, Liu Y. First principles study of the permeability of graphene to hydrogen atoms. *Phys Chem Chem Phys*. 2013;15(38):16132. doi:10.1039/c3cp52318g

215. Casolo S, Løvvik OM, Martinazzo R, Tantardini GF. Understanding adsorption of hydrogen atoms on graphene. *J Chem Phys*. 2009;130(5):054704. doi:10.1063/1.3072333

216. Şahin H, Senger RT. First-principles calculations of spin-dependent conductance of graphene flakes. *Phys Rev B*. 2008;78(20):205423. doi:10.1103/PhysRevB.78.205423

217. Nachimuthu S, Lai P-J, Jiang J-C. Efficient hydrogen storage in boron doped graphene decorated by transition metals – A first-principles study. *Carbon N Y*. 2014;73:132-140. doi:10.1016/j.carbon.2014.02.048

218. Ma F, Guo Z, Xu K, Chu PK. First-principle study of energy band structure of armchair graphene nanoribbons. *Solid State Commun*. 2012;152(13):1089-1093. doi:10.1016/j.ssc.2012.04.058

219. Tao Y, Xue Q, Liu Z, et al. Tunable Hydrogen Separation in Porous Graphene Membrane: First-Principle and Molecular Dynamic Simulation. *ACS Appl Mater Interfaces*. 2014;6(11):8048-8058. doi:10.1021/am4058887

220. Wu H-Y, Fan X, Kuo J-L, Deng W-Q. DFT Study of Hydrogen Storage by Spillover on Graphene with Boron Substitution. *J Phys Chem C*. 2011;115(18):9241-9249. doi:10.1021/jp200038b

221. Shi L, Xu A, Chen G, Zhao T. Theoretical Understanding of Mechanisms of Proton Exchange Membranes Made of 2D Crystals with Ultrahigh Selectivity. *J Phys Chem Lett*. 2017;8(18):4354-4361. doi:10.1021/acs.jpclett.7b01999

222. Mishchenko A, Grigorenko AN, Dryfe RAW, Radha B, Grigorieva I V, Geim AK. Sieving hydrogen isotopes through two-dimensional crystals. *Science (80- ).* 2016.

223. Kroes JMH, Fasolino A, Katsnelson MI. Density functional based simulations of proton permeation of graphene and hexagonal boron nitride. *Phys Chem Chem Phys*. 2017;19(8):5813-5817. doi:10.1039/C6CP08923B

224. Hu W, Yang J. First-principles study of two-dimensional van der Waals heterojunctions. *Comput Mater Sci*. 2016;112:518-526. doi:10.1016/j.commatsci.2015.06.033

225. Giuliani A, Bruni F, Ricci MA, Adams MA. Isotope Quantum Effects on the Water Proton Mean Kinetic Energy. *Phys Rev Lett*. 2011;106(25):255502. doi:10.1103/PhysRevLett.106.255502

226. Krishtalik LI. The mechanism of the proton transfer: an outline. *Biochim Biophys Acta - Bioenerg*. 2000;1458(1):6-27. doi:10.1016/S0005-2728(00)00057-8

227. Klein O, Aguilar-Parrilla F, Lopez JM, Jagerovic N, Elguero J, Limbach H-H. Dynamic NMR Study of the Mechanisms of Double, Triple, and Quadruple Proton and Deuteron Transfer in Cyclic Hydrogen Bonded Solids of Pyrazole Derivatives. *J Am Chem Soc*. 2004;126(37):11718-11732. doi:10.1021/ja0493650

228. Johansson AL, Chakrabarty S, Berthold CL, Högbom M, Warshel A, Brzezinski P. Proton-transport mechanisms in cytochrome c oxidase revealed by studies of

kinetic isotope effects. *Biochim Biophys Acta - Bioenerg*. 2011. doi:10.1016/j.bbabio.2011.03.012

229. Savéant J-M. Concerted Proton-Electron Transfers: Fundamentals and Recent Developments. *Annu Rev Anal Chem*. 2014;7(1):537-560. doi:10.1146/annurev-anchem-071213-020315

230. Laidler KJ, King MC. Development of transition-state theory. *J Phys Chem*. 1983;87(15):2657-2664. doi:10.1021/j100238a002

231. Truhlar DG, Garrett BC, Klippenstein SJ. Current Status of Transition-State Theory. *J Phys Chem*. 1996;100(31):12771-12800. doi:10.1021/jp953748q

232. Truhlar DG, Hase WL, Hynes JT. Current status of transition-state theory. *J Phys Chem*. 1983;87(15):2664-2682. doi:10.1021/j100238a003

233. Du Q, Superfine R, Freysz E, Shen YR. Vibrational spectroscopy of water at the vapor/water interface. *Phys Rev Lett*. 1993;70(15):2313-2316. doi:10.1103/PhysRevLett.70.2313

234. Sobczyk L, Obrzud M, Filarowski A. H/D isotope effects in hydrogen bonded systems. *Molecules*. 2013. doi:10.3390/molecules18044467

235. Maréchal Y. Infrared spectra of water. I. Effect of temperature and of H / D isotopic dilution. *J Chem Phys*. 1991;95(8):5565-5573. doi:10.1063/1.461630

236. Max J-J, Chapados C. Isotope effects in liquid water by infrared spectroscopy. *J Chem Phys*. 2002;116(11):4626-4642. doi:10.1063/1.1448286

237. Max J-J, Chapados C. Isotope effects in liquid water by infrared spectroscopy. III. H2O and D2O spectra from 6000to0cm−1. *J Chem Phys*. 2009;131(18):184505.

doi:10.1063/1.3258646

238. Fecko CJ. Ultrafast Hydrogen-Bond Dynamics in the Infrared Spectroscopy of Water. *Science (80- ).* 2003;301(5640):1698-1702. doi:10.1126/science.1087251

239. Max J-J, Chapados C. Isotope effects in liquid water by infrared spectroscopy. IV. No free OH groups in liquid water. *J Chem Phys*. 2010;133(16):164509. doi:10.1063/1.3505321

240. Colvin ME, Raine GP, Schaefer HF, Dupuis M. Infrared intensities of H 3 O + , H 2 DO + , HD 2 O + , and D 3 O +. *J Chem Phys*. 1983;79(3):1551-1552. doi:10.1063/1.445953

241. Bukola S, Beard K, Korzeniewski C, Harris JM, Creager SE. Single-Layer Graphene Sandwiched between Proton-Exchange Membranes for Selective Proton Transmission. *ACS Appl Nano Mater*. 2019;2(2):964-974. doi:10.1021/acsanm.8b02270

242. Inaba M, Kinumoto T, Kiriake M, Umebayashi R, Tasaka A, Ogumi Z. Gas crossover and membrane degradation in polymer electrolyte fuel cells. *Electrochim Acta*. 2006;51(26):5746-5753. doi:10.1016/j.electacta.2006.03.008

243. Cheng X, Zhang J, Tang Y, et al. Hydrogen crossover in high-temperature PEM fuel cells. *J Power Sources*. 2007;167(1):25-31. doi:10.1016/j.jpowsour.2007.02.027

244. Heinzel A, Barragán VM. A review of the state-of-the-art of the methanol crossover in direct methanol fuel cells. *J Power Sources*. 1999;84(1):70-74. doi:10.1016/S0378-7753(99)00302-X

245. Kocha SS, Deliang Yang J, Yi JS. Characterization of gas crossover and its implications in PEM fuel cells. *AIChE J*. 2006;52(5):1916-1925. doi:10.1002/aic.10780

246. Weber AZ. Gas-Crossover and Membrane-Pinhole Effects in Polymer-Electrolyte Fuel Cells. *J Electrochem Soc*. 2008;155(6):B521. doi:10.1149/1.2898130

247. Pei P, Chen H. Main factors affecting the lifetime of Proton Exchange Membrane fuel cells in vehicle applications: A review. *Appl Energy*. 2014;125:60-75. doi:10.1016/j.apenergy.2014.03.048

248. Jeong K-J, Miesse CM, Choi J-H, et al. Fuel crossover in direct formic acid fuel cells. *J Power Sources*. 2007;168(1):119-125. doi:10.1016/j.jpowsour.2007.02.062

249. Chippar P, Ju H. Numerical modeling and investigation of gas crossover effects in high temperature proton exchange membrane (PEM) fuel cells. *Int J Hydrogen Energy*. 2013;38(18):7704-7714. doi:10.1016/j.ijhydene.2012.07.123

250. Gurau B, Smotkin ES. Methanol crossover in direct methanol fuel cells: A link between power and energy density. *J Power Sources*. 2002. doi:10.1016/S0378-7753(02)00445-7

251. Kreitmeier S, Lerch P, Wokaun A, Büchi FN. Local Degradation at Membrane Defects in Polymer Electrolyte Fuel Cells. *J Electrochem Soc*. 2013;160(4):F456-F463. doi:10.1149/1.023306jes

252. Okada T, Xie G, Gorseth O, Kjelstrup S, Nakamura N, Arimura T. Ion and water transport characteristics of Nafion membranes as electrolytes. *Electrochim Acta*. 1998;43(24):3741-3747. doi:10.1016/S0013-4686(98)00132-7

253. O'Hern SC, Jang D, Bose S, et al. Nanofiltration across defect-sealed nanoporous monolayer graphene. *Nano Lett*. 2015. doi:10.1021/acs.nanolett.5b00456

254. Agius Anastasi A, Ritos K, Cassar G, Borg MK. Mechanical properties of pristine and nanoporous graphene. *Mol Simul*. 2016;42(18):1502-1511. doi:10.1080/08927022.2016.1209753

255. Walker MI, Ubych K, Saraswat V, et al. Extrinsic Cation Selectivity of 2D Membranes. *ACS Nano*. 2017;11(2):1340-1346. doi:10.1021/acsnano.6b06034

256. Drahushuk LW, Strano MS. Mechanisms of Gas Permeation through Single Layer Graphene Membranes. *Langmuir*. 2012;28(48):16671-16678. doi:10.1021/la303468r

257. Huang L, Zhang M, Li C, Shi G. Graphene-Based Membranes for Molecular Separation. *J Phys Chem Lett*. 2015;6(14):2806-2815. doi:10.1021/acs.jpclett.5b00914

258. O'Hern SC, Boutilier MSH, Idrobo J-C, et al. Selective Ionic Transport through Tunable Subnanometer Pores in Single-Layer Graphene Membranes. *Nano Lett*. 2014;14(3):1234-1241. doi:10.1021/nl404118f

259. Surwade SP, Smirnov SN, Vlassiouk I V., et al. Water desalination using nanoporous single-layer graphene. *Nat Nanotechnol*. 2015;10(5):459-464. doi:10.1038/nnano.2015.37

260. Cohen-Tanugi D, Grossman JC. Water Desalination across Nanoporous Graphene. *Nano Lett*. 2012;12(7):3602-3608. doi:10.1021/nl3012853

261. Cohen-Tanugi D, Grossman JC. Nanoporous graphene as a reverse osmosis

membrane: Recent insights from theory and simulation. *Desalination*. 2015;366:59-70. doi:10.1016/j.desal.2014.12.046

262. Cohen-Tanugi D, Grossman JC. Mechanical Strength of Nanoporous Graphene as a Desalination Membrane. *Nano Lett*. 2014;14(11):6171-6178. doi:10.1021/nl502399y

263. Garaj S, Hubbard W, Reina A, Kong J, Branton D, Golovchenko JA. Graphene as a subnanometre trans-electrode membrane. *Nature*. 2010;467(7312):190-193. doi:10.1038/nature09379

264. Umeyama D, Horike S, Inukai M, Itakura T, Kitagawa S. Inherent Proton Conduction in a 2D Coordination Framework. *J Am Chem Soc*. 2012;134(30):12780-12785. doi:10.1021/ja304693r

265. Lapid H, Agmon N, Petersen MK, Voth GA. A bond-order analysis of the mechanism for hydrated proton mobility in liquid water. *J Chem Phys*. 2005. doi:10.1063/1.1814973

266. Gileadi E, Kirowa-Eisner E. Electrolytic conductivity—the hopping mechanism of the proton and beyond. *Electrochim Acta*. 2006;51(27):6003-6011. doi:10.1016/j.electacta.2006.03.084

267. Grancha T, Ferrando-Soria J, Cano J, et al. Insights into the Dynamics of Grotthuss Mechanism in a Proton-Conducting Chiral bio MOF. *Chem Mater*. 2016;28(13):4608-4615. doi:10.1021/acs.chemmater.6b01286

268. Tuckerman ME, Marx D, Parrinello M. The nature and transport mechanism of hydrated hydroxide ions in aqueous solution. *Nature*. 2002;417(6892):925-929.

doi:10.1038/nature00797

269. Mabuchi T, Tokumasu T. Effect of bound state of water on hydronium ion mobility in hydrated Nafion using molecular dynamics simulations. *J Chem Phys*. 2014;141(10):104904. doi:10.1063/1.4894813

270. Saito M, Hayamizu K, Okada T. Temperature Dependence of Ion and Water Transport in Perfluorinated Ionomer Membranes for Fuel Cells. *J Phys Chem B*. 2005;109(8):3112-3119. doi:10.1021/jp045624w

271. Ohshima H, Ohki S. Donnan potential and surface potential of a charged membrane. *Biophys J*. 1985;47(5):673-678. doi:10.1016/S0006-3495(85)83963-1

272. Ohshima H, Kondo T. Membrane potential and Donnan potential. *Biophys Chem*. 1988;29(3):277-281. doi:10.1016/0301-4622(88)85049-X

273. Galama AH, Post JW, Cohen Stuart MA, Biesheuvel PM. Validity of the Boltzmann equation to describe Donnan equilibrium at the membrane–solution interface. *J Memb Sci*. 2013;442:131-139. doi:10.1016/j.memsci.2013.04.022

274. Bandini S, Vezzani D. Nanofiltration modeling: The role of dielectric exclusion in membrane characterization. *Chem Eng Sci*. 2003. doi:10.1016/S0009-2509(03)00212-4

275. Lai W, Haile SM. Impedance Spectroscopy as a Tool for Chemical and Electrochemical Analysis of Mixed Conductors: A Case Study of Ceria. *J Am Ceram Soc*. 2005;88(11):2979-2997. doi:10.1111/j.1551-2916.2005.00740.x

276. Soboleva T, Xie Z, Shi Z, Tsang E, Navessin T, Holdcroft S. Investigation of the through-plane impedance technique for evaluation of anisotropy of proton

conducting polymer membranes. *J Electroanal Chem*. 2008;622(2):145-152. doi:10.1016/j.jelechem.2008.05.017

277. Haufe S, Stimming U. Proton conducting membranes based on electrolyte filled microporous matrices. *J Memb Sci*. 2001. doi:10.1016/S0376-7388(00)00637-2

278. Gardner CL, Anantaraman A V. Studies on ion-exchange membranes. II. Measurement of the anisotropic conductance of Nafion®. *J Electroanal Chem*. 1998. doi:10.1016/S0022-0728(97)00408-7

279. Anantaraman AV, Gardner CL. Studies on ion-exchange membranes. Part 1. Effect of humidity on the conductivity of Nafion®. *J Electroanal Chem*. 1996;414(2):115-120. doi:10.1016/0022-0728(96)04690-6

280. Badessa TS, Shaposhnik VA. ELECTRICAL CONDUCTANCE STUDIES ON ION EXCHANGE MEMBRANE USING CONTACT-DIFFERENCE METHOD. *Electrochim Acta*. 2017;231:453-459. doi:10.1016/j.electacta.2017.02.108

281. Silva R., De Francesco M, Pozio A. Tangential and normal conductivities of Nafion® membranes used in polymer electrolyte fuel cells. *J Power Sources*. 2004;134(1):18-26. doi:10.1016/j.jpowsour.2004.03.028

282. Rikukawa M, Sanui K. Proton-conducting polymer electrolyte membranes based on hydrocarbon polymers. *Prog Polym Sci*. 2000. doi:10.1016/S0079-6700(00)00032-0

283. Mohr R, Kudela V, Schauer J, Richau K. Comparison of different cells for resistance determination of freely standing polymer membranes developed for direct methanol fuel cell (DMFC) applications. *Desalination*. 2002;147(1-3):191-

196. doi:10.1016/S0011-9164(02)00533-7

284. Lehmani A, Turq P, Périé M, Périé J, Simonin J-P. Ion transport in Nafion® 117 membrane. *J Electroanal Chem*. 1997;428(1-2):81-89. doi:10.1016/S0022-0728(96)05060-7

285. Okada T, Møller-Holst S, Gorseth O, Kjelstrup S. Transport and equilibrium properties of Nafion® membranes with H+ and Na+ ions. *J Electroanal Chem*. 1998;442(1-2):137-145. doi:10.1016/S0022-0728(97)00499-3

286. Asaka K, Fujiwara N, Oguro K, Onishi K, Sewa S. State of water and ionic conductivity of solid polymer electrolyte membranes in relation to polymer actuators. *J Electroanal Chem*. 2001;505(1-2):24-32. doi:10.1016/S0022-0728(01)00445-4

287. Slade S, Campbell SA, Ralph TR, Walsh FC. Ionic Conductivity of an Extruded Nafion 1100 EW Series of Membranes. *J Electrochem Soc*. 2002;149(12):A1556. doi:10.1149/1.1517281

288. Napoli L, Franco J, Fasoli H, Sanguinetti A. Conductivity of Nafion® 117 membrane used in polymer electrolyte fuel cells. *Int J Hydrogen Energy*. 2014;39(16):8656-8660. doi:10.1016/j.ijhydene.2013.12.066

289. Kamcev J, Sujanani R, Jang E-S, et al. Salt concentration dependence of ionic conductivity in ion exchange membranes. *J Memb Sci*. 2018;547:123-133. doi:10.1016/j.memsci.2017.10.024

290. Yadav R, Fedkiw PS. Analysis of EIS Technique and Nafion 117 Conductivity as a Function of Temperature and Relative Humidity. *J Electrochem Soc*.

2012;159(3):B340-B346. doi:10.1149/2.104203jes

291. Aziz SB, Abidin ZHZ. Electrical Conduction Mechanism in Solid Polymer Electrolytes: New Concepts to Arrhenius Equation. *J Soft Matter*. 2013;2013:1-8. doi:10.1155/2013/323868

292. Stenina IA, Sistat P, Rebrov AI, Pourcelly G, Yaroslavtsev AB. Ion mobility in Nafion-117 membranes. *Desalination*. 2004. doi:10.1016/j.desal.2004.02.092

293. Peron J, Mani A, Zhao X, et al. Properties of Nafion® NR-211 membranes for PEMFCs. *J Memb Sci*. 2010;356(1-2):44-51. doi:10.1016/j.memsci.2010.03.025

294. Spurgeon JM, Walter MG, Zhou J, Kohl PA, Lewis NS. Electrical conductivity, ionic conductivity, optical absorption, and gas separation properties of ionically conductive polymer membranes embedded with Si microwire arrays. *Energy Environ Sci*. 2011;4(5):1772. doi:10.1039/c1ee01028j

295. Lee CH, Park HB, Lee YM, Lee RD. Importance of Proton Conductivity Measurement in Polymer Electrolyte Membrane for Fuel Cell Application. *Ind Eng Chem Res*. 2005;44(20):7617-7626. doi:10.1021/ie0501172

296. Xie G, He F, Liu X, Si L, Guo D. Sessile multidroplets and salt droplets under high tangential electric fields. *Sci Rep*. 2016;6(1):25002. doi:10.1038/srep25002

297. Yeo RS. Ion Clustering and Proton Transport in Nafion Membranes and Its Applications as Solid Polymer Electrolyte. *J Electrochem Soc*. 1983;130(3):533. doi:10.1149/1.2119746

298. Bolton GR, Boesch AW, Basha J, LaCasse DP, Kelley BD, Acharya H. Effect of protein and solution properties on the donnan effect during the ultrafiltration of

proteins. *Biotechnol Prog*. 2011;27(1):140-152. doi:10.1002/btpr.523

299. Kinniburgh DG, Milne CJ, Benedetti MF, et al. Metal Ion Binding by Humic Acid: Application of the NICA-Donnan Model. *Environ Sci Technol*. 1996;30(5):1687-1698. doi:10.1021/es950695h

300. Roy Y, Warsinger DM, Lienhard JH. Effect of temperature on ion transport in nanofiltration membranes: Diffusion, convection and electromigration. *Desalination*. 2017. doi:10.1016/j.desal.2017.07.020

301. Biesheuvel PM, Zhao R, Porada S, van der Wal A. Theory of membrane capacitive deionization including the effect of the electrode pore space. *J Colloid Interface Sci*. 2011;360(1):239-248. doi:10.1016/j.jcis.2011.04.049

302. Nanda SS, Kim MJ, Yeom KS, An SSA, Ju H, Yi DK. Raman spectrum of graphene with its versatile future perspectives. *TrAC Trends Anal Chem*. 2016;80:125-131. doi:10.1016/j.trac.2016.02.024

303. Bruna M, Ott AK, Ijäs M, Yoon D, Sassi U, Ferrari AC. Doping Dependence of the Raman Spectrum of Defected Graphene. *ACS Nano*. 2014;8(7):7432-7441. doi:10.1021/nn502676g

304. Eckmann A, Park J, Yang H, et al. Raman Fingerprint of Aligned Graphene/h-BN Superlattices. *Nano Lett*. 2013;13(11):5242-5246. doi:10.1021/nl402679b

305. Yoon D, Moon H, Cheong H, Choi J, Choi J, Park B. Variations in the Raman Spectrum as a Function of the Number ofGraphene Layers. *J Korean Phys Soc*. 2009;55(3(2)):1299-1303. doi:10.3938/jkps.55.1299

306. Zabel J, Nair RR, Ott A, et al. Raman Spectroscopy of Graphene and Bilayer under

Biaxial Strain: Bubbles and Balloons. *Nano Lett*. 2012;12(2):617-621. doi:10.1021/nl203359n

307. Seyama H, Soma M, Theng BKG. X-Ray Photoelectron Spectroscopy. In: *Developments in Clay Science*. ; 2013:161-176. doi:10.1016/B978-0-08-098259-5.00007-X

308. Fadley CS. X-ray photoelectron spectroscopy: Progress and perspectives. *J Electron Spectros Relat Phenomena*. 2010. doi:10.1016/j.elspec.2010.01.006

309. Oelhafen P. Practical surface analysis by auger and X-ray photoelectron spectroscopy. *J Electron Spectros Relat Phenomena*. 1984;34(2):203. doi:10.1016/0368-2048(84)80044-4

310. Briggs D. Handbook of X-ray Photoelectron Spectroscopy C. D. Wanger, W. M. Riggs, L. E. Davis, J. F. Moulder and G. E.Muilenberg Perkin-Elmer Corp., Physical Electronics Division, Eden Prairie, Minnesota, USA, 1979. 190 pp. $195. *Surf Interface Anal*. 1981;3(4):v-v. doi:10.1002/sia.740030412

311. TURNER NH. X-RAY PHOTOELECTRON AND AUGER ELECTRON SPECTROSCOPY. *Appl Spectrosc Rev*. 2000;35(3):203-254. doi:10.1081/ASR-100101225

312. Chen C, Levitin G, Hess DW, Fuller TF. XPS investigation of Nafion® membrane degradation. *J Power Sources*. 2007. doi:10.1016/j.jpowsour.2007.03.037

313. Bryce DA, Kitt JP, Harris JM. Confocal Raman Microscopy for Label-Free Detection of Protein–Ligand Binding at Nanopore-Supported Phospholipid Bilayers. *Anal Chem*. 2018;90(19):11509-11516.

doi:10.1021/acs.analchem.8b02791

314. Achtyl JL, Unocic RR, Xu L, et al. Aqueous proton transfer across single-layer graphene. *Nat Commun*. 2015;6(1):6539. doi:10.1038/ncomms7539

315. Losurdo M, Giangregorio MM, Capezzuto P, Bruno G. Graphene CVD growth on copper and nickel: Role of hydrogen in kinetics and structure. *Phys Chem Chem Phys*. 2011. doi:10.1039/c1cp22347j

316. Strupinski W, Grodecki K, Wysmolek A, et al. Graphene epitaxy by chemical vapor deposition on SiC. *Nano Lett*. 2011. doi:10.1021/nl200390e

317. Wang X, You H, Liu F, et al. Large-Scale Synthesis of Few-Layered Graphene using CVD. *Chem Vap Depos*. 2009;15(1-3):53-56. doi:10.1002/cvde.200806737

318. Zhang Y, Zhang L, Zhou C. Review of Chemical Vapor Deposition of Graphene and Related Applications. *Acc Chem Res*. 2013;46(10):2329-2339. doi:10.1021/ar300203n

319. O'Hern SC, Stewart CA, Boutilier MSH, et al. Selective Molecular Transport through Intrinsic Defects in a Single Layer of CVD Graphene. *ACS Nano*. 2012;6(11):10130-10138. doi:10.1021/nn303869m

320. Zhu D, Liu X, Gao Y, et al. In Situ Observation of Thermal Proton Transport through Graphene Layers. *ACS Nano*. 2017;11(9):8970-8977. doi:10.1021/acsnano.7b03359

321. Kidambi PR, Terry RA, Wang L, et al. Assessment and control of the impermeability of graphene for atomically thin membranes and barriers. *Nanoscale*. 2017;9(24):8496-8507. doi:10.1039/c7nr01921a

322. George SM. Atomic Layer Deposition: An Overview. *Chem Rev*. 2010;110(1):111-131. doi:10.1021/cr900056b

323. Puurunen RL. A Short History of Atomic Layer Deposition: Tuomo Suntola's Atomic Layer Epitaxy. *Chem Vap Depos*. 2014;20(10-11-12):332-344. doi:10.1002/cvde.201402012

324. Johnson RW, Hultqvist A, Bent SF. A brief review of atomic layer deposition: From fundamentals to applications. *Mater Today*. 2014;17(5):236-246. doi:10.1016/j.mattod.2014.04.026

325. Lim BS, Rahtu A, Gordon RG. Atomic layer deposition of transition metals. *Nat Mater*. 2003;2(11):749-754. doi:10.1038/nmat1000

326. Pinna N, Knez M. *Atomic Layer Deposition of Nanostructured Materials*. (Pinna N, Knez M, eds.). Weinheim, Germany: Wiley-VCH Verlag GmbH & Co. KGaA; 2011. doi:10.1002/9783527639915

327. Aaltonen T, Ritala M, Sajavaara T, Keinonen J, Leskelä M. Atomic Layer Deposition of Platinum Thin Films. *Chem Mater*. 2003;15(9):1924-1928. doi:10.1021/cm021333t

328. Hwang CS. *Atomic Layer Deposition for Semiconductors*. (Hwang CS, ed.). Boston, MA: Springer US; 2014. doi:10.1007/978-1-4614-8054-9

329. Dasgupta NP, Meng X, Elam JW, Martinson ABF. Atomic Layer Deposition of Metal Sulfide Materials. *Acc Chem Res*. 2015;48(2):341-348. doi:10.1021/ar500360d

330. Puurunen RL. Surface chemistry of atomic layer deposition: A case study for the

trimethylaluminum/water process. *J Appl Phys*. 2005;97(12):121301. doi:10.1063/1.1940727

331. Tripp MK, Stampfer C, Miller DC, et al. The mechanical properties of atomic layer deposited alumina for use in micro- and nano-electromechanical systems. *Sensors Actuators A Phys*. 2006;130-131:419-429. doi:10.1016/j.sna.2006.01.029

332. Meyer J, Schneidenbach D, Winkler T, et al. Reliable thin film encapsulation for organic light emitting diodes grown by low-temperature atomic layer deposition. *Appl Phys Lett*. 2009;94(23):233305. doi:10.1063/1.3153123

333. Meyer J, Görrn P, Hamwi S, Johannes HH, Riedl T, Kowalsky W. Indium-free transparent organic light emitting diodes with Al doped ZnO electrodes grown by atomic layer and pulsed laser deposition. *Appl Phys Lett*. 2008. doi:10.1063/1.2975176

334. Groner MD, George SM, McLean RS, Carcia PF. Gas diffusion barriers on polymers using Al2O3 atomic layer deposition. *Appl Phys Lett*. 2006;88(5):051907. doi:10.1063/1.2168489

335. Toikkanen O, Nisula M, Pohjalainen E, et al. Al2O3 coating grown on Nafion membranes by atomic layer deposition. *J Memb Sci*. 2015;495:101-109. doi:10.1016/j.memsci.2015.08.021

336. Wang X, Tabakman SM, Dai H. Atomic layer deposition of metal oxides on pristine and functionalized graphene. *J Am Chem Soc*. 2008;130(26):8152-8153. doi:10.1021/ja8023059

337. Yankowitz M, Xue J, LeRoy BJ. Graphene on hexagonal boron nitride. *J Phys*

*Condens Matter*. 2014;26(30):303201. doi:10.1088/0953-8984/26/30/303201

338. Alem N, Erni R, Kisielowski C, Rossell MD, Gannett W, Zettl A. Atomically thin hexagonal boron nitride probed by ultrahigh-resolution transmission electron microscopy. *Phys Rev B - Condens Matter Mater Phys*. 2009. doi:10.1103/PhysRevB.80.155425

339. Zhang J, Hong Y, Yue Y. Thermal transport across graphene and single layer hexagonal boron nitride. *J Appl Phys*. 2015;117(13):134307. doi:10.1063/1.4916985

340. Chen C-C, Li Z, Shi L, Cronin SB. Thermal interface conductance across a graphene/hexagonal boron nitride heterojunction. *Appl Phys Lett*. 2014;104(8):081908. doi:10.1063/1.4866335

341. Geick R, Perry CH, Rupprecht G. Normal modes in hexagonal boron nitride. *Phys Rev*. 1966. doi:10.1103/PhysRev.146.543

342. Liu Z, Song L, Zhao S, et al. Direct Growth of Graphene/Hexagonal Boron Nitride Stacked Layers. *Nano Lett*. 2011;11(5):2032-2037. doi:10.1021/nl200464j

343. Reich S, Ferrari AC, Arenal R, Loiseau A, Bello I, Robertson J. Resonant Raman scattering in cubic and hexagonal boron nitride. *Phys Rev B*. 2005;71(20):205201. doi:10.1103/PhysRevB.71.205201

344. Pakdel A, Bando Y, Golberg D. Nano boron nitride flatland. *Chem Soc Rev*. 2014;43(3):934-959. doi:10.1039/C3CS60260E

345. Ci L, Song L, Jin C, et al. Atomic layers of hybridized boron nitride and graphene domains. *Nat Mater*. 2010;9(5):430-435. doi:10.1038/nmat2711

346. Kennedy BJ. Structural trends in pyrochlore-type oxides. *Phys B Condens Matter*. 1997;241-243:303-310. doi:10.1016/S0921-4526(97)00570-X

347. Kennedy BJ, Hunter BA, Howard CJ. Structural and Bonding Trends in Tin Pyrochlore Oxides. *J Solid State Chem*. 1997;130(1):58-65. doi:10.1006/jssc.1997.7277

348. Gardner JS, Gingras MJP, Greedan JE. Magnetic pyrochlore oxides. *Rev Mod Phys*. 2010;82(1):53-107. doi:10.1103/RevModPhys.82.53

349. Wilde P. Defects and diffusion in pyrochlore structured oxides. *Solid State Ionics*. 1998;112(3-4):173-183. doi:10.1016/S0167-2738(98)00190-8

350. Minervini L, Grimes RW, Sickafus KE. Disorder in Pyrochlore Oxides. *J Am Ceram Soc*. 2004;83(8):1873-1878. doi:10.1111/j.1151-2916.2000.tb01484.x

351. Subramanian, M A GA and GV subba R. Oxide Pyrochlores- A review. *Prog Solid State Chem*. 1983;15(2):55-143.

352. Sickafus KE. Radiation Tolerance of Complex Oxides. *Science (80- )*. 2000;289(5480):748-751. doi:10.1126/science.289.5480.748